On the Deformation Mechanics of Hyperelastic Porous Materials

by

Christopher Salisbury

A thesis
presented to the University of Waterloo
in fulfillment of the
thesis requirement for the degree of
Doctor of Philosophy
in
Mechanical Engineering

Waterloo, Ontario, Canada, 2011

I hereby declare that I am the sole author of this thesis. This is a true copy of the thesis, including any required final revisions, as accepted by my examiners.

I understand that my thesis may be made electronically available to the public.

Abstract

The understanding of the deformation mechanics within porous structures is an important field of study as these materials exist in nature as well as can be manufactured industrially influencing our lives daily. The motivation of the research contained within this manuscript was inspired by the desire to understand the mechanics of an elastomeric closed–cell porous material. This type of porous material is often used in load–bearing applications such as sport helmet liners and packing material which can be subjected to large deformations at high rates. Additionally, short term transient effects were explored/

In order to investigate the deformation mechanics of a closed cell elastomeric foam, a polychloroprene (neoprene) material was chosen as it was available in both rubber form and a foam with relatively consistent cell size. Compression tests were conducted on the polychloroprene rubber at strain rates ranging from 0.001/s to 2700/s which identified that it had a hyper–viscoelastic behaviour with a significant strain rate dependence. A newly developed constitutive model was created to capture the response of the polychloroprene rubber.

A coupled finite element model of the polychloroprene foam was created and compared to experimental tests for validation. The model slightly over predicted the stress level response of the experimental tests. The model was used to identify momentum dissipation mechanisms that contributed to the low wave speed measurement of approximately 70 m/s determined from the model. The investigation of wave transit times through use of the model was key to interpreting experimental data. Of the morphological factors investigated, it was determined that wall thickness had the most significant impact on the stress response of the foam. The pore–scale model was useful for visualizing wave propagation effects and deformation mechanics which was not feasible experimentally.

Acknowledgments

There are numerous people whom over the many years I spent at the University of Waterloo I had the pleasure of sharing my academic experience. From the old crew Dino Oliveira, Blake Hodgins, Tom Gawel, Alex Bardelcik and Sooky Winkler, my many thanks for keeping life interesting. I would like to thank Dr. Hari Simha for answering my "What does this mean?" questions without hesitation. Thank you to Jose Imbert who stood with me as we marched to the beat of a different drum.

Thank you to Laurie Wilfong for making sure that I got paid every month when I worked at UW, Andy Barber for keeping me from getting hurt from everything electrical, the MME administration staff for helping me wade through the University's bureaucracy and the crew of the Engineering machine shop.

I would like to thank Dr. Duane Cronin for his support and generosity from the time he was my TA to the completion of my doctoral thesis. Thank you to Dr. Michael Worswick who supported me through my graduate studies and the start of my professional career. I would also like to thank Dr. Fue–Sang Lien for his thought provoking conversations and guidance throughout this work.

Most of all, I would like to thank my wife and my sons. Of all the people in my life, they bore the consequences of my decision to do another degree. For the time with them that I sacrificed to conduct this research and their continuous encouragement to "finish your book" I shall forever be indebted.

For Karen, Connor and Logan

Table of Contents

List of Tables

List of Figures

Nomenclature

α	Hyperelastic constitutive model constants
β	Viscoelastic constitutive model constant
τ	Kirchhoff stress
$\mathbf{B}$	Left Cauchy deformation tensor, $\mathbf{F}\mathbf{F}^{\mathbf{T}}$
$\mathbf{C}$	Right Cauchy deformation tensor, $\mathbf{F}^{\mathbf{T}}\mathbf{F}$
$\mathbf{F}$	Deformation Gradient represented defined as $F_{ij} = \frac{\partial x_i}{\partial X_j}$ where X_j is the reference coordinates of a particle and x_i is the current coordinates of a particle
$\mathbf{n}$	Normal vector
$\mathbf{R}$	Rotation matrix
$\mathbf{U}$	Right stretch tensor
$\mathbf{V}$	Left stretch tensor
$\dot{e}$	Engineering strain rate
ϵ	Logarithmic strain
Γ	Viscoelastic constitutive model modifier
γ	Viscoelastic constitutive model constant
λ_i	Principle stretches, also eigenvalues
μ	Hyperelastic constitutive model constants
ρ	Density
σ	Cauchy stress
^{e}	Elastic portion

^{T}	Sum of the elastic and viscoelastic portions
^{v}	Viscoelastic portion
C_0	Initial wave speed
e	Engineering strain
G	Relaxation function, kernel function in convolution integral
H	History variable
I_1	First invariant
I_2	Second invariant
I_3	Third invariant
P	Pressure
p	Arbitrary pressure
U_0	Velocity of quiescent gas
U_P	Particle velocity
U_S	Wave velocity
V	Volume
W	Strain energy

Chapter 1

Introduction

Porous materials are classified based on whether they are comprised of open or closed cells. Open cell materials generally have an interconnected lattice type structure such as that shown in figure 1.1a) where the pores (also called cells) of the material are open to each other. A closed cell porous material has pores which are approximately spherical in nature and is separated by walls as in figure 1.1b). In industrial applications, porous materials such as an aluminium foam, are increasingly being used to create light weight but strong structures. Other foams, such as those created from polymers, are used in a wide variety of applications ranging from seat cushions to protective equipment liners as seen on the inside of helmets [1].

In nature, materials ranging from bone and lungs to the wood found in trees all have a porous structure [3]. Bones, which are relatively stiff compared to most biological material, have a porous structure which reduces their inherent density, and thus mass, while still providing the required strength to support the body's structure. In contrast, lungs, which are hyperelastic in nature, contain pores called alveoli which facilitated the transfer of oxygen to the blood stream (and carbon dioxide out of the blood stream). The human lung is comprised of approximately three million alveoli which contain approximately

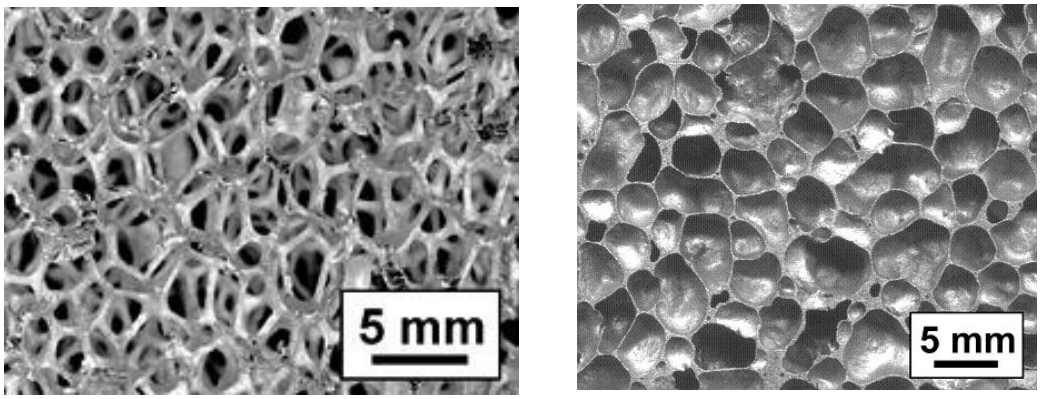

a) Open cell metal foam. b) Closed cell metal foam.

Figure 1.1: Example of open cell a) and closed cell b) foams in metal. [2]

three litres of air when fully inflated [4]. Figure 1.2 is a scanning electron micrograph of an alveolar duct (AD in the figure) and alveoli (A in the figure) of a human taken at 240 times magnification. As identified in the figure, the lung structure is not a fully closed cell structure.

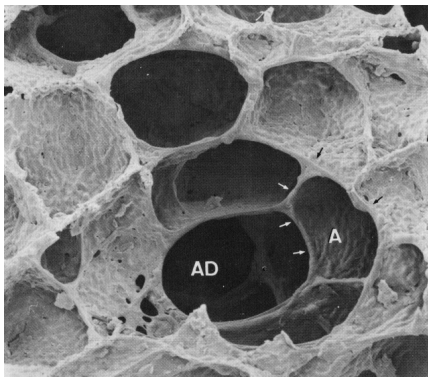

Figure 1.2: Human alveoli (A) and alveolar duct (AD) (240X magnification) from [4].

The motivation of the research contained within this manuscript was inspired by the desire to understand the mechanics of an elastomeric (loosely described here as a material which recovers its original shape after deformation) porous material. Industrial

manufactured porous materials are often used in load–bearing applications such as sport helmet liners and packing material which can be subjected to large deformations at high rates [5][6][7]. Several researchers have identified unique properties in porous materials such as a reduced wave speed [8][9][10]. For example, experimental tests conducted identified that the speed at which a wave propagates through the lung structure was approximately 30–40 m/s [11][12][13][14] which is below that of its constituent materials [15]. Additionally, researchers have identified that porous materials significantly attenuate pressure waves as they propagate [16][17][18][19]. As such, an in–depth understanding of how elastomeric porous materials deform and the factors which contribute to the mechanical response was desired.

Historically, deformation mechanics in porous media have been viewed from the continuum scale where the characteristics of individual pores are ignored such as in the field of poroelasticity [20][21][22][23]. Although these types of models are generally thought to adequately describe the mechanical properties of porous materials on a macro–scale level, they don't describe the behaviour of the material on the micro–scale level which is important when trying to identify the various factors upon which the material depends [6]. As such, the purpose of this work was to conduct a fundamental study to determine the effect of the presence of closed cells on the deformation response of elastomeric porous materials.

The objectives of the present research were: to construct and validate a numerical model of an elastomeric closed–cell porous material and to identify factors which affect the response of the elastomeric closed–cell porous material. The morphological factors investigated were: cell size, cell wall thickness and anisotropy. Additionally, loading rate and the effect the enclosed air had on the response were investigated.

In order to create a numerical model of a porous material which had realistic con-

stituent properties, an investigation was undertaken at the onset of the study to identify a porous material whose constituent material properties could be measured at the macroscale level separately. *Id est*, it is extremely difficult to measure the properties of the cell walls at the pore scale and so a porous material whose cellular material properties could be measure was desired. Fortuitously, a polychloroprene (also know as neoprene) foam (trade name G207) fabricated by Rubatex International LLC was an ideal candidate for this study. Initial tests of the polychloroprene foam indicated that it was elastomeric and was comprised of closed cells relatively equal in size. Rubatex International LLC was also able to provide sheets of solid polychloroprene rubber from the same manufacturing run prior to the foaming process. Additionally, the foaming process used had the added benefit that it was done through a nitrogen injection process, outlined subsequently, and not done chemically as with many polymeric foams which may alter the cellular material properties.

Figure 1.3 shows the general fabrication process for the foamed polychloroprene. Polychloroprene chips are put in to a mixer where they were heated. Following this, the material was then extruded into sheets where they then undergo a vulcanization process to cure the material. This is accomplished using a zinc oxide formulation. After the curing stage, the sheet material is subjected N_2 gas at a pressure of 34.5 MPa (5000 psi) for 1.5 hours which created the closed cell structure of the foam. Sheets of solid polychloroprene prior to the foaming process were extracted from the production line to facilitate testing on the foam's constituent material as indicated in the figure.

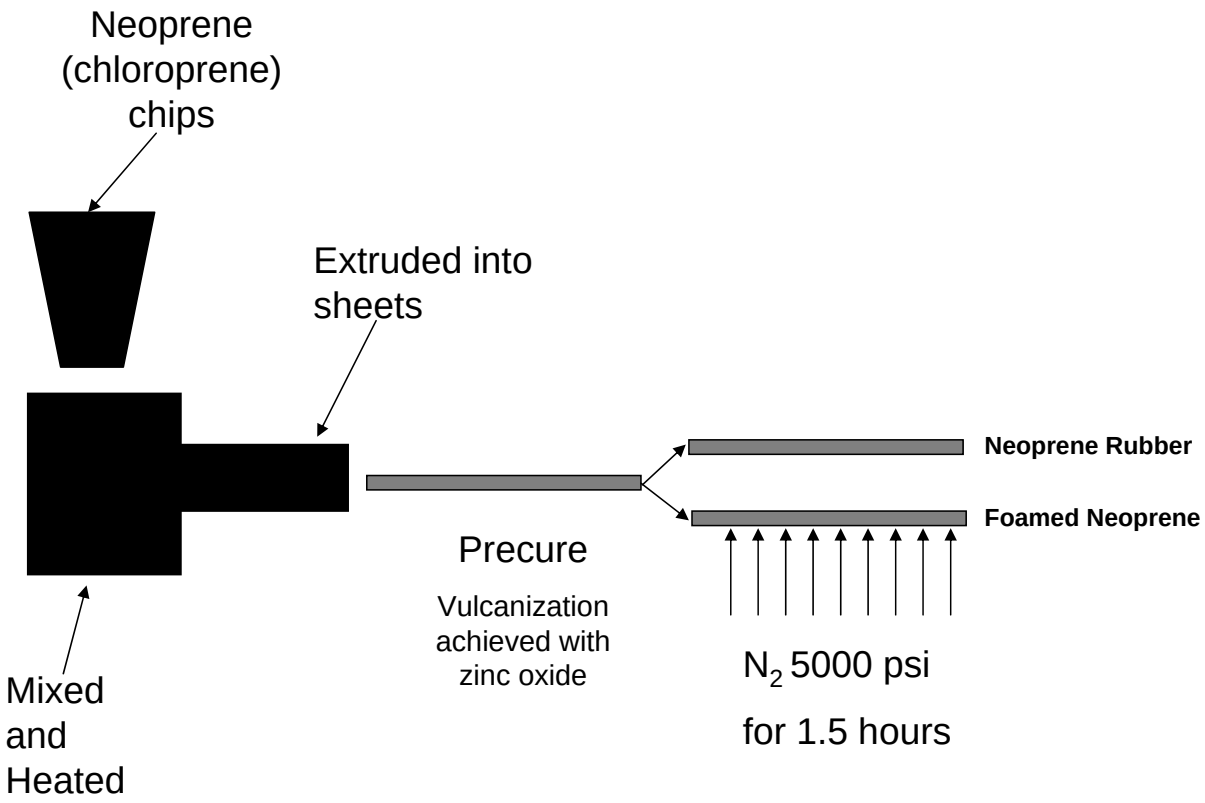

Figure 1.3: A schematic of the foaming process.

The research methodology used in this manuscript is shown in figure 1.4. In the figure, the blue boxes indicated the material which was examined, the black boxes indicate experimental tasks, the red boxes indicate modeling tasks and the green boxes represent outcomes of the model.

The process to create the numerical model of the elastomeric foam material involved three major components. The first task was to characterize the rubber polychloroprene at a range of strain rates as detailed in chapter 3 (material testing box figure 1.4). The second major component was to determine the physical structure of the foam (microscopic analysis box figure 1.4) and represent it geometrically (cellular geometric representation box figure 1.4). This was accomplished through microscopic analysis as detailed in chapter 3 and its corresponding geometric representation in chapter 5. The third major task

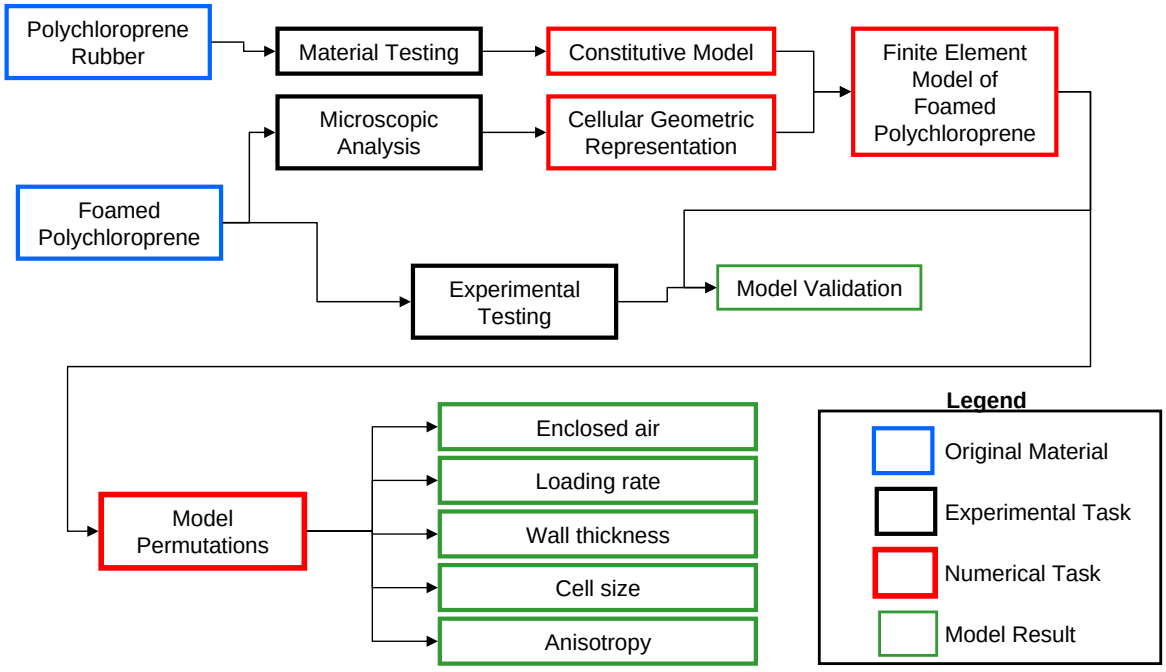

Figure 1.4: Schematic of research methodology.

was to use this data to determine constants for a constitutive material model which was implemented into a finite element program which is discussed in chapter 4 (constitutive model box figure 1.4). Validation of the numerical model (model validation box figure 1.4) was done through comparison of the results of experimental tests performed at multiple strain rates to the numerical values as outlined in chapter 5. The experiments performed on the polychloroprene foam were similar to those performed on the polychloroprene rubber, however, it was not the intent of this study to characterize the foam at a macroscale level but instead to identify if the foamed polychloroprene material had a dependence on strain rate and to provide a set of experimental data against which the numerical models developed could be validated. The factors which affect the response of the polychloroprene foam are discussed in chapter 5(model permutations box figure 1.4). Chapter 2 contains background aspects of wave propagation in materials,

modelling methodologies, experimental techniques used, and a discussion of the preliminaries of constitutive models. Chapter 6 contains conclusions and recommendations from the study.

Chapter 2

Background

This chapter is composed of five sections. Section 2.1 details how stress waves develop, propagate and interact within materials. Section 2.2 discusses methods used to model fluid–structure interaction. Section 2.3 discusses models available in the literature which have been used to understand the deformation of foams at the pore level. Section 2.4 details the background for the dynamics experiments conducted. Section 2.5 discusses the preliminaries of constitutive modelling of visco–elastic material.

2.1 Waves Mechanics

2.1.1 General Wave Propagation

One can imagine that a material is composed of a series of particles as identified in figure 2.1. The figure shows a sequence of times during which a wave, which is generated by F_A applied to one face, propagates through the material. At $t = 0$, the force is initially applied to the left face and at that moment all particles within the material are at rest. At some time later, $t = \Delta t$, the force applied to the left face has caused the particles on

the left to move to the right where they contact their neighbours. At time $t = 2\Delta t$ more of the particles are moving to the right and contacting with their neighbours. At time $t = 3\Delta t$, the propagation of the collisions between the particles has reached the right side where the force, F_M, is measured. Prior to $t = 3\Delta t$, F_M is zero. The rate at which the momentum transferred from one particle to another is called the wave speed. As will be discussed later, the speed at which the wave propagates is dependent on factors such as the stiffness and density of the material. Since there is a finite speed of propagation, the force measured lags the force applied by a function of the wave speed and the distance between the two ends.

The timescale of the force being applied in comparison to the wave speed in the material was important. For instance, consider a "quasi-static" compression test of an aluminum cylinder, 100 mm in length, being compressed at a rate of 0.01 mm/s. Assuming the cylinder remains elastic, and considering wave propagation in one dimension only, the wave speed in aluminum for this case is approximately 6000 m/s [24]. Therefore, the lag in time between the force being applied and that measured at the opposite end is approximately 1.67 $\times 10^{-5}$ s or 16.7 μs. In comparison, the length of time it would take the sample to compress 1 mm (1 % of its overall length) would be approximately 100 s or almost 6 million times slower than it took for the wave to propagate to the end of the cylinder. To an observer, the delay between the applied force and that measured at the end would be insignificant. However, if the cylinder was loaded at a much faster rate, say 10 m/s, the length of time for the cylinder to compress 1 mm would be 100 μs or only 6 times slower. In this case, the delay between the time the force was applied and the time the force was measured becomes significant.

In reality, the particles shown in figure 2.1 are atoms which oscillate about an equilibrium position. The atoms are joined, in essence, through interatomic forces. Wave

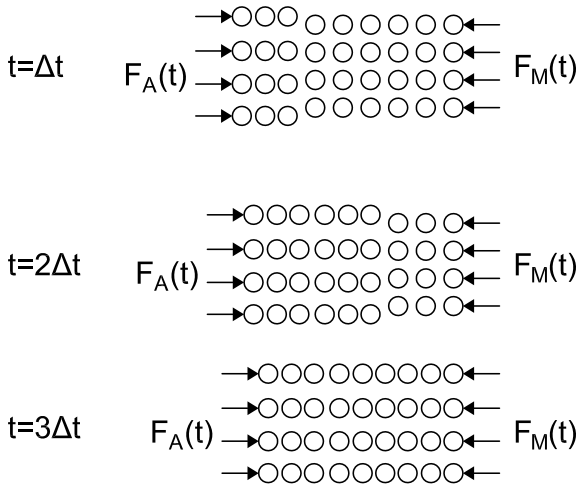

Figure 2.1: Example of wave propagating through media composed of small particles.

propagation is then caused by the transfer of momentum from one atom to its neighbour. A more detail discussion of wave propagation at the atom level is given in reference [24].

2.1.2 Formation of a Finite Wave

The formation of a finite wave can be understood by visualizing a piston, of unit area, moving in a cylinder which contain stationary gas as shown in figure 2.2. In this model, the piston moves into an area of undisturbed gas. The thick line $(1/U_P)$ of figure 2.3 shows that the piston is gradually accelerated to a constant velocity. U_P is referred to as the particle velocity. This diagram is called a "x–t" diagram and is used to show the propagation of waves as a function of time and position. Note that time is plotted on the ordinal axis meaning that the slope of a line is the inverse of velocity. As the piston begins to move, a region of compressed gas is formed in front of the piston, figure 2.2, which propagates at c_H representing the head of the compressed region in figure 2.3. At a small instant of time later, the piston has moved slightly farther and a second wave, which propagates at $u+c$, the particle speed plus the wave propagation speed, is created.

Since this wave is propagating through a region which has already been compressed, the current speed at which it propagates, c, is greater than that of the head, c_H. This is represented by a line of reduced slope as shown in figure 2.3. This process continues until the piston begins to move at a constant velocity at time t_a. The last wave which propagates from the piston into the compression region is moving at $U_P + c_T$, where c_T is the speed of the tail of the wave. In reality, this is a continuous process and the $1/(U_P + c_T)$ and the $1/c_H$ lines bound the compression region. As shown in figure 2.3, the waves in the compression region coalesce (since $U_P + c_T > c_H$) into a steep wave front (called a shock) at t_b as shown in figures 2.2 and 2.3. This wave propagates at U_S which is greater than U_P as shown at time t_c in figures 2.2 and 2.3.

If the piston had stopped moving after a very short time period (for illustration purposes, say the first characteristic line in figure 2.3), the wave created would correspond to an infinitesimal wave or sound wave. Across this wave front, the change in state variables (pressure, temperature, density) are very small in comparison to a finite wave. The equations which describe the motion of these waves are similar to those detailed in the subsequent section, however since the change in state variables are small, the equations are often simplified ignoring the higher order terms. Similar to the discussion in the previous section, time scales for the creation of the finite wave are important.

This process can be further illustrated by examining figure 2.4 which shows pressure as a function of propagation distance as outlined by Hayes [25]. The initial disturbance centred about point A, propagates to the right. Since different parts of the wave move at different velocities the wave changes shape as shown about B. Given that the wave at point two propagates faster than that a point one, $c_2 + u_2 > c_1 + u_1$, the wave steepen until a nearly discontinuous front is formed as shown about point C. The equations which govern the motion of these waves are detailed in the subsequent section. Although the

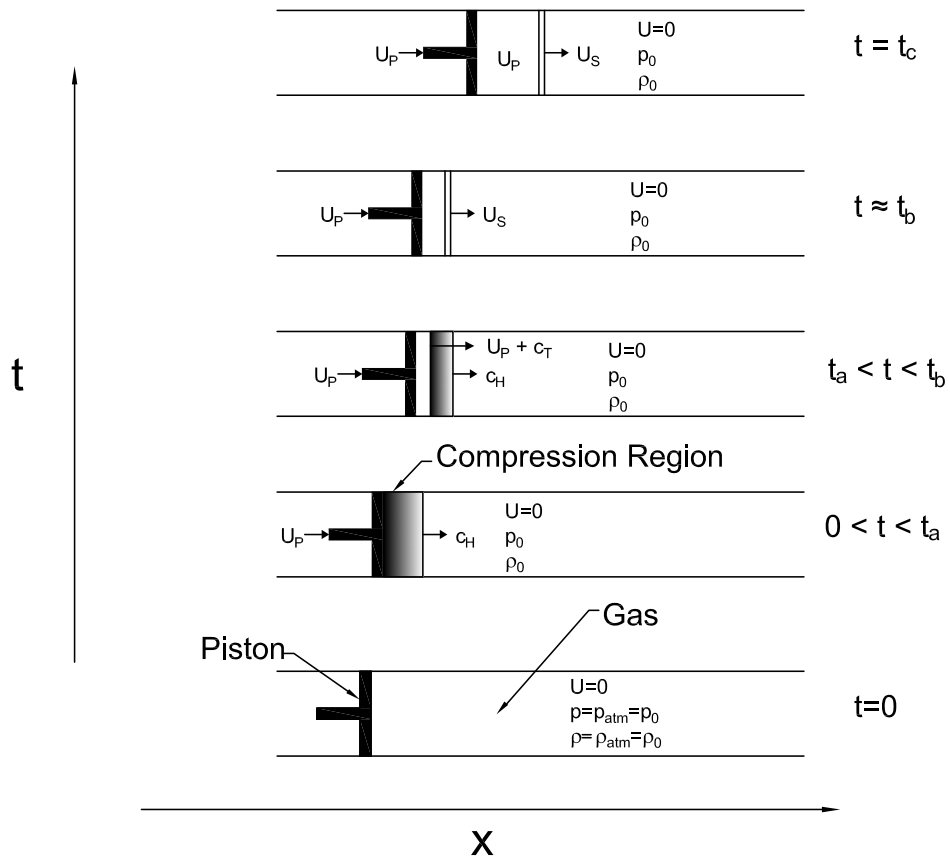

Figure 2.2: Model of a piston moving in a cylinder of stationary gas.

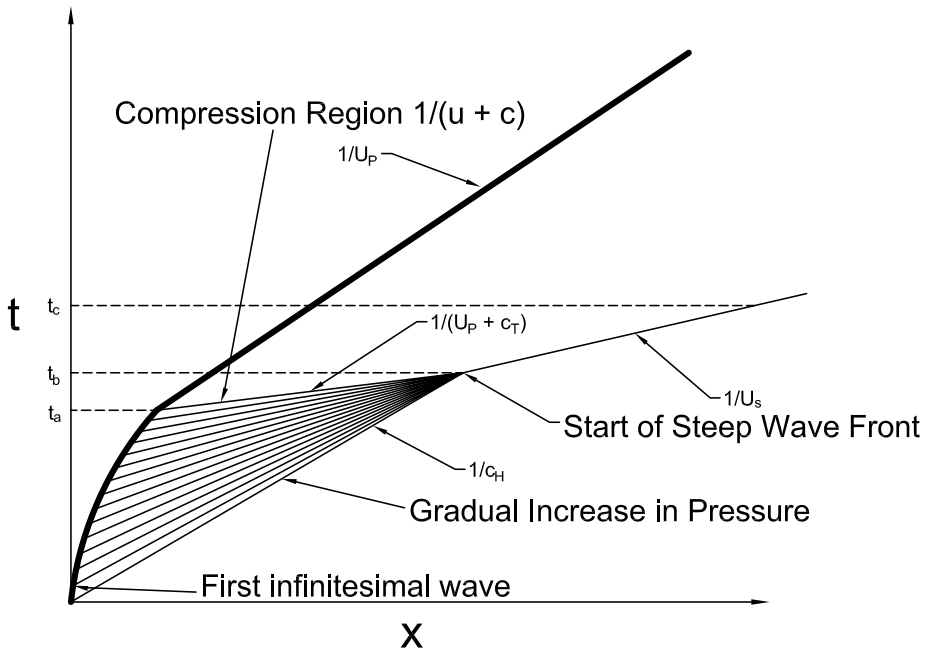

Figure 2.3: x–t diagram showing finite wave formation.

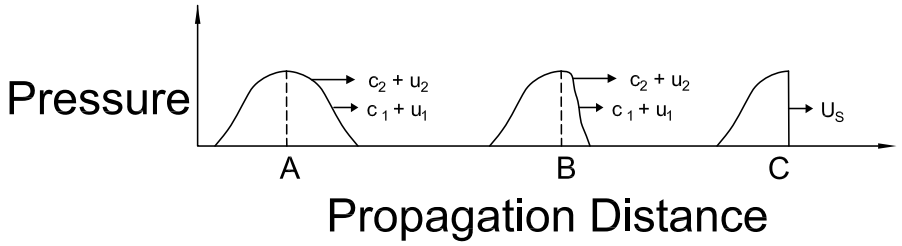

Figure 2.4: Illustration of the transition from a wave with a gradual increase in pressure to the formation of a shock wave.

subsequent sections focus on shock waves, the governing equations of mass, momentum and energy encompasses the range of finite waves. The reader is referred to the work by Anderson[26] or Yahya [27] for further explanation of the development of finite waves as they transition from infinitesimal waves to shock waves.

2.1.3 Governing Equations

In 1870 Rankine [28] presented the governing equations for mass, momentum and energy conservation across a shock. Hugoniot [29] independently formulated the same equations in 1887. Consequently, equations that describe the change in properties across a shock wave are often called the Rankine–Hugoniot relations. This section outlines the governing equations across shock waves. Appendix A contains further discussion regarding equations which describe particle motion.

For the purposes of the development of these equations, the shock wave is considered to be of negligible thickness. The development of the conservation equations follows from the analysis of the flow from the viewpoint of the shock as illustrated in figure 2.5. The variables shown in the figure and used in the development of the conservation equations are given in the subsequent list.

- ρ_0, p_0, e_0 and U_0 are the density, pressure and energy of the material into which the shock wave is propagating.
- ρ, p, e and U_P are the density, pressure, energy and particle velocity behind the shock wave.
- U_S is the velocity of the shock wave.
- C_0 is the speed of sound in the undisturbed material.

- V is the relative volume given as $1/\rho$.

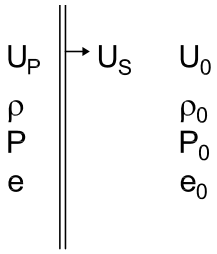

Figure 2.5: Illustration of a shock wave across which properties vary.

If the shock wave is used as a frame of reference (moving frame of reference) then the material on the stationary side would appear to move towards the observer at U_S (assuming that the material is initially stationary i.e. U_0=0) and away at $U_S - U_P$.

Conservation of Mass In the absence of mass to energy conversion, the flow of mass into the shock front must be equal to the flow of mass out of the shock front thereby conserving mass. If the area of the shock front in figure 2.5 is A, then the conservation of mass for can be expressed mathematically as

$$\underbrace{A\rho_0 \left(U_S - U_0\right) dt}_{Mass\ In} = \underbrace{A\rho \left(U_S - U_P\right) dt}_{Mass\ Out} \tag{2.1}$$

which reduces to

$$\rho_0 U_S = \rho \left(U_S - U_P\right) \tag{2.2}$$

for a stationary material.

Conservation of Momentum In essence, the conservation of momentum principal states that the change in momentum (the product of mass and velocity) of a body over time is balanced by the net force acting on the body. Forces are usually split into the

two categories of body forces and surface forces. Body forces are forces which act upon a body from afar such as gravity, and surface forces are forces which develop from direct contact such as pressure. Across a shock wave, body forces and shear surface forces are usually neglected and so the change in momentum is equal to the applied impulse (Newton's second law). The applied impulse at a shock interface can be expressed as

$$\begin{aligned} Impulse &= Force \bullet dt \\ &= (PA - P_0 A)\, dt. \end{aligned} \tag{2.3}$$

The change in momentum can be expressed as

$$d\,(Mass \bullet Velocity) = \underbrace{\rho A\,(U_S - U_P)\,dt}_{mass}\ \underbrace{U_P}_{velocity} - \underbrace{\rho_0 A\,(U_S - U_0)\,dt}_{mass}\ \underbrace{U_0}_{velocity}. \tag{2.4}$$

Equating equations 2.3 and 2.4 results in

$$\rho A\,(U_S - U_P) dt U_P - \rho_0 A\,(U_S - U_0) dt U_0 = (PA - P_0 A)\, dt \tag{2.5}$$

which simplifies to

$$\rho\,(U_S - U_P)\,U_P - \rho_0\,(U_S - U_0)\,U_0 = (P - P_0)\,. \tag{2.6}$$

Rearranging equation 2.2 for ρ and substituting into equation 2.5 gives

$$\frac{\rho_0 U_S}{(U_S - U_P)}\,(U_S - U_P)\,U_P - \rho_0\,(U_S - U_0)\,U_0 = (P - P_0) \tag{2.7}$$

which simplifies to

$$\rho_0 U_S U_P - \rho_0 \left(U_S - U_0\right) U_0 = \left(P - P_0\right). \tag{2.8}$$

If $U_0 = 0$ this further reduces to

$$\left(P - P_0\right) = \rho_0 U_S U_P. \tag{2.9}$$

Conservation of Energy The basis of the conservation of energy is that energy can only change form but cannot be created or destroyed. Thus the change in energy, ΔE, is the sum of the work applied to the material, and the heat addition, Q. The change in work is given as

$$\Delta Work = \underbrace{PA}_{Force}\ \underbrace{U_P dt}_{Distance} - \underbrace{P_0 A}_{Force}\ \underbrace{U_0 dt}_{Distance} \tag{2.10}$$

The change in total energy, ignoring body forces, is a function of the kinetic energy, K and the internal energy, E. Mathematically, these can be expressed as

$$\Delta K = \frac{1}{2}\left[A\rho\left(U_S - U_P\right)dt\right]U_P^2 - \frac{1}{2}\left[A\rho_0\left(U_S - U_0\right)dt\right]U_0^2 \tag{2.11}$$

$$\Delta E = \rho e A\left(U_S - U_P\right)dt - \rho_0 e_0 A\left(U_S - U_0\right)dt \tag{2.12}$$

where e is the internal energy per unit mass. Equating equation 2.10 with the sum of equations 2.11 and 2.12 with $U_0 = 0$ gives

$$PU_P = \frac{1}{2}\rho\left(U_S - U_P\right)U_P^2 + \rho e\left(U_S - U_P\right) - \rho_0 e_0 U_S. \tag{2.13}$$

As before, using the conservation of mass equation and substituting in for ρ results in

$$PU_P = \frac{1}{2}\frac{\rho_0 U_S}{(U_S - U_P)}(U_S - U_P)U_P^2 \tag{2.14}$$

$$+ \frac{\rho_0 U_S}{(U_S - U_P)} e(U_S - U_P) - \rho_0 e_0 U_S \tag{2.15}$$

rearranging becomes

$$PU_P = \frac{1}{2}\rho_0 U_S U_P^2 + \rho_0 U_S (e - e_0) \tag{2.16}$$

which rearranged becomes

$$e - e_0 = \frac{PU_P}{\rho_0 U_S} - \frac{1}{2}\frac{\rho_0 U_S U_P^2}{\rho_0 U_S}. \tag{2.17}$$

Often equation 2.17 is modified further to obtain a different form. If the conservation of momentum equation, equation 2.9, is rearranged for U_P and substituted into equation 2.17, the result is

$$e - e_0 = P\frac{P - P_0}{(\rho_0 U_S)^2} - \frac{1}{2}\frac{(P - P_0)^2}{(\rho_0 U_S)^2}. \tag{2.18}$$

Equation 2.2 can be rearranged to give

$$(\rho_0 - \rho)U_S = -\rho U_P \tag{2.19}$$

which can be combined with the conservation of momentum equation to give

$$(\rho_0 - \rho)U_S = -\rho\frac{(P - P_0)}{\rho_0 U_S} \tag{2.20}$$

rearranging

$$\rho_0 U_S^2 = -\rho \frac{(P - P_0)}{(\rho_0 - \rho)} \tag{2.21}$$

which multiplying both sides by ρ_0 gives

$$(\rho_0 U_S)^2 = -\rho\rho_0 \frac{(P - P_0)}{(\rho_0 - \rho)}. \tag{2.22}$$

If instead of the densities (ρ and ρ_0) the relative volumes (V and V_0) are used, equation 2.22 becomes

$$(\rho_0 U_S)^2 = \frac{(P - P_0)}{(V_0 - V)}. \tag{2.23}$$

Substituting $(\rho_0 U_S)^2$ into equation 2.18 gives

$$e - e_0 = P \frac{(P - P_0)(V_0 - V)}{(P - P_0)} - \frac{1}{2} \frac{(P - P_0)^2 (V_0 - V)}{(P - P_0)} \tag{2.24}$$

which simplifies to

$$e - e_0 = \frac{1}{2} (P + P_0)(V_0 - V). \tag{2.25}$$

Equation 2.25 is referred to as the Hugoniot equation.

Equation of State The equation of state is a relation for e, P and V used to define all equilibrium states that can exist for a material [25]. Thus, if the material behind a shock is in equilibrium, there exists a point where both the equation of state and energy equation are solved simultaneously. In this manner, one can then generate a series of P–V states behind the shock wave for a particular material. This relationship between P

and V is called the Hugoniot. There are several methods for experimentally determining the equation of state as described by Meyers [24]. As indicated by McQueen et al. [30] many materials can be reasonably represented by a linear relationship between U_S and U_P given as

$$U_S = C_0 + sU_P \tag{2.26}$$

where s is an experimentally fit parameter usually around 1.5 [25] and C_0 is the minimum speed at which the wave propagates (sometimes called the sonic speed). Nonlinear terms can be added as discussed in Meyers [24]. Factors such as porosity, large elastic waves or phase changes can cause the U_S–U_P relationship to become non-linear. Given the equation of state given by equation 2.26 which relates U_S to U_P, equation 2.25, in combination with equation 2.17, can be rewritten as

$$P = \frac{C_0^2 \left(V_0 - V_1\right)}{\left[V_0 - s\left(V_0 - V_1\right)\right]^2} \tag{2.27}$$

resulting in a relation for P–V.

An ideal Hugoniot is shown in figure 2.6 as a solid line with a gentle concave upward profile. In reality, most materials do not have such an ideal profile for a variety of reasons such as a material can respond elastically up to a yield point, undergo a phase change, be composed of multiple heterogeneous materials or have irreversible crushing [25]. Shown in the figure are the initial, P_0, V_0, and end states P, V for a shock on the ideal Hugoniot. The line which connects the two points is called the Rayleigh line and its slope is proportional to the square of the shock wave velocity U_S through equation 2.22. An elastic-plastic material is represented by a dashed line in the figure. The point at which the material yields is called the Hugoniot Elastic Limit (HEL) and represents the transition from elastic behaviour to plastic. A similar line to the ideal Hugoniot can be created for

isentropic compression for waves where a steep shock front does not exist.

Consider the three shocked states represented by points A, B and C on the graph for the elastic-plastic material. A separate Rayleigh line exists for each of these three points all with different slopes. Figure 2.7 shows the propagation of the shock wave in an elastic–plastic material with this type of behaviour for the three different shocked states (at offset distances for clarity). At shock state A, only a single shock wave is formed as shown. However, at shock state B, two shocks waves are formed. The first shock wave propagates at a velocity higher than that of the second as can be seen from the difference in the two Rayleigh lines (the one formed at A and then at B, figure 2.6). At point C, two waves are formed again but the second wave travels faster than the first rapidly creating a single wave as shown in figure 2.7.

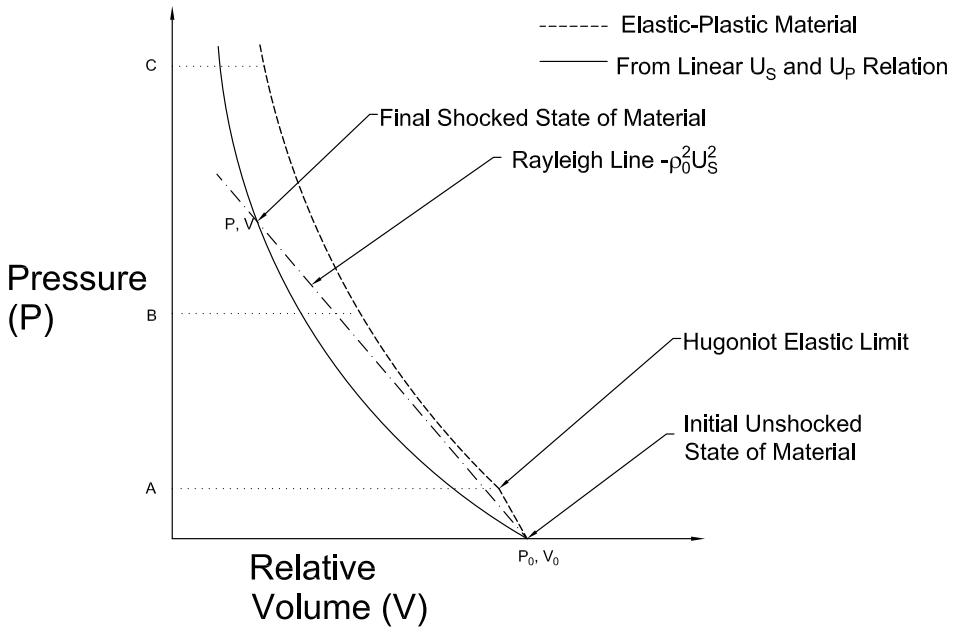

Figure 2.6: Hugoniots for ideal and elastic–plastic material.

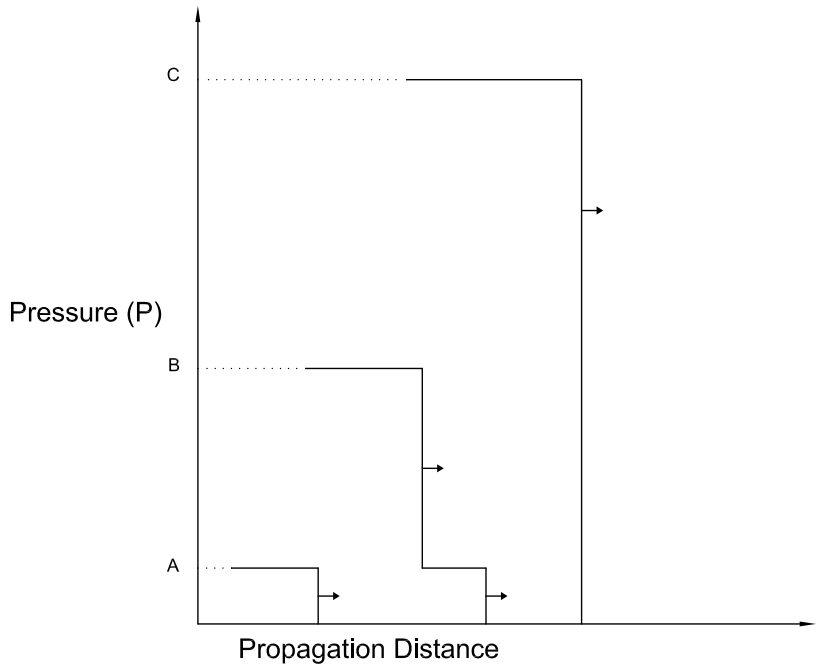

Figure 2.7: Propagation of a shock wave in an elastic–plastic material.

2.1.4 Release or Expansion Waves

The opposite of waves coalescing to create a shock wave is a release or expansion (sometimes also called rarefaction) wave which does not propagate as a discontinuity. An example of this is when a balloon breaks as shown in figure 2.8. The instant after the balloon membrane bursts, a wave propagates outwards while a release wave propagates inwards to lower the pressure at the centre of the region of high pressure. This wave has a head and a tail similar to the discussion in section 2.1.2. This can be illustrated by examining portion to the left of the piston cylinder arrangement as shown in figure 2.9. This time the piston is being pulled to the right at a velocity U_P (note that a shock wave would form to the right of the piston as before). As the piston begins to move, the head and tail of an expansion wave is created as shown at $t = t_a$ in figure 2.9. As before, the head and tail of the expansion wave move at different velocities but in this case the

tail moves slower than the head causing the wave to expand. This expansion is further shown in x–t diagram in figure 2.10. The head of the expansion wave has the highest velocity and propagates at the sonic speed in the high pressure region. Although the wave is propagating to the left, the motion of the material is propagating to the right lowering the pressure in this region. The decrease in pressure causes a decrease in the speed which causes the tail to move slower than the head. Comparing the length of the wave at time t_a to time t_b, it is evident that the expansion wave is increasing in size.

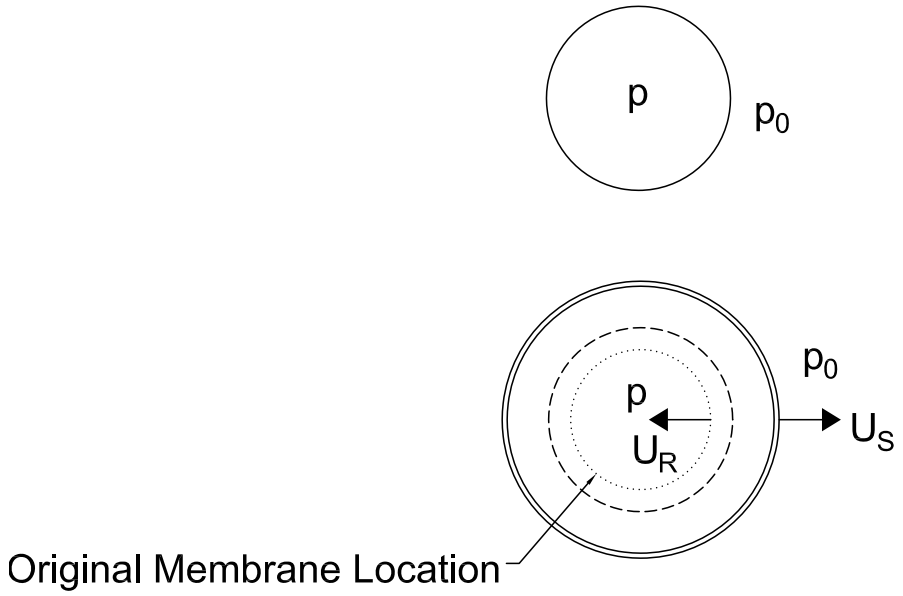

Figure 2.8: Model of a release wave created by the bursting of a balloon membrane.

2.1.5 Wave Interactions

As a wave propagates through a material it can encounter different types of boundaries or waves that will cause different behaviours to occur. Often impedance matching techniques are used to determine how a wave reacts to a boundary that it encounters. The impedance of a material, usually denoted by Z, is approximated as the product between the initial density, ρ_0, and the initial sonic wave velocity, C_0. In this manner, materials with

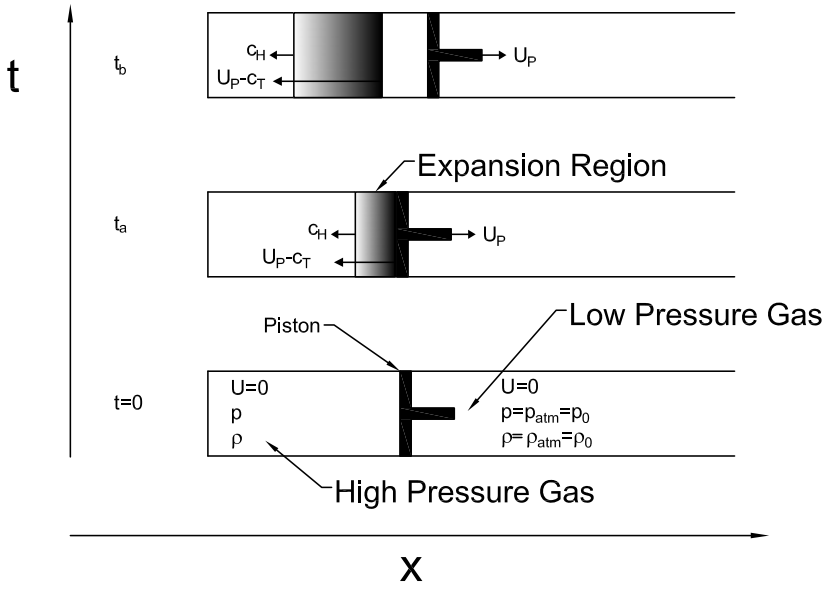

Figure 2.9: Model of a piston in a cylinder showing the formation of an expansion wave.

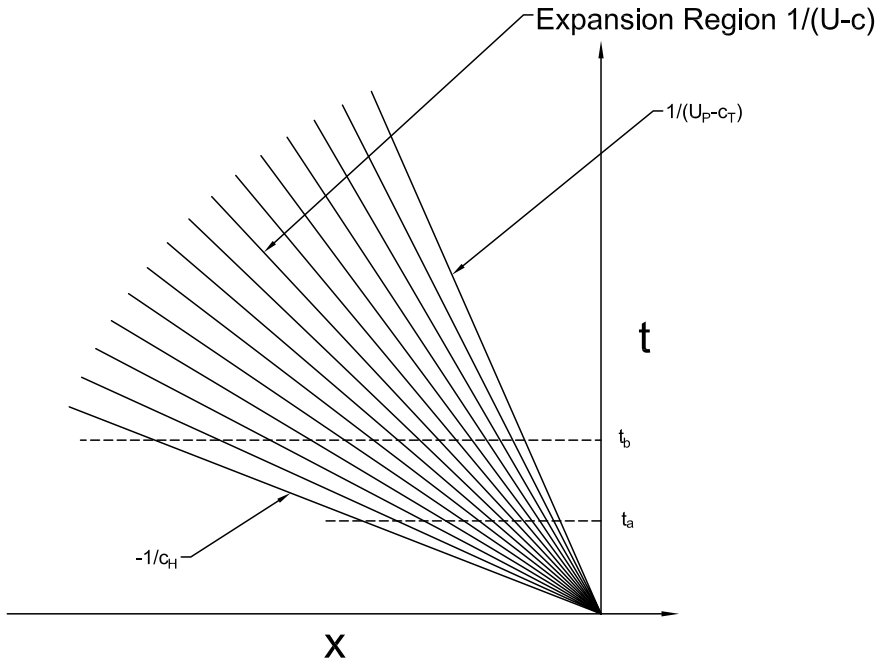

Figure 2.10: x–t diagram showing expansion wave formation.

low densities and low sonic velocities (and hence strength) such as rubber have a lower impedance than that of higher density and strength materials such as aluminum. At the interface of the two materials, while they remain in contact, it is assumed that equal particle velocity and pressure exist at the boundary. Several different cases will be described to illustrate the different aspects of wave interaction. Although the following discussion uses shock Hugoniots, a similar analysis can be performed for finite waves up to the shocked state. This is further detailed in Meyers [24].

Transition from a Low Impedance to a High Impedance Material In figure 2.11 two materials, A and B, are in contact. Consider a wave propagating towards the boundary between the two materials when $Z_A < Z_B$. The x–t diagram shown in figure 2.12 shows the state of each material before and after the arrival of the wave at the interface as A_1, A_2 and B_1, B_2. At the interface, part of the wave is transmitted into material B and part is reflected in material A. The states of the materials before and after the wave propagates to the interface are shown on the P–U_P diagram shown in figure 2.13.

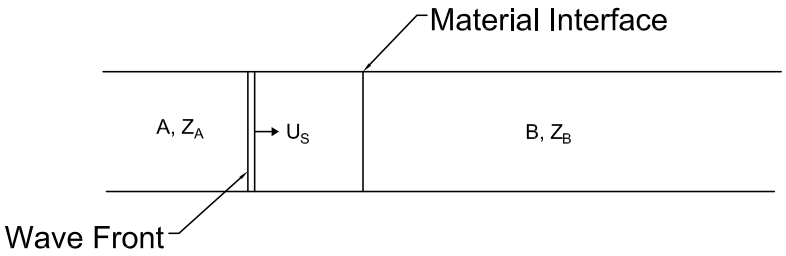

Figure 2.11: Stress wave propagating from material A into material B.

The instant the wave arrives at the boundary, Material A is at the state shown as A_1 with a velocity $U_P\,(A1)$ and pressure P_{A1} (dash–dot line). All of material B is at the a stationary state ($P_{B1} = U_{P(B1)} = 0$). During the interaction of the wave at the material interface, the pressures and velocities will be equal. This can only occur if a

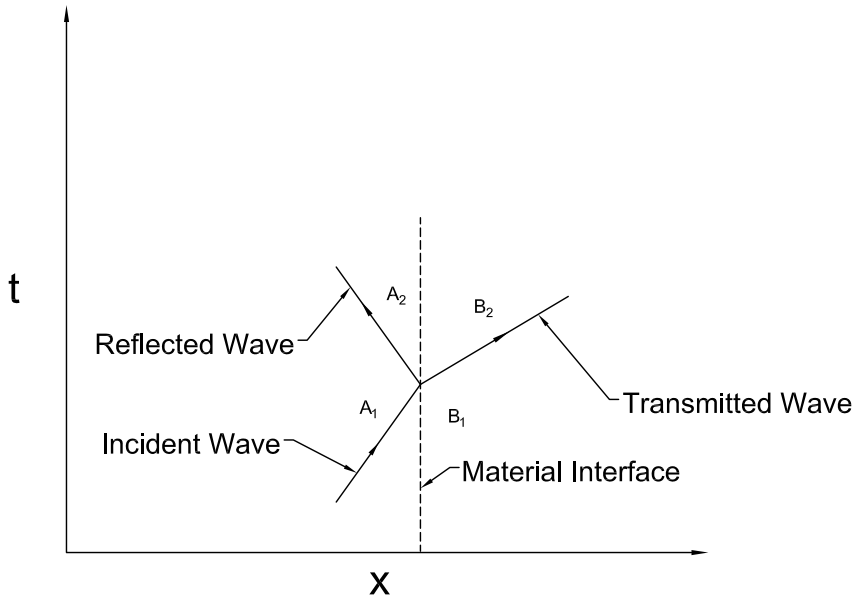

Figure 2.12: x–t diagram showing the transmission of the wave from material A to material B be when $Z_A < Z_B$.

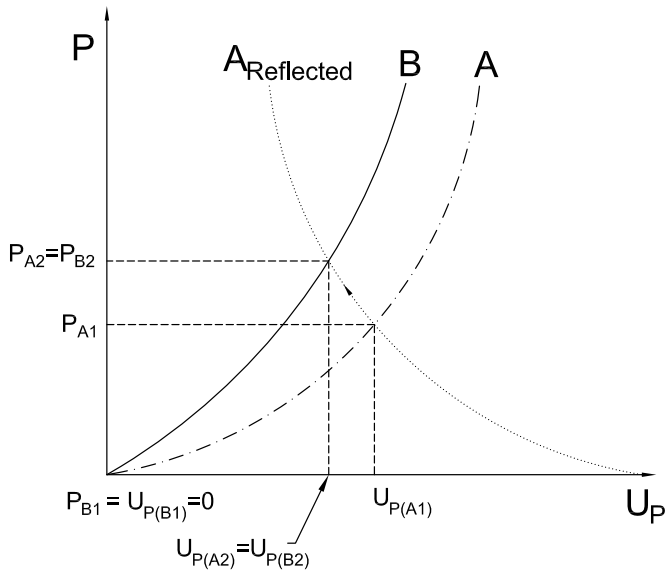

Figure 2.13: P–U_P diagram showing the different states in material A and B when $Z_A < Z_B$.

wave propagating back into material A is created. This is illustrated by the reflection of A about $U_P\,(A1)$ (dotted line). The intersection of the reflected curve for A and the curve for B dictates the particle velocity and developed pressure at the interface. i.e. $U_P\,(B2) = U_P\,(A2)$ and $P_{A2} = P_{B2}$. This is further illustrated by the P–x diagram for a square wave shown in figure 2.14. This figure illustrates that as the wave encounters the boundary, the pressure increases in material A to maintain continuity.

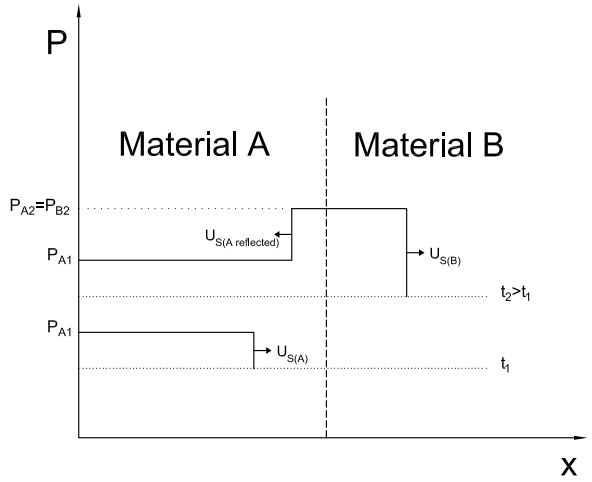

Figure 2.14: P–x diagram showing the different states in material A and B when $Z_A < Z_B$.

Transition from a High Impedance to Low Impedance Material If $Z_A > Z_B$ the reverse situation occurs as illustrated by the x–t diagram in figure 2.15 and the P–U_P diagram in figure 2.16. As illustrated in the x–t diagram, as the wave encounters the boundary a release wave propagates in A and a wave is transmitted into B. In this case the pressure in A in lowered as shown in figure 2.17

A bounding case of this interaction occurs when $Z_B = 0$ (a free surface). The P–U_P diagram, figure 2.18, shows that in this case material B is represented by a vertical line.

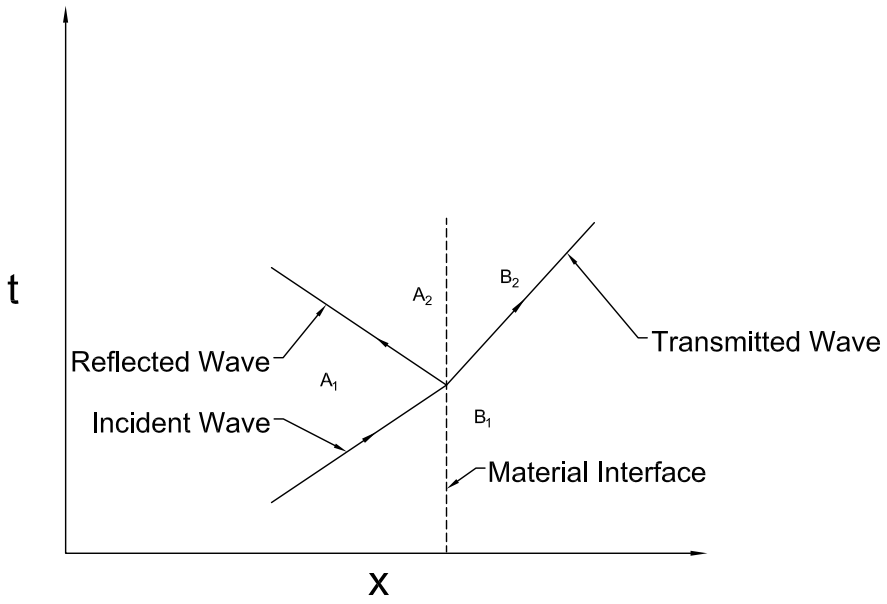

Figure 2.15: x–t diagram showing the different states in material A and B when $Z_A > Z_B$.

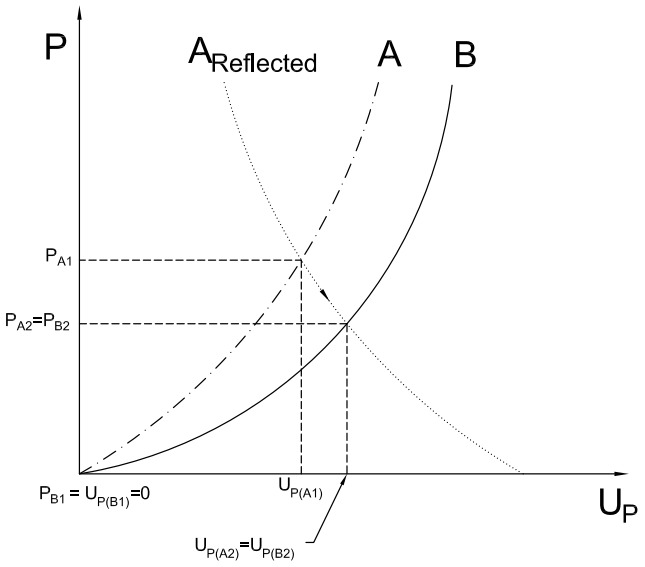

Figure 2.16: P–U_P diagram showing the different states in material A and B when $Z_A > Z_B$.

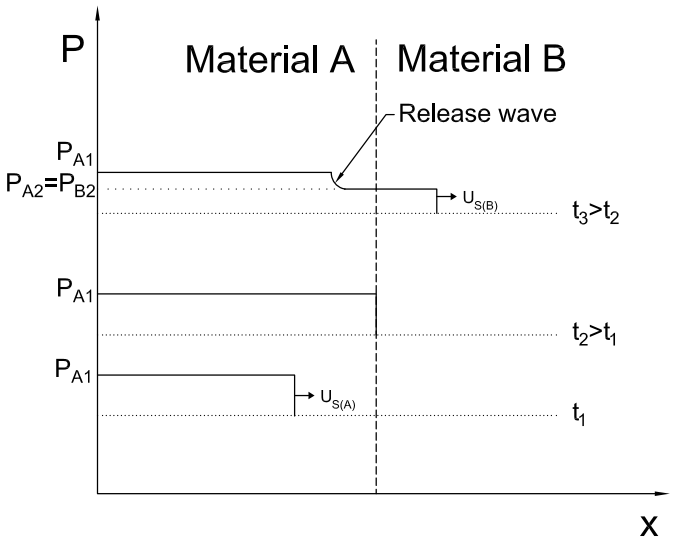

Figure 2.17: P–x diagram showing the different states in material A and B when $Z_A > Z_B$.

The curve for A is then reflected at this point as before. However, for this case the pressure at the interface is zero (zero force since there is nothing to react against) and the particle velocity is $2U_P$.

Interaction of Two Waves in One Material Using the same procedure outlined in the preceding discussion, the interaction of two waves within one material can be analysed. Consider two waves propagating towards each other and interacting as shown in figure 2.19 at four different times. The waves, initially at two different pressures and wave velocities (A and B in the figure) at t_1 begin to interact at t_2. As this interaction occurs, another state, AB, is created as shown at t_3 by creating a right going wave and left going wave of equal magnitude. The left and right going waves continue to propagate in their new state as shown at t_4. The new state, AB, can be determined through the use of the P–U_P curves as shown in figure 2.20. The material behind the front of wave

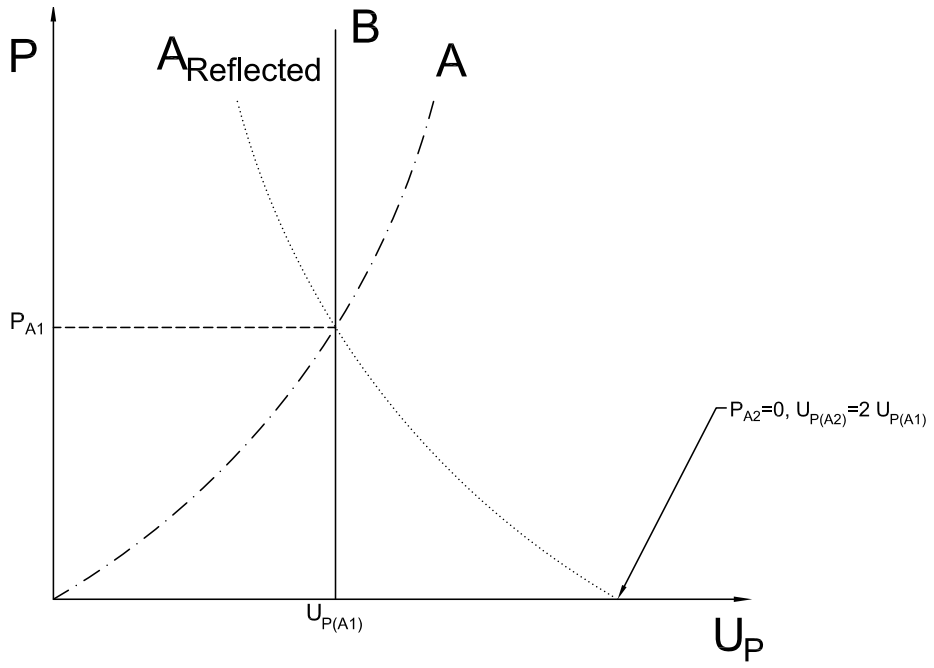

Figure 2.18: P–U_P diagram showing the different states in material A and B when $Z_A > Z_B = 0$.

A is at P_A with particle velocity $U_{P(A)}$ and behind wave front B is at P_B with particle velocity $U_{P(B)}$. Note that the curves are of the same shape (B is a reflection of A about 0) and that the negative particle velocity in B represents the left going wave. The new state is found by reflecting curves A and B about their state prior to the interaction and determining their intersection as shown in the figure. The new state is shown as the $U_{A(AB)}$, P_{AB} point.

Finite Wave Attenuation Consider a square wave propagating into a material that is generated by the application of a constant pressure to the boundary. If the applied pressure condition is suddenly removed a release wave is created. Assuming an ideal Hugoniot, a wave similar to that shown in figure 2.21 at t_2 is created. The release portion of the wave propagates faster than the head of the wave and will eventually catch up to the wave front. At time t_3, the head of the release, U_{RH} wave catches the

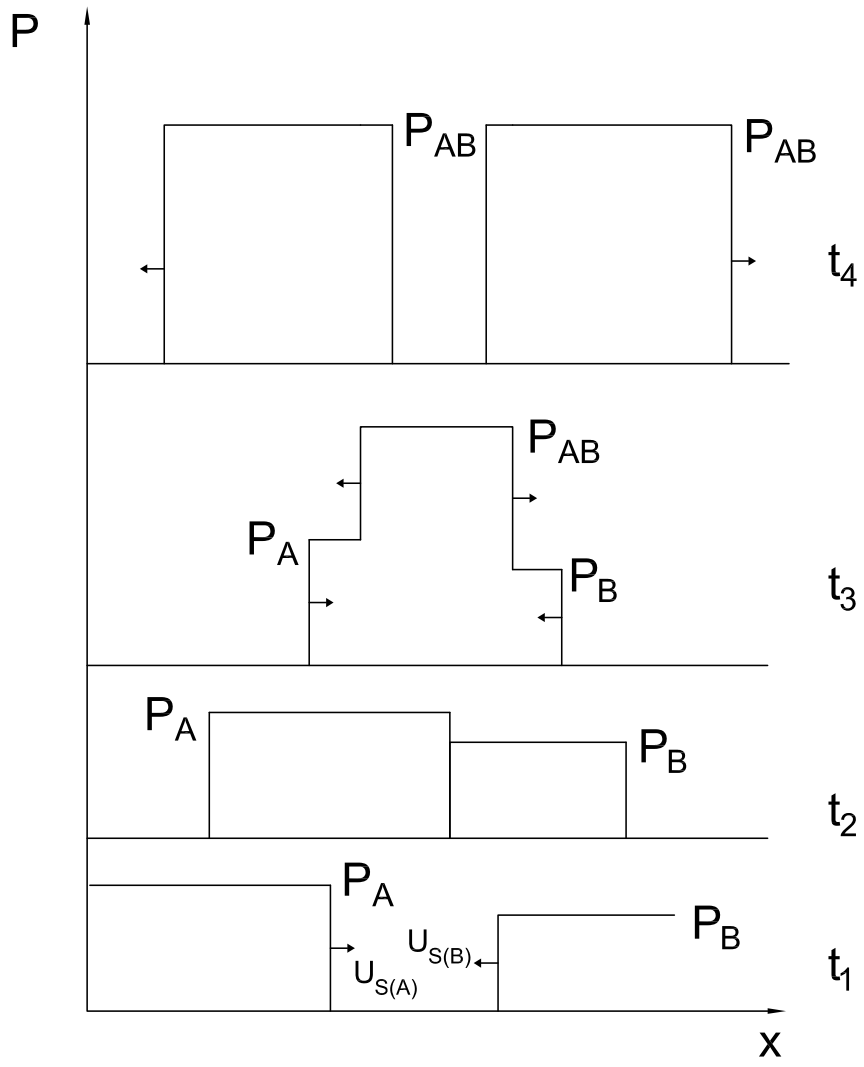

Figure 2.19: P–x diagram showing the interaction of two waves at different times.

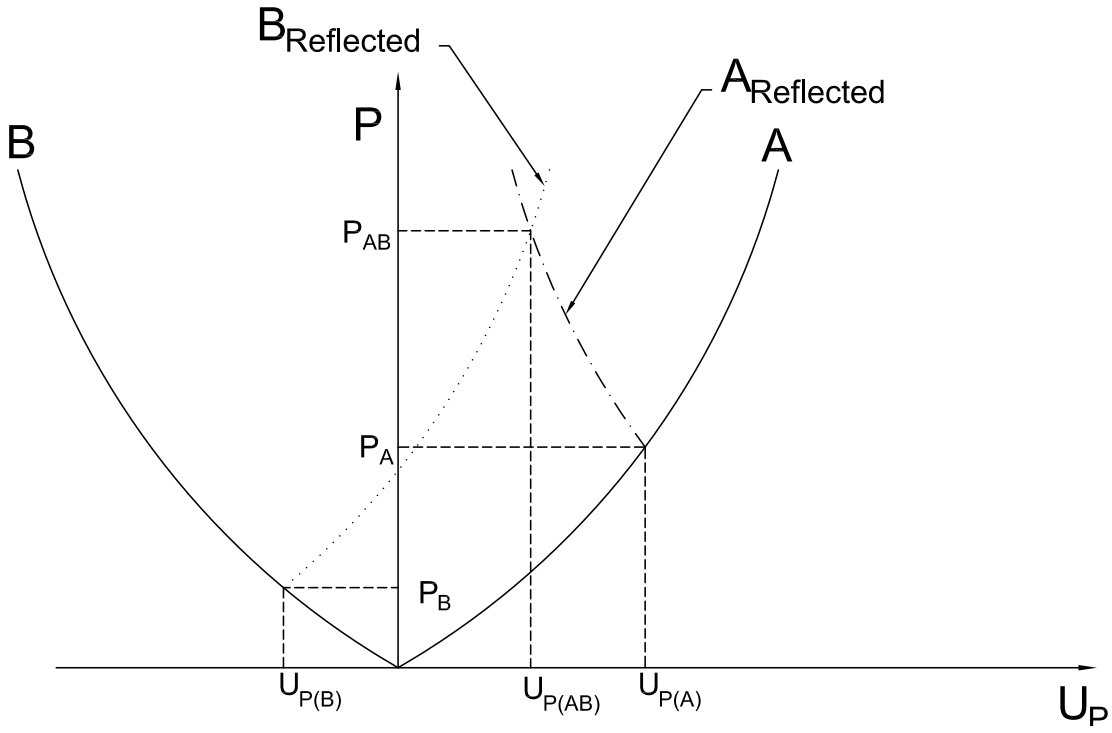

Figure 2.20: P–U_P diagram showing the different states in the material before and after the two waves interact.

wave front and begins to reduce the amplitude of the wave and its velocity. This process continues until the wave is fully attenuated as illustrated in the x–t diagram, figure 2.22 (exaggerated in the figure).

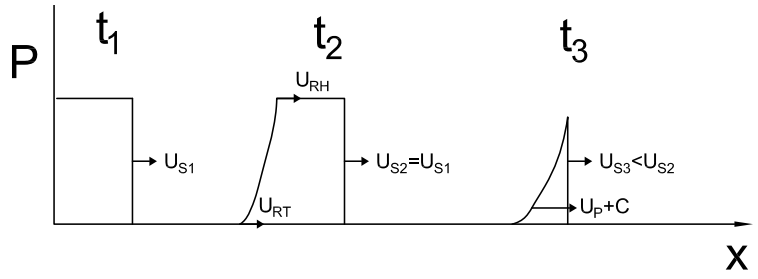

Figure 2.21: P–x diagram showing the attenuation of a wave as it propagates in a material.

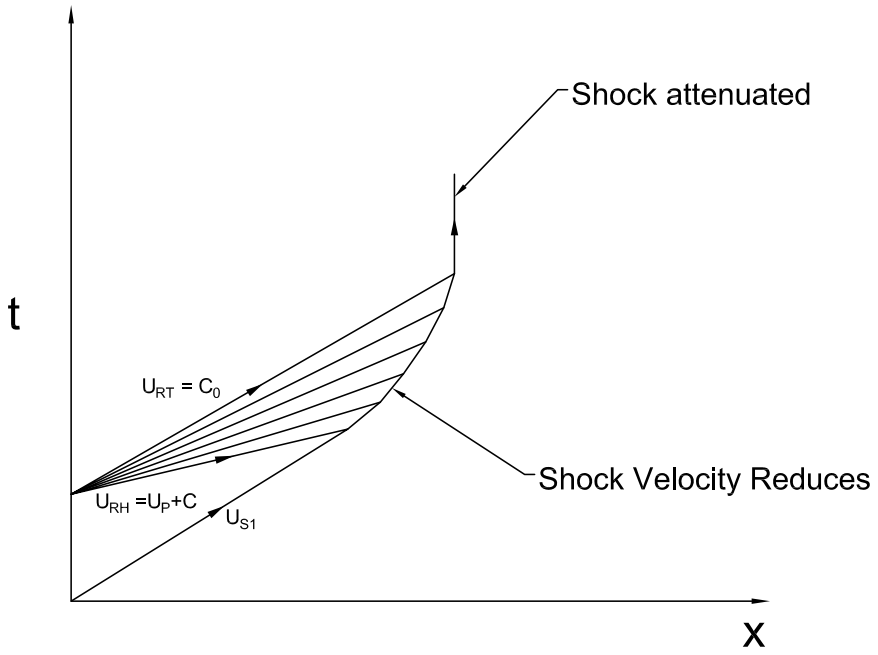

Figure 2.22: x–t diagram showing the interaction of the release portion of the wave with the wave and how it attenuates.

2.1.6 Impact

The impact of two finite bodies can be analysed using a combination of the interactions discussed in section 2.1.5. Consider a plate of finite thickness moving initially at velocity V, plate A, impacting another stationary plate that is significantly thicker, plate B. In this case $Z_A < Z_B$. Figure 2.23 shows the x–t diagram for this scenario. As the impact occurs (at $t = 0$), a stress wave is created in both in plate A and plate B. At $t = t_1$, the wave in A interacts with the free surface at the back of A. At this point, the pressure drops to zero and a release wave is created. The sequence is illustrated by the P–U_P diagrams in figure 2.24. Figure 2.24(a) shows the Hugoniots of the two materials A and B. At $t = 0$, impact occurs and the pressures and velocities at the interface must be equal. As such, the Hugoniot for A is reflected and given a zero pressure at $U_p = V$ as shown in figure 2.24(b). The pressure and velocity at the interface is then given as P_{AB} and $U_{P(AB)}$. At time $t = t_1$, the pressure in A drops to zero at the free surface (back of the plate) creating a release wave. As shown in figure 2.24(c), the corresponding U_P point for a zero pressure in A indicates that the material is moving with a negative magnitude. In this case the material is moving to the left (bouncing off) as shown in the x–t diagram.

At time $t = t_2$, the release wave encounters the interface between the materials and attempts to create a tensile interface between them. Assuming that the material can freely come apart, Material A moves away from B creating a gap. This causes the pressure applied to B to drop to zero. This interaction is shown in figure 2.24(d)which illustrates that A and B are in different states (moving at different velocities) since the materials are no longer in contact. This reduction of the pressure to zero creates a rarefaction wave to develop in B. As before, the rarefaction fan spreads out and eventually interacts with the stress wave at t_3 which causes the square stress wave to change shape and attenuate

as shown in figure 2.23(exaggerated in the figure).

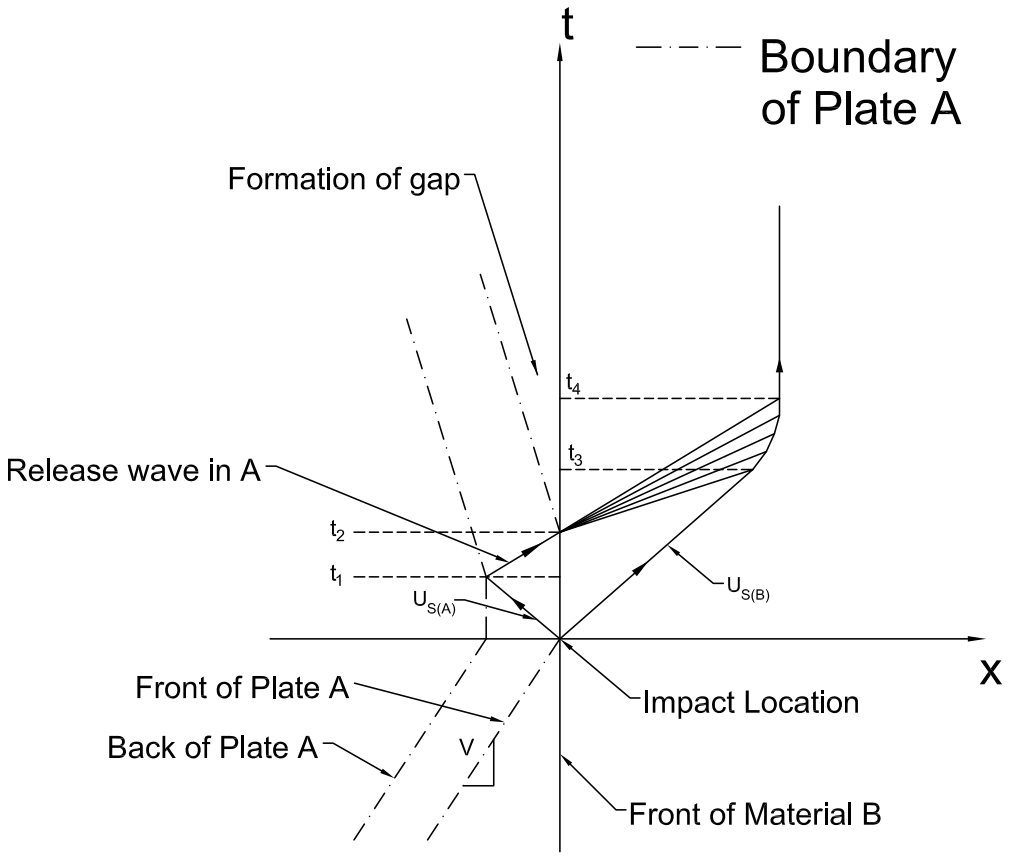

Figure 2.23: x–t diagram showing the impact of a thin plate (A) on a thick plate (B) when $Z_A < Z_B$.

Figure 2.24: a) Hugoniots of Material A and B, b) state of A and B at impact $t = t_0$, c) state of A at free surface at $t = t_1$, d) state of A and impacted side of B at $t = t_2$.

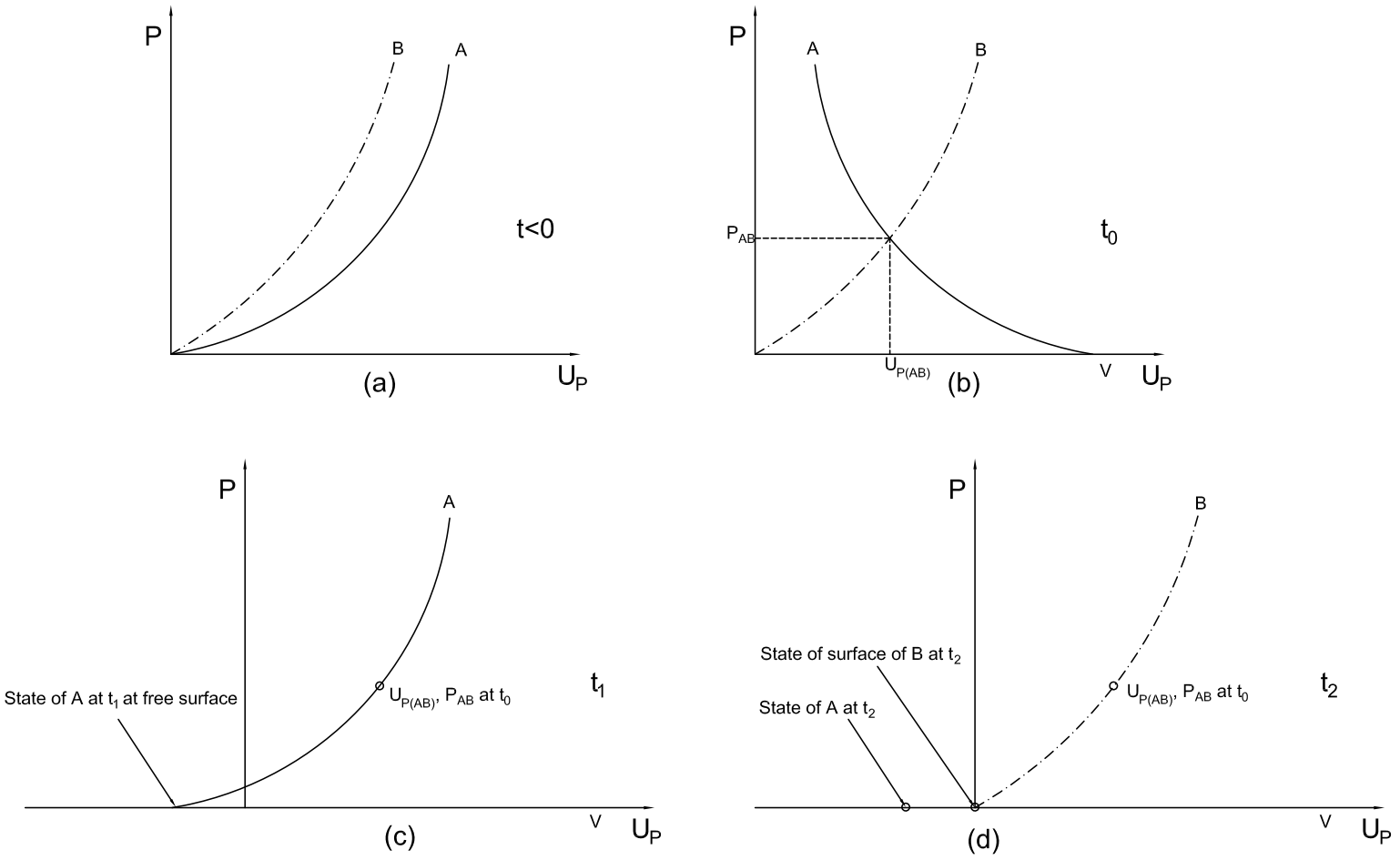

2.2 Fluid Structure Interaction

As fluids interact with structures, several aspects of the flow change. A discussion of the interaction of fluids with rigid and deformable structures, identifying the relevant aspects to the current study, follows.

2.2.1 Rigid Non-deforming Body

When waves encounter a rigid non-deforming body, the flow can be reflected and/or refracted depending on the shape of the body. If a wave encounters a planar wall, the flow would be reflected causing an increase in pressure above the incident wave pressure due to the superposition of the incident and reflected waves. The level to which the pressure increases is dependent upon the incident pressure profile. Various geometries, such as a corner, will cause a focusing of the wave which can increase the pressure even above that seen with a planar wall.

If a wave encounters a non-planar body, such as a falling angle, the flow will undergo an isentropic expansion such as the release wave described previously. In contrast to a shock wave, the pressure, temperature and density decrease while the Mach number increases [26]. When a wave encounters a more realistic obstruction, such as a body, a combination of the above effects occur. Since, by its very nature, transient waves are unsteady and the flow field is constantly changing, numerical solutions are required for all but the simplest of cases.

2.2.2 Deformable Body

The flow field that is established around a deformable body follows the same principles as a non-deformable body described previously. However, as a wave impinges upon a

deformable body, the shape of the body may change which in turn influences the flow field. This indicates that both the structural response of the body and the flow field must be considered in a coupled manner to accurately model the situation. The response of the structure is dependent on the material properties, geometry, duration and magnitude of the wave.

This coupled effect may be significant in terms of the overall response of the structure. Upon first contact, a wave imparts a stress wave in the structure which, particularly in the biological case, can cause severe damage. Measurements of the flow around the structure and the stress waves within a structure are critical in terms of determining the structural response. However, instrumentation to measure internal pressure waves in all but axisymmetric structures is difficult to implement and evaluate since internal reflected stress waves superimpose on each other making interpretation of recorded data challenging.

2.2.3 Modeling Methods

An approximation of the structural response can be ascertained by modeling the structure as a spring-mass-damper system with an applied forced loading using unsteady pressure boundary conditions [31][32]. However, the complexity of most realistic loading situations and associated structural response led to several studies which use an uncoupled method wherein the blast load was determined analytically or empirically [33][34][35][36], and then applied separately to the structure in a finite element code [37][38]. Jacinto [39][40] performed analysis using a similar method and then compared the numerical results with experimental tests. Similarly, others [41][42] have used CFD codes to predict the loading conditions on a rigid structure and then applied the loading history to the deformable structure using a different numerical code, achieving one-way coupling between the fluid

and structure. Although these methods work well for simple cases, they begin to fail when more complex loading cases are considered. Fully coupled models capable of predicting fluid structure interaction have been implemented with success [43][44][45][46]. In general, the previous studies conducted focused on more rigid structural materials such as metals and concrete.

Typically, dynamic impact problems for structures may be accurately modeled using an explicit Lagrangian based finite element code whereas, an Eulerian approach is better suited to address fluid modeling, with correspondingly large deformations and material flow [24]. The fluid structure interaction (FSI) capabilities in LS-DYNA [47], outlined in appendix C, which uses an Arbitrary Lagrangian Eulerian (ALE) formulation to model the compressible flow was selected for this study. The ALE algorithm adequately captures the wave mechanics discussed previously as outlined in [48]. This study determined that reduction of the mesh density beyond a characteristic length of 0.005 had only minimal effects on the ability of the algorithm to resolve discontinuous shocks. This mesh resolution was also necessary to resolve flow when at 45° to the face of the element.

The fluid structure interaction in LS-DYNA is achieved through a penalty coupling algorithm [46][49][50] (discussed further in appendix C). Use of this coupling method is facilitated by the Lagrangian time step used in the ALE algorithm. The algorithm first calculates the movement of the fluid as if the Lagrangian part did not exist. The distance that the fluid "penetrated" the surface of Lagrangian part is then used to calculate a coupling force based on the material properties. This force is then distributed to the nodes of the Lagrangian part near the coupling point. The calculation of the Lagrangian material response then continues with the updated external force

2.3 Deformation Mechanics in Porous Materials

Recently, researchers have investigated the deformation of porous materials on the micro–scale level in order to describe the effect of pore size, geometry and other mechanical variables [51][52][53][54][55]. The majority of these studies focus on the response of foams. This section is separated into two parts. The first part describes the morphology of a closed cell foam and how was it modeled geometrically. The second part discusses how numerical modeling techniques have been used in the literature to better understand the behaviour of closed cell foams at the pore level.

2.3.1 Closed Cell Foam Morphology

Several studies regarding the structure of foams have been conducted. In 1887 Lord Kelvin published a manuscript which outlined the problem of how to model space filling foams using geometrical shapes [56] of equal volume with the least surface area. Henceforth this became know as the Kelvin problem. Kelvin proposed that the tetrakaidecahedron with slightly curved edges solved this problem. More recently, Weaire and Phelan [57] found a structure which solved the Kelvin problem more efficiently. Their structure used two types of shapes which are equal in volume. In addition to the tetrakaidecahedron, they used an irregular dodecahedron. Weaire and Phelan continued their investigation into foam structures through which they describe a dry foam as a foam with a nearly infinitesimal volume fraction of liquid. In contrast, a wet foam was described as a foam for which there was enough liquid to render the bubbles almost spherical [58]. Although these descriptions are based on liquid foams (such as that created by blowing bubbles into soapy water) much of practical application of this knowledge occurs in solid porous type structures such as the work performed by Fung [59] where he correlated the shape of a tetrakaidecahedron to morphological data of an alveolar structure in the

lung. In this case the "foam" structure would be a wet type as the alveolar walls have a finite thickness. An example of a model of an alveolar duct structure is shown in figure 2.25. Similarly, research performed on polymeric closed cell foams also use the tetrakaidecahedron as the base unit shape for modeling [60][61][6][62].

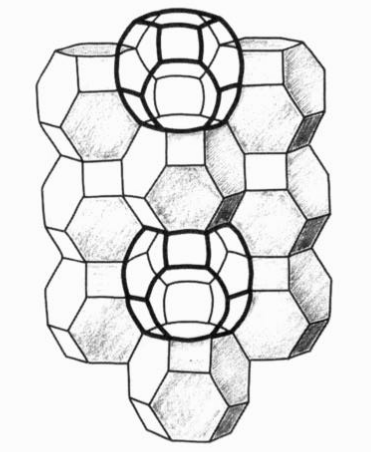

Figure 2.25: Two order–2 polyhedra combined to form alveolar duct with one additional face removed (dark edges) to ventilate alveoli. Several polyhedra have been removed to show duct. [59]

2.3.2 Numerical Models of Foams

Several researchers have used numerical modelling techniques to analyse the response of open cell foams. In general, the research can be split up into polymeric and metallic foams as discussed subsequently.

Metallic Foam Modelling Gibson and Ashby [5] developed a microscale model of a foam for open cell based on a lattice structure. This model described the mechanics of the foam based on the properties of the parent material but ignored the effects of air. They ignored the effects of air by assuming that the process was sufficiently slow to allow the air to evacuate from the foam unobstructed. Vesenjak et al. investigated

the deformation mechanics of open and closed cell aluminum foams [63][64]. They used Smooth Particle Hydrodynamics (SPH) to model different materials (including air using a modified numerical technique) which filled the pores. Their structure used was composed of spherical shaped pores and they accounted for strain rate effects using a Cowper–Symonds constitutive relation [65]. The foams that they modeled had very thick walls that were between a third and half the pore diameter. They concluded that the gas inside the pores influences the macroscopic behaviour of the structure. They also concluded that the filler influence increases with increasing relative density, size of the cellular structure and the number of cells. Similarly, finite element models of aluminum foams at the structure level have been conducted as outlined in references [66][67]. Vehyl et. al created a geometric representation of both an open and closed cell aluminum foam using tetrahedral elements [68]. Their models showed the same general shape as experiments conducted. Michailidis et. al examined an open celled aluminum foam at the microscale level using finite element methods. Through this study the researchers were able to visualize the stress fields developed in the Al foam [69]. Michailidis further extended the study to model Ni open cell foams tested at rates ranging from 0.005 to 50/s [70]. This study showed that there the numerical model was able to accurately predict the mechanical response of the material. Tasdemirci et. al modeled as repeating structure of stainless steel hollow spheres which deformed at high rates [71]. As in the current manuscript the authors used LS-Dyna to model the deformation of the spheres. Their model exhibited a similar response to that of the experimental tests performed.

The models discussed in the preceding literature focused on metallic foams. The material of the cellular structure is significantly stronger than than of polymeric foams. Additionally, although the modelling techniques had application to elastomeric foams, these materials deform plastically.

Polymeric Foam Modelling Lakes modeled the buckling of the struts which formed an open cell structure for an elastomeric foam [72]. Wismans et. al used 2D sections to model a closed cell polymeric foam [73]. They did not know mechanical properties and so a material model was assumed. Zhu et al. [74] developed a model of an open cell material using tetrakaidecahedrons. The model was to determine the elastic modulus and Poisson's ratio for a foam. The material was assumed to be linear elastic and the elastic constants were found analytically. The effect of air was ignored. A similar study by Zhu et al. [75] investigated the high strain compression of polyurethane foams. This study looked at the effect of buckling of the cell edges and compared predicted deformations to experiments. A plateau in the compressive stress–strain behaviour was not predicted by their model which was seen in the experiments. This model was further extended by Zhu et al. [76] to capture creep behaviour using viscoelastic theory. Mills [77] created a finite element model to predict the viscoelastic effects in the compression of polyurethane open cell foam during impact. Two models were investigated. The lattice structure model developed by Gibson and Ashby [5] and a "Wet" Kelvin model. Mills used a visco–elastic material model to simulate the polyurethane foam. Through use of this model Mills suggests that the majority of the energy absorption can be attributed to the viscosity in the polymer. In 2007 Mills [61] further investigated the response of an open cell polyurethane foam to predict the elastic modulus of the material as it changed during compression (densification of the foam).

The models discussed previously suffer from several limitations. The majority of the models are confined to open–cell foams without the consideration of the effect of air. Additionally, none of the previous studies address wave effects such as reduced wave speed or the importance morphological factors.

Mills et al. [6] modeled closed cell polyethylene and polystyrene foams at a microscopic

scale. In this study, the cells were modeled with an outer structure composed of shell elements of approximately 30 μm in size, while the fluid was modeled with a special fluid cavity which acted on the outer shell. The author indicated in this manuscript that he was unable to model the edges of the foam structure using solid elements. The study used 2, 4 and 6 cells. A model of a rigid striker was given an initial velocity and the was used to apply the loading to the cell structure. Mills used a bilinear curve to model the polyethylene and polystyrene materials. The stresses were then increased by 20% to account for the increased stress levels exhibited by polyethylene and polystyrene materials. Through this study Mills found that the increase in compressive stresses in the strain range of 10 to 60% was a function of the compression of air with the contribution by the polymer being almost constant. Above strains of 60% cell faces contacted each other further contributing to the increase in stress. His models showed that the cells compressed uniformly (even at strain rates of 500/s). Although an important study, Mills' model suffers from several limitations. Although Mills [6] incorporates air cavities into his model wave propagation effects are not discussed. This could be a limitation of the air cavity model that was used. Additionally, although they indicated that the polymer material that he used are strain rate sensitive, he uses a simple bilinear curve that was then scaled by 20% to approximate a response when subjected to a strain rate of 50/s. The 50/s strain rate was an overall rate for the macroscale deformation of the sample. The morphology that Mills used in his study was also limited in that he modeled only quarter section of entire cells without consideration of domain size.

The research contained within this manuscript sought to address the limitations of the models described previously. A predictive constitutive model for the properties of the cellular material was created and validated as discussed in the subsequent chapters. The morphology of the polychloroprene foam was determined using similar methods as

that discussed in section 2.3.1. Importantly, once the finite element model of the foam was created, it was verified using experimental techniques which loaded an axisymetric sample thereby reducing complex stress states which occur at the boundaries of previous validation studies. Additionally, the model developed in the current manuscript identified the contribution of the enclosed air which had not been identified in the previous studies. The relative sensitivity of the mechanical response of the foam to morphology factors was also addressed, as outlined in the subsequent chapters, which had not been investigated previously.

2.4 Dynamic Experiments

A compressive split Hopkinson pressure bar was used to test the materials in compression at high rates. The following is brief overview of Hopkinson bar theory. A detailed description of the apparatus used and the governing theory can be found in reference [78] and [79][80] A more general overview of Hopkinson bar theory and high rate material testing is given in reference [24].

A schematic of the compressive Hopkinson bar apparatus is shown in figure 2.26. In the compression test, the striker bar is propelled via a pneumatic gun and impacts the incident bar. A compressive stress wave propagates down the incident bar where it encounters the sample. At this point, a portion of the wave is transmitted through the sample into the transmitter bar as a compressive stress wave while the balance is reflected as a tensile wave. The proportion of the wave that is transmitted and reflected is dependent on the impedance and geometric difference between the bar and the sample. Strain gauges on each bar are used to record the strain time history of the passing waves. The material behaviour can be determined from these waves using the analysis outlined subsequently.

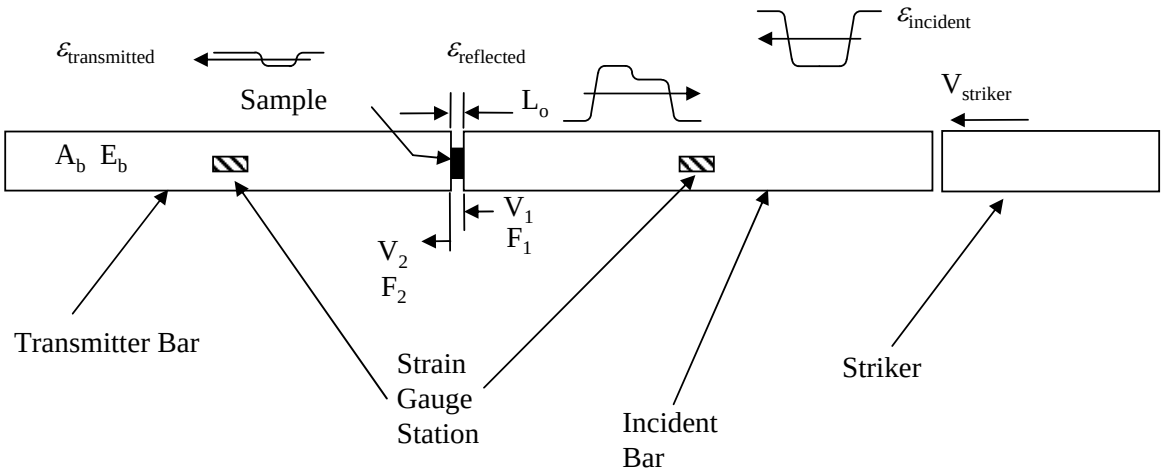

Figure 2.26: Schematic of Hopkinson Bar apparatus.

2.4.1 Hopkinson Bar Theory

In the compressive split Hopkinson bar, the material behaviour is determined from the difference in velocities of the bar ends (V_1, V_2) and forces (F_1, F_2) acting on the ends of the sample. As the stress wave interacts with the bar end, it begins to move reaching V_1.

The engineering strain rate of the sample, $\dot{e}_s$ can be calculated as

$$\dot{e}_s(t) = \frac{V_1(t) - V_2(t)}{L_o}. \tag{2.28}$$

where V_1 and V_2 are the velocities of the bar ends. The measurement of the velocity at the end of each bar is difficult. Therefore, a different approach using wave propagation in the incident and transmitter bars is often adopted. The velocity at which wave propagates in a rod is given as

$$C_o = \sqrt{\frac{E}{\rho}}. \tag{2.29}$$

where C_o is the velocity of the propagating wave, E is Young's Modulus and ρ is the density of the rod material.

In order to determine the stress, strain and strain rate history of the sample, the incident strain, ε_I, the reflected strain, ε_R, and the transmitted strain, ε_T, histories in the bar can be used. The velocities at the interface can then be related to the strain by

$$V_1(t) = C_o \varepsilon_I(t) \text{ at } (t = 0) \tag{2.30}$$

$$V_2(t) = C_o \varepsilon_T(t) \tag{2.31}$$

where $t = 0$ refers to the arrival time of the incident wave at the bar end.

At $t > 0$ the incident and reflected waves are superimposed so that the velocity is reduced and V_1 becomes

$$V_1(t) = C_o(\varepsilon_I(t) - \varepsilon_R(t)). \tag{2.32}$$

Combining equations 2.31, 2.32 and 2.28 the strain rate can then be written in terms of the strain histories as

$$\dot{\varepsilon}_s(t) = \frac{C_o}{L_o}(\varepsilon_I(t) - \varepsilon_R(t) - \varepsilon_T(t)) \tag{2.33}$$

assuming that the bars are made from the same material.

The engineering stress in the sample, (conventionally represented as σ) is based on the average force acting on the sample which is expressed as

$$\sigma_s(t) = \frac{1}{2}\frac{F_1(t) - F_2(t)}{A_s} \tag{2.34}$$

where F_1 and F_2 are the forces applied at the specimen ends by the bars and A_s is the

area of the sample. The forces in the bar can be related to the strains in the bar as

$$F_1(t) = A_b E_b (\varepsilon_I(t) + \varepsilon_R(t)) \tag{2.35}$$

$$F_1(t) = A_b E_b (\varepsilon_T(t)) \tag{2.36}$$

where A_b and E_b are respectively the area and Young's Modulus of the bar. The stress in the sample is then is then

$$\sigma_s(t) = \frac{A_b E_b}{2A_s} (\varepsilon_I(t) + \varepsilon_R(t) + \varepsilon_T(t)). \tag{2.37}$$

For equilibrium to exist ($F_1(t) = F_2(t)$) and from conservation of momentum principles,

$$\varepsilon_T(t) = \varepsilon_I(t) + \varepsilon_R(t).$$

Equations 2.33 and 2.37 simplify to

$$\dot{e}_s(t) = -2\frac{C_o}{L_o}\varepsilon_R(t) \tag{2.38}$$

and

$$\sigma_s(t) = \frac{A_b E_b}{A_s} (\varepsilon_T(t)). \tag{2.39}$$

The total strain in the sample is determined by integrating the strain rate, equation 2.38 as

$$e_s(t) = -2\frac{C_o}{L_o}\int_0^t \varepsilon_R(t)\, dt. \tag{2.40}$$

By applying equilibrium and conservation principles, the stress, strain and strain rate of the sample can be determined from the known bar properties and recorded strain gauge signals. From equation 2.40, the maximum strain that can be achieved is a function of

the reflected strain wave duration and amplitude.

2.4.2 Dynamic Equilibrium Constraints

One of the assumptions made when using a Hopkinson bar for testing requires that dynamic equilibrium must exist in the sample during the test. In essence this means that the sample must be in a uniform stress state. One method which is used to determine if dynamic equilibrium is achieved is to compare the force history in the incident and transmitted bars. If the forces are approximately equivalent then equilibrium is said to exist [81]. Optical methods have also been used to identify non–uniform deformation [82] but the view of the sample is often disrupted by the lubricant.

Kolsky suggested that the specimen length should be small compared to the wavelength of the shortest operative wave in the Fourier spectrum of the pulse [83]. Davies and Hunter established that equilibrium is achieved when the loading pulse travels back and forth inside the specimen more than π times [84]. Dioh et al. conducted tests through a range of strain rates to determine the strain rate sensitivity due to material dimensions [85]. They suggested that it was critical to choose appropriate specimen dimensions when testing at higher strain rates in order to correctly determine the material's behaviour. Dioh et al. further concluded, through numerical simulation, that at high striker velocities, plastic wave fronts were developed in the sample, increasing the strain rates and flow stress, which causes inaccuracies in representing the material's inherent behaviour [86]. By reducing the specimen length, lower velocities can be used, resulting in lower stress and strain gradients throughout the specimen. Further research was conducted by Dioh et al. using a different type of numerical simulation which resulted in similar conclusions [87].

2.5 Constitutive Modeling – Nonlinear Elasticity and Viscoelasticity

One of the first steps in finite element modeling is to develop and implement a constitutive model which is capable of representing the materials behaviour. In general there are several classes of materials such as foams, rubbers, metals and ceramics which have unique behaviour and similarly unique constitutive models. Ultimately, the stress inside a material at any given point can be a function of strain, strain rate, strain history (path dependent materials), temperature and other variables such as phases in metals. In simulations involving large deformations it is especially important to characterize the material over a large range of strains which can be as high as 80–90% in the case of foams.

This section is composed of three parts. Section 2.5.1 outlines the background and constitutive modeling for elastic and hyperelastic materials. Section 2.5.2 outlines the background and constitutive modeling for viscoelastic materials. Section 2.5.3 discusses methods used for combined hyperelastic and viscoelastic constitutive modeling as well as some existing constitutive models.

2.5.1 Modeling of Elastic and Hyperelastic Materials

One of the basic idealizations of a simple material is that of a purely elastic solid. A Neo–Hookean model can be used to model an elastic solid undergoing large deformations. A simple model of a linear elastic solid is that of a spring as shown in figure 2.27. The linear spring of figure 2.27a) subject to an applied velocity has a force response that is directly proportional to the displacement (x). In this case, K is the proportionality constant. For a nonlinear spring, as shown in figure 2.27b), the force is proportional to

the displacement but this time K is a function of x such that $F = ax + bx^2 + cx^3 + ...$

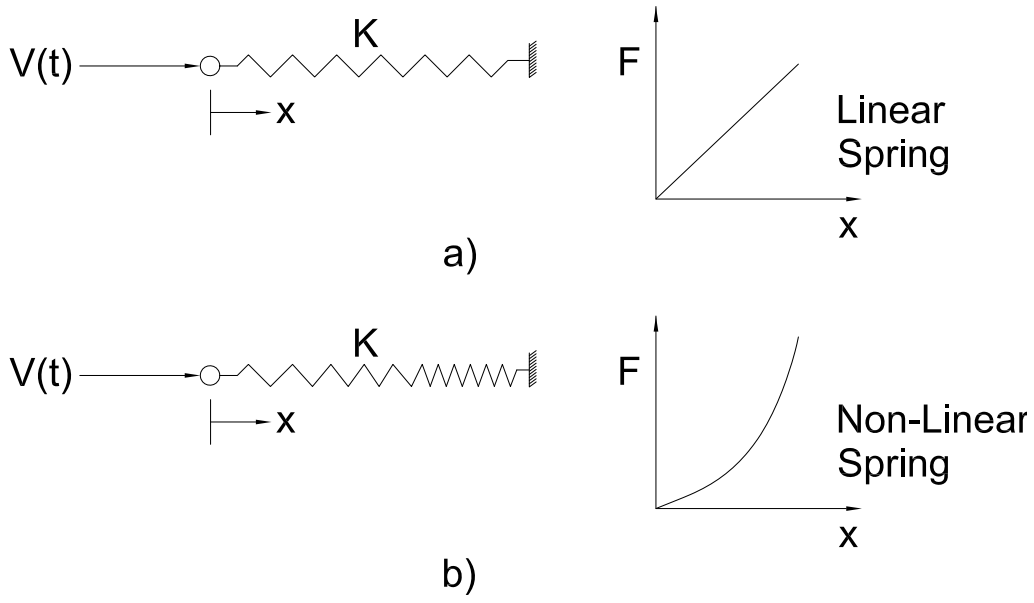

Figure 2.27: A linear a) and non-linear b) spring system.

A hyperelastic material is one that possess a strain energy density function which is an analytical function of strain [88]. This is represented by:

$$\sigma_{ij} = \frac{\partial W}{\partial \epsilon_{ij}} \tag{2.41}$$

where W is the strain energy function. As indicated by Rivlin [89], for finite deformations in an isotropic material, the rigid body rotations of the material are not included in the strain energy function. For a strain energy function that is indifferent to the coordinate system it must be a function of the strain invariants. i.e. $W(I_1, I_2, I_3)$ where using the

right Cauchy–Green deformation tensor $\mathbf{C}$, the invariants are expressed as

$$I_1 = \mathrm{tr}\,(\mathbf{C}) = C_{ii} = \lambda_1 + \lambda_2 + \lambda_3 \tag{2.42}$$

$$I_2 = \frac{1}{2}\left[(\mathrm{tr}\mathbf{C})^2 - \mathrm{tr}\mathbf{C}^2\right] = \frac{1}{2}\left[C_{ik}C_{ki} - C_{jj}^2\right] = \lambda_1^2\lambda_2^2 + \lambda_2^2\lambda_3^2 + \lambda_1^2\lambda_3^2 \tag{2.43}$$

$$I_3 = \det\,(\mathbf{C}) = \lambda_1^2\lambda_2^2\lambda_3^2 \tag{2.44}$$

where λ_i are the stretches in the principal directions. Stretch is a quantity used to measure deformation of a member and is related to engineering strain by

$$\lambda_i = 1 + e_i \tag{2.45}$$

where e_i is the principle components of engineering strain (change in length/original length). Through inspection of equation 2.45, it can be identified that an undeformed member will have a stretch of one, a member in tension will have a stretch greater than one and a member in compression will have a stretch less than one. This indicates that as a member is being compressed the values of stretch will start at one and approach zero. i.e. a stretch of 0.8 corresponds to an engineering strain of 20% whereas a stretch of 0.2 corresponds to a engineering strain of 80%. Consequently, for the remainder of the manuscript, stretches will be quoted as going from one towards zero thereby implying compression.

Rivlin Hyperelastic Constitutive Equations

The strain energy function proposed by Rivlin [90] for an isotropic, incompressible material was an infinite series of the form:

$$\sum_{i=0,j=0,k=0}^{\infty} A_{ij} \left(I_1 - 3\right)^i \left(I_2 - 3\right)^j \left(I_3 - 3\right)^k,\ A_{00} = 0 \tag{2.46}$$

The -3 term comes from the observation that in the unstressed state, the principal stretch ratios λ_i are equal to 1 and so the first two invariants are equal to 3. If the material is isotropic and incompressible the third invariant is approximately equal to 1 from equation 2.44 and not included. Expanding equation 2.46 for two terms gives

$$\begin{aligned} W = A_{00} &+ A_{01}\left(I_2 - 3\right) + A_{02}\left(I_2 - 3\right)^2 + A_{10}\left(I_1 - 3\right) + A_{20}\left(I_1 - 3\right)^2 \\ &+ A_{11}\left(I_1 - 3\right)\left(I_2 - 3\right) + A_{12}\left(I_1 - 3\right)\left(I_2 - 3\right)^2 \\ &+ A_{22}\left(I_1 - 3\right)^2\left(I_2 - 3\right)^2 + A_{21}\left(I_1 - 3\right)^2\left(I_2 - 3\right) \end{aligned} \tag{2.47}$$

where A_{00} is set to zero to represent zero strain energy in the undeformed state.

The deformation tensor F_{ij} can be written as

$$\mathbf{F} = \begin{bmatrix} \lambda_1 & 0 & 0 \\ 0 & \lambda_2 & 0 \\ 0 & 0 & \lambda_3 \end{bmatrix} \tag{2.48}$$

where the off diagonal components are zero since the deformations are uniaxial and inline with the loading direction. Since rubbers are generally considered to be incompressible, the Jacobian was approximately unity and so $J = 1 = \lambda_1\lambda_2\lambda_3$. As well, since the experimental samples were axisymmetric $\lambda_2 = \lambda_3$. This lead to $\lambda_1\lambda_2^2 = 1$ and so $\lambda_2 =$

$\lambda_1^{-1/2} = \lambda_3$. The deformation tensor is then

$$\mathbf{F} = \begin{bmatrix} \lambda_1 & 0 & 0 \\ 0 & \lambda_1^{-1/2} & 0 \\ 0 & 0 & \lambda_1^{-1/2} \end{bmatrix} \tag{2.49}$$

where the principal stretch in the loading direction was determined from the engineering strain, e strain via

$$\lambda_1 = (1 + e_1)\,.$$

In this case the Left and Right Green–Cauchy deformation tensors are equal ($\mathbf{C} = \mathbf{F}^T\mathbf{F} = \mathbf{B}$)and given as

$$B_{ij} = \begin{bmatrix} \lambda^2 & 0 & 0 \\ 0 & \lambda^{-1} & 0 \\ 0 & 0 & \lambda^{-1} \end{bmatrix} \tag{2.50}$$

which leads to the invariants

$$I_1 = tr\,(\mathbf{B}) = B_{ii} = \lambda^2 + 2\lambda^{-1/2} \tag{2.51}$$

$$I_2 = \frac{1}{2}\left[(\mathrm{tr}\mathbf{B})^2 - \mathrm{tr}\mathbf{B}\mathbf{B}\right] = \lambda^{-2} + 2\lambda \tag{2.52}$$

where λ is the stretch in the principle direction.

Rivlin [91] showed that for an incompressible, isotropic solid, the Cauchy stress can be written as

$$\sigma_{ij}^e = \alpha_1\mathbf{B} + \alpha_2\mathbf{B}\mathbf{B} - p\mathbf{I} \tag{2.53}$$

where

$$\alpha_1 = 2\left(\frac{\partial W}{\partial I_1} + I_1\frac{\partial W}{\partial I_2}\right) \tag{2.54}$$

$$\alpha_2 = -2\frac{\partial W}{\partial I_2} \tag{2.55}$$

and p is an arbitrary pressure. This pressure is arbitrary due to the incompressibility assumption. For a stress state under uniaxial loading equation 2.53 becomes

$$\sigma^e_{11} = \alpha_1 B_{11} + \alpha_2 B^2_{11} - p \tag{2.56}$$

The pressure p can be determined from the fact that $\sigma^e_{22} = \sigma^e_{33} = 0$ and $B_{22} = B_{11}^{-1/2}$ resulting in

$$\sigma^e_{22} = 0 = \alpha_1 B_{22}^{-1/2} + \alpha_2 B_{22}^{-1/2} - p \tag{2.57}$$

Combining equations 2.57 with 2.56 gives

$$\sigma^e_{11} = 2\left(\lambda^2 - \lambda^{-1}\right)\left(\frac{\partial W}{\partial I_1} + \lambda^{-1}\frac{\partial W}{\partial I_2}\right) \tag{2.58}$$

which is a general form of a model based on strain energy for uniaxial loading of a hyperelastic, incompressible, isotropic material. It should be noted that alone this equation does not have any time dependency. However, it is often used as the basis for viscoelastic analysis as outlined in a subsequent section.

Ogden Constitutive Model

Ogden proposed a strain energy functional which was a function of the principal stretches. The strain energy functional given by Ogden [92] was

$$W = \sum_{k=1}^{N_k} \frac{\mu_k}{\alpha_k} \left(\lambda_1^{\alpha_k} + \lambda_2^{\alpha_k} + \lambda_3^{\alpha_k} - 3\right) \tag{2.59}$$

where μ_k and α_k are constants fit to the experimental data and λ_i are the principal stretches. In LS-Dyna a slight variation of equation 2.59 was given as

$$W = \sum_{k=1}^{N_k} \frac{\mu_k}{\alpha_k} \left(\tilde{\lambda}_1^{\alpha_k} + \tilde{\lambda}_2^{\alpha_k} + \tilde{\lambda}_3^{\alpha_k} - 3\right) - p \tag{2.60}$$

where

$$\tilde{\lambda}_i = \frac{\lambda_i}{J^{1/3}}$$

and $J = \lambda_1\lambda_2\lambda_3$. This leads to the principal Kirchhoff stresses being

$$\tau_{ii}^e = J\sigma_{ii}^e = \lambda_i \frac{\partial W}{\partial \lambda_i} = \sum_{k=1}^{N_k} \mu_k \left(\tilde{\lambda}_i^{\alpha_k} - \frac{1}{3} a_k\right) + p \tag{2.61}$$

where

$$a_k = \tilde{\lambda}_1^{\alpha_k} + \tilde{\lambda}_2^{\alpha_k} + \tilde{\lambda}_3^{\alpha_k}.$$

In the current work, the superscript e represents the elastic stress and the superscript v represents viscoelastic stress discussed later. Special cases of the Ogden model exist for specific selection of the material constants. When $k = 1$ and $\alpha = 2$ the Neo–Hookean model was obtained. When $k = 1$, 2, $\alpha_1 = 2$ and $\alpha_2 = -2$ the Mooney–Rivlin model was obtained.

One of the main issues in implementing the Ogden formulation was the requirement

for the principal stretches. Mathematically, these are the eigenvalues of the left ($\mathbf{V}$) or right ($\mathbf{U}$) stretch tensor. The deformation gradient can be decomposed into rotation ($\mathbf{R}$) and stretch components. The difference between the left and right stretch tensors can determined by which whether or not the rotation is performed first. This is expressed mathematically as

$$\mathbf{F} = \mathbf{RU} = \mathbf{VR}. \tag{2.62}$$

In practice, however, the rotation matrix is not known and so an alternative approach is taken. The right, $\mathbf{C}$, and left, $\mathbf{B}$, Cauchy–Green deformation tensors are related to the stretch tensor and deformation gradient by

$$\mathbf{B} = \mathbf{F}\mathbf{F}^{\mathbf{T}} = \mathbf{V}^{\mathbf{2}} \tag{2.63}$$

$$\mathbf{C} = \mathbf{F}^{\mathbf{T}}\mathbf{F} = \mathbf{U}^{\mathbf{2}}. \tag{2.64}$$

Methods, such as those proposed by Hoger and Carleson [93][94] exist to find the stretch tensors from the Cauchy–Green deformation tensors. These methods require repeated applications of the Cayley–Hamilton theorem and then the solution of a characteristic polynomial to determine the invariants of $\mathbf{U}$ from which $\mathbf{U}$ can be determined [95]. However, for the Ogden constitutive model the stretches on a principal basis are required. The principal stretches can be found through solving the eigenvalue problem stated as

$$(\mathbf{A} - \lambda\mathbf{I})\,\mathbf{n} = 0 \tag{2.65}$$

where $\mathbf{A}$ in this case is a symmetric three by three matrix (such as $\mathbf{U}$, $\mathbf{V}$, $\mathbf{C}$ or $\mathbf{B}$), λ is an eigenvalue and $\mathbf{n}$ is the corresponding eigenvector. Since the Cauchy–Green tensors are symmetric they will have real positive eigenvalues and so the square root of the

eigenvalue will be positive as well. As such, once the eigenvalues (and vectors) of $\mathbf{C}$ and $\mathbf{B}$ are determined, the principal stretches can be found by taking the square root of the eigenvalue. Normalizing the eigenvector then gives the principal directions. The left Cauchy–Green tensor can then be written in terms of its eigenvalues and eigenvectors as [96]

$$B_{ij} = \lambda_i^2 n_i n_j \tag{2.66}$$

where the eigenvalues are squared since we ultimately want to find the values of the stretch tensor. There are a variety of methods available to solve for the eigenvalues and eigenvectors. Closed form solutions for the eigenvalues are described in Malvern [97] and the book by Simo and Huges [98]. Subsequently the dyadic product of the eigenvectors can be found using the method in Morman [99]. These methods can lead to numerical problems though when two eigenvalues are close to each other as described by Scherzinger [100]. As described previously, this occurs frequently in the uniaxial incompressible case. Iterative numerical methods such as those described by Bathe are employed in numerical codes to solve for the eigenvalues and vectors instead [101] .

Thus, once the principal Kirchhoff stresses have be determined as in equation 2.61, which is on the principal basis, they are rotated back to the standard basis using the relationship in equation 2.66 to give

$$\tau_{ij} = \tau_i n_i n_j \text{ (summation in force).} \tag{2.67}$$

The Cauchy stress, which is used in most finite element codes, is then determined by $\sigma = \tau/J$. The left Cauchy–Green deformation tensor was used to determine the principal directions in the deformed solid. If the right Cauchy–Green deformation tensor was used instead, the principal directions would have been in terms of the undeformed solid [96].

2.5.2 Viscoelasticity

Preliminaries

Viscoelastic materials, as the name implies, have not only a dependency on strain but also time. Following the description by Fung [88], consider the force applied to a bar to be $F(t)$ and the displacement of the bar end to be $u(t)$. The force at time t is a function of the history of all of the increments in displacement up to t. If we consider the displacement to be C^1 then over a small increment in time, $d\phi$, the increment in displacement at time ϕ is $(du/dt)\, d\phi$. The effect of this increment in displacement contributes to the overall force component as a function of $k(t-\phi)$ where k is a proportionality constant and $\phi \leq t$. Mathematically this can be expressed as

$$dF(t) = k(t-\phi)\frac{du}{dt}(\phi)\, d\phi \tag{2.68}$$

If we integrate the above equation from $-\infty$ to t we get an expression for $F(t)$

$$F(t) = \int_{-\infty}^{t} k(t-\phi)\frac{du}{dt}(\phi)\, d\phi \tag{2.69}$$

In essence, integrating from $-\infty$ indicates that the summation is to take place from the start of motion (as opposed to some arbitrarily defined $t = 0$). Equation 2.69 is an example of a convolution integral which is often used to model time dependent responses [97]. Note that in the literature, τ is often used instead of ϕ however for the present manuscript τ is reserved for Kirchhoff stress.

Figure 2.28 shows a possible response of a viscoelastic solid subjected to a continuous increasing displacement (green line) up to unity where it is then held constant. The blue line shows the loading as would be measured at the end of the bar. The red curves

show the contribution that each increment in displacement has on the measured force. In reality this is a continuous process. The principle of the integral in equation 2.69 is that each visco increment has a finite time over which it acts according to the proportionality constant. This is indicated by the decay of each increment illustrated by the thin red lines in the figure. As time progresses, the contribution of each increment decays, in this case to zero as only the viscous stress in considered. As indicated in the figure, once the displacement is held constant the overall measured force decays.

The viscous portion of the force can then be summed with the elastic portion of the force such that the total stress in the rod is given by

$$\sigma = \sigma^e \left[W \left(I_1, I_2, I_3 \right) \right] + \sigma^v \left(t, k, \dot{u} \right) \tag{2.70}$$

where σ is the total stress, σ^e is the elastic portion which can be define as a function of strain energy, and σ^v is the viscous portion which is a function of time and deformation rate. In this manner, the total stress as a function of the elastic stress and viscous component can account for strain rate effects. In essence, the increments in force increase with increasing deformation rate. A similar analysis can be performed such that the displacement is solved for in terms of stress.

The Maxwell and Voigt models are often used to further illustrate the response of a viscoelastic type system subjected to various types of inputs. The reader is referred to the work by Fung [88] and Doman [102] for an analysis of these systems. Consider the schematic of the standard linear solid (Maxwell form) which is in essence a combination of the Maxwell and Voigt models, such as a bar made from a viscoelastic material fixed at one end with a force applied to the other, as shown in figure 2.29.

In this case, the solid is comprised of a combination of a spring and a dashpot in series that is in parallel with another spring. If one considers the response of this system to a

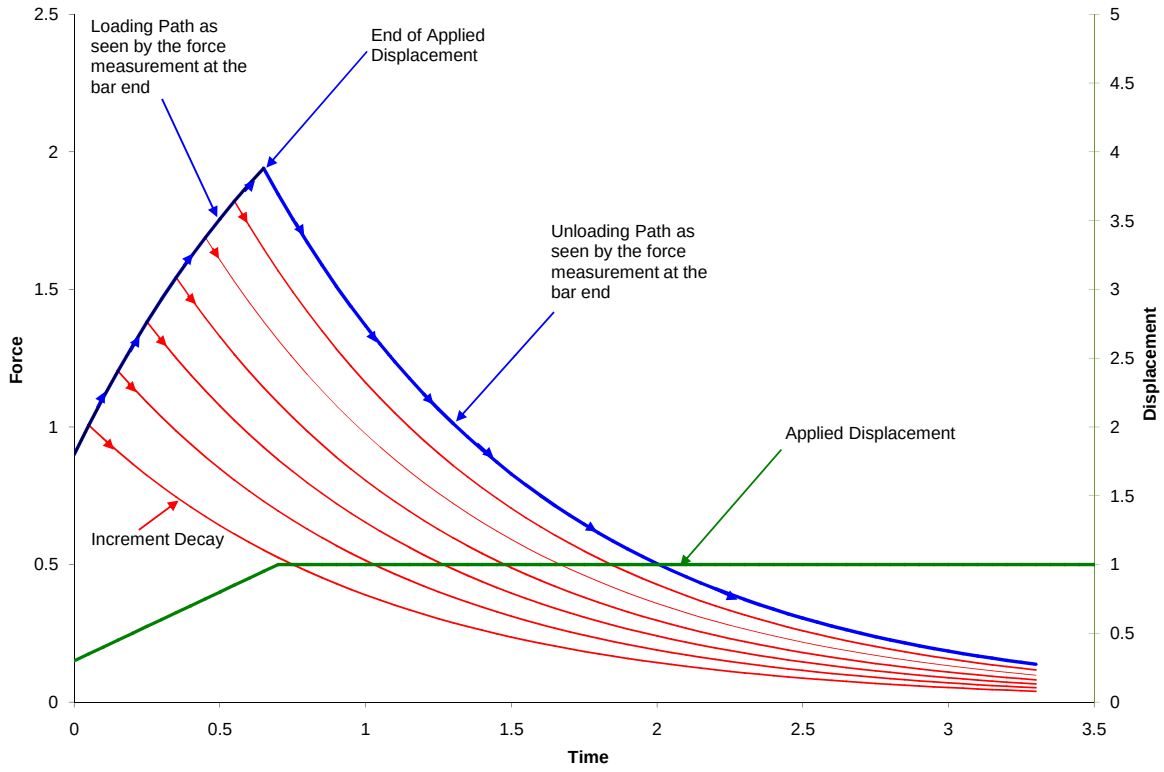

Figure 2.28: Schematic of the response of a viscous solid subjected to a continuous increase in displacement.

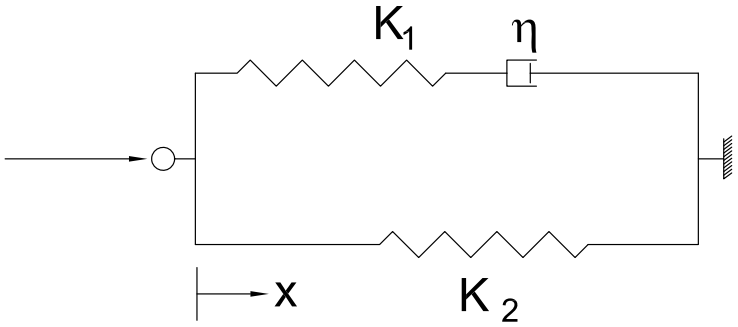

Figure 2.29: Schematic of a standard linear solid.

step function in deformation (often called a relaxation test) the force response over time would look like that shown in figure 2.30a). If a step in force is applied (called a creep test) the deformation would follow that of figure 2.30b). In the relaxation test, the measured force approaches the elastic force of the material as $t \rightarrow \infty$. Thus, the level above the elastic response is the addition of the viscoelastic component as described previously. More complex models can be achieved through the combination of Maxwell and Voigt

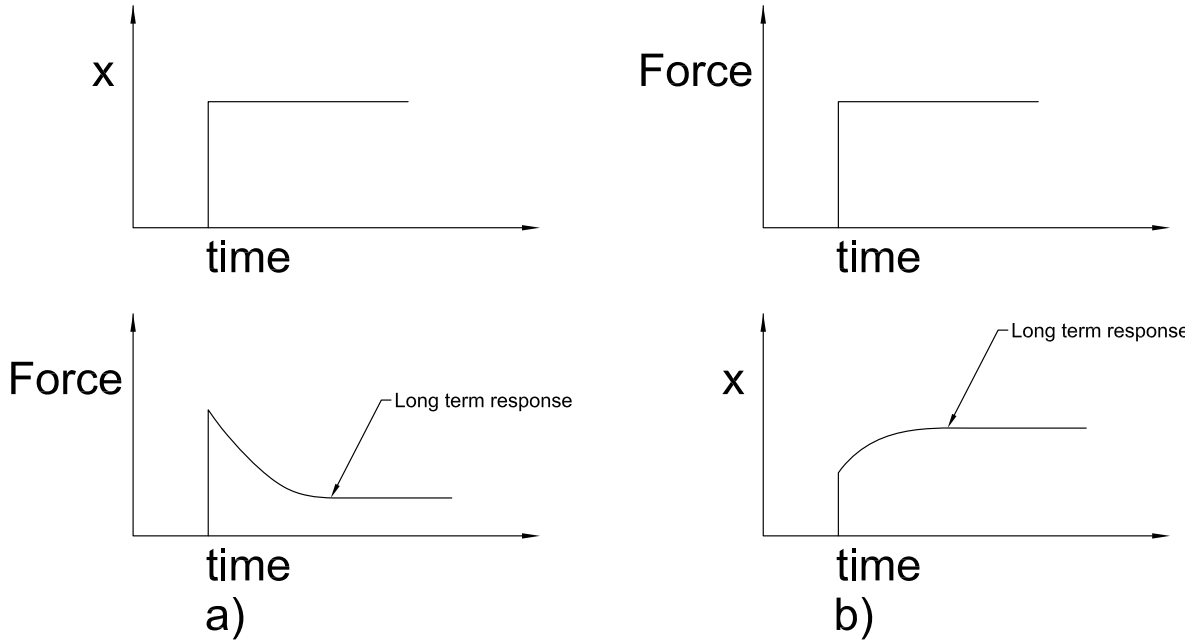

Figure 2.30: Schematic of the response of a standard linear solid a step input in displacement a) and a step input in force b).

solids in series and parallel. Further explanation of this is given in references [88] and [102].

General Discretization of the Convolution Integral

Recursive techniques can be used to solve the convolution integral of the type in equation 2.69 using a numerical time marching approach [103][104]. This can be explained

through investigation of a generic convolution integral as that given by

$$B(t) = \int_{-\infty}^{t} G(t-\phi) \frac{dA(\phi)}{d\phi} d\phi \tag{2.71}$$

where for this section only B and A can be stress and strain quantities respectively (written in a one dimensional form here) and G is an independent function of time. It is usually assumed that the deformation starts at time zero resulting in

$$B(t) = \int_{0}^{t} G(t-\phi) \frac{dA(\phi)}{d\phi} d\phi \tag{2.72}$$

If a time marching technique is used and we take an increment in time Δt, equation 2.72 becomes

$$B(t+\Delta t) = \int_{0}^{t+\Delta t} G(t+\Delta t-\phi) \frac{dA(\phi)}{d\phi} d\phi \tag{2.73}$$

which can be split into the two intervals $[0, t]$ and $(t, t+\Delta t]$ resulting in

$$\begin{aligned} B(t+\Delta t) = & \int_{0}^{t} G(t+\Delta t-\phi) \frac{dA(\phi)}{d\phi} d\phi \\ & + \int_{t}^{t+\Delta t} G(t+\Delta t-\phi) \frac{dA(\phi)}{d\phi} d\phi \end{aligned} \tag{2.74}$$

The kernel function, $G(t+\Delta t-\phi)$, can be approximated by a Prony series, $\sum_{k=1}^{N_k} \gamma_k e^{-\beta_k (t+\Delta t-\phi)}$ where N_k is the number of terms in the Prony series. The second term in equation 2.74 is then written as

$$\int_{t}^{t+\Delta t} G(t+\Delta t-\phi) \frac{dA(\phi)}{d\phi} d\phi = \sum_{k=1}^{N_k} \gamma_k \int_{t}^{t+\Delta t} e^{-\beta_k (t+\Delta t-\phi)} \frac{dA(\phi)}{d\phi} d\phi \tag{2.75}$$

where γ_k and β_k are constants. Using the exponential property $e^{c(a+b)} = e^{ca} e^{cb}$, equation 2.75 becomes

$$\sum_{k=1}^{N_k} \gamma_k \int_t^{t+\Delta t} e^{-\beta_k (t+\Delta t-\phi)} \frac{dA\left(\phi\right)}{d\phi} d\phi = \sum_{k=1}^{N_k} \gamma_k \int_t^{t+\Delta t} e^{-\beta_k (t+\Delta t)} e^{\beta_k \phi} \frac{dA\left(\phi\right)}{d\phi} d\phi \tag{2.76}$$

Applying the mean value theorem to equation 2.76 to extract the A term from the integrand results in

$$\sum_{k=1}^{N_k} \gamma_k \int_t^{t+\Delta t} e^{-\beta_k (t+\Delta t)} e^{\beta_k \phi} \frac{dA\left(\phi\right)}{d\phi} d\phi = \sum_{k=1}^{N_k} \gamma_k \frac{dA\left(\xi\right)}{d\phi} \int_t^{t+\Delta t} e^{-\beta_k (t+\Delta t)} e^{\beta_k \phi} d\phi \tag{2.77}$$

where $\xi \in [t, t+\Delta t]$. The integral can now be evaluated to give

$$\sum_{k=1}^{N_k} \gamma_k \frac{dA\left(\xi\right)}{d\phi} \int_t^{t+\Delta t} e^{-\beta_k (t+\Delta t)} e^{\beta_k \phi} d\phi = \sum_{k=1}^{N_k} \gamma_k \frac{dA\left(\xi\right)}{d\phi} \left[\frac{e^{-\beta_k (t+\Delta t-\phi)}}{\beta_k} \right] \Bigg|_t^{t+\Delta t} \tag{2.78}$$

which simplifies to

$$= \sum_{k=1}^{N_k} \frac{\gamma_k}{\beta_k} \frac{dA\left(\xi\right)}{d\phi} \left[1 - e^{-\beta_k \Delta t}\right]. \tag{2.79}$$

If $d\phi$ is sufficiently small and equal to Δt, $dA/d\phi$ can be approximated linearly by

$$\frac{dA}{d\phi} = \frac{A\left(t+\Delta t\right) - A\left(t\right)}{\Delta t} \tag{2.80}$$

and finally equation 2.78 becomes

$$\int_t^{t+\Delta t} G\left(t+\Delta t-\phi\right) \frac{dA\left(\phi\right)}{d\phi} d\phi = \sum_{k=1}^{N_k} \frac{\gamma_k}{\beta_k} \frac{A\left(t+\Delta t\right) - A\left(t\right)}{\Delta t} \left[1 - e^{-\beta_k \Delta t}\right] \tag{2.81}$$

which can be implemented into a time marching numerical approach.

Similarly, if we apply the Prony series approximation for the first term of equation 2.74

we get

$$\int_0^t G\left(t+\Delta t-\phi\right)\frac{dA\left(\phi\right)}{d\phi}d\phi=\sum_{k=1}^{N_k}\int_0^t \gamma_k e^{-\beta_k\left(t+\Delta t-\phi\right)}\frac{dA\left(\phi\right)}{d\phi}d\phi \tag{2.82}$$

separating the exponential terms results in

$$=\sum_{k=1}^{N_k}\int_0^t \gamma_k e^{-\beta_k\left(t-\phi\right)}e^{-\beta_k\Delta t}\frac{dA\left(\phi\right)}{d\phi}d\phi \tag{2.83}$$

which rearranged becomes

$$=\sum_{k=1}^{N_k}e^{-\beta_k\Delta t}\int_0^t \gamma_k e^{-\beta_k\left(t-\phi\right)}\frac{dA\left(\phi\right)}{d\phi}d\phi \tag{2.84}$$

If we substitute a Prony series, given by $\sum_{k=1}^{N_k}\gamma_k e^{-\beta_k\left(t-\phi\right)}$, into equation 2.72 we get

$$B\left(t\right)=\int_0^t\sum_{k=1}^{N_k}\gamma_k e^{-\beta_k\left(t-\phi\right)}\frac{dA\left(\phi\right)}{d\phi}d\phi \tag{2.85}$$

$$\equiv\sum_{k=1}^{N}H_k\left(t\right) \tag{2.86}$$

where $H_k\left(t\right)$ is defined as a history variable for each k and $H_k\left(0\right)=0$. Substituting this result into equation 2.82 results in

$$\int_0^t G\left(t+\Delta t-\phi\right)\frac{dA\left(\phi\right)}{d\phi}d\phi=\sum_{k=1}^{N_k}e^{-\beta_k\Delta t}H_k\left(t\right). \tag{2.87}$$

Substituting equations 2.81 and 2.87 into equation 2.74 gives the recursive formula

$$B\left(t+\Delta t\right)=\sum_{k=1}^{N_k}e^{-\beta_k\Delta t}H_k\left(t\right)+\frac{\gamma_k}{\beta_k}\frac{A\left(t+\Delta t\right)-A\left(t\right)}{\Delta t}\left[1-e^{-\beta_k\Delta t}\right]. \tag{2.88}$$

Using a time marching approach, one can then evaluate $B\left(t+\Delta t\right)$ using the values of A at t and $t+\Delta t$ and the history variable H_k at t along with the constants γ_k and β_k where $k=1$ to N_k.

There are different variations of the convolution in the literature which lead to different formulations. For instance

$$\sigma_{\text{viscoelastic}}=\int_0^t g_{ijkl}\left(t-\phi\right)\frac{d\epsilon_{kl}\left(\phi\right)}{d\phi}d\phi, \tag{2.89}$$

relates Cauchy stress to true (logarithmic) strain,

$$S_{\text{viscoelastic}}=\int_0^t G_{ijkl}\left(t-\phi\right)\frac{dE\left(\phi\right)}{d\phi}d\phi, \tag{2.90}$$

relates 2^{nd} Piola–Kirchhoff stress to Green's strain,

$$\sigma_{\text{viscoelastic}}=\int_0^t g\left(t-\phi\right)\frac{d\sigma\left[\epsilon\left(\phi\right)\right]}{d\phi}d\phi, \tag{2.91}$$

as implemented in the modified quasi-linear form by Fung. Although G_{ijkl} and g_{ijkl} are 4^{th} order tensor quantities, they can be decomposed into scalar functions which act on the deviatoric and hydrostatic components.

2.5.3 Hyper–viscoelastic Constitutive Models

Existing Constitutive Models

Common to several finite element programs, such as LS-Dyna [47] and Abaqus [105], viscoelastic effects are modeled through the superposition of the viscoelastic contribution on a base hyperelastic model as detailed previously. This linear sum is given as

$$\sigma_{ij} = \sigma^e_{ij} + \sigma^v_{ij} \tag{2.92}$$

where σ^e_{ij} is the hyperelastic contribution and σ^v_{ij} is the viscoelastic contribution to the Cauchy stress. The base hyperelastic curve can take different forms such as the Ogden model as described previously. The implementation of the convolution integral described previously is based on equation 2.89 and implemented in LS-Dyna as

$$\sigma^v_{ij} = \sum_{k=1}^{N_k} 2\gamma_k \int_0^t e^{-\beta_k(t-\phi)} \frac{d\varepsilon^{dev}_{ij}}{d\phi} dt. \tag{2.93}$$

where the deviatoric strain is given by

$$\varepsilon^{dev}_{ij} = \varepsilon_{ij} - \frac{1}{3}\varepsilon_{ij}\delta_{ij}. \tag{2.94}$$

The numerical implementation is as discussed previously with the usage of the prony series approximation for the relaxation function, γ. Abaqus implements a similar model but includes a separate component for modeling viscoelastic effects in terms of volumetric components.

The issue that arises with these models is the inability to predict the strain rate sensitivity of rubber–like materials through the convolution integral alone. As discussed, the idea of the convolution integral is to give the material a "fading memory" [97] which

acts over a period of time similar to that of a stress relaxation or creep test. The above formulation results in a constitutive model which is relatively insensitive to different loading rates over a short period of time even for small time steps.

Yang et. al. [106] developed a model to account for higher loading rates. Their formulation was based on the summation of a hyperelastic base curve, which is based on the Mooney-Rivlin model described previously and a modifier on the convolution integral. The form of the visco–elastic contribution was given as

$$\sigma^v = -p^v + \mathbf{F}(t) \cdot \overset{t}{\underset{\phi=-\infty}{\Omega}} \{\mathbf{C}(\phi)\} \mathbf{F}^T(t) \tag{2.95}$$

where Ω is a functional which describes how the strain history acts upon the stress and p^v is an arbitrary pressure. They assumed this functional to be of the form

$$\overset{t}{\underset{\phi=-\infty}{\Omega}} \{\mathbf{C}(\phi)\} = \int_{-\infty}^{t} \Phi(I_1, I_2)\, m(t-\phi)\, \dot{\mathbf{E}} d\phi \tag{2.96}$$

where the strain rate, $\dot{\mathbf{E}}$, is given by

$$\dot{\mathbf{E}} = \frac{1}{2}\left(\dot{\mathbf{F}}^T \cdot \mathbf{F} + \mathbf{F}^T \cdot \dot{\mathbf{F}}\right). \tag{2.97}$$

The function Φ is assumed to be given by

$$\Phi = A_4 + A_5 (I_2 - 3) \tag{2.98}$$

where I_2 is the second invariant of $\mathbf{C}$, A_4 and A_5 are constants. The function m is a prony series with one coefficient. Through the combination of the Mooney-Rivlin hyperelastic model and the viscoelastic addition Yang et. al. were able to obtain reasonable fits to data at high rates of strain for two similar rubbers.

Chapter 3

Experimental Material Testing

This chapter outlines the testing methodology used and the mechanical behaviour of the constituent polychloroprene rubber. The main goal of this aspect of the study was to determine the strain rate sensitivity of the material. Many metals and especially polymers show a significant increase in strength as the deformation rate increases. Characterization of the material at different loading rates is therefore important when developing a model which predicts the overall material behaviour. The results from the current chapter will be used in chapter 4 where a constitutive model which describes the material behaviour was developed and implemented.

3.1 Density Measurement

A primary task in characterizing a material is to determine its density. A relatively simple method was employed to determine the density of both the foamed polychloroprene and rubber materials. For each material type, four squares approximately 125 mm by 125 mm were cut. The relative position of each corner was then determined to give the volume of the specimen. Each specimen was then weighed and the density determined. Table 3.1

Table 3.1: Measured densities of the polychloroprene rubber and foam material.

Material	Average Density (kg/m^3)	Standard Deviation
Unfoamed Neoprene	1213.25	8.43
Foamed Neoprene	335.05	3.46

shows the average densities and standard deviation for each material.

3.2 Microscopic Analysis

3.2.1 Sample Preparation

In addition to the mechanical tests, samples were prepared so that the structure of the foam could be investigated. In order to facilitate the microscopic analysis, a foam specimen with perpendicular faces was created. This was accomplished by first adhering the piece of foam to an aluminum block. The foam was then cut using a special rotary blade in a lathe with the aluminum block attached to the compound rest so that a constant feed rate could be achieved. A picture of this setup is shown in figure 3.1. The aluminum block was then rotated 90 degrees so that three perpendicular, flat faces were created. Distilled water was used as a lubricant to reduce friction and prevent tearing of the material during the cutting process. The resultant specimen was approximately 7 mm square.

3.2.2 Results

An Olympus BX61 microscope fitted with a digital imaging system and overall magnification of approximately 10 times was used to create images of the foam specimen. A grid of three by three individual images were taken and then combined to give a com-

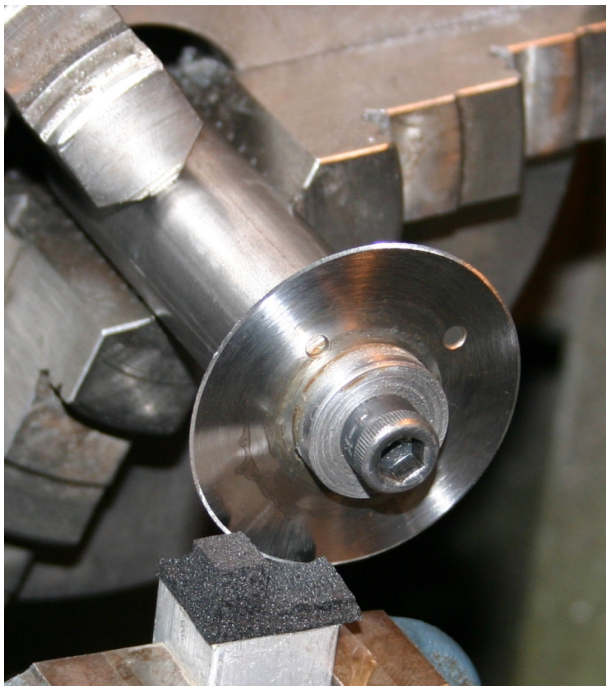

Figure 3.1: Preparation of the foamed specimen for micrographic analysis.

posite image which was used for analysis. This procedure was repeated for each face. Measurements of wall thickness, characteristic length and aspect ratio were determined using Image Pro Plus software by Media Cybernetics.

Figure 3.2 shows the composite image obtained for the polychloroprene foam. The Z direction was the foaming direction through the thickness. As indicated in the figure, the foam had a relatively consistent structure with largely equal sized cells. Through the foaming direction, as shown in the XZ and YZ planes, the cells exhibited a different aspect ratio than that seen in the cross-sectional XY plane.

Figure 3.3 shows the typical measurements taken for each of the foams. A minimum of 100 measurements were taken in each plane to determine the characteristic length, Lc, and wall thickness of the cells. Additionally, the anisotropic nature of the cells was determined by taking the ratio of the inside dimensions of the cells along the principle axes (x and y in the figure).

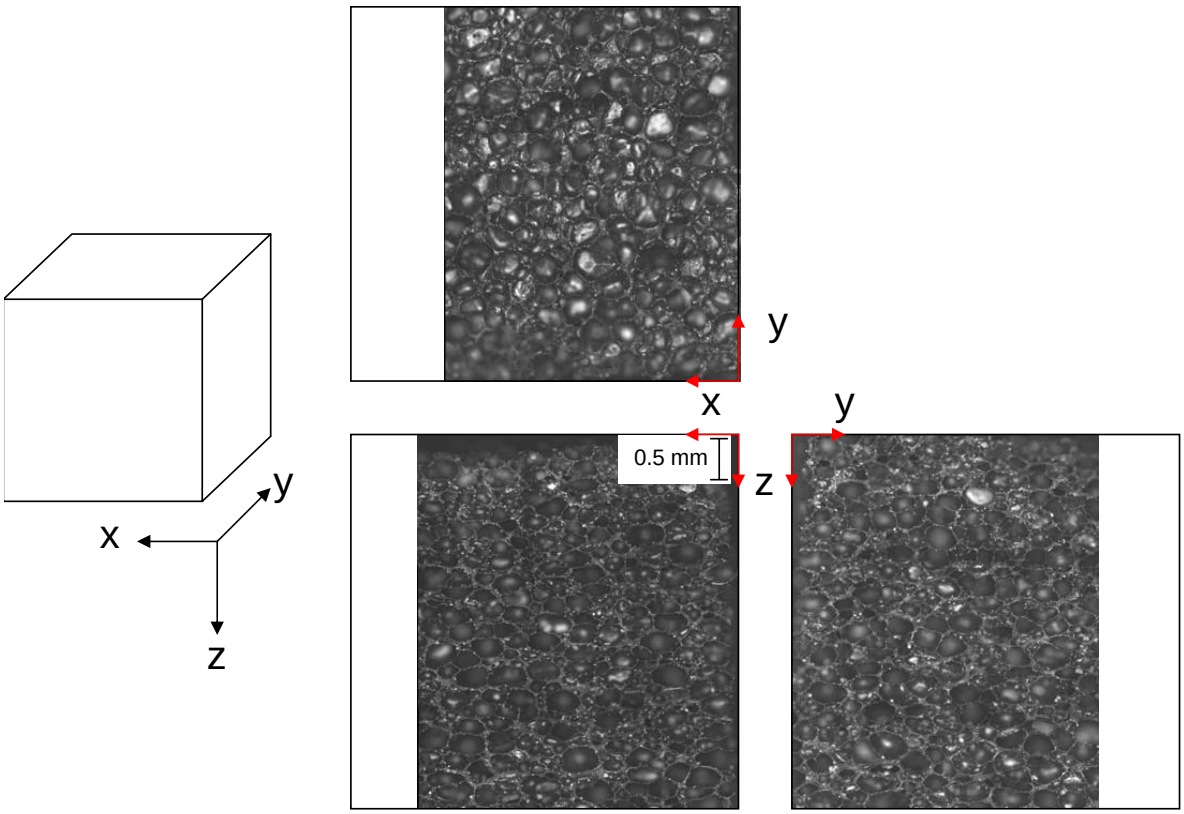

Figure 3.2: Structure of polychloroprene foam.

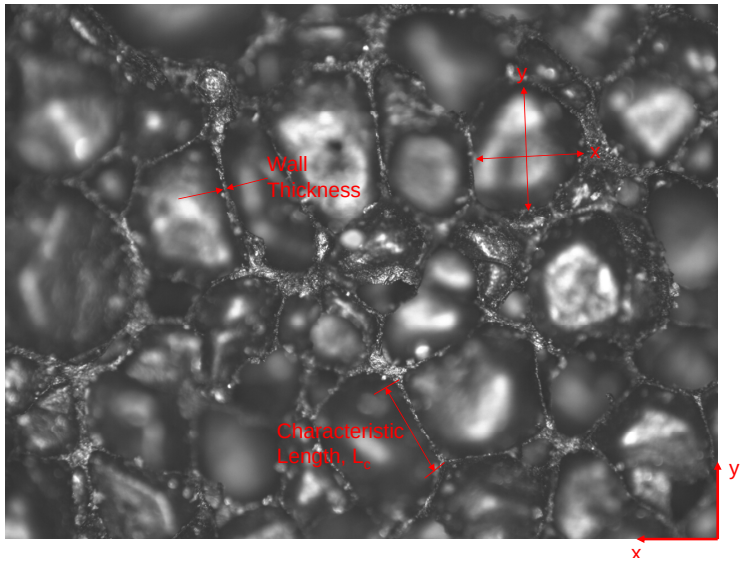

Figure 3.3: Close–up view of foam micro–structure showing typical measurements.

Table 3.2 to 3.4 show the measured values for the wall thickness, characteristic length and aspect ratio respectively. Relatively consistent wall thickness was seen in the XZ and YZ planes with a slight increase in thickness in the XY plane as indicated in table 3.2. The overall average of all wall thickness measurements was 11.78 μm with a standard deviation of 3.46μm.

Table 3.2: Measured values of wall thickness for each plane for polychloroprene foam (n=100).

Plane	Wall Thickness (μm)	Standard Deviation
XY	13.4	4.8
XZ	11.6	3.0
YZ	11.2	2.8

Similar results were noted for the characteristic length as shown in table 3.3. Overall, the cells had a characteristic length of 154.77μm with a standard deviation of 52.79 μm.

Table 3.3: Measured values of characteristic length for each plane for polychloroprene foam (n=100).

Plane	Characteristic Length (μm)	Standard Deviation
XY	180.4	56.5
XZ	135.9	49.7
YZ	148.9	42.0

As identified in figure 3.2, table 3.4 indicates that the cells had a near uniform cell size in the X:Y plane but showed some anisotropy in the Z (foaming) direction.

Table 3.4: Calculated aspect ratios of cell size for each plane of polychloroprene foam (n=30).

Plane	Aspect Ratio	Standard Deviation
X:Y	1.06	0.20
X:Z	1.79	0.41
Y:Z	1.56	0.28

3.3 Mechanical Testing

3.3.1 Specimen Preparation

Both quasi–static and dynamic experiments were conducted on right circular cylinders cut from the supplied sheets of material. Due to the flaccid nature of the material, special cutting techniques were developed to obtain consistent samples.

Initially, a coring tool, shown in figure 3.4, was used to cut cylindrical samples from the sheet material. A milling machine was used in order to apply a consistent feed rate of 3.75 mm/s with the tool spinning at 1500 rpm. Distilled water was used a lubricant in order to reduce friction between the tool and the material which would readily build up otherwise. This method gave satisfactory results for the polychloroprene rubber material. However, for the foamed materials, a 6 mm sheet of polyethylene foam was gently held (with less than 5 N) in contact with the surface of the polychloroprene foam sheets acting as a binder to prevent the sheet from twisting during cutting. This additional step resulted in satisfactory specimens with consistent surface quality and dimensions along its length.

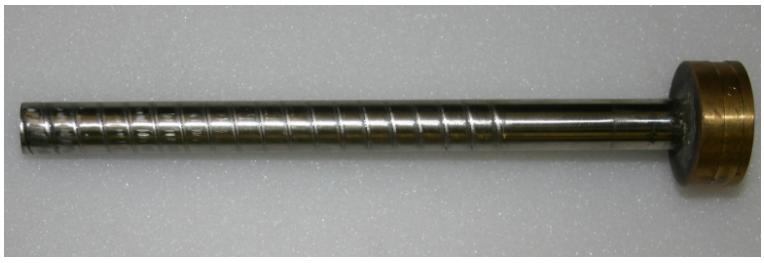

Figure 3.4: Coring tool for cylindrical samples.

The specimens were then cut to the desired length by placing them into a custom fixture shown in figure 3.5. The hole in the fixture is slightly smaller than that of the sample allowing a minimal clamping force to be exerted. A sharp utility knife was then

used to cut the sample to the appropriate length. Distilled water was used to minimize friction and generate consistent samples with parallel faces.

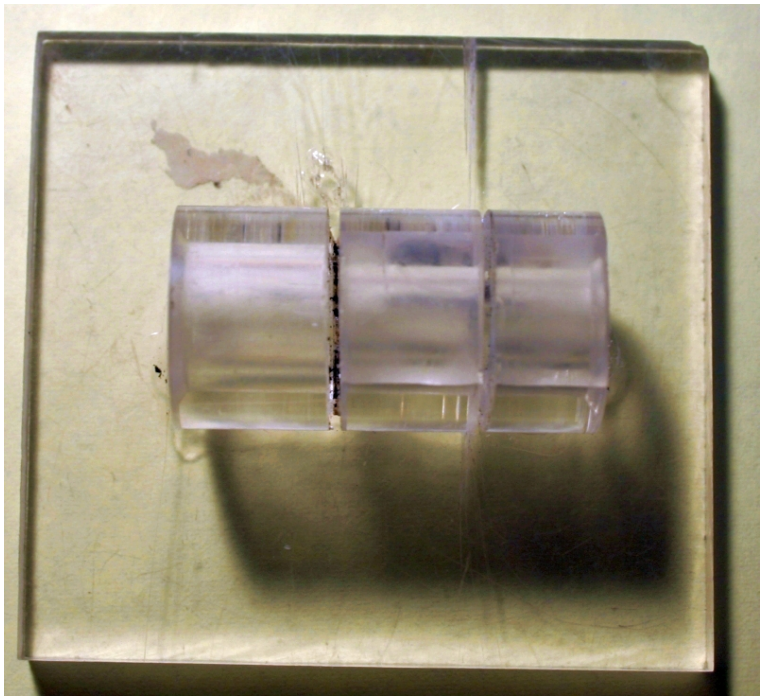

Figure 3.5: Holder used to cut specimens to desired length.

From work conducted previously, it was determined that the required length of the specimens was 4 mm to ensure dynamic equilibrium during the high rate tests as discussed in section 2.4.2. Additional tests were performed on specimens of different length at a quasi-static rate to identify length effects (discussed in more detail later). Figure 3.6 shows the dimensions of the specimen used in the testing.

3.3.2 Quasi-Static Tests

The quasi–static experiments utilized a custom–built hydraulic test fixture. A schematic of the test fixture is shown in figure 3.7 and a picture of it with a specimen in figure 3.8. The load cell used on this unit has a capacity of 2225N (500 lbf), which results in very

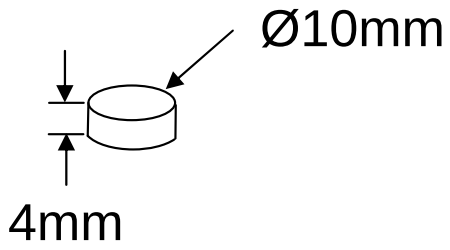

Figure 3.6: Dimensions of sample used for mechanical testing.

good load resolution for soft materials. Specimen displacement was measured using the displacement of the crosshead using a linear variable differential transformer (LVDT). This method of displacement measurement was necessary due to the extremely large displacements (on the order of 80%) for all materials. The specimen was compressed between two aluminum platens that were lightly lubricated with a lithium based grease. The time that the specimen was in contact with the grease was minimized to prevent possible deterioration of the material. The lubrication was necessary to prevent barreling of the specimen which would result in high internal stresses that are not of a uniaxial nature. The platens were manufactured in such a way to ensure that they were parallel to each other in the apparatus. Additionally, they were lapped after machining to ensure a smooth flat surface.

3.3.3 Dynamic Experiments

As discussed in chapter 2, a compressive split Hopkinson pressure bar was used to test the materials in compression at high rates.

3.3.4 Experimental Procedure

From previous testing on RTV rubbers [82] and ballistic gelatin [81], it was determined that a length of 4 mm would be suitable for the characterization of the material. The

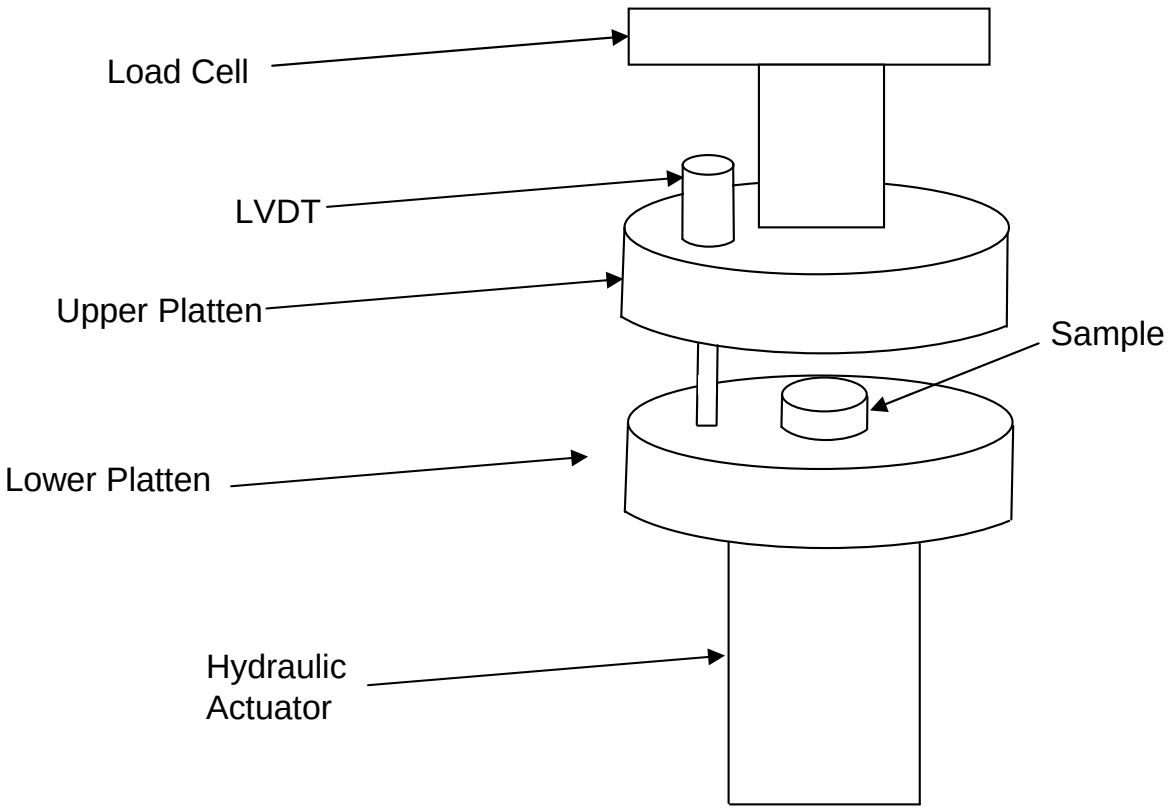

Figure 3.7: Schematic of quasi–static test apparatus.

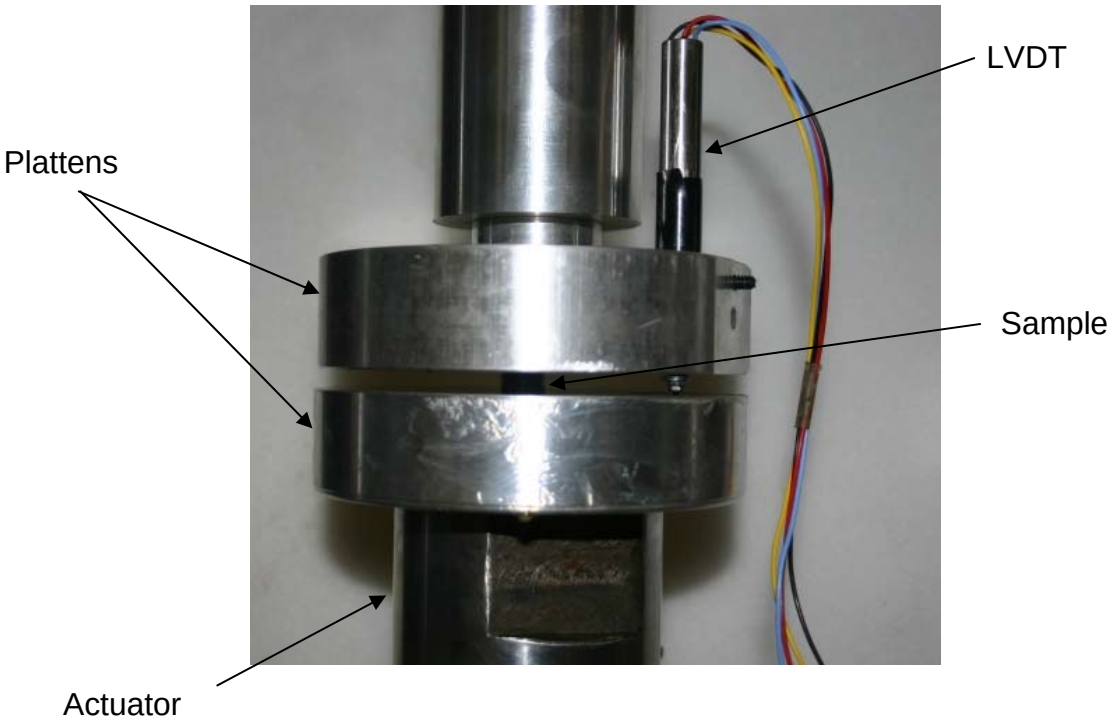

Figure 3.8: Photograph of quasi-static compressive test apparatus with sample.

bars were made from polymethyl methacrylate (PMMA or Acrylic) to better match the impedance of the polychloroprene rubber and foam. Although wave propagation in PMMA is not linear elastic, as shown in equation 2.29, methods exist to account for dispersion and attenuation effects of the wave as it propagates.

The ends of the bars were lubricated with a thin layer of high pressure lithium grease which was necessary to prevent barreling of the sample which would result in a non–uniaxial test with inappropriate stresses. Tests were conducted within 1 minute of placing the sample in contact with the lubricant to prevent any degrading effects it might have on the sample. The sample was aligned with the center of the bars to minimize any off center loading of the sample. In order to prevent any preloading of the samples, the gap between the bars was set to the measured gauge length of the sample using precisely machined slip gauges. This allowed the bars to just contact the sample without preloading it.

3.4 Experimental Results for the Polychloroprene Rubber

As discussed in section 2.4.2, a constraint of the Hopkinson Bar testing methodology for high rate material characterization was that the sample remains in dynamic equilibrium. As discussed previously, this necessitates a sample with a smaller sample length. To identify the effect that sample length has on the material response, samples of different length were tested at the same loading rate. The aspect ratio (length:diameter) for the samples used for the high rate testing was 0.4. Two other samples with the same diameter but lengths of 10 mm and 12 mm (aspect ratios of 1 and 1.2) were also tested at the same rate as the 0.1/s, 4 mm case. Figure 3.9 shows the stress–stretch response for the samples tested. In the figure, the dashed line shows the results from each sample tested. The solid thick lines show the average curve for the samples of each length. The 12 mm long sample, blue curve, exhibited a minor increase in stress at stretches ranging from 0.35 to 0.2 compared to the 10 mm and 4 mm long samples (green and red curves respectively) which showed similar responses over the loading history. As indicated in the figure, the results from these tests indicated that the effect of sample length for the solid polychloroprene rubber is minimal.

As outlined in the discussion given in section 2.4.2, dynamic equilibrium in the sample can be determined by examining the forces at end of the incident and transmitted bars for the high rate tests. Figure 3.10 show the typical incident, transmitted and reflected strain waves. These waves had been propagated to the end of the Hopkinson bars using the analysis detailed in reference [81]. Subsequently, the force was calculated from these waveforms and presented in figure 3.11 for a typical case. As indicated in the figure, the forces at the end of the incident and transmitted bars coincide well during the loading

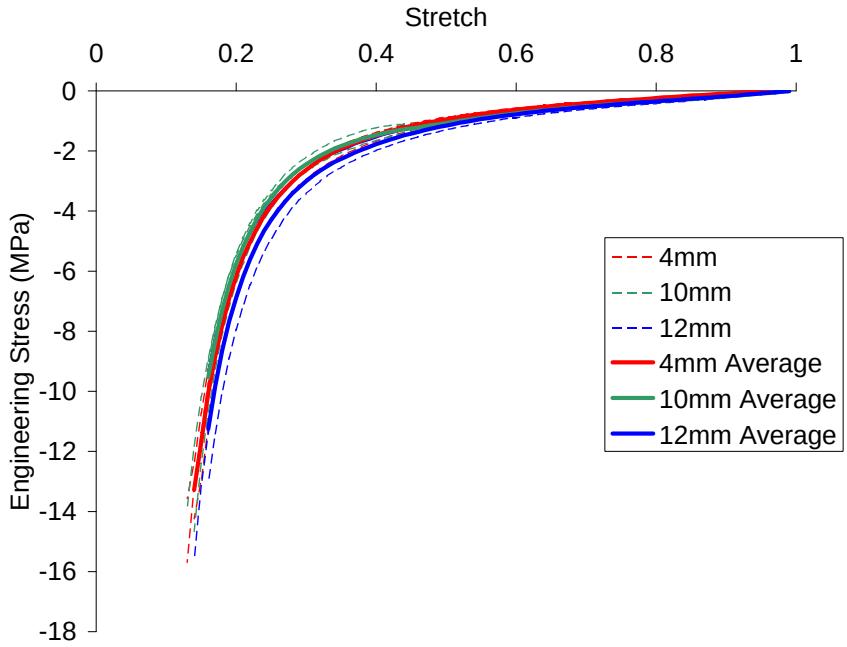

Figure 3.9: Stress–stretch response of polychloroprene rubber for different sample lengths.

section of the curve from 0 to 0.0012 s. After this point the unloading phase begins and the forces do not coincide well especially after 0.0014 s. It should be noted that only the 0 to 0.0012 s range of data is used. This indicates that the sample was in dynamic equilibrium during the pertinent section of the test.

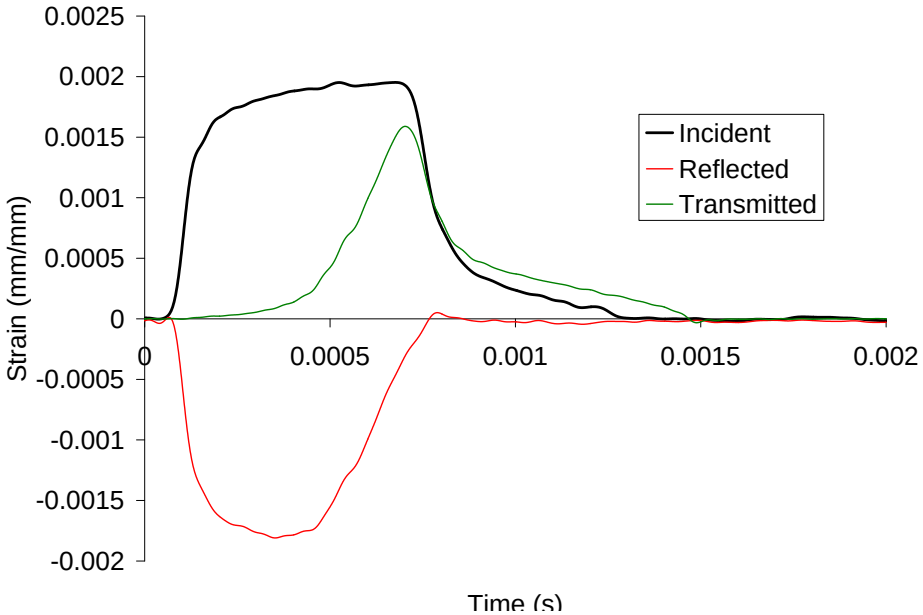

Figure 3.10: Typical incident, transmitted and reflected strain waveforms.

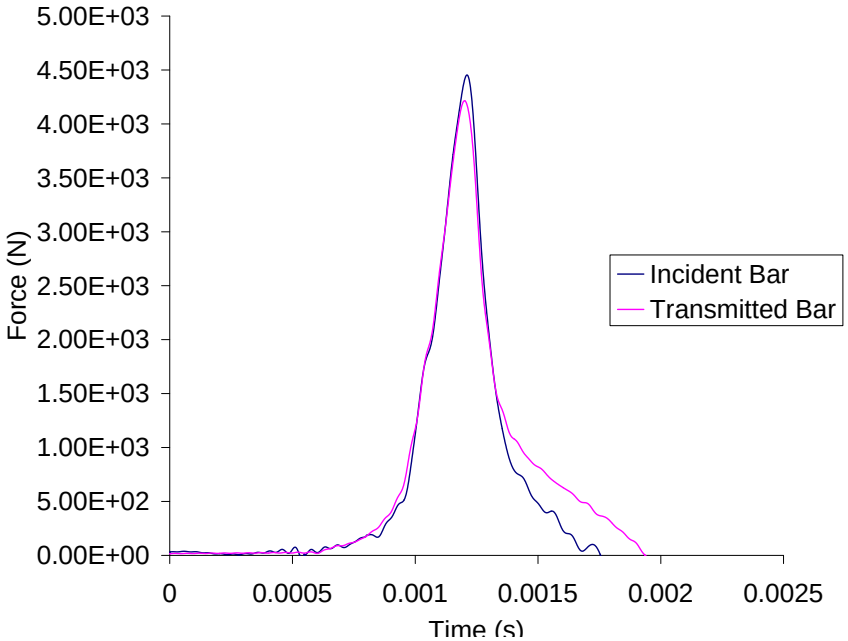

Figure 3.11: Forces in the incident and transmitted bars.

For completeness, figures 3.12 to 3.17 show stress–stretch response for polychloroprene at rates from 0.001/s to 2700/s. In each graph the result from each test is represented by the blue, red and green lines. The thick black line represents the average of these curves. Figures 3.12 to 3.15 show that there was good consistency between the results of the tested specimens. Only minor deviations from the average curve are noted through this range of strain rates. Slightly more spread between the stress–stretch curves at 7.9/s is evident in figure 3.16. The tests performed at 2700/s, shown in figure 3.17, show the largest spread between tests. Between stretches of 1 and 0.4 there is only minor deviations in the curves. In the 0.4 to 0.2 stretch range, two of the curves exhibit a similar response with one curve showing a larger stress level. Throughout the range of strain rates the curves exhibit a hyperelastic material response as detailed in chapter 2.

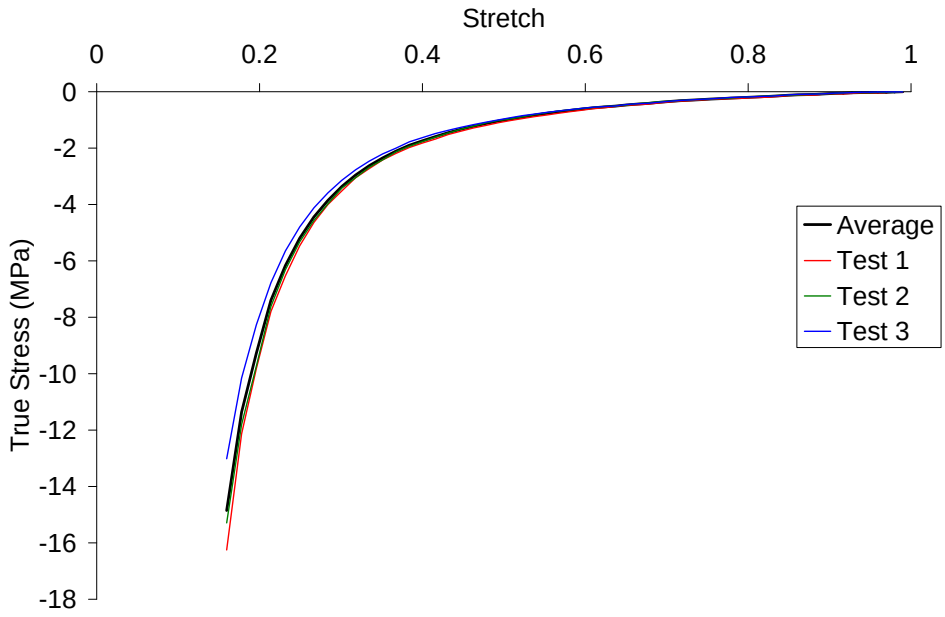

Figure 3.12: Stress–stretch response for the polychloroprene rubber at a strain rate of 0.001/s.

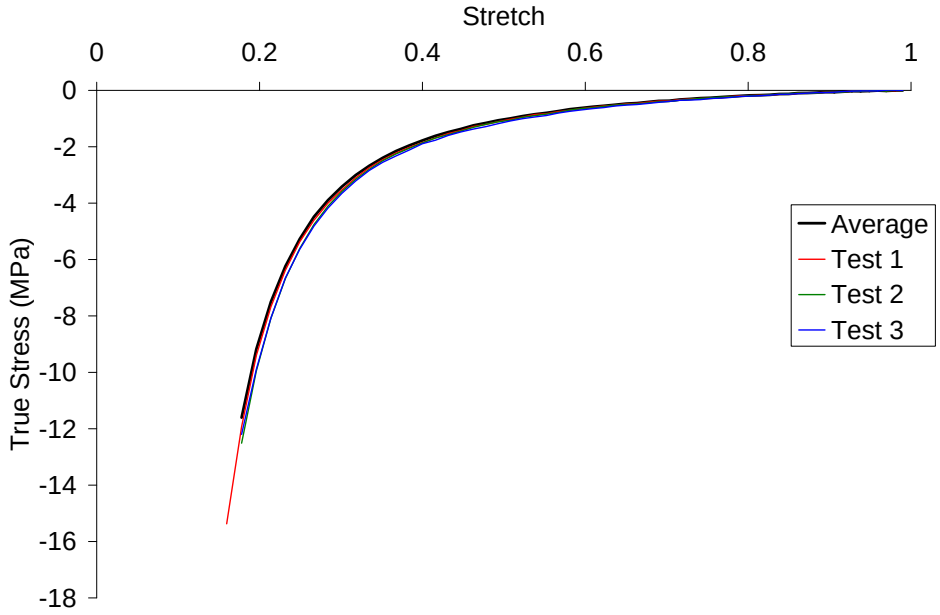

Figure 3.13: Stress–stretch response for the polychloroprene rubber at a strain rate of 0.01/s.

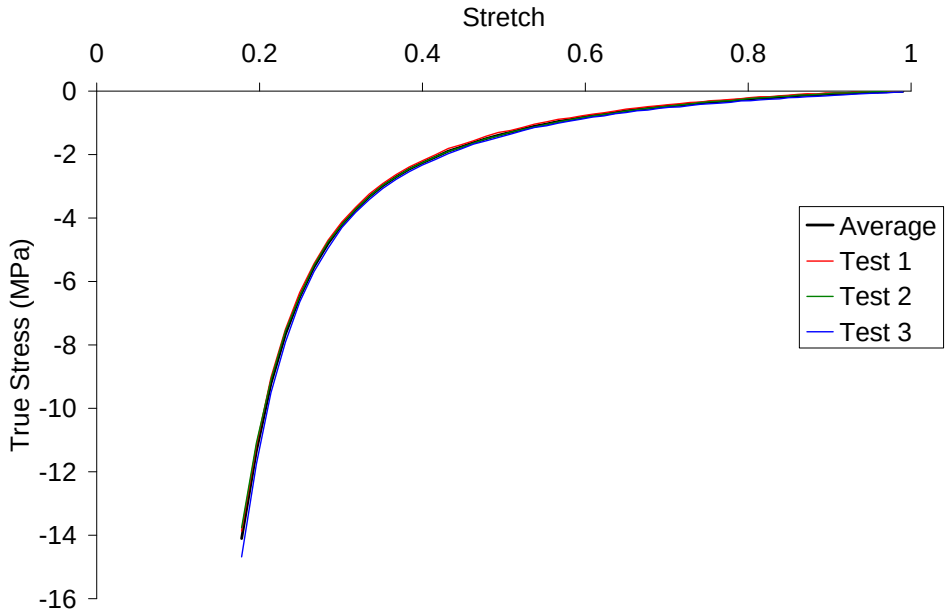

Figure 3.14: Stress–stretch response for the polychloroprene rubber at a strain rate of 0.1/s.

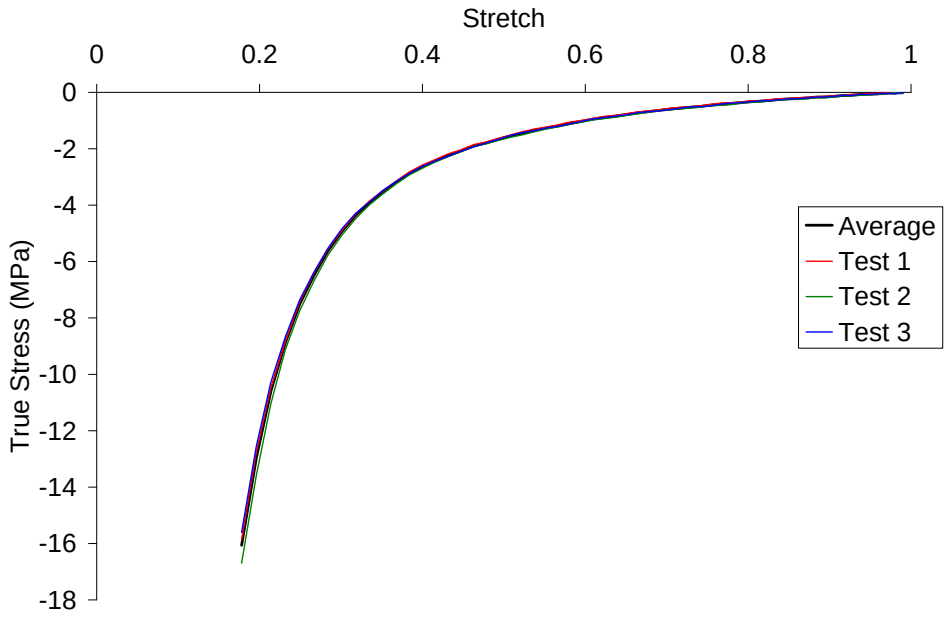

Figure 3.15: Stress–stretch response for the polychloroprene rubber at a strain rate of 1/s.

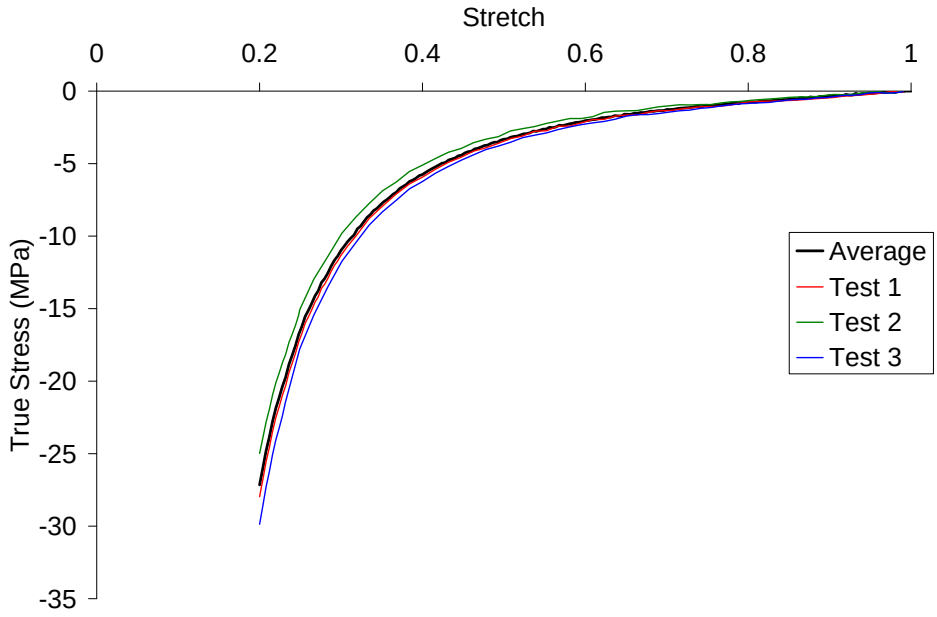

Figure 3.16: Stress–stretch response for the polychloroprene rubber at a strain rate of 7.9/s.

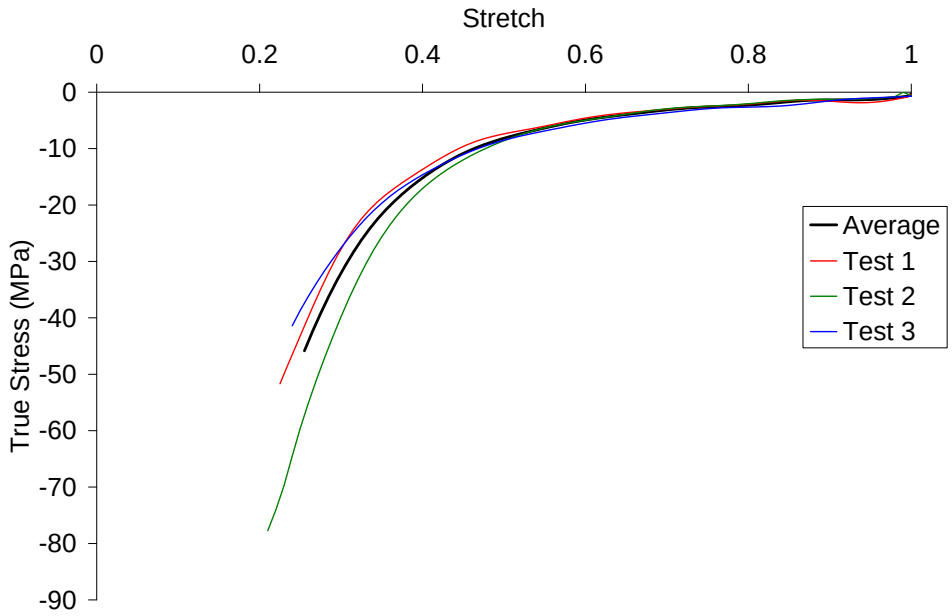

Figure 3.17: Stress–stretch response for the polychloroprene rubber at a strain rate of 2700/s.

The average curves for each strain are shown in figure 3.18. As indicated in the figure, polychloroprene rubber had a dependence on strain rate over the entire loading history. This is further highlighted in figure 3.19 which plots the value of stress at different values of stretch versus strain rate (on a logarithmic scale). As indicated in figure 3.19, as the strain rate increased from 0.001/s to 2700/s, the resulting stress values increase from -1.75 MPa to -15.5 MPa at a stretch of 0.4. Similarly, at a stretch of 0.2 the stress increases from -8.75 MPa to -74.25 MPa over the same increase in strain rate. Additionally, figure 3.19 indicates that the polychloroprene had a non–linear viscoelastic effect since the values of stress do not increase linearly with strain rate.

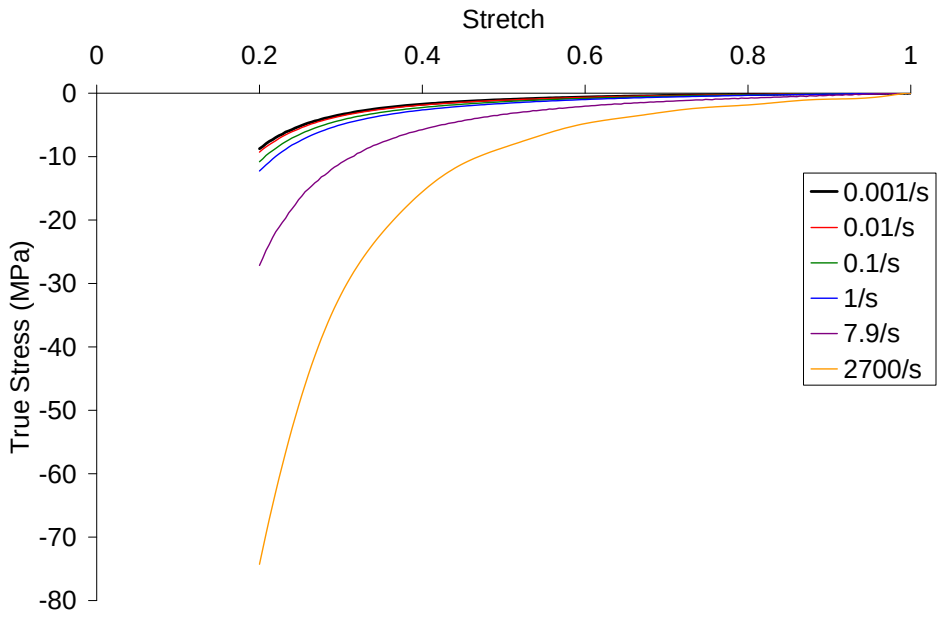

Figure 3.18: Average stress–stretch curves for the polychloroprene rubber over the strain rates tested.

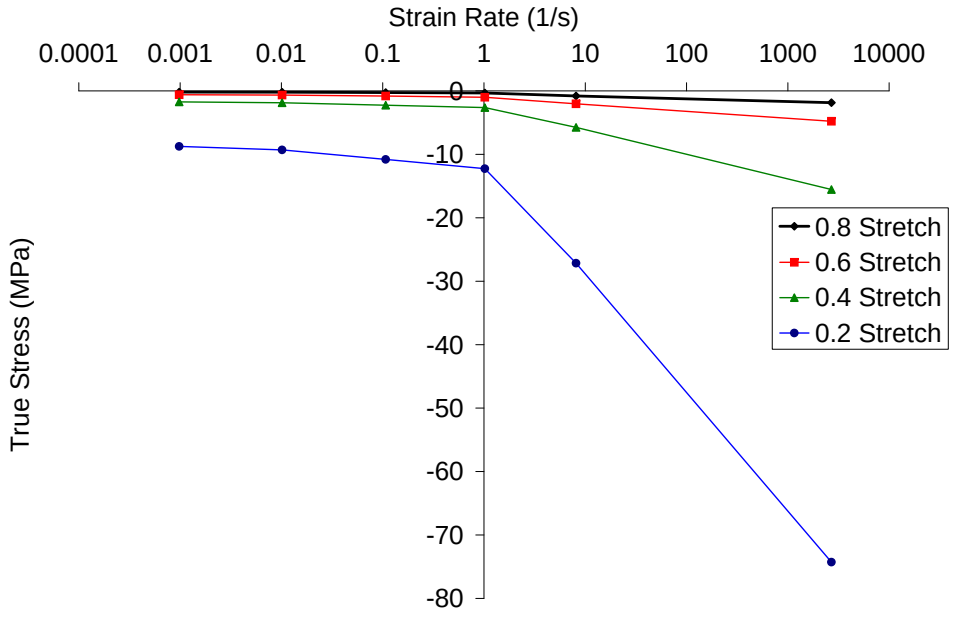

Figure 3.19: Stresses at different stretch values over the range of strain rates tested.

3.5 Experimental Results for the Foamed Polychloroprene

The purpose of performing experimental tests on the polychloroprene foam was not to characterize the foamed material at a macroscopic scale as was done for the polychloroprene rubber in the previous section, but was instead meant to identify if the foamed polychloroprene material had a dependence on strain rate and to provide a set of experimental data against which the numerical models developed in chapter 5 could be validated. As will be discussed in chapter 5, only the high rate tests were modeled.

For the purpose of this study, the tests performed on the polychloroprene rubber were repeated on the polychloroprene foam. As before, figures 3.20 to 3.25 show the stress–stretch response for polychloroprene at rates from 0.001/s to 3000/s. Similar to the polychloroprene rubber, figures 3.20 to 3.22 show that there was good consistency

between the results of the tested specimens. Only minor deviations from the average curve are noted through this range. Slightly more spread between the stress–stretch curves at 1/s is evident in figure 3.23. The tests performed at 2050/s and 3000/s, shown in figure 3.24 and figure 3.25, exhibit larger deviations between tested samples. The specimens tested at the higher rate exhibited oscillations at stretches from 1 to 0.5 after which they exhibited a hyperelastic response similar to the polychloroprene rubber. The curves from the samples tested at 2050/s and 3000/s were used for for the validation of the numerical model of the foam. As such, an interpretation of these curves is given in chapter 5.

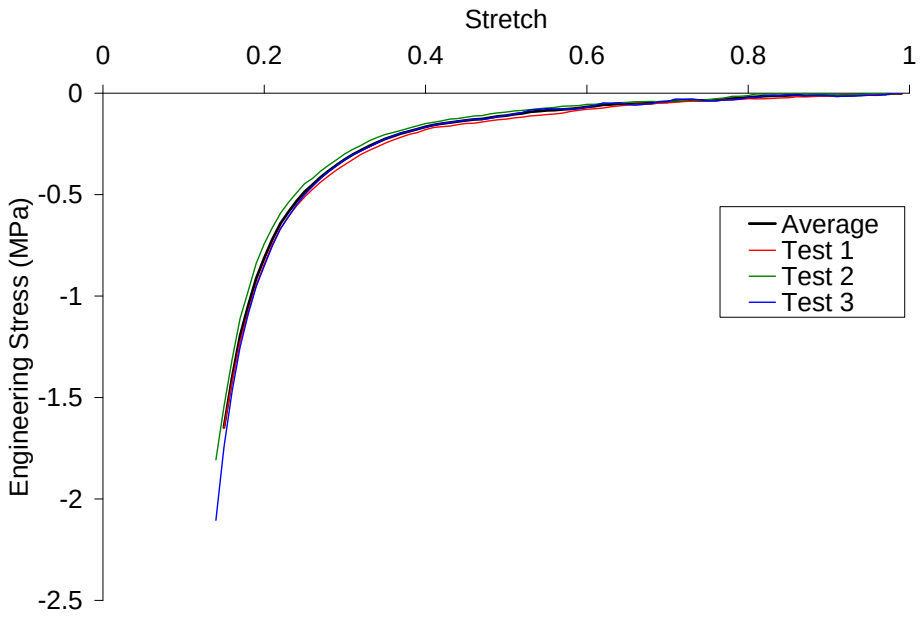

Figure 3.20: Stress–stretch response for the polychloroprene foam at a strain rate of 0.001/s.

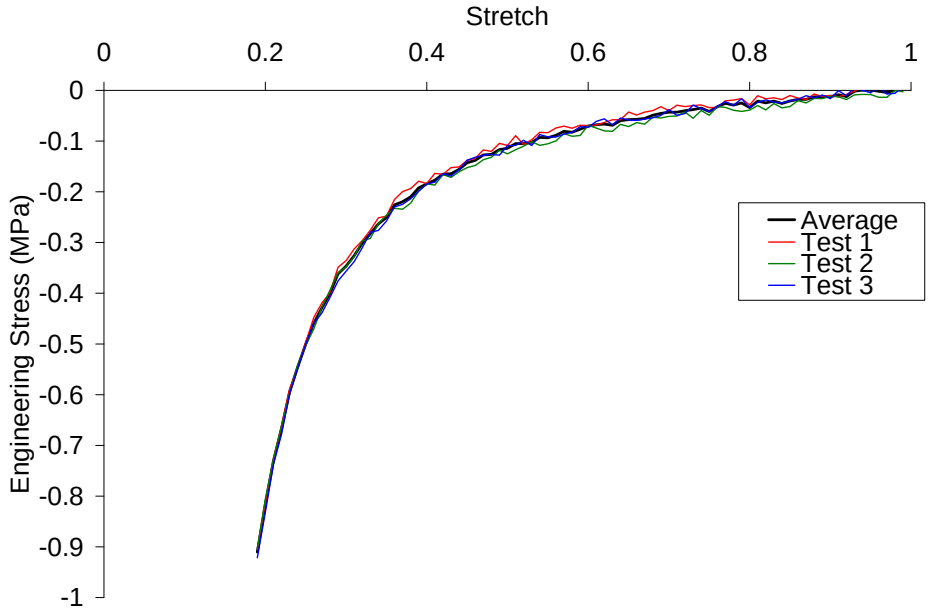

Figure 3.21: Stress–stretch response for the polychloroprene foam at a strain rate of 0.01/s.

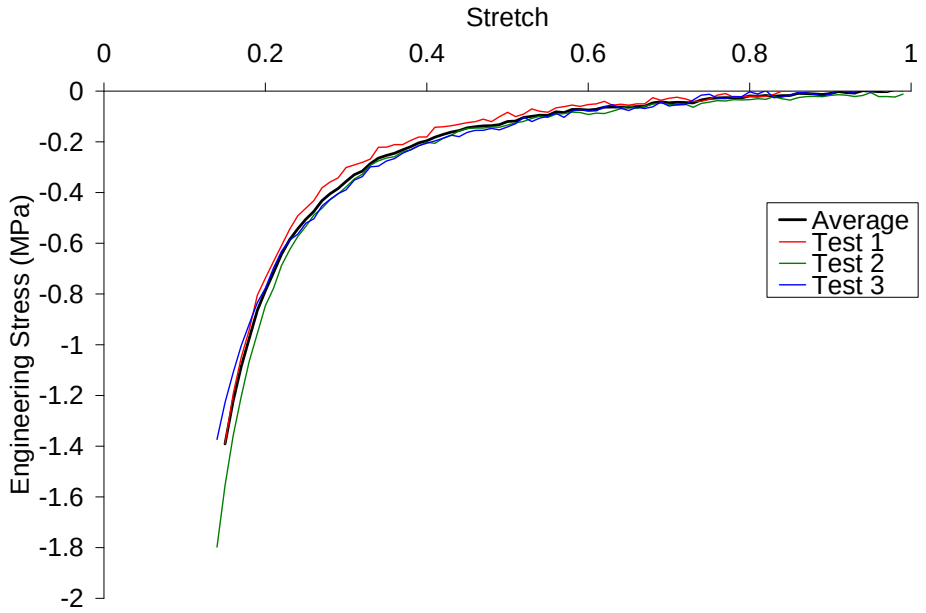

Figure 3.22: Stress–stretch response for the polychloroprene foam at a strain rate of 0.1/s.

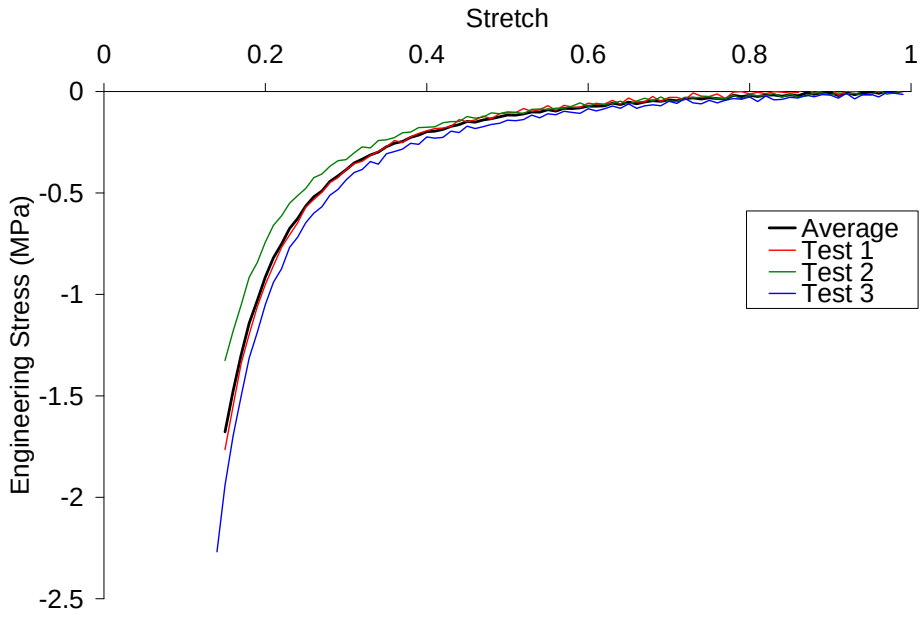

Figure 3.23: Stress–stretch response for the polychloroprene foam at a strain rate of 1/s.

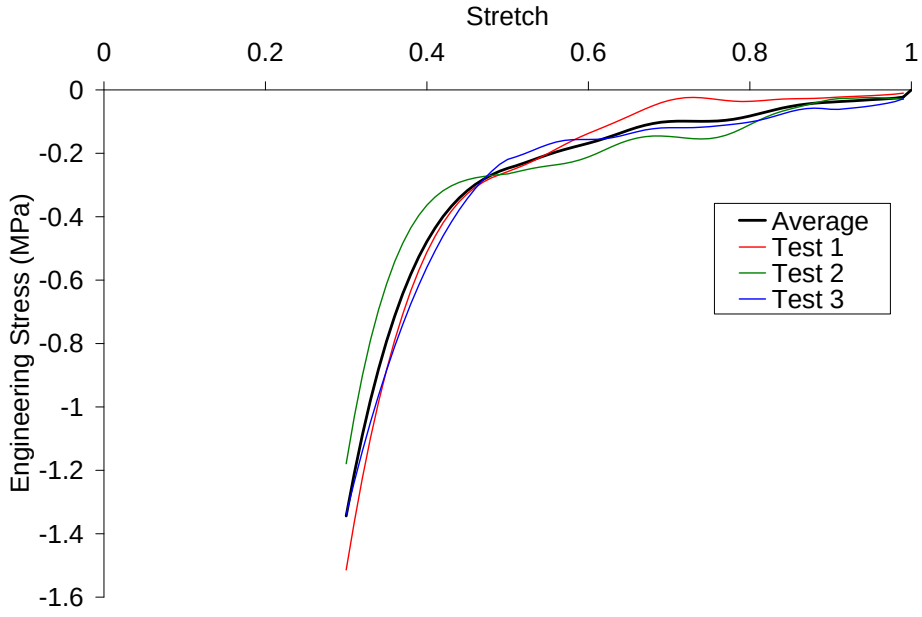

Figure 3.24: Stress–stretch response for the polychloroprene foam at a strain rate of 2050/s.

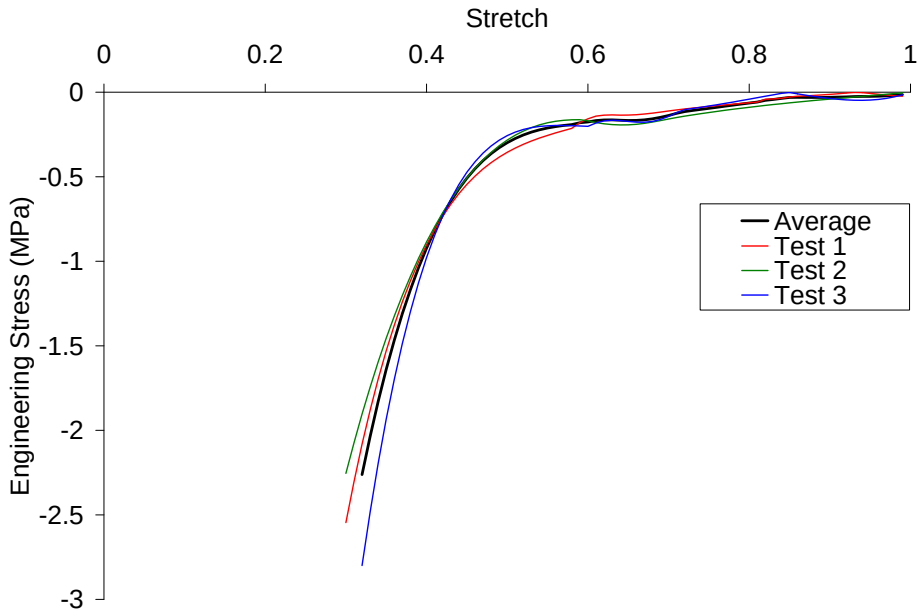

Figure 3.25: Stress–stretch response for the polychloroprene foam at a strain rate of 3000/s.

Similar to before, the average curves for each strain rate for the polychloroprene foam are shown in figure 3.26. As indicated in the figure, polychloroprene foam exhibits a dependence on strain rate although it is not as significant as the polychloroprene rubber discussed previously. This is further highlighted in figure 3.27 which plots the value of stress at different values of stretch versus strain rate. The relatively flat curves at stretches of 0.8 and 0.6 show only minor increases with strain rate. At 0.4 stretch a greater increase in stress was seen with strain rate.

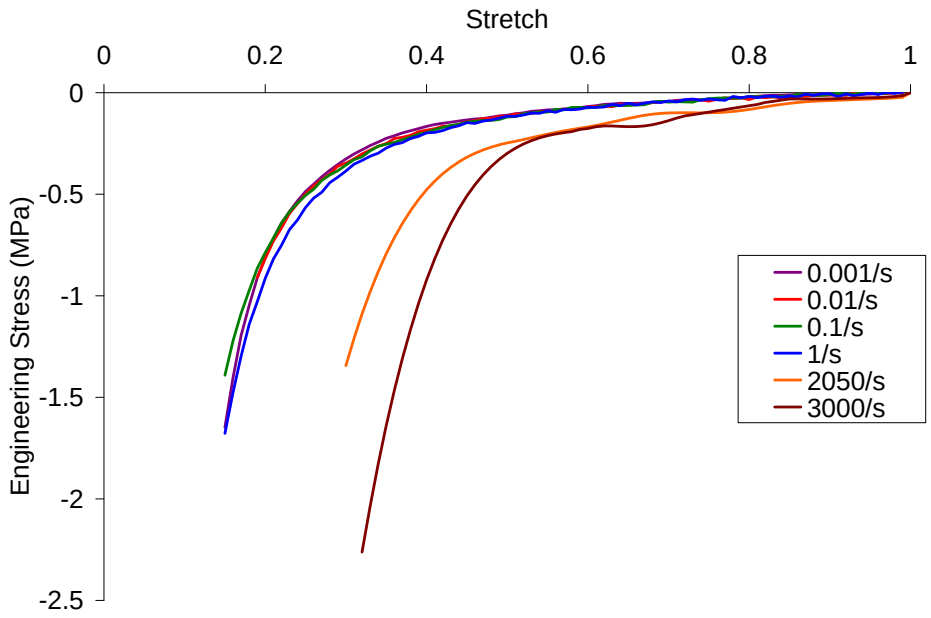

Figure 3.26: Average stress–stretch curves for the polychloroprene foam over the strain rates tested.

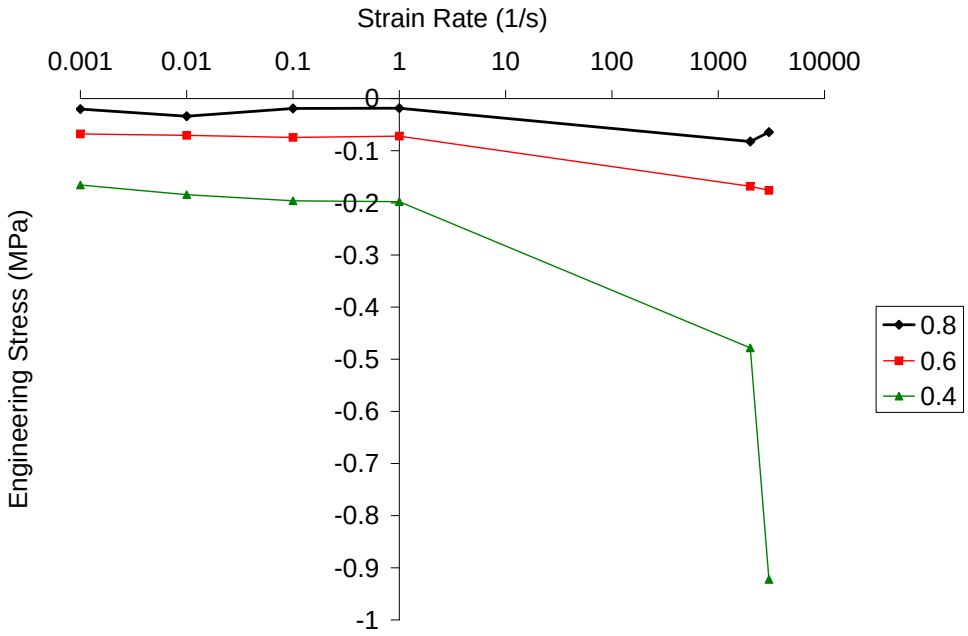

Figure 3.27: Stresses at different stretch values over the range of strain rates tested.

3.6 Summary

The mechanical behaviour of polychloroprene rubber was investigated. Tests indicated that the polychloroprene rubber had a density of approximately 1210 kg/m^3. From the range of compression tests performed at different loading rates, it was evident that the polychloroprene rubber material had a significant dependence on strain rate. The polychloroprene rubber showed a rise in stress as the material is compressed characteristic of a hyperelastic material. Additionally, a non–linear viscoelastic effect was identified for the polychloroprene rubber.

The polychloroprene foam material had a density of 335 kg/m^3. Micrographic examination of the polychloroprene foam identified a relatively homogeneous structure with approximately equal sized cells. The cells showed some slight anisotropy through the foaming (Z) direction. Microscopic measurements of wall thickness, characteristic length and aspect ratio were taken. The foamed materials exhibited a dependence on strain rate as rates changed from 0.001/s to 3000/s. However, there is only a minimal change in the mechanical behaviour of the material as strain rates increase from 2050/s to 3000/s indicating that was sensitive to decade (factors of 10) changes in strain rate. The behaviour of the foam is discussed further in chapter 5.

Chapter 4

Constitutive Modelling

This chapter is composed of four sections. Section 4.1 outlines the proposed constitutive model. Section 4.2 outlines the procedure used to determine the constitutive model parameters to the experimental data collected in chapter 3. Section 4.3 discusses the results of the procedure used to determine the constitutive model constants and its correlation to the experimental results. Section 4.4 discusses the validation of the constitutive model using single element simulations.

4.1 Proposed Constitutive Model

The inability of the models discussed in section 2.5.3 to capture the materials response over a variety of strain rates required the development of a new constitutive model. The model that was developed had several advantages to those discussed in section 2.5 as will be discussed later. The current approach combines the Ogden hyperelastic constitutive model and viscoelasticity through the convolution integral combined with a modifier to account for non–linear effects.

The viscoelastic contribution is based on the convolution integral, as before, but

modified with a Rivlin type series, equation 2.46, based on the invariants of the stretch tensor on a principal basis. Rewriting equation 2.71 in terms of the principal viscoelastic stresses, τ_{ii}^{v}, principal stretches, λ_i, and modifier terms is given as

$$\tau_{ii}^{v}(t) = \int_{-\infty}^{t} \Gamma G(t-\phi) \frac{d\lambda_i(t)}{d\phi} d\phi + p^{v} \text{ (no summation)} \tag{4.1}$$

where p^{v} is the viscoelastic contribution to the arbitrary pressure as defined previously and the modifier, Γ, is given as

$$\Gamma \equiv \sum A_{pqr} (I_1 - 3)^p (I_2 - 3)^q (I_3 - 3)^r. \tag{4.2}$$

Here p, q and r each range from 0 to the number of terms required in the fit to the material data. As discussed in chapter 2, the third invariant is approximately equal to 1 for an incompressible material and so the last term in equation 4.2 is not included. Therefore, equation 4.2 can be expressed as

$$\Gamma \equiv \sum A_{pq} (I_1 - 3)^p (I_2 - 3)^q \tag{4.3}$$

which when expanded out gives

$$\Gamma = \sum A_{pq} (I_1 - 3)^p (I_2 - 3)^q \tag{4.4}$$

$$= A_{00} + A_{01}(I_2 - 3) + A_{02}(I_2 - 3)^2 + A_{10}(I_1 - 3) + A_{11}(I_1 - 3)(I_2 - 3) + ... \tag{4.5}$$

Following the evolution of the time marching technique to solve the convolution integral as discussed previously, the increment in viscoelastic stress, equation 2.81, is given

as

$$\int_t^{t+\Delta t} \Gamma G\left(t+\Delta t-\phi\right)\frac{d\lambda\left(\phi\right)}{d\phi}d\phi = \sum_{k=1}^{N_k}\Gamma\frac{\gamma_k}{\beta_k}\frac{\lambda\left(t+\Delta t\right)-\lambda\left(t\right)}{\Delta t}\left[1-e^{-\beta_k\Delta t}\right]. \tag{4.6}$$

The history variable, equation 2.85, was then given as

$$\sum_{k=1}^{N_k} H_k\left(t\right) \equiv \int_0^t \Gamma\sum_{k=1}^{N}\gamma_k e^{-\beta_k(t-\phi)}\frac{d\lambda\left(\phi\right)}{d\phi}d\phi. \tag{4.7}$$

As with equation 2.88, equations 4.6 and 4.7 was combined to give

$$\tau_{ii}^{v}\left(t+\Delta t\right) = \sum_{k=1}^{N_k} e^{-\beta_k\Delta t}H_k\left(t\right) + \Gamma\frac{\gamma_k}{\beta_k}\frac{\lambda\left(t+\Delta t\right)-\lambda\left(t\right)}{\Delta t}\left[1-e^{-\beta_k\Delta t}\right] + p^v. \tag{4.8}$$

The total state of stress was then determined using equation 4.8 with equation 2.61 through the linear sum $\tau_{ii}^{p} = \tau_{ii}^{e} + \tau_{ii}^{v}$ (no summation). The total principal stresses was then expressed as

$$\tau_{ii}^{p}\left(t+\Delta t\right) = \tau_{ii}^{e} + \tau_{ii}^{v} \text{ (no summation)} \tag{4.9}$$

$$= \sum_{d=1}^{N_d}\mu_d\left(\tilde{\lambda}_i^{\alpha_d} - \frac{1}{3}a_d\right) + p$$

$$+ \sum_{k=1}^{N_k} e^{-\beta_k\Delta t}H_k\left(t\right) + \Gamma\frac{\gamma_k}{\beta_k}\frac{\lambda\left(t+\Delta t\right)-\lambda\left(t\right)}{\Delta t}\left[1-e^{-\beta_k\Delta t}\right] + p^v \tag{4.10}$$

but p and p^v are scalars which can be combined into p^T to give

$$\begin{aligned}\tau_{ii}^{p}\left(t+\Delta t\right) = & \sum_{d=1}^{N_d}\mu_d\left(\tilde{\lambda}_i^{\alpha_d}-\frac{1}{3}a_d\right)\\ & +\sum_{k=1}^{N_k}e^{-\beta_k\Delta t}H_k\left(t\right)\\ & +\Gamma\frac{\gamma_k}{\beta_k}\frac{\lambda\left(t+\Delta t\right)-\lambda\left(t\right)}{\Delta t}\left[1-e^{-\beta_k\Delta t}\right]+p^T\end{aligned} \tag{4.11}$$

The general solution procedure used a time marching technique as follows. At each increment(n) with time step (dt):

1. Given F_{ij} solve for the principal stretches (eigenvalues) $\lambda_i = U_{ii}^p$ and the principal directions (eigenvectors).

2. Calculate the principal hyperelastic Kirchhoff stresses, τ_{ii}^e, via equation 2.61 using λ_i and material coefficients.

3. Calculate principal invariants of $\mathbf{U}$ so that

   $I_1 = \mathrm{tr}\left(\mathbf{U}\right) = \lambda_1+\lambda_2+\lambda_3$

   $I_2 = \frac{1}{2}\left[\left(\mathrm{tr}\mathbf{U}\right)^2-\mathrm{tr}\left(\mathbf{U^2}\right)\right] = \left(\lambda_1+\lambda_2+\lambda_3\right)^2-\left(\lambda_1^2+\lambda_2^2+\lambda_3^2\right)$.

4. Calculate viscoelastic modifier via equation 4.2 without the last term ($\left(I_3-3\right)^r$).

5. Use recursive techniques to solve convolution integral as follows:

   (a) If not in first cycle (otherwise set the history variables to zero, set previous stretch to one) calculate the stretch rate

   $\dot{\lambda}_i = \frac{\lambda_i^n-\lambda_i^{n-1}}{\Delta t}$.

   (b) Calculate the increment for each prony series coefficient and each direction via equation 4.7. These are the new history variables.

(c) Store the new history variables and new principal stretches for the next time step.

(d) Calculate the increment in viscoelastic stress for each direction via equation 4.8 by summing the new history variables calculated in step 5b.

6. Sum the principal elastic and principal viscoelastic stresses to obtain the total principal stresses, i.e. $\tau_{ii}^{p} = \tau_{ii}^{e} + \tau_{ii}^{v}$ (no summation on subscripts).

7. Calculate the dyadic product of the principal direction vectors, $n_i n_j$.

8. Rotate the stresses back to the standard basis using equation 2.67.

9. Calculate the Cauchy stress via $\sigma_{ij} = \tau_{ij}/J$.

Note that in the above procedure $\sigma \approx \tau$ since $J \approx 1$. The time–marching technique used to solve the convolution integral as described in the above procedure made it an ideal formulation to implement into an explicit finite element program. As such, a material subroutine was written using the above procedure and used in the analysis which follows in the subsequent sections and chapters.

This formulation offered several advantages. As indicated by Ogden [92], the use of principal stretches highlights the isotropic nature of the elasticity of the material. Through the use of invariants in the modifier term, the material maintains its objectivity and no further rotations, outside of those already required by the Ogden material model, need to be considered. When implemented into finite element programs, the deformation gradient, $\mathbf{F}$, is often available whereas $\dot{\mathbf{F}}$ as required by the implementation in equation 2.97 requires further calculation [47]. It has been shown that the Ogden model is capable of capturing material behaviour of rubber up to very large stretches (as high as 0.2 which corresponds to an engineering strain of 80% as discussed in chapter 2) [96].

Additionally, the use of principal stretches requires the storage of three less variables than that of the standard implementation in finite element codes which requires the storage of each stress component instead of the three principal components in the current implementation. As will be seen in the subsequent sections, there was an excellent correspondence between the proposed material model and the experimental data over the range of stretches and strain rates tested.

4.2 Determination of Constitutive Model Constants

This section contains the procedure used to determine the constitutive material model constants for the proposed model in section 4.1 and the results from the fitting procedure.

4.2.1 Data Preparation and Fitting Considerations

Prior to determining the constants for the constitutive model, the experimental data was manipulated into a form that was compatible with the constitutive model. As detailed in chapter 2 equation 2.49, the deformation tensor F_{ij} for the uniaxial incompressible case can be written as

$$F_{ij} = \begin{bmatrix} \lambda_1 & 0 & 0 \\ 0 & \lambda_1^{-1/2} & 0 \\ 0 & 0 & \lambda_1^{-1/2} \end{bmatrix} \tag{4.12}$$

Using equations 4.11 and 4.8, and the fact that the stresses $\tau_{22}, \tau_{33} = 0$ since the tests are uniaxial, the arbitrary pressure, p^T, can be calculated as follows. At each time step the principal stretches, λ_i, are determined from the deformation gradient as detailed previously. The material constants μ, α, λ, β are known, and the history variable H_k is available from the previous time step. Since the total principal stresses τ_{22}, τ_{33} are equal to zero, equation 4.11 can be rearranged to give

$$p^T = -\sum_{d=1}^{N_d} \mu_d \left(\tilde{\lambda}_i^{\alpha_d} - \frac{1}{3} a_d \right) - \sum_{k=1}^{N_k} e^{-\beta_k \Delta t} H_k(t) - \Gamma \frac{\gamma_k}{\beta_k} \frac{\lambda(t+\Delta t) - \lambda(t)}{\Delta t} \left[1 - e^{-\beta_k \Delta t} \right]. \tag{4.13}$$

If the arbitrary hyperelastic and viscoelastic pressure components are desired, they can be solved for individually using a similar analysis.

The data from each experimental test was resampled in such a manner to ensure that equal spacing between stretch points was achieved as well as equal numbers of points for each curve. The data was manipulated to this form to prevent biasing of the coefficients to one of the curves or one area of a particular curve. *Id est*, if one of the six curves used had 1000 points instead of 100, when the fitting of the material constants was performed, the coefficients would be biased towards the curve with 1000 points. Similarly, if one area of a curve had more points (for example 1000 points between stretches of 1 to 0.8 and 100 points from 0.79 to 0.2) the coefficients would be biased towards that area.

4.2.2 Fitting Methodology

Several difficulties were encountered when attempting to use conventional fitting procedures such as those found in SYSTAT [107]. The difficulty was in the determination of the convolution integral, which as discussed in the previous section, requires a time marching approach that does not lend itself to these types of programs and so specialized programs are required [108]. As such, a program in MATLAB [109] was created to determine the material parameters using optimization techniques as discussed subsequently.

The procedure for fitting the material constants was based on the desire for the predicted stresses from the constitutive model to match the experimental stress given

the loading history (stretch and time). For a single curve this can be written as

$$\sigma^{\text{model}}(t,\lambda) = \sigma^{\text{experiment}}(t,\lambda) \tag{4.14}$$

where σ represents the Cauchy uniaxial stress. A measure of how "good" the fit of the model to the experiments was needed. Based on the classical definition of the R^2 value, the "goodness" of the fit, EG, can be expressed as

$$EG = \frac{\sum (\sigma_i - f_i)^2}{\sum (\sigma_i - \overline{\sigma})^2} \tag{4.15}$$

where σ_i are the experimental values of stress at each stretch point i, f_i is the calculated stress via the constitutive equation and $\overline{\sigma}$ is the average of the experimental stresses given by

$$\overline{\sigma}_{exp} = \frac{1}{n}\sum_{1}^{n} \sigma_n \tag{4.16}$$

where n, is the number of samples. As the calculated values approach the experimental values, EG approaches 0.

Equation 4.15 can be extended out for multiple curves by

$$EG_{total} = \sum_{1}^{nc} EG_{nc} \tag{4.17}$$

where nc is the number of curves. The normalized R^2 value is obtain by subtracting EG_{total} from the number of curves and then dividing by the number of curves.

An optimization problem is the motivation to minimize the objective function, such as equation 4.17, towards zero by varying the input parameters $(\mu, \alpha, \gamma, \beta, A_{p,q})$. Mathematically, this is expressed as

$$\min_{x} \left(EG_{total} \left(\mu, \alpha, \gamma, \beta, A_{p,q} \right) \right) \tag{4.18}$$

subject to the constraints

$$\mu, \alpha, \gamma, \beta, A_{p,q} > 0.$$

The basic optimization sequence was as follows

1. Determine the stress values given stretch, time and the material constants.
2. Calculate the objective function via equations 4.15 and 4.17.
3. Through analyzing the current and previous values of the objective function, along with the material constants from previous iterations, a prediction of the new coefficients which further minimize the objective function was performed.
4. Repeat until the change in the objective function was within a specified tolerance.

There are several optimization methods implemented in MATLAB which could have been used to minimize the objective function. The constrained nonlinear optimization method "fmincon" was used in combination with the objective function, equation 4.18 to determine the coefficients for the constitutive model. This optimization method allowed for a variety of different constraints to be imposed on the determination of variables which was necessary for this analysis. Specifically, the coefficients in the material model should be positive. This requirement was necessary since the finite element formulation

of the constitutive model approximated the shear modulus, G, by

$$G_{elastic} = \sum_{1}^{k} \mu_k \alpha_k \tag{4.19}$$

$$G_{visco} = \sum_{0,0}^{p,q} A_{p,q} \sum_{1}^{n} \gamma_n \tag{4.20}$$

$$G_{total} = G_{elastic} + G_{visco} \tag{4.21}$$

Optimization algorithms can be sensitive to initial guesses [102]. As such, a varying number of parameters in the Ogden and Prony series as well as the viscoelastic modifier were tested. In general, one wishes to minimize the number of parameters required to describe material behaviour [106], however this should not be done at the sacrifice of a better fit to the observed data.

The initial guess for the Ogden parameters was found through a fit of the Ogden material model given in equation 2.61 to the curve at 0.001/s and at 2700/s. It was found that an initial guess of $\mu_1 = 100$ and $\alpha_1 = 1$ gave reasonable results in both cases. Since the Prony series and viscoelastic modifier terms were multiplicatively coupled, a similar process could not be undertaken for the viscoelastic component of the stress. However, upon inspection of the equation for the viscoelastic stress, it can be seen that γ has units compatible with stress and as such, the values of γ were initially set to that of μ. Similarly, the values of β are in inverse time units similar to strain rate. As such, the values of β were set to increase by decades based on the number of terms to encompass the strain rates tested. Traditionally strain rates are quoted in terms of 1/s however, the units in the subsequent finite element analysis are in mm–mg–ms and therefore the β parameters are in 1/ms (and hence the initial guesses start at 10^{-6} and not 10^{-3}).

To determine the necessary number of coefficients required to capture the experi-

mental data, a program was written to cycle through a number of sets of parameters as outlined subsequently. The number of parameters were limited to three sets for each of the Ogden constants and ten for the Prony series constants. The number of terms in the viscoelastic modifier was also limited to four. The general flow of the program written which exercised the number of variables was as follows:

1. Set the number of Ogden constants
    - Initial value of the Ogden Constants $\mu_k = 100$ and $\alpha_k = 1$.
    - Number of Prony Series Constants set to 1.
2. Set the number of initial values (k) of the Prony series constants.
    - γ initially set to 100, initial guess of β is 10^{-7+k} where $k = 1$ to 6.
3. Set the number of modifier terms (initially one).
    - $A_{p,q}$ initially set to 100.
4. Perform the optimization using the initial guesses for the constants.
5. Save the resulting value of the objective function and constants.
6. If the number of modifier terms is less than 4, increase number of terms by one and go to 3.
7. If the number of Prony series pairs is less than 10, increase by one pair and go to 2.
8. If the number of Ogden series pairs is less than 3, increase by one pair and go to 1.

This sequence resulted in the cases as shown table 4.1.

Table 4.1: Abbreviated table of parameters tested.

Case 1:	μ=	100	α=	1
	γ=	100	β=	10^{-6}
	A_{00}=	100		
Case 2:	μ=	100	α=	1
	γ=	100	β=	10^{-6}
	A_{00}=	100	A_{10}=	100
Case 5:	μ=	100	α=	1
	γ=	100, 100	β=	10^{-6},10^{-5}
	A_{00}=	100		
Case ...:	μ=	100, 100, 100	α=	1, 1, 1
	γ=	100, 100, 100	β=	10^{-6},10^{-5},10^{-4}
	A_{00}=	100	A_{10}=	100
	A_{11}=	100	A_{01}=	100

4.3 Constitutive Fitting Results

Table 4.2 shows the results for the best R^2 (the value that closes approaches unity) value of the cases tested as discussed in the previous section. As indicated in the table, an excellent R^2 value of 0.996 was achieved using the constitutive model. This result was achieved with one set of Ogden parameters, five sets of Prony Series constants and two nonlinear modifier terms. Inspection of the Prony series constants indicates that the β parameters span six decades ranging from 10^{-7} to 10^{-1}.

Figures 4.1 to 4.6 shows the experimental data and the results from the constitutive model over the six strain rates that were used in the fitted data. As can be seen from the figures, in general there was a good correspondence between the constitutive model and the experimental data over the tested strain rates. At rates between 0.001/s and 0.1/s, figures 4.1 to 4.3, the data was well modeled with a slight under prediction of the stress at stretches of 0.2. Similarly, at 1/s, figure 4.4, the stress is slightly over predicted at

Table 4.2: Constitutive parameters for best fit case.

Best Fit: R^2= 0.9962

Number of Ogden Coefficient Sets: 1
Number of Prony Series Coefficients Sets: 5
Number of Modifier Terms: 2

μ_1=	199.7	kPa	α_1=	1.118	-
γ_1=	43.61	kPa	β_1=	5.26E-07	ms^{-1}
γ_2=	6.381	kPa	β_2=	2.38E-04	ms^{-1}
γ_3=	88.08	kPa	β_3=	0.141	ms^{-1}
γ_4=	123.3	kPa	β_4=	0.2478	ms^{-1}
γ_5=	147.9	kPa	β_5=	0.2181	ms^{-1}
A_{00}=	11.02	-			
A_{01}=	94.42	-			

large deformations. As show in figure 4.5 for the 7.9/s case, the stress is slightly under predicted at stretches between 0.65 and 0.2. There was an excellent correspondence at 2700/s with only very minor deviations of the model from the data as shown in figure 4.6.

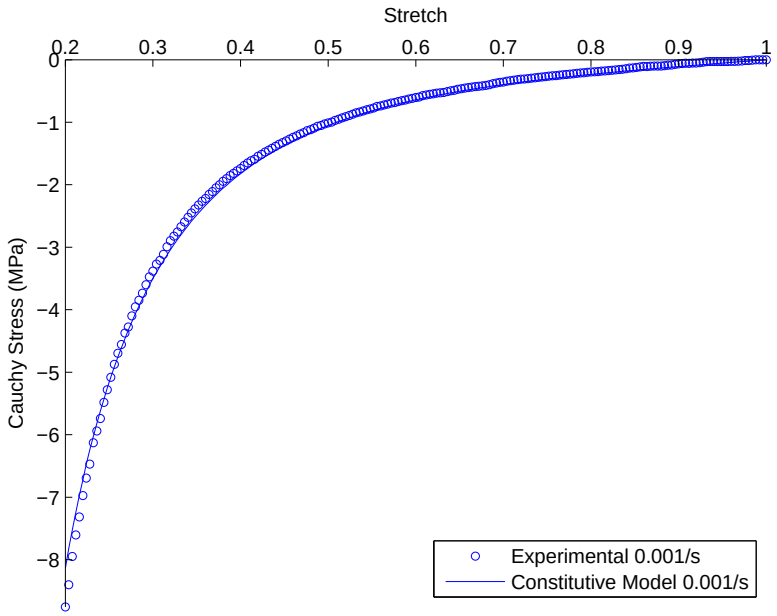

Figure 4.1: Results of the constitutive model and experiments for the best R^2 case at 0.001/s.

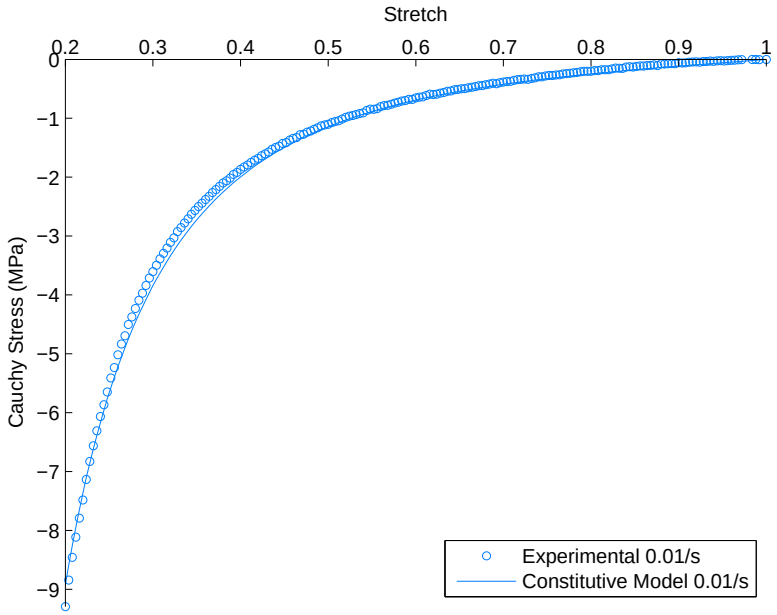

Figure 4.2: Results of the constitutive model and experiments for the best R^2 case at 0.01/s.

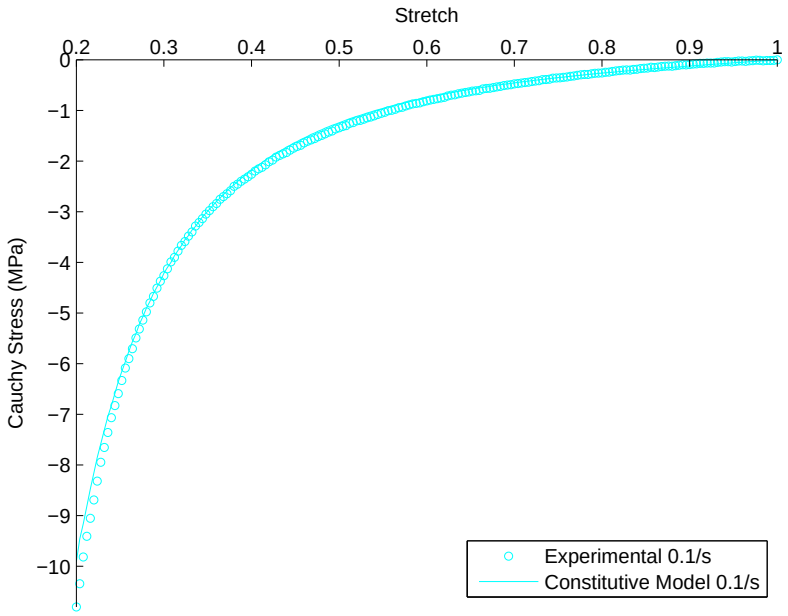

Figure 4.3: Results of the constitutive model and experiments for the best R^2 case at 0.1/s.

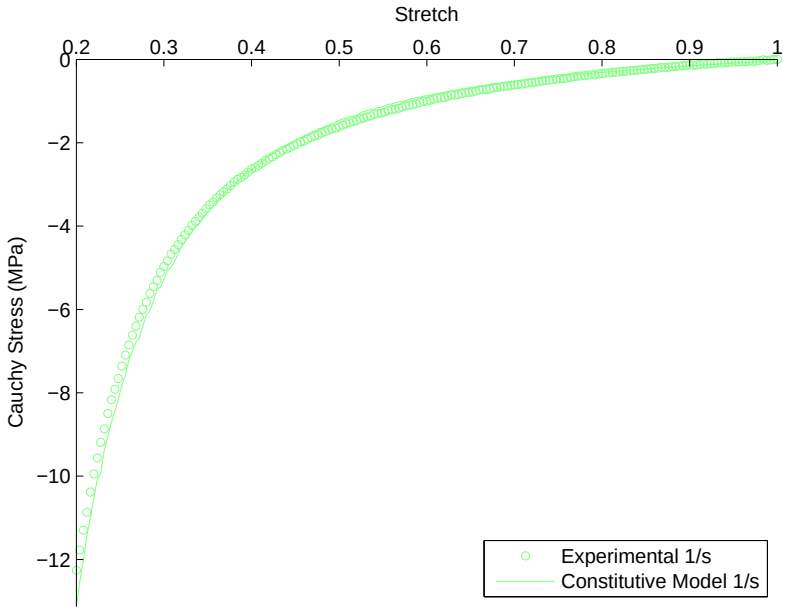

Figure 4.4: Results of the constitutive model and experiments for the best R^2 case at 1/s.

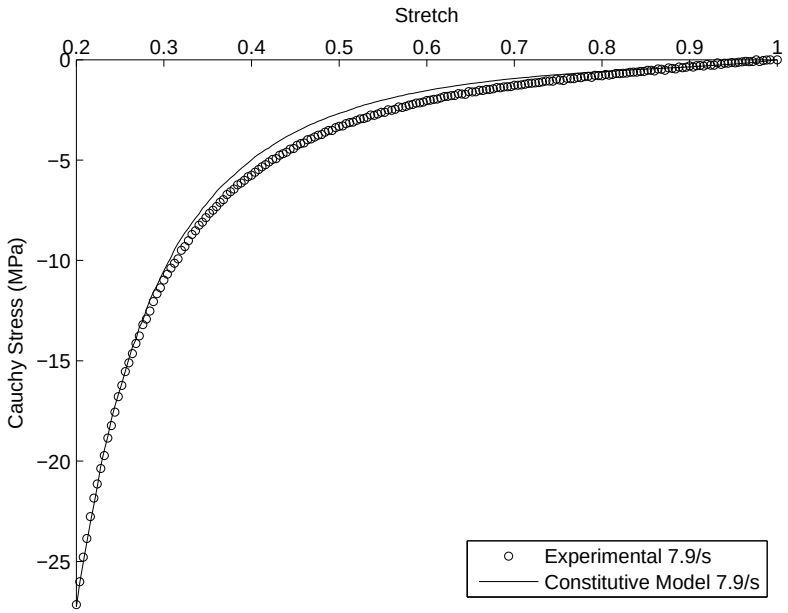

Figure 4.5: Results of the constitutive model and experiments for the best R^2 caseat 7.9/s.

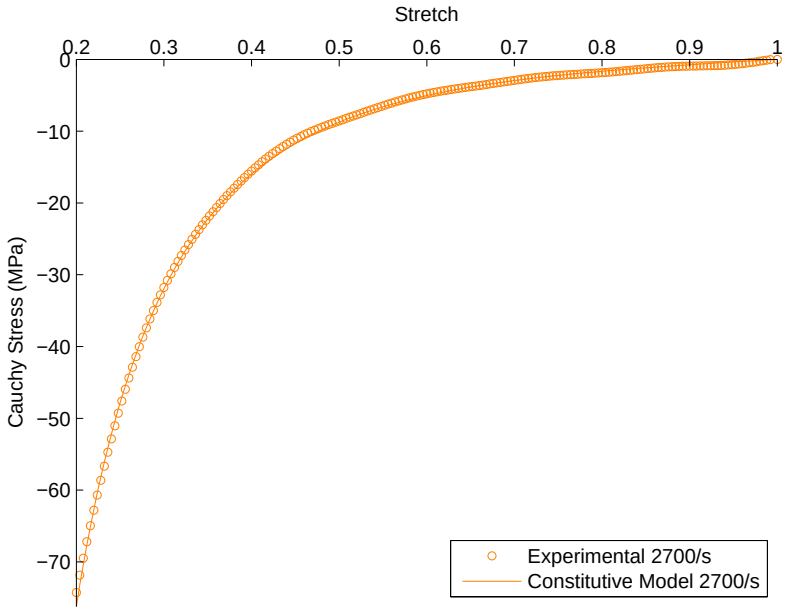

Figure 4.6: Results of the constitutive model and experiments for the best R^2 case at 2700/s.

As a test of the optimization solver to determined the constants in table 4.2 as a solution of the optimization problem, the analysis was rerun with the same initial guesses as recommended in reference [102]. Additionally, the optimization analysis was rerun with the constants in table 4.2 as the initial guess. In both cases, the same set of parameters and R^2 value was found.

Table 4.3 shows the parameters for the second best R^2 value. As indicated in the table, the R^2 value was considerably lower than that of the previous case. Similar to the previous case, the values of β spanned almost seven decades ranging from 10^{-5} to 10^{0}. Figure 4.7 shows the results of the second best R^2 case and the experimental data. In comparison to the previous case, there was a significant deviation in the constitutive model from the experimental results. Similar to before, there was a slight over prediction of the stress at stretches of 0.2 for the 0.001/s and 0.01/s cases. There was a good correlation between the model and the experiments at 0.1/s and 1/s. However, at 7.9/s and 2700/s there was at first a significant over prediction followed by a under prediction of the stress as the stretch goes from unity to 0.2 as the shape of the curves was not captured. From inspection of the case with the second best R^2 value, it was apparent that visual confirmation to identify the best fit was required. As such, the parameters from the first case outlined in table 4.2 were used in all subsequent analyses.

Table 4.3: Constitutive parameters for the second best fit case.

2^{nd} Best Fit: R^2= 0.934

Number of Ogden Coefficient Sets: 1
Number of Prony Series Coefficients Sets: 6
Number of Modifier Terms: 1

μ_1=	127.4	kPa	α_1=	5.41	-
γ_1=	12.6	kPa	β_1=	4.90E-05	ms^{-1}
γ_2=	145.8	kPa	β_2=	0.0186	ms^{-1}
γ_3=	127.68	kPa	β_3=	0.2129	ms^{-1}
γ_4=	136.63	kPa	β_4=	0.2094	ms^{-1}
γ_5=	132.37	kPa	β_5=	0.2095	ms^{-1}
γ_6=	0.78	kPa	β_6=	9.5189	ms^{-1}
A_{00}=	32.02	-			

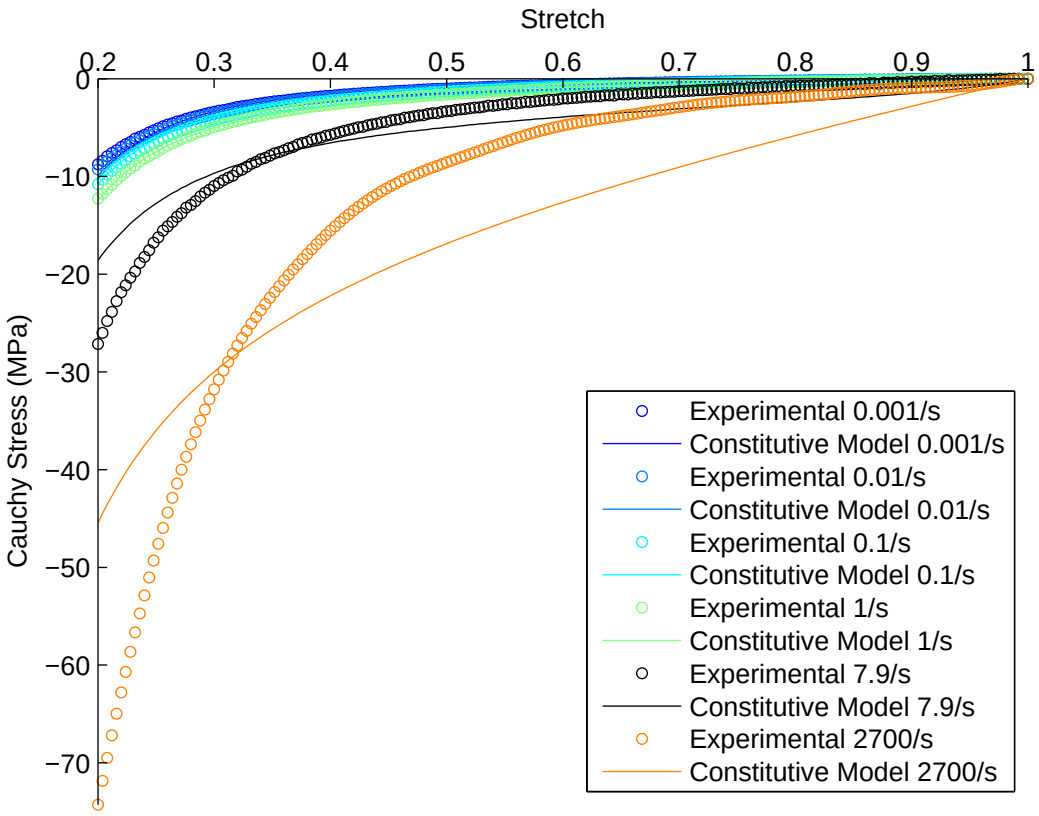

Figure 4.7: Results of the constitutive model and experiments for the second best R^2 case.

4.4 Numerical Implementation of Constitutive Model Validation

A user material model subroutine was written to incorporate the equations described in section 4.1 into the non–linear explicit finite element program LS-Dyna [47]. As a means of verification of the material model subroutine, single element simulations were conducted and the output compared to the results of the constitutive model and experiments.

4.4.1 Simulation Configuration

For the present analysis a single solid element model was created. The element had uniform, unity dimensions. Displacement constraints were applied to the element as shown in figure 4.8 where the red arrows indicate that the nodes have a fixed coordinate and the experimental displacement history was applied to the nodes indicated by the open black arrows in the x direction. The experimental displacement history was scaled to account for the unity element dimensions so that the strain rate was maintained.

Time–Scaling Due to the long simulation time and the necessarily small timestep which was required for numerical stability, the numerical technique of time scaling was used for the single element calculations at rates from 0.001/s to 7.9/s. The process for time scaling was as follows:

1. Determine the time scale that you wish to use. In this case, the factor was selected so that the run times of the simulation would be on the same order as that of the 2700/s case.

2. Scale the applied displacement loading history with the time factor determined.

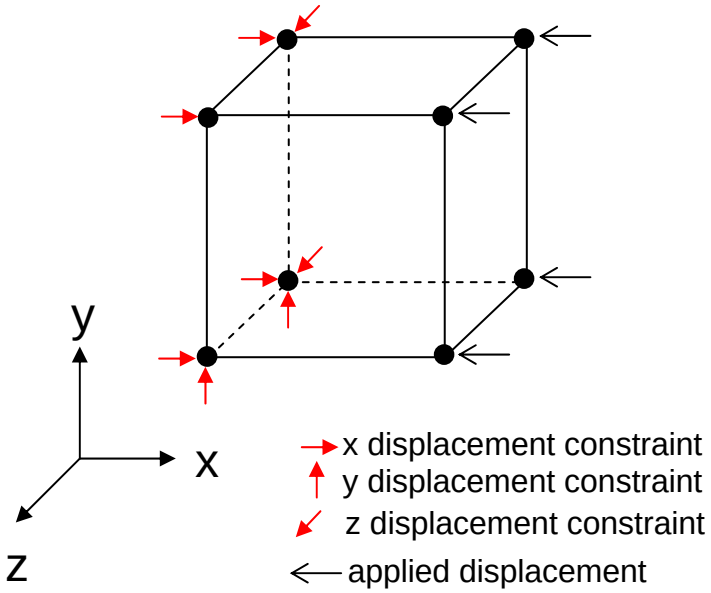

Figure 4.8: Schematic of the simulations performed on the single solid element.

3. Scale the material model parameters which are solely a function of time using the time factor. In this case, it was just the β terms.

4. Leave all other parameters the same.

It is worthwhile to note that if you change all the parameters which involve time, not just the β parameters, the time step will be scaled accordingly and there will be no reduction in run time. As well, any temporal results recorded from the simulation have to be scaled back to the initial time base. This technique can be used in this situation since only one element was used and so any wave effects are not simulated.

4.4.2 Simulation Results

In total six single element simulations were conducted where the applied displacement was determined from the experimental tests. The stress and stretch for the unit element was recorded for each of the simulations. The material model parameters used were those

determined in section 4.3 for the best R^2 case.

Figures 4.9 to 4.14 show the results of the single element calculations in comparison to the results calculated from the constitutive model for each strain rate tested. As can be seen in the figures, in general there was excellent correspondence between the numerical and constitutive model results. There are some slight oscillations in the range of ± 0.1 MPa for the numerical results for the 0.001/s to 1/s cases (figures 4.9 to 4.12) which were a result of the time scaling approach used and the explicit nature of the numerical algorithm. As a further check of the accuracy of the numerical models, the R^2 value for the numerical results in comparison to the constitutive equation were calculated via equations 4.15 and 4.17. This resulted in a R^2 value of 0.9974 which was very similar to the value in table 4.2.

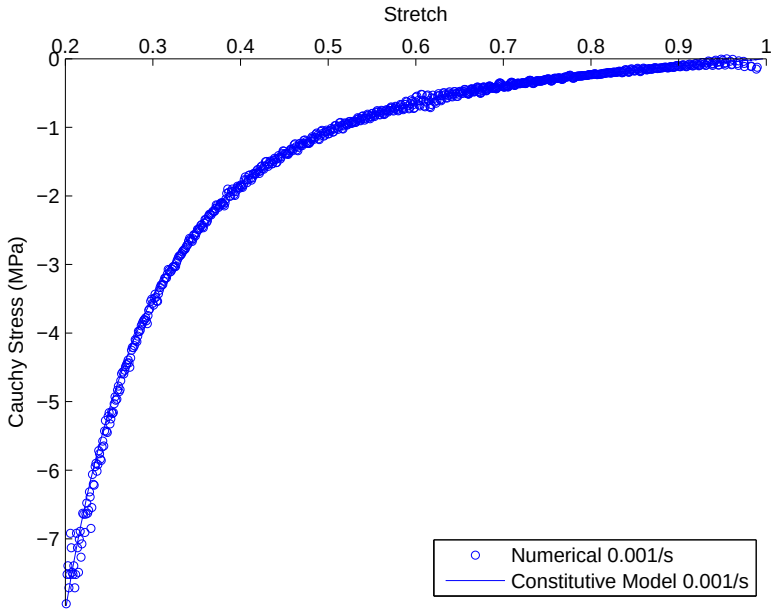

Figure 4.9: Results of the numerical analysis and constitutive model at 0.001/s.

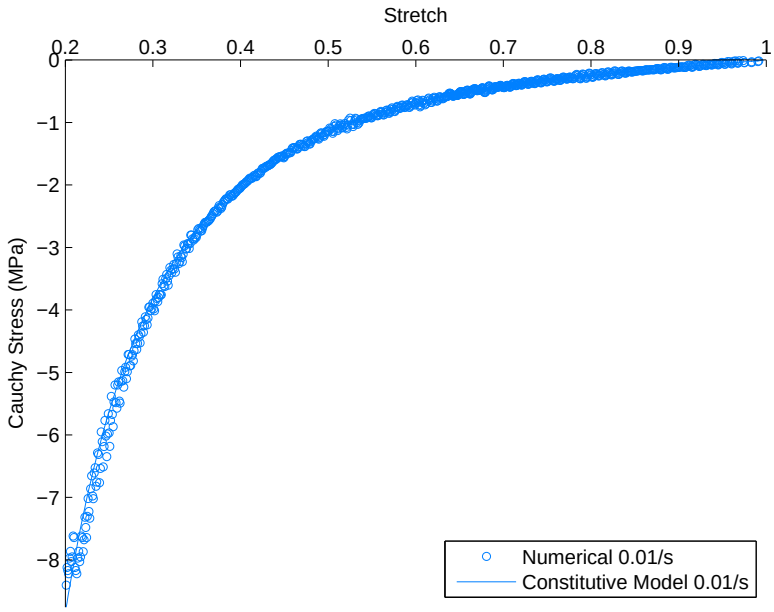

Figure 4.10: Results of the numerical analysis and constitutive model at 0.01/s.

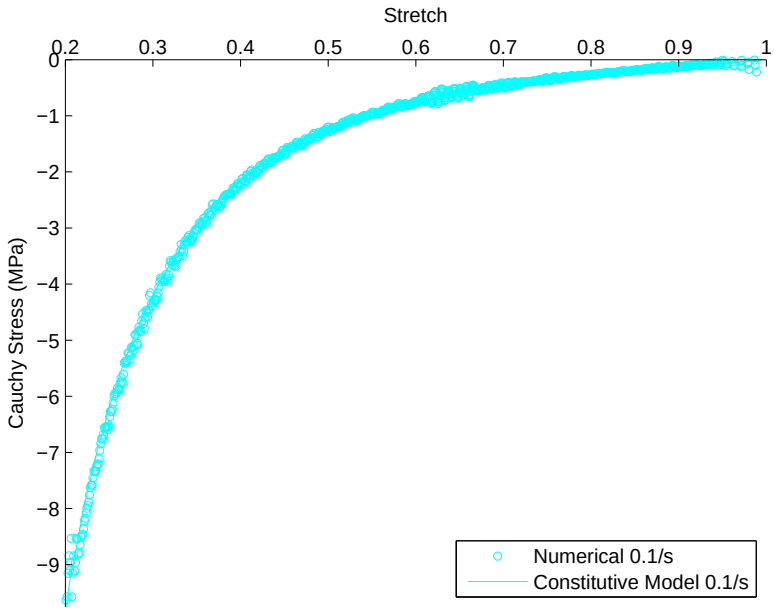

Figure 4.11: Results of the numerical analysis and constitutive model at 0.1/s.

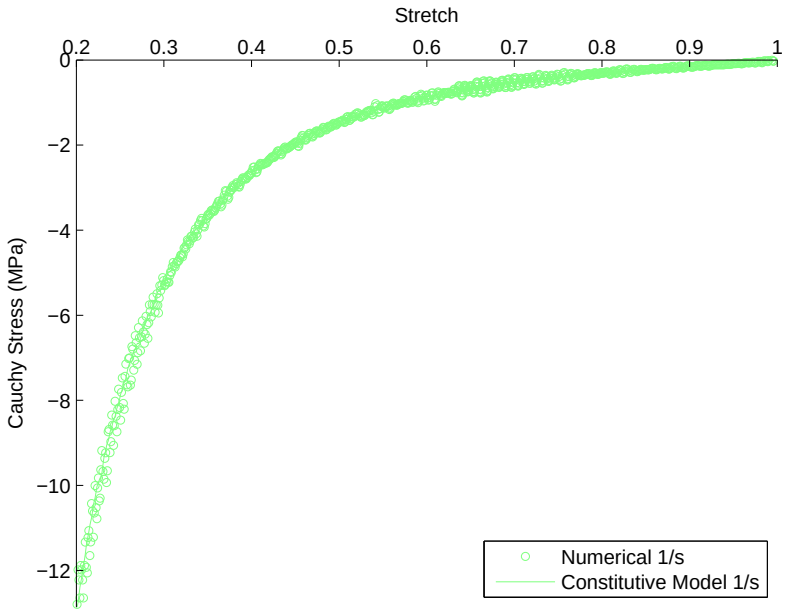

Figure 4.12: Results of the numerical analysis and constitutive model at 1/s.

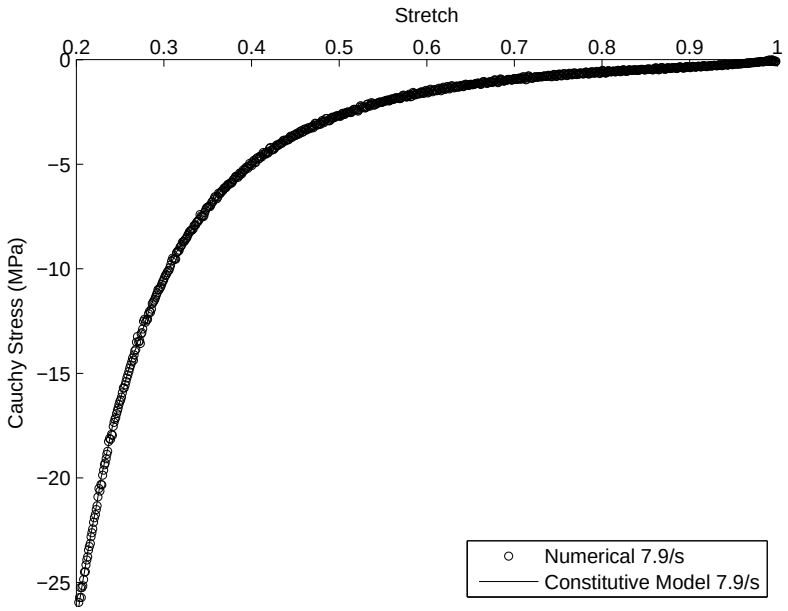

Figure 4.13: Results of the numerical analysis and constitutive model at 7.9/s.

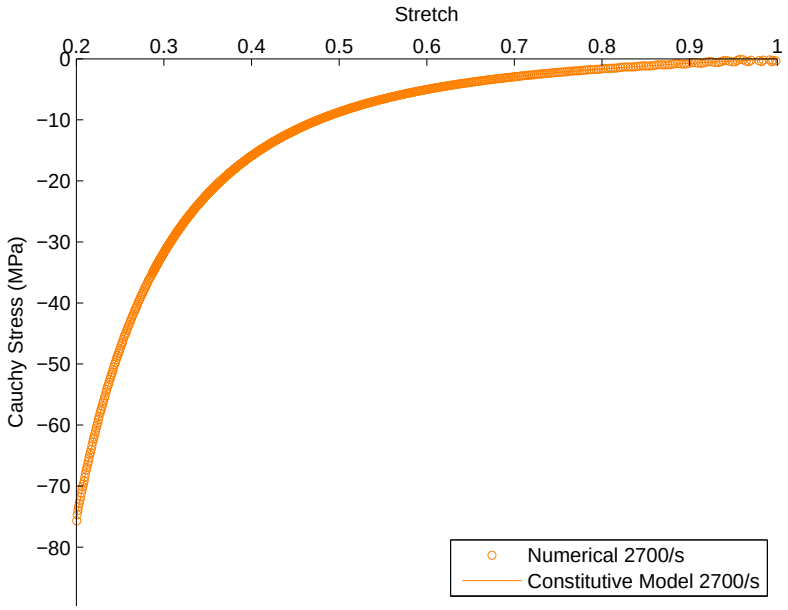

Figure 4.14: Results of the numerical analysis and constitutive model at 2700/s.

Chapter 5

Numerical Modelling

This chapter is composed of five sections. Section 5.1 outlines the development of the numerical model in terms of how the morphology of the foam was captured, the modelling of the fluid enclosed in the pores as well as the boundary conditions applied. Section 5.2 details the deformation of a model at the cellular level. Section 5.3 discusses the simulations of experiments performed on the foam material. Section 5.4 illustrates the different effects of the model parameters such as loading rate, wall thickness, pore size and anisotropy. Section 5.5 discussed the relative effects of the morphological parameters.

5.1 Numerical Model Development

5.1.1 Foam Morphology

As discussed in chapter 2, the tetrakaidecahedron was an ideal candidate to model the pore structure of the foam. As identified in chapter 3 the cells are relatively equal in size and so, similar to the assumptions in [59], the pores of the foam were assumed to be space filling and equal in size. Through successive splitting as shown in figures 5.1a)

to 5.1d), the tetrakaidecahedron can be broken down into eighths. The blue lines in the figure show the boundaries of solids (not solid elements) used to create the cell. As can be seen in the figure, the solids which comprised the cells were created in such a way to minimize the skewness of any element and to allow each solid to be exclusively meshed with hexahedral solid elements. Eighth symmetry was used to create the base unit for the tessellation as shown in figures 5.2a) to 5.2e). Figure 5.2b) shows the translation of the rear quadrant highlighted by the red area to the front right. Similarly, figures 5.2c) and d) show the translation of the top right quadrant to the bottom left and the bottom right to the top left. Figure 5.2e) shows how the solids generated in figure 5.2b) to d) were rotated about the y axis centered in the tetrakaidecahedron to generate the base tessellation unit.

The mesh density of the base unit was determined from two parameters. These parameters were a function of the method by which the base tessellation, as described previously, was generated. Inspecting the eighth portion of the tetrakaidecahedron as shown in figure 5.3, the mesh path can be identified as illustrated by the dotted lines. Along each of the seven dotted lines, equal numbers of elements were required. In order to have a relatively uniform mesh, each of these paths were meshed with the same number of elements identified by the parameter N_l in the figure. The second parameter used to define the mesh is N_{tt} which defines the number of elements through the half thickness. i.e. through the thickness of the base tessellation the number of elements was $2N_{tt}$.

Figure 5.4a) shows a mesh of the base tessellation unit where $N_l = 3$ and $N_{tt} = 1$. The cross-section view in figure 5.4b) shows the inside of the cell (highlighted by the dark lines). As evident in the figures, the cell walls along the diagonal have at least two cells through the thickness. These result in the smallest element length of 6.1 μm and a total wall thickness of approximately 12.2 μm which corresponds with the measurements taken

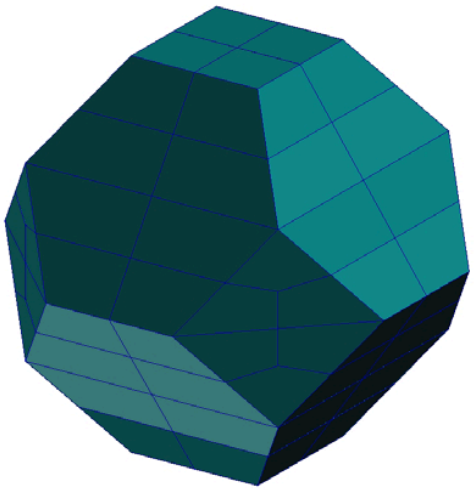

a) Full tetrakaidecahedron.

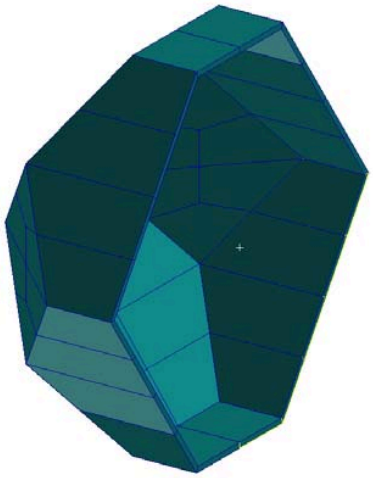

b) Half tetrakaidecahedron.

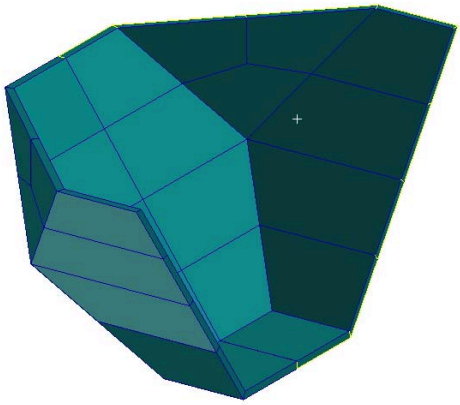

c) Quarter tetrakaidecahedron.

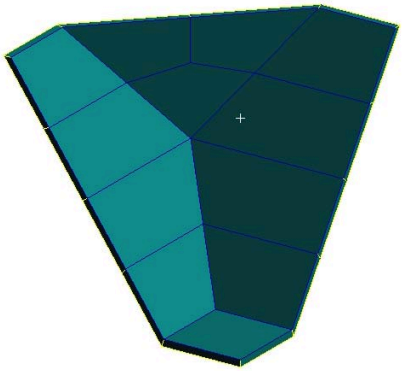

d) Eighth tetrakaidecahedron.

Figure 5.1: Decomposition of the tetrakaidecahedron into eights.

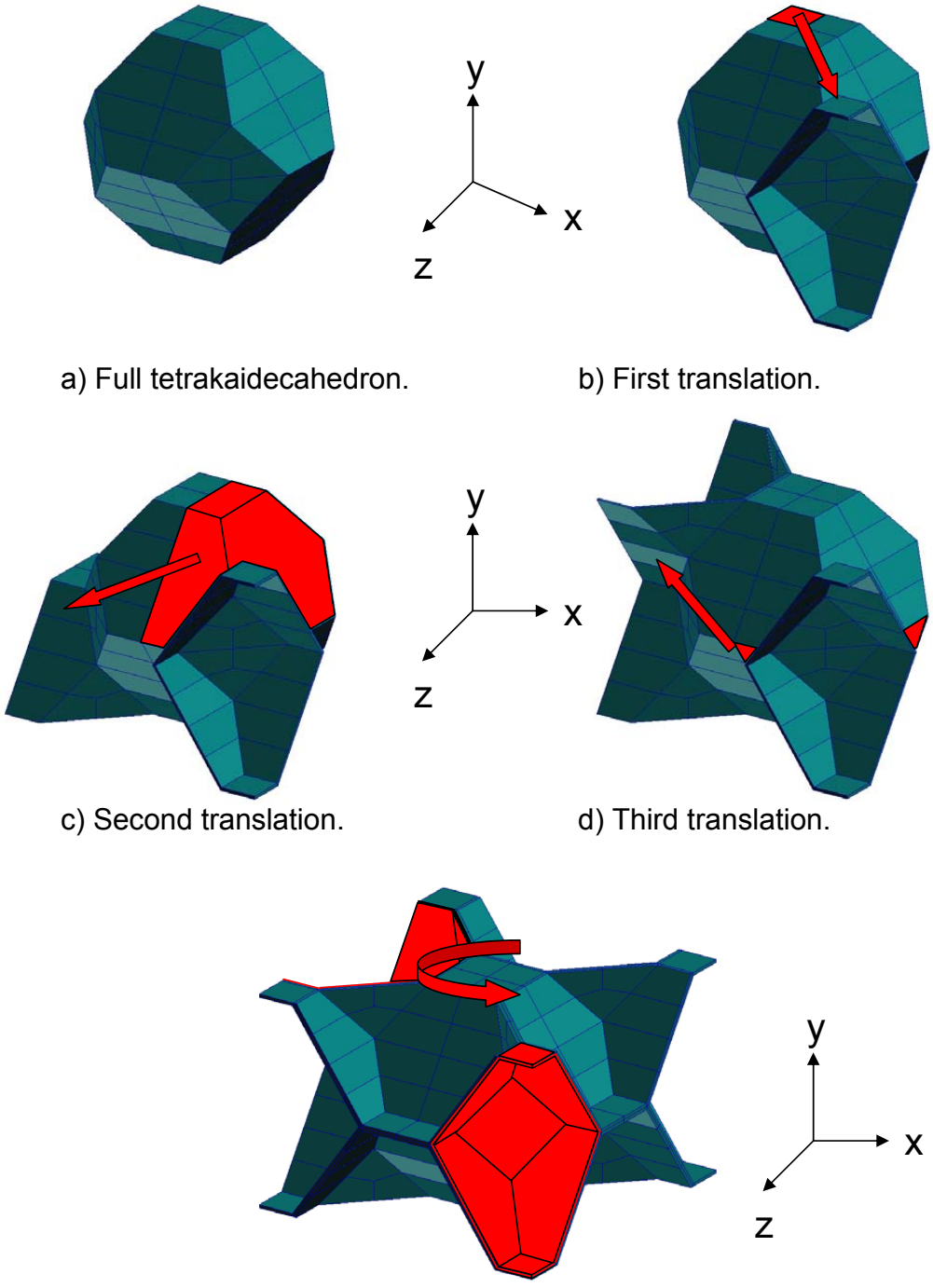

Figure 5.2: Generation of the base unit for the tessellation through successive translations and rotations.

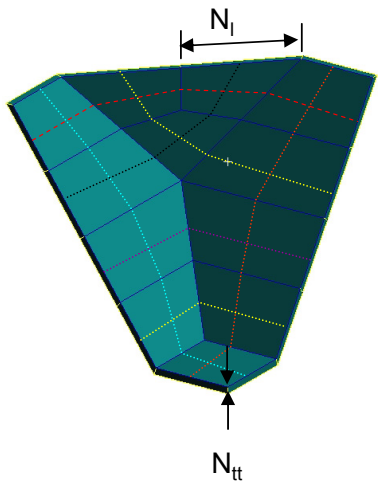

Figure 5.3: Identification of the mesh parameters on one eighth slice of the tetrakaidecahedron.

in chapter 3. Similarly, the characteristic length, L_c in figure 5.4b), was chosen to match that of the measurements taken. The base unit in figure 5.4a) can then be repeated through successive translations to give a resulting tessellation as shown in figure 5.5 that had n_x by n_y by n_z repeats in space. In figure 5.5, $n_x = 2$, $n_y = 3$ and $n_z = 2$ which resulted in a domain size of approximately 1.28 mm by 1.35 mm by 1.28 mm (x, y, z). This resulted in approximately 48 000 solid elements. When the base unit was tessellated, the square faces will also be at least two elements thick except on the "y" boundaries.

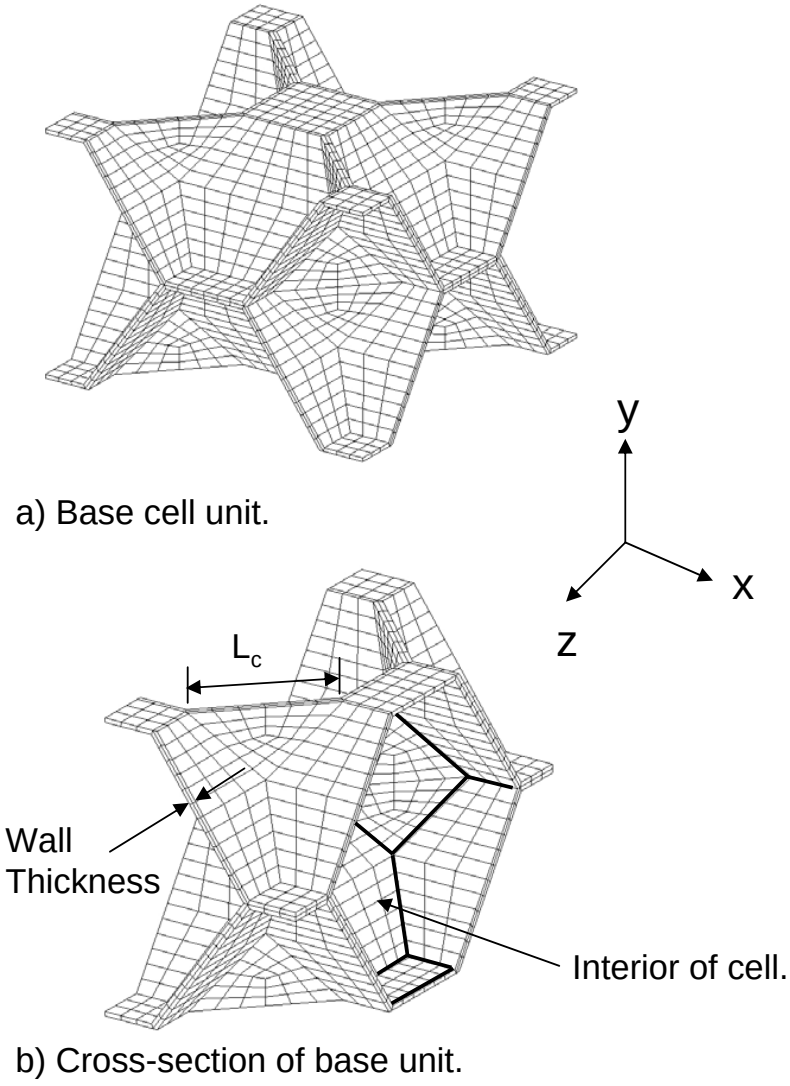

Figure 5.4: Mesh of base unit a) and cross-sectional view b).

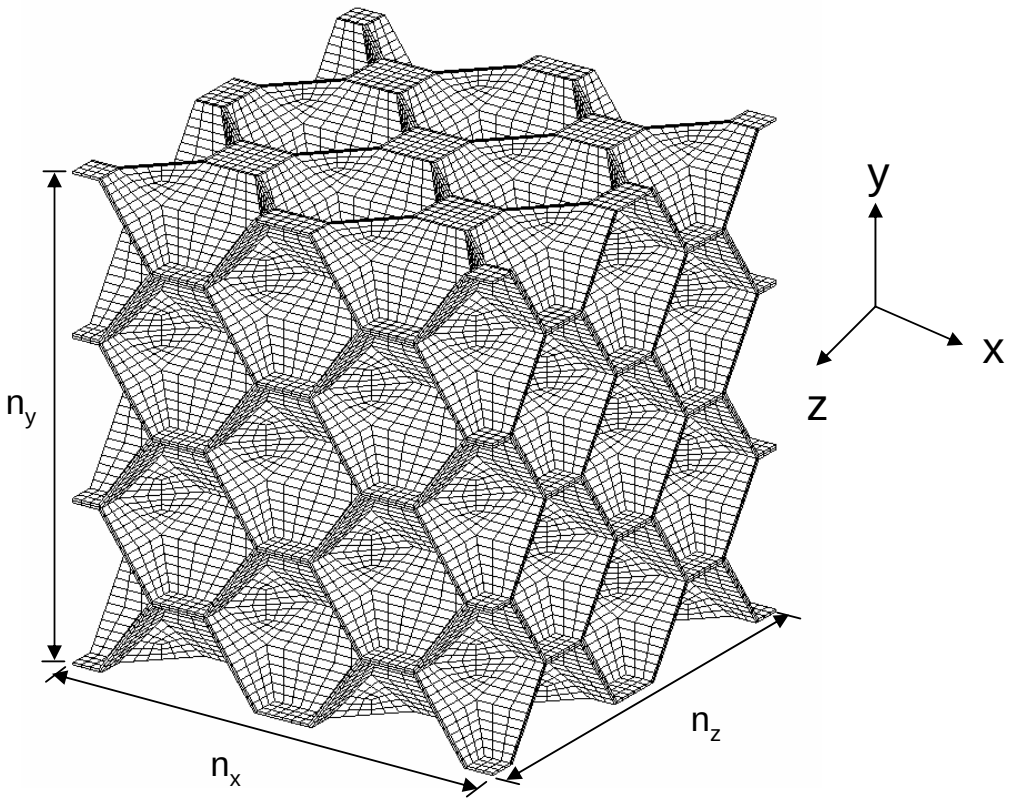

Figure 5.5: A 2 by 3 by 2 tessellation of the cellular base unit.

5.1.2 Eulerian Domain to Model Air

As discussed in chapter 2, the Arbitrary Lagrangian Eulerian (ALE) method was used to model the movement of the fluid air. The ALE method allows the fluid domain to contract and expand arbitrarily and independent of the fluid flow. This aspect was used to help reduce the number of fluid elements required. The movement of the fluid domain was controlled to ensure that the cells inside the tessellation were encompassed during the complete simulation time. Figure 5.6a) shows the initial fluid domain size used in conjunction with the 2 by 3 by 2 tessellation shown previously in figure 5.5. Figure 5.6b) shows the fluid domain at end of the simulation. Initially, the fluid domain was comprised of cubic elements measuring 20 μm length, width, and height. By allowing the fluid domain to contract in the "y" direction and expand in the "x" direction with the material, the requirement to have a large domain size to account for the deformation of the cellular walls was reduced as shown in figure 5.6b).

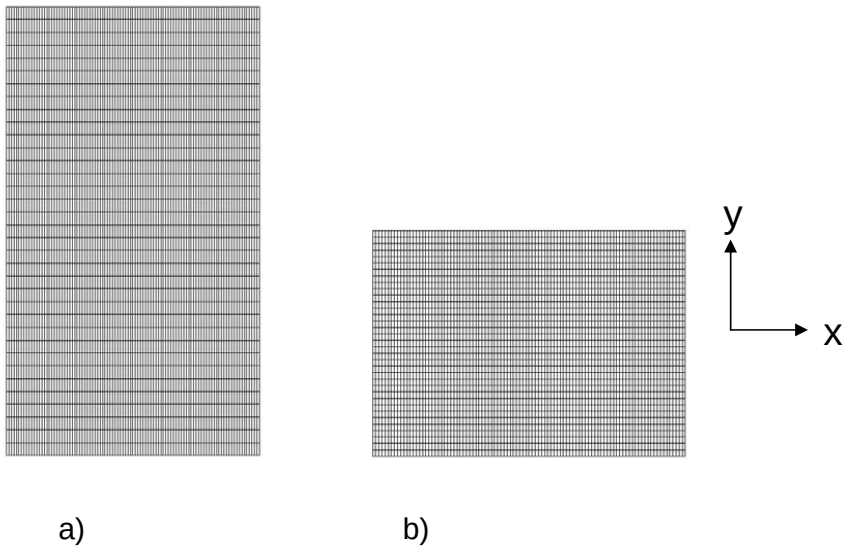

Figure 5.6: a) Initial fluid domain mesh, b) Contracted fluid domain mesh

The fluid domain elements were initialized with a 1 atm (101.4 kPa) pressure with

a 1 atm pressure applied to the surrounding surfaces to provide the necessary reaction force to prevent movement of the air without an applied load.

5.1.3 Boundary Conditions

One of the inherent difficulties in modeling cellular materials numerically was the application of boundary conditions to the material as described in [6]. The issues arise from the non–continuous nature of the material as illustrated in figure 5.5. In essence, it becomes very difficult to apply nodal constraints to the boundaries of the material due to the oscillating surface. As such, a surface on the boundaries was created as illustrated in figure 5.7. As seen in the figure, the surfaces were comprised of a layer, which was $2N_{tt}$ elements thick, for a total thickness of 12 μm. As also illustrated in figure 5.7, the square faces on the boundary shown in figure 5.5 which were only one element thick became three elements thick. The consequence of applying surfaces to the top and bottom of the tessellation was that cells near the boundary were half that of the others.

With the boundary surfaces in place, nodal constraints could be applied. Nodes on the bottom surface of the model were constrained from moving in the y direction as indicated by the blue cones and nodes on the top surface have an applied loading history (either displacement or velocity as discuss later) in the y direction as indicated by the red arrows as shown in figure 5.7. As detailed further in the subsequent sections, the reaction force at the constrained nodes (blue) was monitored during the simulation.

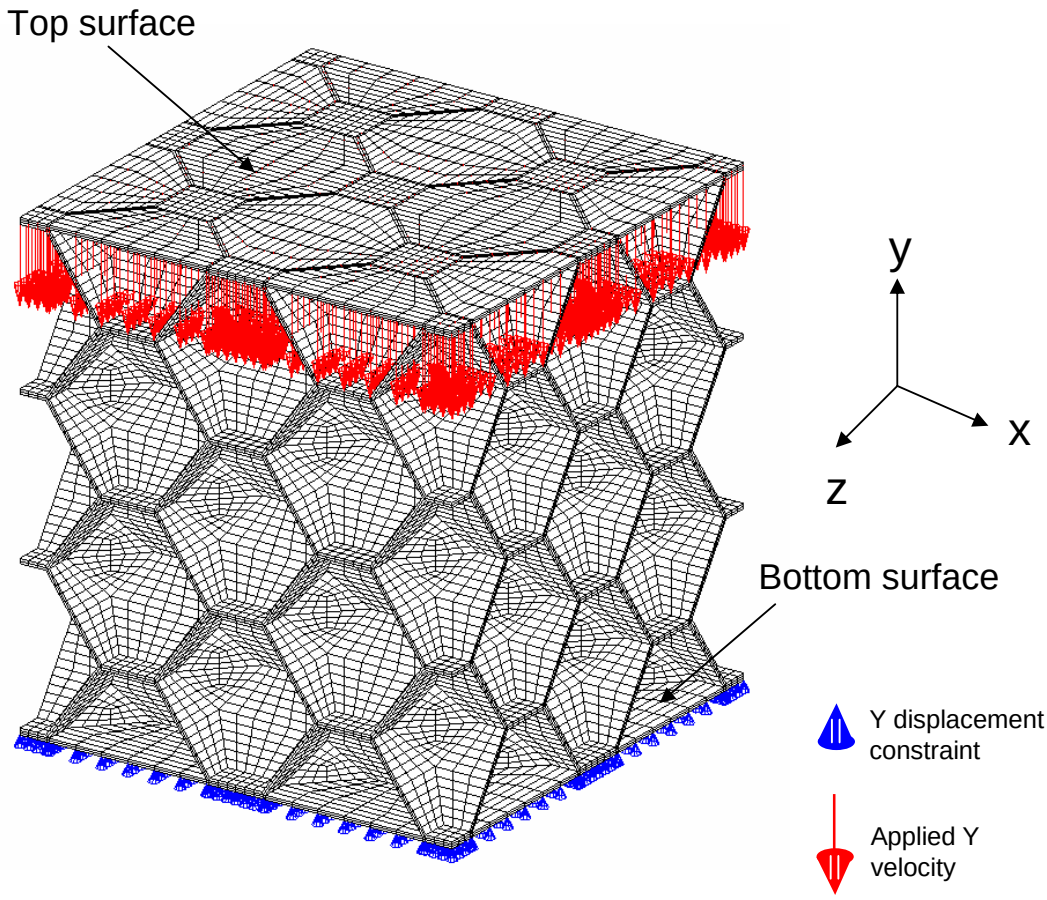

Figure 5.7: A 2 by 3 by 2 tessellation of the base unit with top and bottom surfaces and constraints.

5.1.4 Numerical Implementation

The following analyses were run on a computer cluster at the University of Waterloo which was based on the AMD 2352 architecture. Each simulation used the Massively Parallel Processing (MPP) version 971 release 5 of LS-Dyna which was compiled to integrate the user material subroutine described in chapter 4. Appendix B outlines the finite element algorithms used in LS-Dyna. The Open source Message Passing Interface (Open–MPI) protocol was used to invoke the MPP version of the finite element code. Several initial models were conducted to identify computational efficiencies of the analysis in comparison with the number of processors used. It was determined that by utilizing four processors a reduction of computational time of approximately 2.5 times was achieved when compared to the case run with a single model. Beyond four processors, there was very little reduction in computational time. As such, all of the models presented in this chapter were run using four processors. The analysis of the 4 by 10 by 4 tessellation detailed subsequently with the mesh density of $N_l = 3$ and $N_{tt} = 1$ mesh took approximately 790 hours to complete. The analysis without the fluid structure coupling algorithm invoked for the same mesh took approximately 51 hours to complete. This identifies the computational cost of including the fluid–structure interaction component.

5.2 Deformation at the Pore Level

A detailed investigation of the deformation of a single pore is given in this section. This discussion illustrates several of the stress wave propagation and deformation mechanisms that occur in the subsequent sections. The first subsection details the short term transient stress wave response while the second subsection identifies the longer term deformation mechanics at the pore level.

5.2.1 Short Term Transients

As identified in chapters 1, porous materials exhibit low stress wave propagation velocities on the order of 40 m/s. These velocities are lower than those of the constituent materials [15]. In the present case, for air, the approximate sonic velocity at room temperature was 330 m/s whereas in polychloroprene, the sonic velocity was approximately 1400 m/s as discussed in [110][111]. To illustrate the reduced wave speed in porous material in comparison to the constituent materials, a simulation of solid polychloroprene rubber and one of air were conducted with domains the same size as the 2 by 3 by 2 tesselation. The solid polychloroprene rubber had a 10 m/s loading history applied to one surface as was done for the simulations of the polychloroprene foam. The simulation of the block of air was carried out by creating a block mesh of ALE elements and then having a plate of rubber elements with an applied velocity of 10 m/s move through it. Figure 5.8a) shows the wave as it reaches the fixed end for the air compared to the porous structure of the foam at the same time. Figure 5.8b) shows the stress wave as it reaches the fixed end of the solid rubber compared to the porous structure at the same time. As evident in the figures, the stress wave in the porous structure significantly lags that in the air and solid rubber. From the simulations of the 2 by 3 by 2 tessellation, the apparent wave speed through the material ranged from 68.3 m/s (using the peak of the effective

stress measured in an element at the fixed end as the arrival time) to 115.5 m/s (using the point at which the effective stress starts to change from zero as the arrival time).

Several factors combined to give the porous material an apparent low wave speed. If one considers the cellular material by itself (without the enclosed air) identified in figure 5.9, as the structure was loaded the stress wave propagated in multiple directions as indicated by the red arrows. The cross sectional view illustrates that in comparison to the overall length of the pore, the stress wave had to propagates over a longer distance. The ratio of these lengths was a function of the cell size and isotropy. The initial ratio (length of stress wave path:overall length) of these lengths for the current analysis was 1.21:1 along the path through the square face and 1.26:1 along the mid–plane of the hexagonal faces. The illustration in figure 5.9 is simplistic in compared to the real situation where stress waves from multiple pores interact with each other creating multiple complex states.

Additionally, the multiple interfaces between the air contained within the pore and the surrounding cellular structure caused multiple reflections and interactions. The x–t diagram for the center of a pore, shown in figure 5.10, outlines the initial waves propagation. In figure 5.10b), the black lines indicate the cellular boundaries through the middle of the cell shown in figure 5.10a). The boundary at the $x = 0$ mark moves at 10 m/s as indicated by the steep slope. As the boundary begins to move, a wave propagates through the air within the pore as indicated by the red line extending from 0,0 point to the right. As the wave encounters the cellular boundary, which has a greater impedance, the wave was reflected in order to maintain continuity as indicated by the red line extending up to the left as discussed in section 2.1.5. The interaction at the boundary also created a stress wave in the cellular material which propagated through the thickness of the wall indicated by the green lines in the figure. When this wave encountered the next

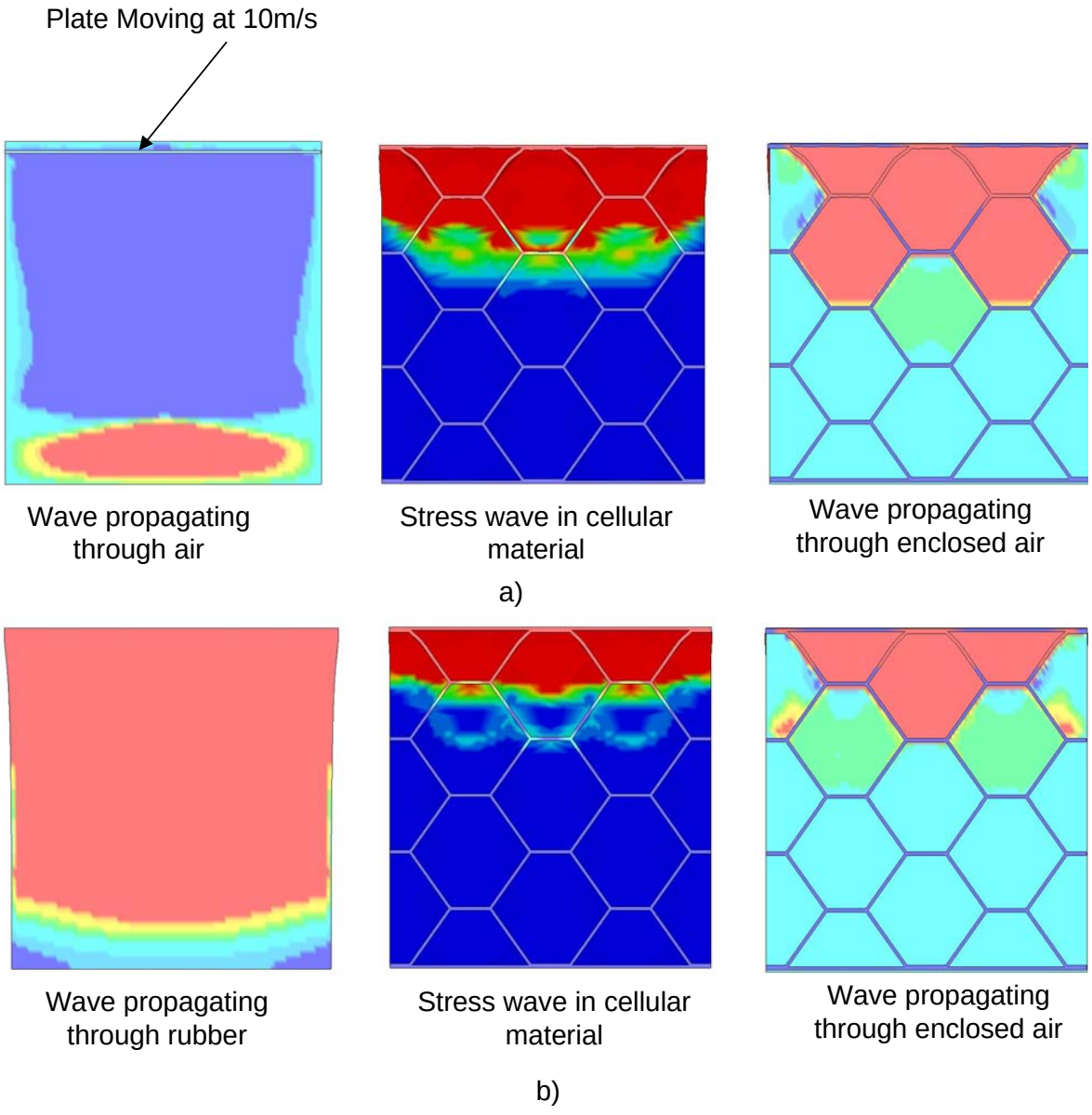

Figure 5.8: Figure showing the wave propagation through a cellular material compared to air a) and solid rubber b).

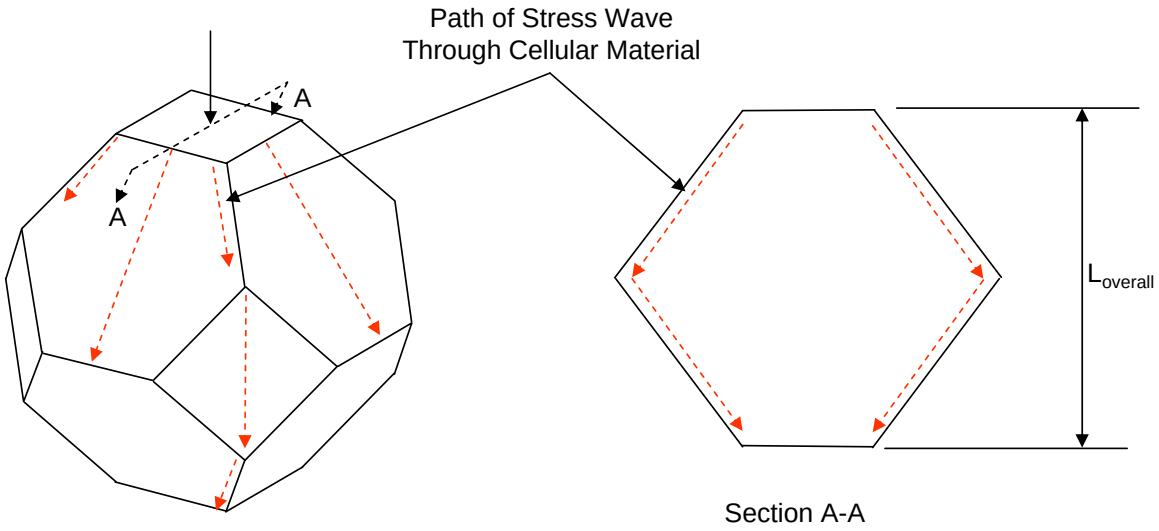

Figure 5.9: Simple representation of wave propagation through the cellular material.

boundary with the adjacent pore, it then reflects (high impedance to a low impedance, discussed in section 2.1.5) as a tensile wave. This creates a compression wave in the adjacent pore indicated by the dashed blue lines. When the tensile wave inside the cell wall encounters the boundary, it creates a release wave in the initial pore also indicated by the blue lines. These two waves are very small in magnitude and attenuate quickly. The preceding description is further complicated by waves which propagates through the cellular structure. Additionally, the waves are not planar and the geometric nature of the cells cause complex interactions which cannot be shown easily on a x–t diagram.

The preceding mechanisms result in a material which quickly attenuates weak waves. This is illustrated in the simulation of the 4 by 10 by 4 tessellation discussed in section 5.3. Figure 5.11 shows the propagation of a wave that was less than 1 kPa above atm. As indicated in the figure, at t=0.0078 ms to t=0.023 ms the wave propagates but quickly decreases in magnitude. At t=0.031 ms the initial pulse was almost completely attenuated

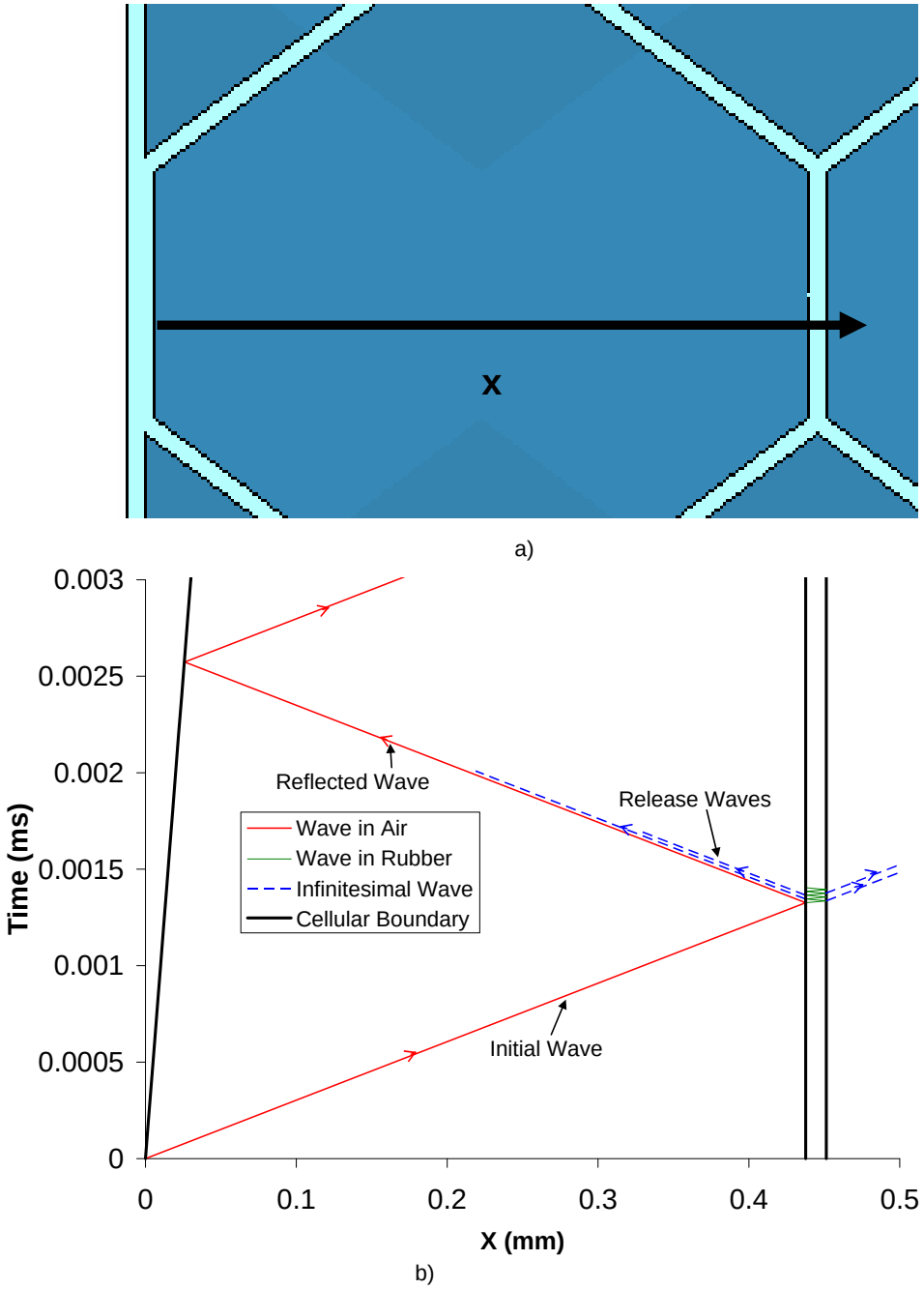

Figure 5.10: a) Cross section through mid plane of a pore (loaded on left side at 10m/s) and b) x–t schematic showing the interaction of waves with the cellular wall.

and a small release (darker blue) wave following the initial wave. A secondary wave was generated as the cellular structure deformed which continued to propagate with a greater magnitude as shown at t=0.039 ms.

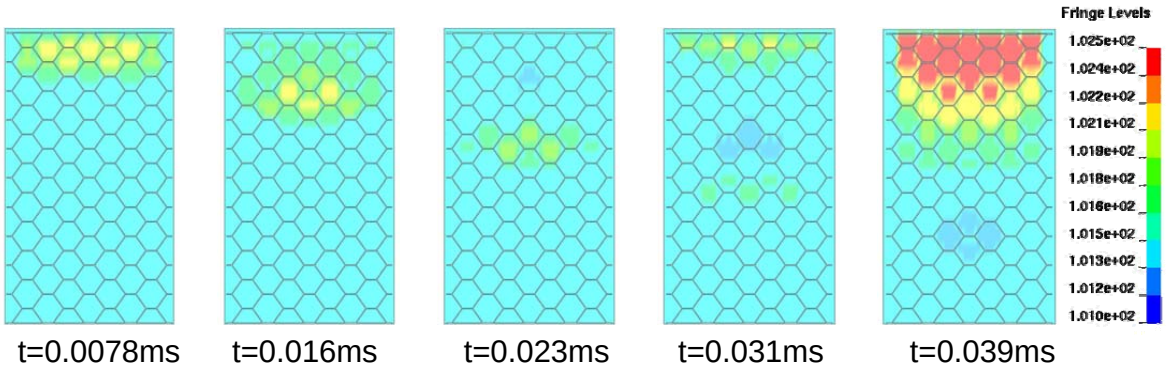

Figure 5.11: Attenuation of the initial wave in a 4 by 10 by 4 tessellation of cells.

5.2.2 Long term

This section discusses the longer term deformation mechanisms of a porous material at the pore level. As loading on the pore occurs, the pore itself collapses in the manner shown in figure 5.12a)–d). As illustrated in figure 5.12b), the cell walls begin to buckle in the mid part of the upper half of the cell. The cell begins to bulge slightly and the top and bottom sides approach each other, figure 5.12c). As deformation continues, the sides of the cells eventually touch creating a center pocket and ring of compressed gas, figure 5.12d). This compressed gas, along with the inherent elasticity in the cell wall, acts as a restoring force on the cell.

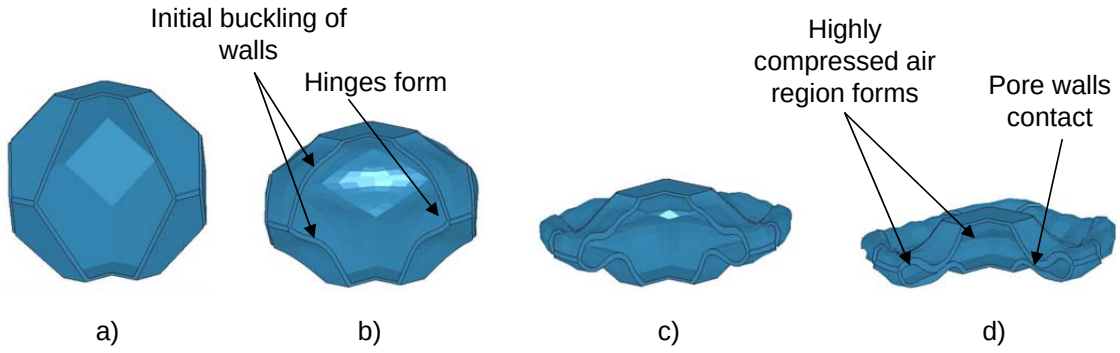

Figure 5.12: Example of the collapse of a pore from the initial configuration a) to complete collapse d).

5.3 Comparison of Numerical Models to Experimental Results

The experimental results of the foamed polychloroprene rubber discussed in chapter 4 were used as a method of validation of the modeling techniques described in the previous section. For the simulations of the experiments the domain size of the tessellation was 4 by 10 by 4 repeats of the base unit in the x, y and z directions. This resulted in a cellular mesh that was approximately 2.6 mm by 4.5 mm by 2.6 mm in size. Although the length of the model of the cellular structure was similar to that of the experimental specimen, the cross–sectional area was significantly different with the area of the simulation being 6.51 mm^2 while the area of the experimental sample was 72.0 mm^2. The area of the simulation was necessarily reduced due to computational limitation as discussed previously. For the simulations of the experiments with the mesh density of $N_{tt} = 1$ and $N_l = 3$ as described before, approximately 578 000 solid elements were created for the 4 by 10 by 4 tessellation. If an equivalent area was used, 5 800 000 elements would have been required.

Figure 5.13 shows the model used to simulate the experiments. The bounds of the fluid mesh are outlined in orange in the figure. As discussed previously, the surface at the bottom of the model was constrained from movement in the y direction and the forces were recorded at each node. The loading history from the experiments was then applied to the top surface.

Due to the simulation time required, the domain size and the necessity of a small time step required by explicit finite element programs, only the high rate experiments (those conducted with the Hopkinson Bar) were simulated. The technique of time–scaling used in chapter 4 could not be applied in this situation to reduce the simulation time. For the simulations, stress wave effects were significant and, as such, time–scaling did not appropriately capture the physics of the problem. For instance, initial models using a moderate time scale factor showed that significant deformation, in excess of that seen with the simulations of the high rate experiments without time scaling, occurred near the loading surface occurred.

The loading history used for the simulation of the 2050/s and 3000/s tests are shown in figure 5.14. As can be seen from the figure, due to the rise time experienced in the Hopkinson bar, the loading history had a non–linear portion where the velocity increases from zero to a relatively steady state (linear increase in displacement). During the rise time portion, the strain rate was changing as well via equation 2.28. Thus, the strain rates quoted were those in relation to the linear portion of the loading history from 0.1 ms to 0.375 ms.

Figure 5.15 shows the results of the numerical model in comparison to the experiments for the 2050/s case. The blue lines represent the results from the experiments conducted for each test. The red line represents the result from the numerical simulation. The increase in the stress as the material was compressed was well modeled as the

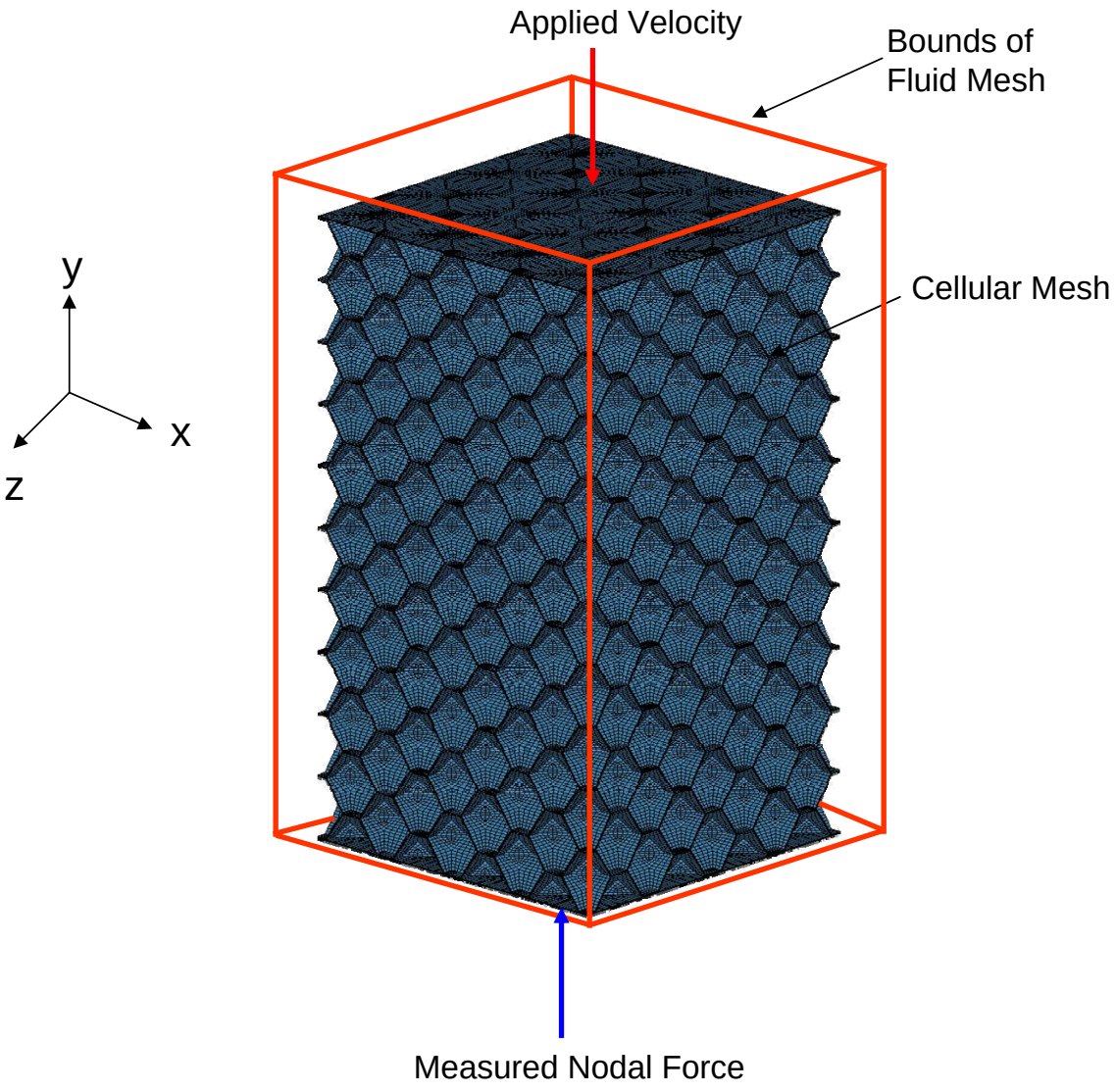

Figure 5.13: Numerical models used to represent the experimental sample.

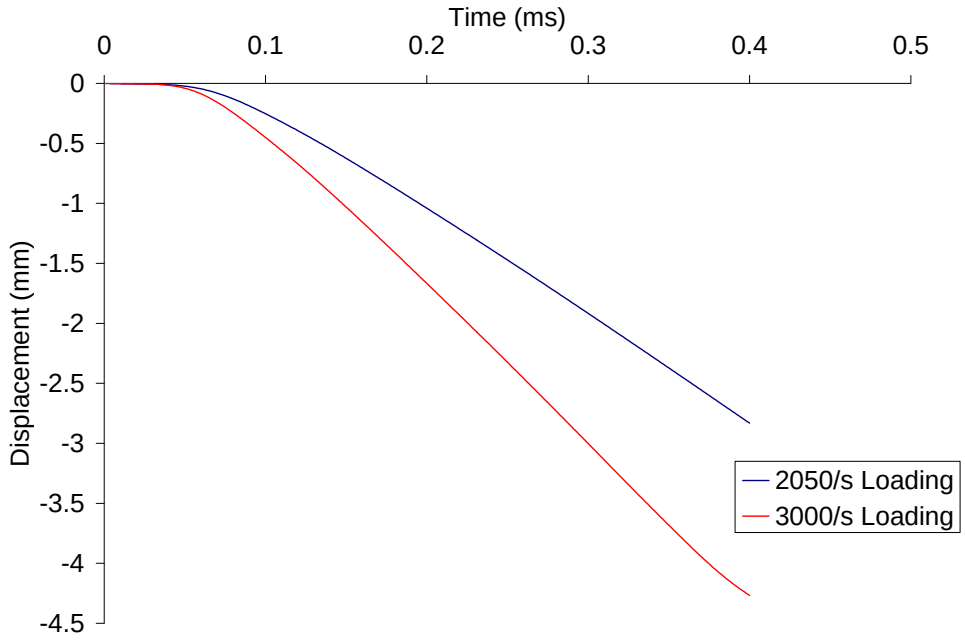

Figure 5.14: Loading history applied to the top surface of the model for the 2050/s and 3000/s case.

stretch decreases from 1 to 0.65 (35% compressive engineering strain). After this point, the cells begins to collapse significantly with a resulting increase in stress. The model overpredicted the stress through the 0.6 to 0.4 region and intersects the experimental results at a stretch of approximately 0.35. Similarly, the numerical prediction of the results at 3000/s, shown in figure 5.16, indicates that the model overpredicted the experimental stress until a stress of approximately 0.45. After this point the experimental and numerical results correlate well. Since the deformation for 2050/s and 3000/s cases are similar with only a minor change in mechanical response as strain rate increased, subsequent discussion will investigate the 2050/s case only. From the preceding analysis was concluded that the polychloroprene foam could be modeled numerically at the cellular level. For both cases simulated, the timestep reduced significantly as the cells collapse making it computationally prohibitive to continue and so the simulation was terminated

at the points indicated in the figures.

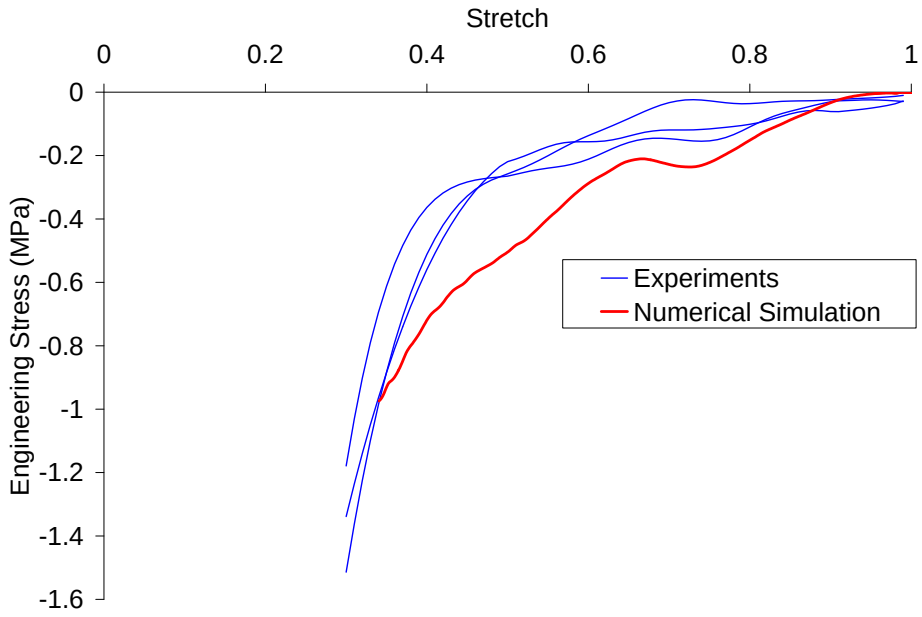

Figure 5.15: Comparison of numerical models and experiments for the 2050/s loading case.

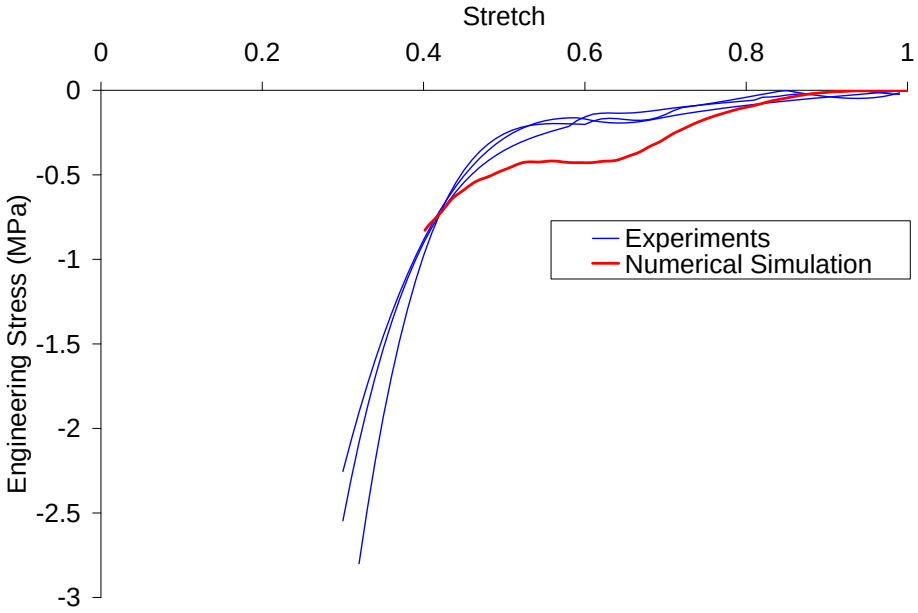

Figure 5.16: Comparison of numerical models and experiments for the 3000/s loading case.

Figure 5.17 shows the effect that the air coupling had on the response of the material. The blue line in figure 5.15 represents the and is scaled off the left ordinate axis. The red line represents a simulation where the fluid structure coupling was ignored and is scaled off the right ordinate axis. In this simulation, the fluid domain was removed and the analysis run with the same 2050/s loading history. As is clearly evident from the figure, the fluid contributes significantly to the response of material. The response of the model without the fluid structure coupling is an order of magnitude below the experiments and the coupled simulation. This clearly identifies the requirement for coupled analyses. Additionally, the effect of the fluid changed the shape of the curve significantly. Both curves exhibit the steep rise, plateau and densification region as identified by Gibson and Ashby [5] (note, although in the literature it is common to call this region densification, the density of porous materials changes throughout the compression history). However, the coupled simulation had a significantly reduced plateau region as indicated by the brace in the figure. Following the shortened plateau region, the model exhibits an extended densification region.

Figure 5.18 illustrates the differences between the coupled and uncoupled simulations through the mid–plane of the model. Since a displacement was applied to the top surface and the bottom surface was constrained in the y direction, the change in length for both simulations were the same. The uncoupled simulation showed a nearly fully compressible material (a material with little lateral expansion corresponding to a low Poisson's ratio), whereas as the coupled simulation exhibited some lateral expansion. The figures at 0.2 ms, 0.3 ms and 0.4 ms show that significantly more non–uniform deformation occurred in the uncoupled case.

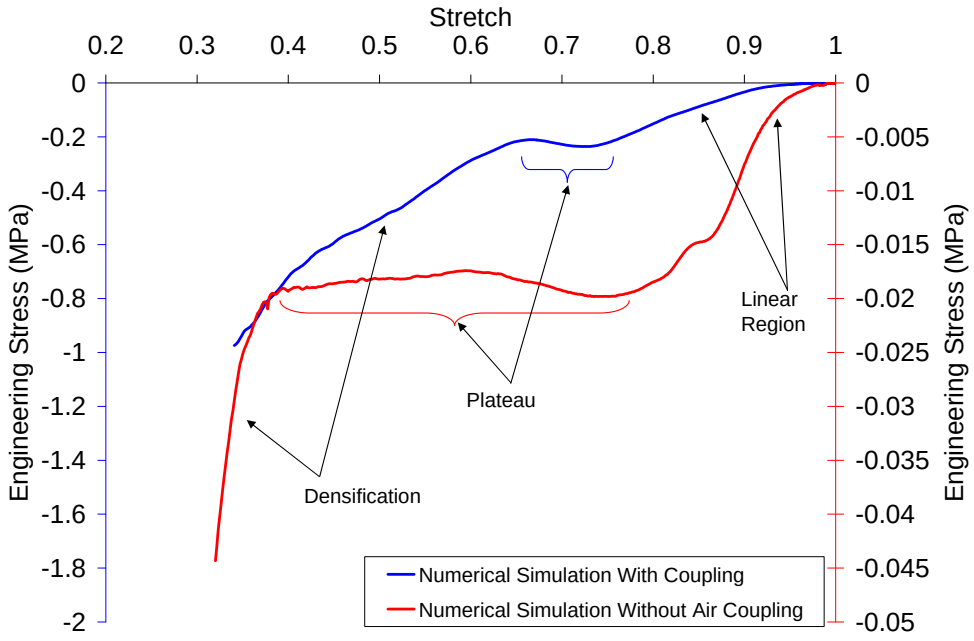

Figure 5.17: Comparison of numerical model result for the coupled (left axis) and uncoupled (right axis) case at 2050/s.

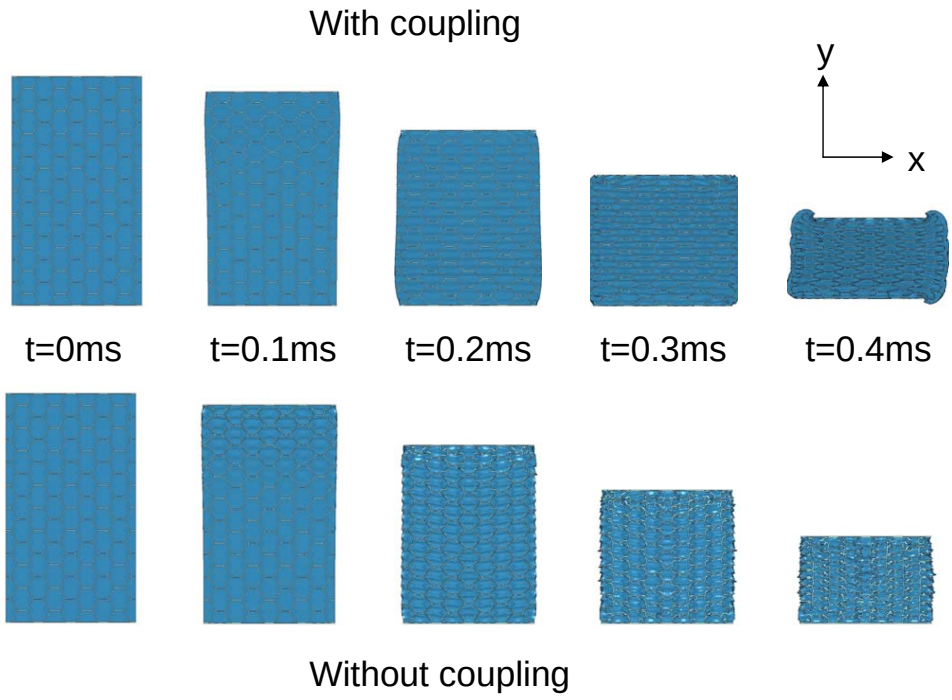

Figure 5.18: Simulations of the compression of the foam with (top) and without (bottom) coupling with the enclosed fluid.

Figure 5.19 shows the initial propagation of the stress wave using effective stress (top) and the corresponding wave in the air in the enclosed pores (bottom). The head of the wave in the air (bottom) is identified by the dotted line for clarity. As identified in the figure, the stress wave in the cellular material takes approximately 0.11 ms to reach the bottom of the sample which, by that time, the sample had deformed a significant amount with the length of the sample decreasing by approximately 10%. The corresponding pressure wave in the air enclosed by the pores lags the stress wave in the cellular material with it reaching approximately halfway through the sample in the same amount of time.

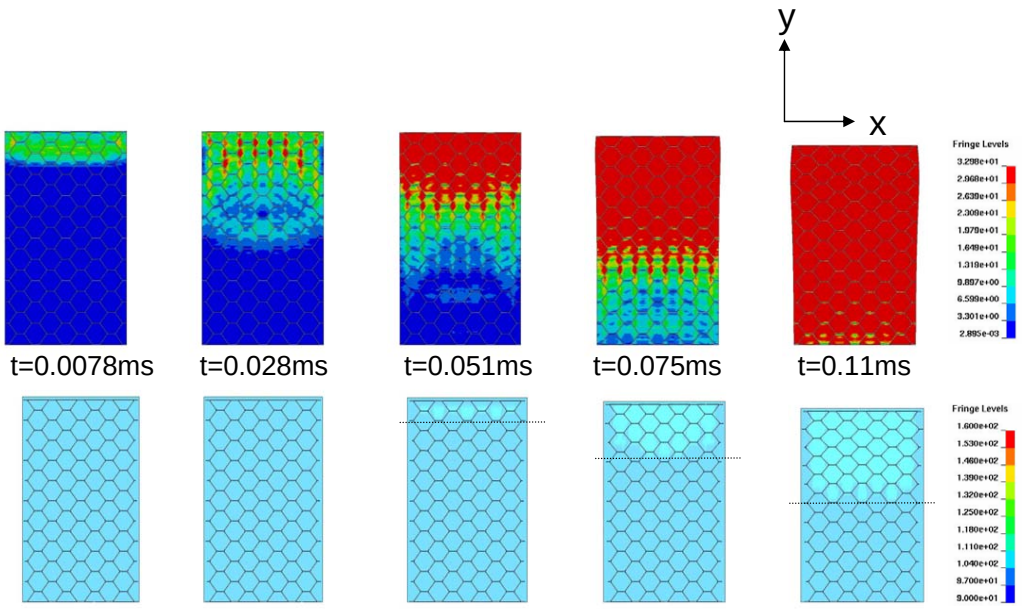

Figure 5.19: Propagation of stress wave in cellular material (top, effective stress in kPa) and corresponding wave through air in enclosed pore (bottom, pressure in kPa).

Figure 5.20 shows the propagation of the stress wave through the air enclosed in the pores highlighted by the dotted line (top). In this figure, the scale of the fringe levels

was set to highlight the wave interaction with the boundary and as such, the initial wave magnitude is slightly higher than that discussed in section 5.2.1. A x–t schematic corresponding to the wave front is shown in figure 5.20 bottom at various times. At point b, the wave had reached the bottom of the sample (approximately 0.03 ms after the stress wave in the cellular material) and reflects towards the top of the sample as shown by point c. Similarly, point d and e show the stress wave before and after it reflects off the top surface. As indicated in the x–t diagram, the top surface had displaced significantly by this time. Point f shows the point prior to the second interaction of the pressure wave with the fixed boundary.

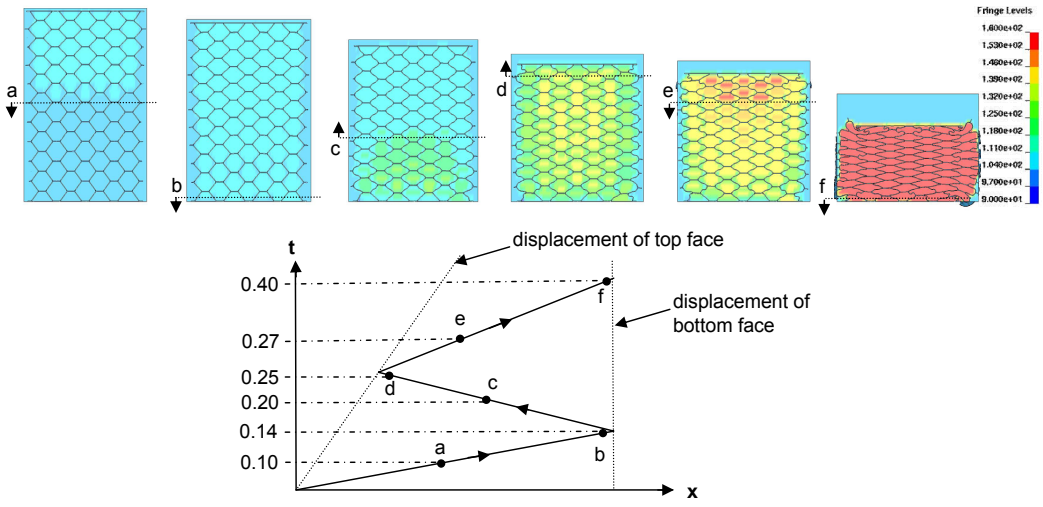

Figure 5.20: Propagation of stress wave through air in enclosed pores (top, pressure in kPa). Schematic of x–t wave propagation through air enclosed in pores (bottom).

The preceding analysis highlights the necessary requirement to account for stress wave propagation in the sample during testing. From these simulations, it is apparent that the dynamic equilibrium conditions (example three wave reflections) discussed in section 2.4.2 are not met under the tested conditions. Additionally, the analysis indicates that one

cannot necessarily scale the results from a sample of one length to that of another. *Id est*, in order to obtain a true representation of the properties of a material, one must test a sample of the same length as would be seen in the application.

5.4 Model extension

In order to identify relevant parameters which affect the response of porous materials, several variants of the numerical model were created and simulated as described subsequently. The effects that were investigated were loading rate and the morphological factors wall thickness, cell size and anisotropy. In order to reduce the computational burden, two reduced tessellations were created against which the various models were compared. The 2 by 3 by 2 mesh, shown in figure 5.7, was chosen as the width (x), height (y) and depth (z) were nearly equal giving an aspect ratio (x=z:y) of 0.94 for the overall domain. This tessellation was used to identify mesh density effects, rate effects, wall thickness effects and the effect of anisotropy. A different tessellation of 2 by 2 by 2 with an overall corresponding aspect ratio (x:y) of 1.4 was used to investigate the cell size effects. As will be discussed, this tessellation was chosen to ensure that the domain size remained the same while the number of cells inside the foam was varied.

5.4.1 Mesh Density Effects

As a standard simulation, the 2 by 3 by 2 tessellation was used with an applied velocity of 10 mm/ms. This was approximately equal to the applied velocity in the experimental case of 2050/s which was approximately 9.2 mm/ms and was below the 3000/s rate which corresponds to approximately 13.5 mm/ms. The velocity of the nodes was applied without a rise time similar to that shown in figure 5.14. Three different mesh densities

were explored. The coarsest mesh density corresponded to a mesh with $N_l = 1$ and $N_{tt} = 1$. This represented the coarsest mesh possible with two elements along L_c and through the thickness resulting in approximately 5600 elements. A medium mesh of $N_l = 3$ and $N_{tt} = 1$, which corresponded to the same mesh used to model the experimental tests discussed in the previous section, was created resulting in approximately 48 000 elements. A fine mesh with $N_l = 6$ and $N_{tt} = 2$ (corresponding to 12 elements along L_c and four elements through the wall thickness) was created resulting in approximately 381 000 elements for the 2 by 3 by 2 tessellation. No further refinements beyond this point ($N_l = 12$ and $N_{tt} = 4$) were conducted as it would have been computationally prohibitive with over 3 000 000 elements solid elements.

The effect of the varying mesh densities on the force–stretch response is illustrated in figure 5.21. The coarsest mesh, represented by the green line, shows significant oscillations as the pores collapse and the material densifies. These oscillations are not seen in the two refined meshes. The $N_l = 3$ and $N_{tt} = 1$ mesh, as represented by the blue line exhibits an initial rise, followed by a plateau and then an exponential rise as the pores collapse. A similar behaviour is seen for the finest mesh represented by the red line. Both the medium and fine mesh have the same initial rise followed by similar force levels over the plateau region. The densification region for the medium mesh occurs earlier and had a slightly different slope than that of the fine mesh. Due to the exponential nature of the force history during densification, a small difference in the predicted stretch at that point results in a significant difference between curves. This is evident by looking at the orange curve, which is the same as the fine mesh with a stretch offset of 0.03, that indicates a similar rise in force as the pores collapse. The initial section of the curves for both the medium and fine mesh are offset from a stretch of 1 since they undergo some deformation prior to the stress wave arriving at the bottom of the sample. This effect is similar to

that discussed in section 5.2.

Figure 5.22 shows a mid–sectional view through the 2 by 3 by 2 tessellation for the three mesh densities at 0.0686 ms. Although the distortion of the mesh walls is similar for all three meshes as indicated in the figure, the coarsest mesh resulted in significant hinges effects and severely distorted elements. The medium and fine mesh exhibit similar deformations with a relatively consistent wall thickness being maintained.

The simulation using the coarse mesh took approximately 73 hours to complete, with the medium mesh it took 135 hours to complete and the finest mesh took 765 hours to complete using the same procedure described previously. As such, the medium mesh was chosen to ease the computational requirement for the following analyses.

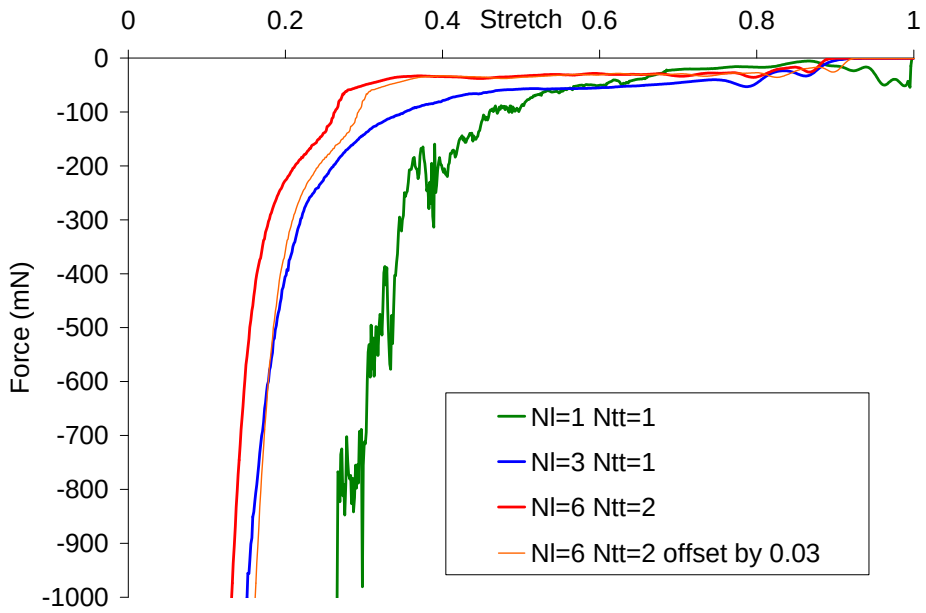

Figure 5.21: The effect of mesh density on the force response for three different meshes.

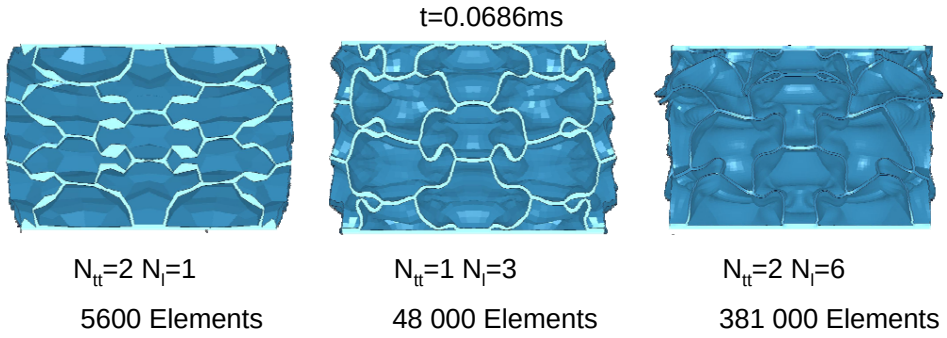

Figure 5.22: The effect of mesh density on the deformation behaviour for three different meshes.

5.4.2 Loading Rate Effects

Three different loading rates were investigated as shown in figure 5.23. The slowest loading rate at 1 m/s had a slightly lower stress plateau than the 10 m/s case and a similar exponential rise as the models compressed as indicated by the red and blue lines. However, as indicated in the deformation history prior to a stretch of 0.9 in the figure, the 1 m/s did not experience the same amount of deformation prior to the arrival of the stress wave at the stationary side. This indicates that the stress wave had sufficient enough time to propagate to the end of the sample prior to significant deformation at the loading end. In contrast, the loading rate at 100 m/s shows significant deformation with a stretch of approximately 0.3 being reached prior to any measurable stress (green line).

Figure 5.24 shows the force–stretch history for the 10 m/s and 100 m/s cases with the force measured from both sides (the loading and the stationary side). As evident from the figure, the initial force response for the 10 m/s case on the loading side, scaled on the left axis of the graph, is immediate and did not show the same lag as the result from the stationary side. The two results quickly coincide and show the same response after

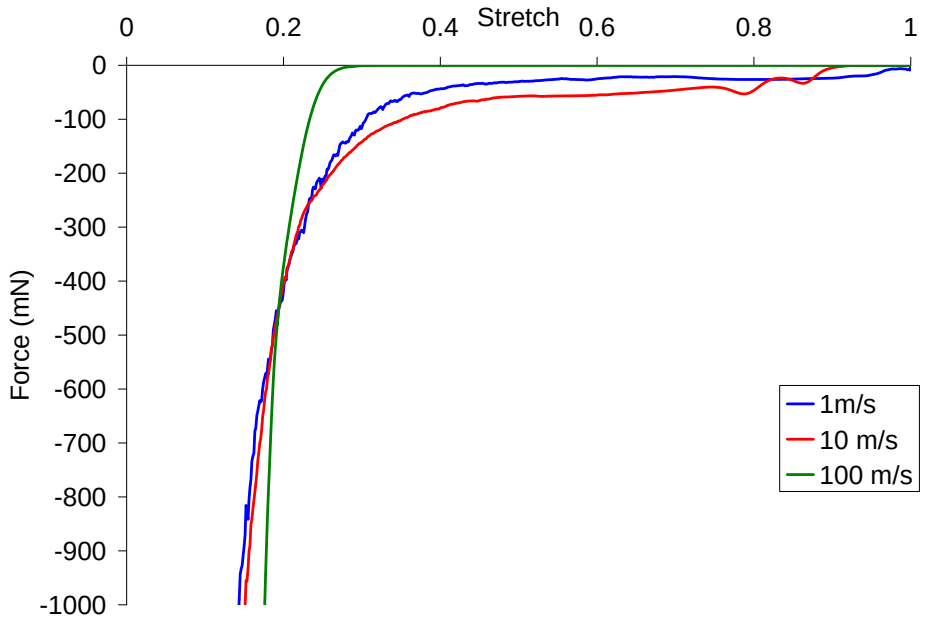

Figure 5.23: The effect of loading rate on the deformation behaviour over three loading rates.

a stretch of approximately 0.85. The 100 m/s case shows that there was a significant difference in force measured from the stationary side in comparison to the loading side. As can be seen in the figure, the force for the 100 m/s case shows an approximate value of 2500 mN, scaled of the right axis, during the majority of the compression of the material while nearly zero force is measured on the stationary side. The force levels do not coincide until a very large amount of compression occurs (not shown). The initial oscillations of the force on the loading side for the 100 m/s case occurs from the acceleration of the loading surface to the constant velocity. These same oscillations occurred in the 10 m/s case but to a lesser extent.

The difference between the loading rates is further illustrated by figure 5.25 which shows the deformation of the material at stretches of 0.9 and 0.25 for both the 10 m/s and 100 m/s case. As evident from the figure at 0.9 stretch, the stress wave in the

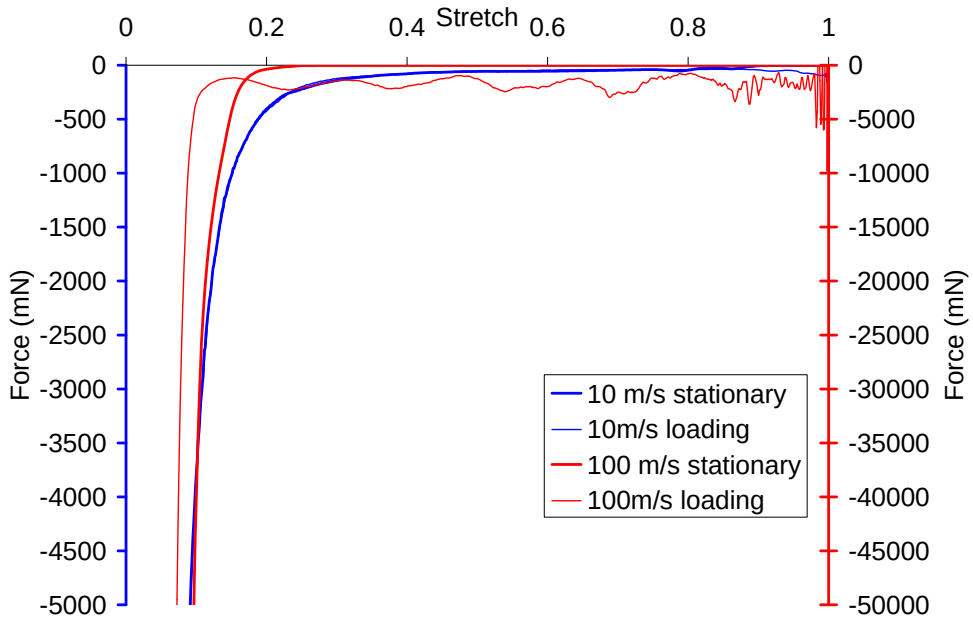

Figure 5.24: The force history for both the loading and stationary sides for the 10 m/s (left axis) and 100 m/s (right axis) cases.

100 m/s case is just beyond the deformation region whereas in the 10 m/s case the stress wave had reached the stationary boundary. Additionally, the pores at the loading surface had nearly completely collapsed for the 100 m/s case whereas for the 10 m/s case the deformation was more uniform (albeit more deformation occurs at near the loading surface). Similarly, for the 0.25 stretch case as shown in the bottom of the figure, the stress wave had reached the stationary surface for the 100 m/s with significant pore collapse near the loading surface. As before, the 10 m/s case show relatively equal deformation across the cells.

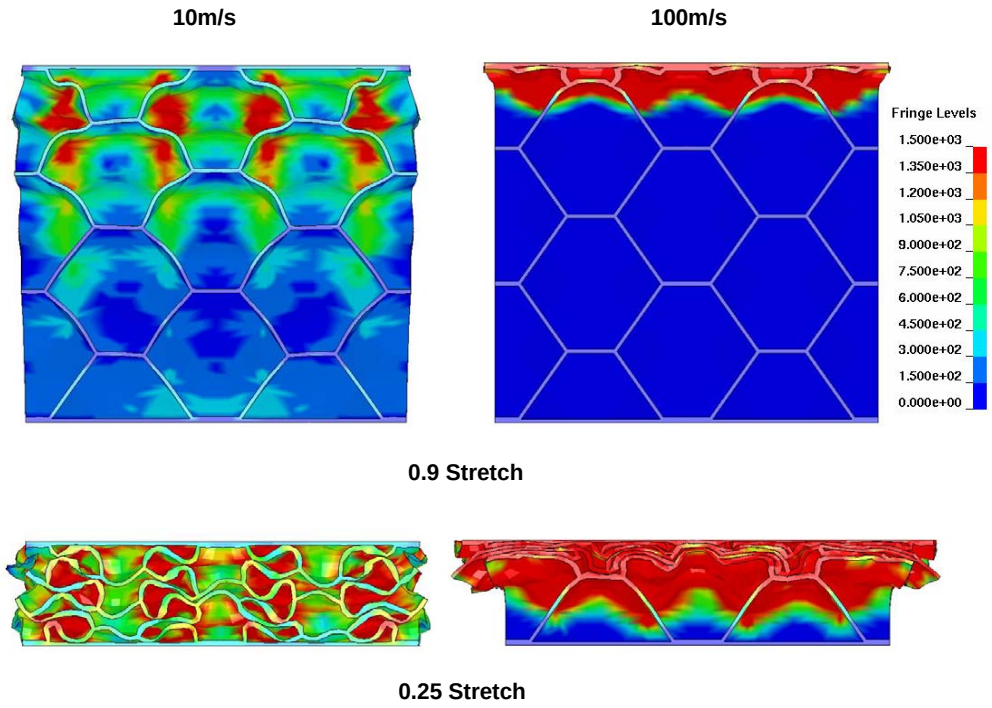

Figure 5.25: Models showing the mid–plane for the 10 m/s and 100 m/s cases at stretches of 0.9 and 0.25,contours of effective stress.

The oscillations shown in figure 5.24 are explored further in figure 5.26 which shows the force–time history for the 100 m/s case. At the peaks of each oscillation cycle, the resulting model is shown. As indicated in the figure, the more negative peaks, points a and c, coincide with the initial interaction of the compressed region with a undeformed cell as shown by the arrows. The more positive peaks of the oscillations, points b and d, occur after the cells that have contacted the compressed region begin to buckle.

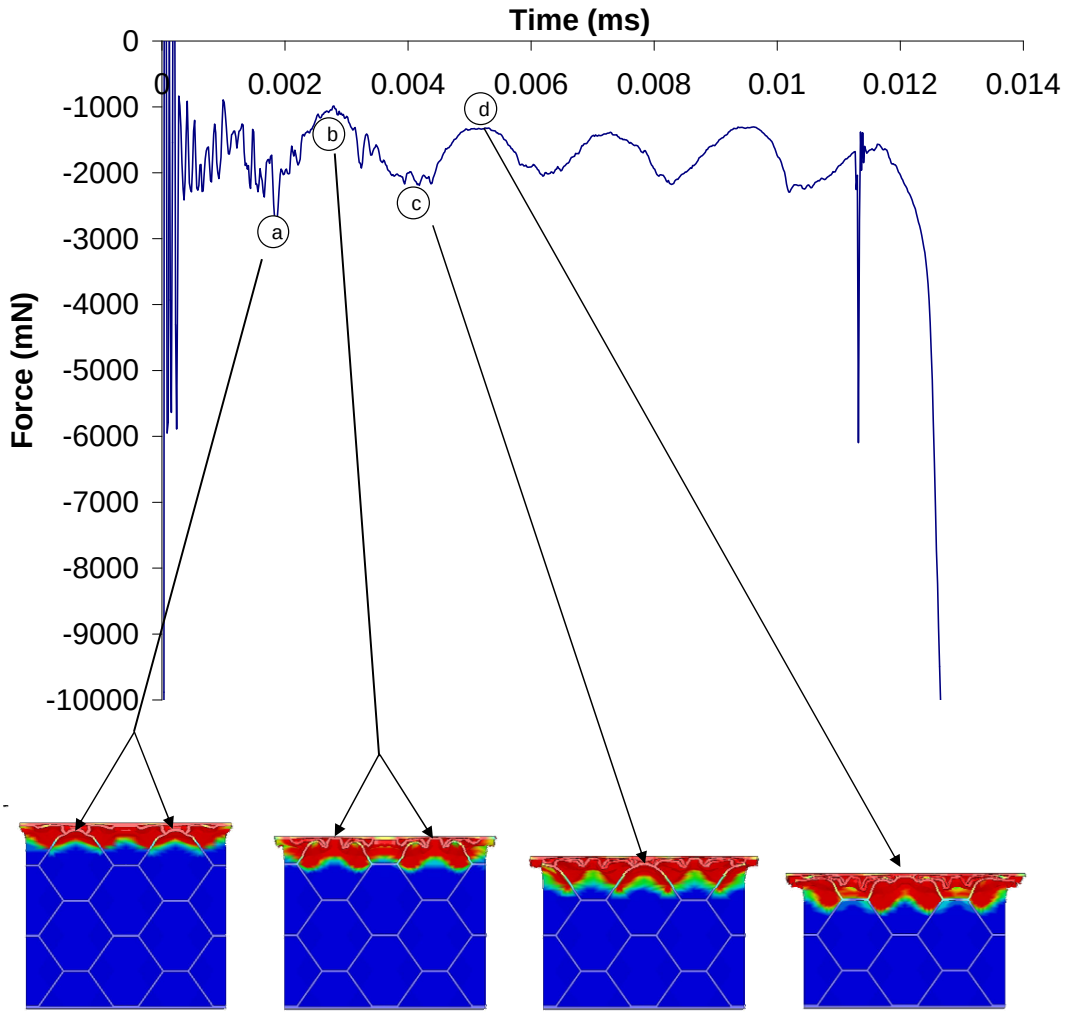

Figure 5.26: Oscillations in the force response and the corresponding deformations in the model mid–plane.

From the preceding analysis the deformation mechanisms for different loading rates are clearly distinct. As described in section 5.3, care must be taken when performing analyses of situations that involve length scaling. *Id est*, you cannot using strain rate scaling for porous materials as you would with homogeneous materials. *Exempli gratia*, if the domain length of a piece of foam used in a helmet is 25 mm thick and subjected to a loading rate of 28 m/s (approximately 100 km/h) resulting in a strain rate of approximately 1100/s, it is inappropriate to perform experimental tests on a sample 9 mm in length at 10 m/s (corresponding to an approximate strain rate of 1100/s) and expect to obtain an answer representative of the actual response of the 25 mm thick piece.

5.4.3 Wall Thickness Effects

Five numerical models which increased the thickness of the wall by a factor of 2^a, where a is an integer and ranging from 0 to 4, were used to investigate the effect of wall thickness. The initial mesh, 2^0, corresponds to the actual wall thickness measured as discussed before while the $2^4 = 16$ case represented the largest mesh, scale by 2^a, before the pore completely disappeared. This progression resulted in wall thicknesses of approximately 12 μm, 24 μm, 48 μm, 96 μm and 192μm. Figure 5.27 shows the resulting models used. For the 12 μm to 48 μm cases the mesh density was that used before ($N_l = 3$, $N_{tt} = 1$), for the 96 μm case N_{tt} was set to two and for the 192 μm case N_{tt} was set to four. The mesh density was changed in this manner to prevent severely skewed elements from occurring.

Figure 5.28 shows the difference in the force–stretch response for the different wall thicknesses. As is evident from the figure, as the wall thickness increases, the stretch to densification is reduced. This is caused by the reduced pore size and so the onset of pore collapse occurs sooner. Additionally, upon inspection of the initial portion of the loading curve, the stretch, and hence time, before the stress wave reaches the fixed end is reduced as indicated by the 96 and 192 μm cases.

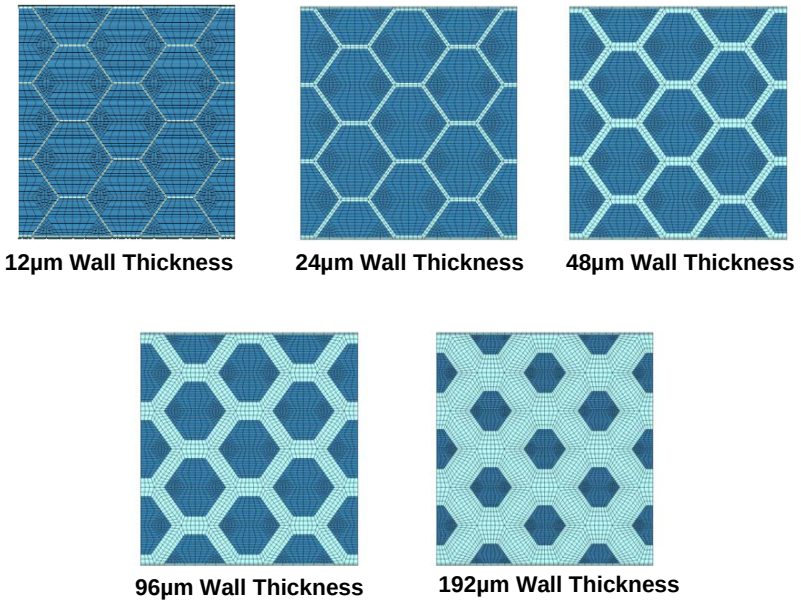

Figure 5.27: The five different models used to investigate the wall thickness effects.

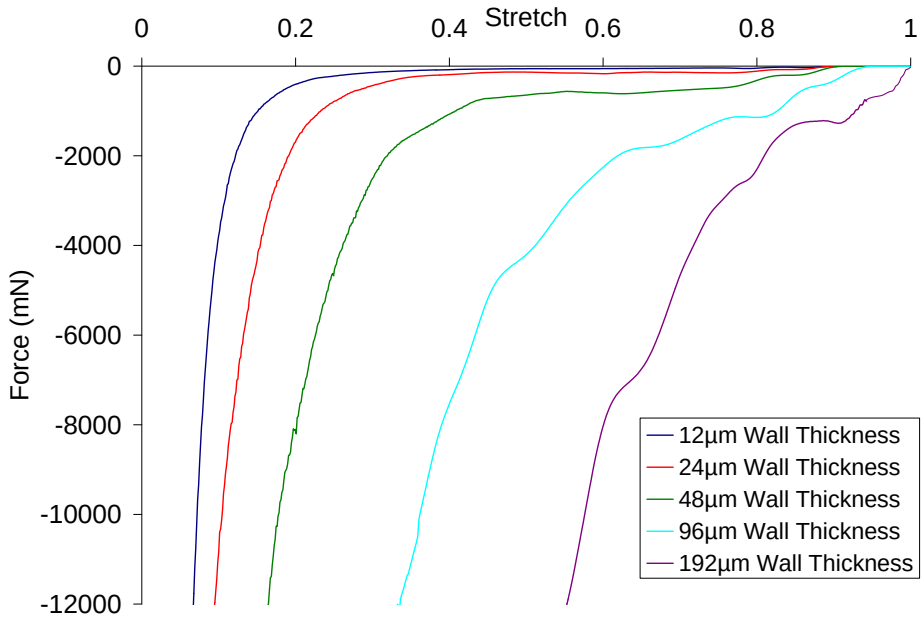

Figure 5.28: The effect of wall thickness on the force response for five different models.

5.4.4 Cell Size Effects

An investigation into the effect that cell size was conducted. In order to keep the overall domain size the same, the modification of the cell size was required to be in multiples of 2 of the standard cell size. Therefore, a new base tessellation of 2 by 2 by 2 was created. If the cell size is halved, then the tessellation required to maintain the domain size was then 4 by 4 by 4. Similarly, if the cell size is doubled, the tessellation required was 1 by 1 by 1. These three tessellations are shown in figure 5.29 at a time of 0.011 ms. As indicated in the figure, the stress wave had reached the stationary surface at approximately the same time for each cell size. This is also evident in the force–stretch history shown in figure 5.30 as there was an equal offset in stretch with each case (approximately at 0.9). As the cell size decreased the plateau level of force increased and the stretch at which the pores collapse is decreased as indicated by the figure. Figure 5.29 does indicate however that as the cell size decreased, a greater lateral expansion (higher Poisson's ratio) was observed. From this analyses it can be concluded that as the number of cells increase, so too does the stress level for the same amount of stretch. However, this material appears to be relatively insensitive to cell size with a large change in the cell density required to have any affect on the response of the material.

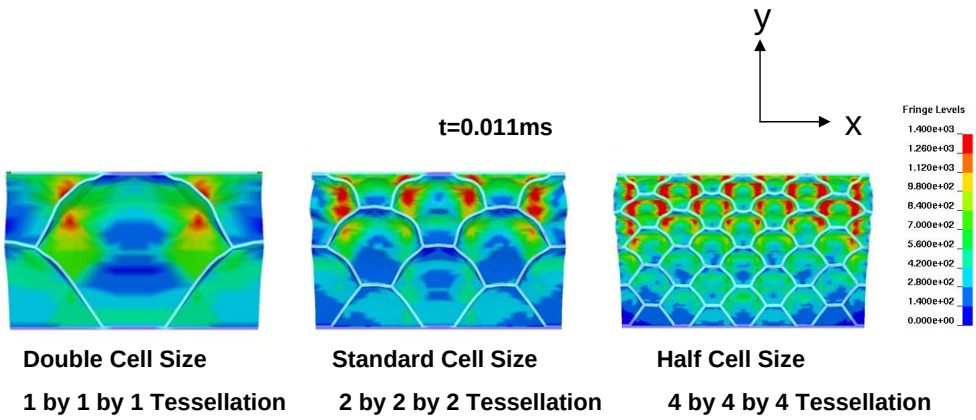

Figure 5.29: The three different models used to investigate cell size effects, contours of effective stress shown.

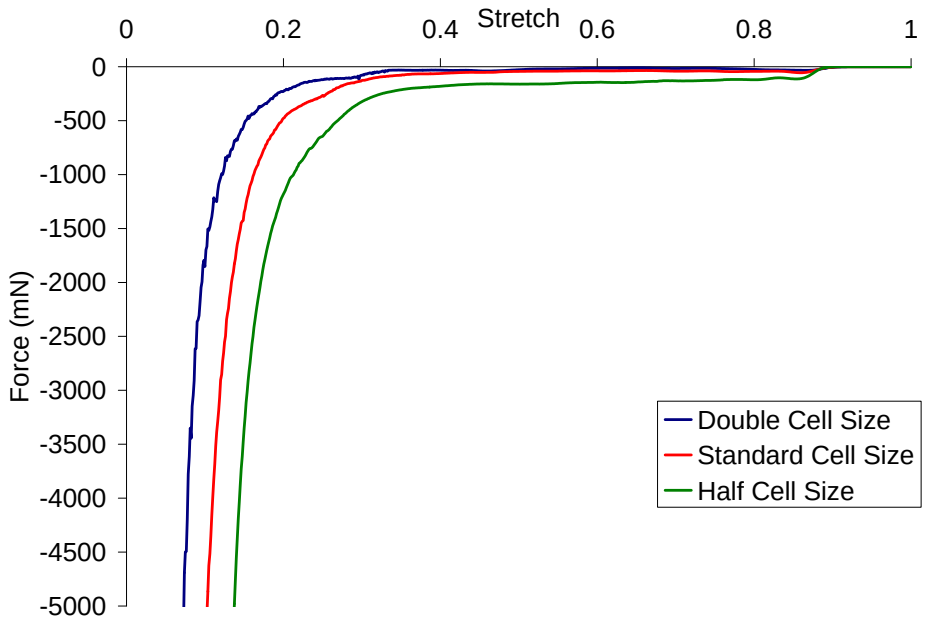

Figure 5.30: The effect of cell size on the force response for three different models loaded at 10 m/s.

5.4.5 Effect of Anisotropy

Two different cell size aspect ratios were modeled to identify the affect anisotropy had on the deformation behaviour of the model. The aspect ratios (height:width=depth, y:x=z) chosen were 0.5 and 1.5 and compared to the standard 2 by 3 by 2 case. Note that the standard cell size had a small inherent aspect ratio with the height (distance from the square face to square face) being 0.438 mm and the width (as measure from the vertex of the intersecting hexagon) being 0.464 mm resulting in a height to width ratio of 1.08:1. Figure 5.31 shows the models used. The models had the same tessellation and mesh density but due to the anisotropic arrangement of the cells, the domain size was reduced from 1.38 mm for the standard case to approximately 0.7 mm for the 0.5 case and increased to 2.05 mm for the 1.5 aspect ratio. Figure 5.32 shows the affect the anisotropy had on the force–stretch response. As indicated in the figure, the 1.5 aspect ratio and the standard case exhibit nearly the same response. The 0.5 aspect ratio shows a reduced stretch prior to the cell collapse region in compared to the standard case. As with the effect of cell size, significant changes in anisotropy were required to have a measurable effect on the response of the material. As well, as the aspect ratio reduces the stretch to cell collapse decreases. One could extrapolate this out to an aspect ratio where the cells are initially disk like resulting in a negligible plateau region.

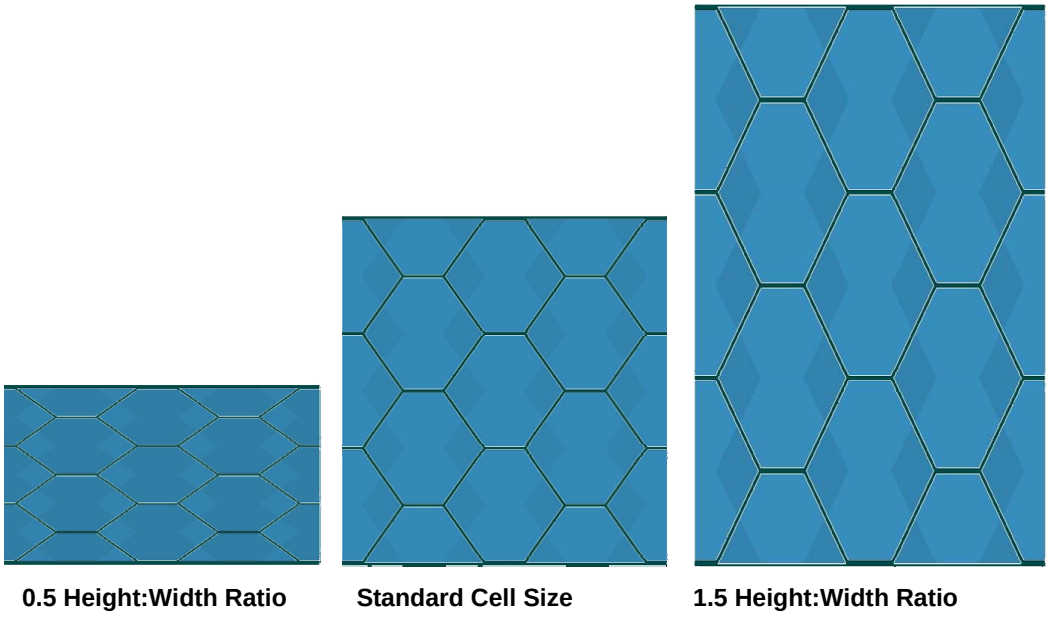

Figure 5.31: The three different models used to investigate effects of anisotropy.

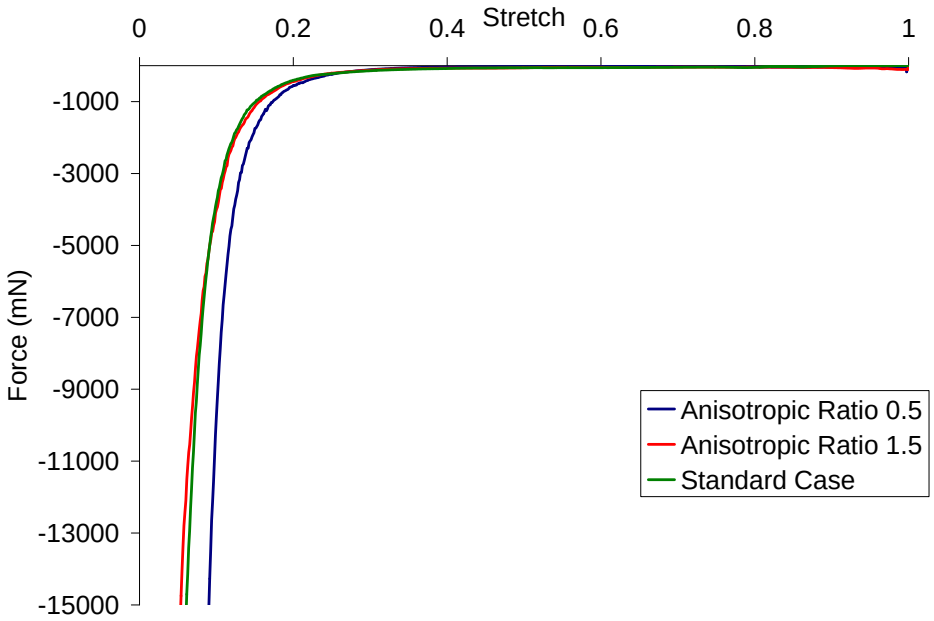

Figure 5.32: The effect of anisotropy on the force response for three different models.

5.5 Discussion

Stress wave effects are critically important when investigating the response of porous materials as identified in the analysis of the transient effects at the pore level, the model of the experiments and the loading rate simulations. As identified in those models, there is a finite time that the stress wave takes to propagates through the material which can have a significant impact on the initial response of the material. This is critically important when performing characterization experiments on porous materials since the specimens have large deformations without a corresponding increase in force depending on where the force is being measured (loading or stationary side). Even with the gradual rise time of the loading, as shown in the models of the experiments, the significantly low stress wave speed results in finite deformation before a uniform stress state can be achieved. If the overall elastic wave speed was measured in the model to be between 68 m/s and 115 m/s, loading rates that are well below the lower bound of these values would not be as influenced by wave propagation effects. *Id est*, the loading rate modeled at 10 m/s was almost 15% of the wave speed which was significant. Lower rates, such as those tested at approximately 8/s, are below 0.05% of the wave speed and so will be less influenced by wave effects. Additionally, the models of the experiments without fluid structure interaction showed that the enclosed air had a significant influence.

The models of cell size, wall thickness and anisotropy allowed morphological factors to be explored which had not been identified in the literature as discussed in section 2.3. The stress wave propagation was dependent on the wall thickness as the propagation through the model was reduced as thickness increased. Additionally, it was shown that a significant shift to the right of the force–stretch response occurred with increasing wall thickness. The models of varying cell size showed that as cell size decreases, the deformation to the pore collapse region reduced, shifting the curve to the right on a

force–stretch graph. A similar effect was noted for the anisotropic cases with a shift to the right on the force–stretch curve with decreasing height to width ratio. As shown in figure 5.33, the relative effect of anisotropy is less than that of wall thickness or cell size cases. The effect of cell size and wall thickness for the 24 μm case are relatively the same as indicated by the light blue and red lines. However, when the wall thickness is increased to 48 μm a significant decrease in the amount of stretch prior to pore collapse region is seen.

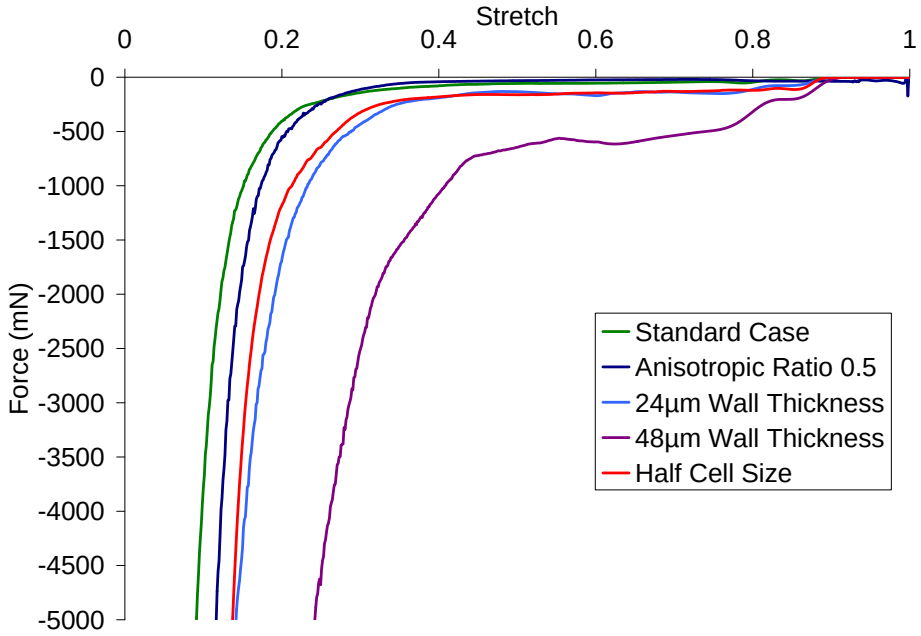

Figure 5.33: The relative effects of the parameters compared in the models.

Chapter 6

Conclusions and Future Considerations

The purpose of the current study was to create and validate a model of a closed cell hyperelastic porous material so that their deformation mechanisms and the factors that contribute to the mechanical response could be investigated. This model was used to investigate phenomena such as stress wave speed, the contribution of the enclosed air to the response of the material and the deformation mechanisms seen under large amounts of compression. The first step of this process was to identify the strain rate sensitivity of the material tested. The material chosen for the study was polychloroprene in both the solid rubber and foamed states. This material was unique in that the foaming process was achieved through application of high pressure gas into the polychloroprene to create the foam not through a chemical process as is done with other foams such as expanded polystyrene. The assumption was made that by testing the solid rubber, the properties of the cellular structure of the foam could be determined.

6.1 Conclusions

An investigation into constitutive models for hyper non–linear viscoelastic materials identified that there were no available constitutive models that were capable of capturing the polychloroprene rubber mechanical response. A new constitutive model was proposed which incorporated nonlinear viscoelastic effects. In addition to being able to capture the nonlinear viscoelastic effects, this model offered other advantages such as material objectivity and a reduced memory requirement which was lacking in the available models. Material parameters were determined and the measured R^2 value was 0.9962 indicating that the constitutive model was capable of capturing the material response over a range of strain rates and stretches.

Simulations run without the fluid structure coupling algorithm invoked identified that the enclosed air had a significant contribution to the materials response not only increasing the reaction force by ten times but by also changing the shape of the curve reducing the plateau region of the curve. These effects had often been neglected in finite element models at the microscopic level due to the inherent computational cost. Through analysis of the numerical model, it was determined that the response of porous materials had significant transient effects. By investigating the mechanism through which momentum is transferred, stress path tortousity and impedance coupling effects were shown to dissipate and attenuate stress waves propagating through porous materials. During the time the stress wave took to propagate through the cellular material, the sample deformed significantly illustrating the requirement to account for transient effects during experimental testing of porous materials. Simulations with varying loading rates identified that as the loading rate increased, the requirement to account for stress wave effects when analysing deformation became increasingly necessary. When comparing the force history of the loading and stationary surfaces it was determined that at loading

velocities of 1 m/s the forces were approximately equal while at 10 m/s, there was a significant lag between the time the force was applied to the surface and the time it arrived at the stationary surface; this was further amplified at 100 m/s. These simulations also showed that strain rate scaling is not appropriate for this type of material. The pore–scale model developed in this research allowed visualization of the deformation mechanics of the foam which cannot be obtained through experimental methods.

Several models were simulated to identify morphological effects on the response of the foam. Of the morphological factors investigated, it was concluded that wall thickness had the most dominant effect over cell size and anisotropy.

6.2 Future Considerations

The following recommendations for future work are made.

1. Further investigation into the deformation mechanics of more complex porous structures comprised of cells of unequal volumes could be considered.

2. A porous material with interconnecting ducts, such as that seen in lung tissue, could be simulated to identify the influence of the semi–open celled structure.

3. A model which includes surface tension at the air and rubber interface could be conducted to identify its influence.

4. As computing power increases, larger domain sizes should be studied to identify further domain size effects on stress wave propagation and deformation mechanisms.

5. Implicit finite element techniques could be modified to include fluid–structure interaction algorithms which could allow lower rate experiments to be simulated.

References

[1] L. DiLandro, G. Sala, and D. Oliviera. Deformation mechanisms and energy absorption of polystyrene foams for protective helmets. *Polymer Testing*, 21:217–228, 2002.

[2] Wikipedia. Metal — wikipedia, the free encyclopedia, 2011.

[3] S.R. Reid and C. Peng. Dynamic uniaxial crushing of wood. *International Journal of Impact Engineering*, 19:531–570, 1997.

[4] E.R. Weibel and J. Gill. Structure–function relationships at the alveolar level. In J.B. West, editor, *Bioengineering Aspects of the Lung*. Marcel Dekker, New York, 1977.

[5] L.J. Gibson and M.F. Ashby. *Cellular Solids–Structure and Properties 2nd ed.* Cambridge University Press, Cambridge U.K., 1997.

[6] N.J. Mills, R. Stampfli, F. Marone, and P.A. Bruhwiler. Finite element micromechanics model of impact compression of closed–cell polymer foams. *International Journal of Solids and Structures*, 46(3-4):677 – 97, 2009.

[7] A. Gilchrist and N.J. Mills. Impact deformation of rigid polymeric foams: experiments and FEA modelling. *International Journal of Impact Engineering*, 25:767–786, 2001.

[8] K.B. Kann. Sound waves in foams. *Colloids and Surfaces A: Physiochem. Eng. Aspects*, 263:315–319, 2005.

[9] R.A. Thuraisingham. Sound speed in bubbly water at megahertz frequencies. *Ultrasonics*, 36:767–773, 1998.

[10] P.S. Wilson. Low–frequency dispersion in bubbly liquids. *Acoustic Research Letters*, 6(3):188–194, 2005.

[11] R.T. Yen, Y.C. Fung, H.H. Ho, and G. Butterman. Speed of stress wave propagation in lung. *J. Appl. Physiol.*, 61(2):701–705, 1986.

[12] D.A. Rice. Sound speed in pulmonary parenchyma. *Journal of Applied Physiology*, 54(1):304–308, 1983.

[13] A.I. D'yachenko and G.A. Lyubimov. Propagation of sound in pulmonary parenchyma. *Fluid Dynamics*, 23(5):641–652, 1988.

[14] A.I. D'yachenko and O.V. Manyuhina. Modeling of weak blast wave propagation in the lung. *J. Biomech.*, 2006. In Press.

[15] A. Greer. Numerical modeling for the prediction of primary blast injury to the lung. Master's thesis, University of Waterloo, 2006.

[16] K. Kitagawa, K. Takayama, and M. Yasuhara. Attenuation of shock waves propagating in polyurethane foams. *Shock Waves*, 15:437–445, 2006.

[17] P.J. Berger, E.M. Skuza, C.A. Ramsden, and M.H. Wilkinson. Velocity and attenuation of sound in the isolated fetal lung as it is expanded with air. *Journal of Applied Physiology*, 98(6):2235–2241, 2005.

[18] O. Umnova, K. Attenborough, and A. Cummings. High amplitude pulse propagation and reflection from a rigid porous layer. *Noise Control Eng. J.*, 50(6):204–210, 2002.

[19] M. Olim, M.E.H. Van Dongen, T. Kitamura, and K. Takayama. Numerical simulation of the propagation of schock waves in compressible open–cell porous material. *Int. J. Multiphase Flow*, 20(3):557–568, 1994.

[20] M.A. Biot. Theory of propagation of elastic waves in a fluid–saturated porous solid I. low–frequency range. *The Journal of the Acoustical Society of America*, 28(2):168–178, 1956.

[21] M.A. Biot. Theory of propagation of elastic waves in a fluid–saturated porous solid I. higher frequency range. *The Journal of the Acoustical Society of America*, 28(2):179–191, 1956.

[22] M.A. Biot. The elastic coefficients of the theory of consolidation. *Journal of Applied Mechanics*, 24:594–601, 1957.

[23] M.A. Biot. Mechanics of deformation and acoustic propagation in porous media. *Journal of Applied Physics*, 33:1482–1498, 1962.

[24] Marc A. Meyers. *Dynamic Behavior of Material*. Wiley, New York, 1994.

[25] D.B. Hayes. Introduction to stress wave phenomena. Technical Report SLA-73-0801, Sandia National Laboratories, Albuquerque, N.M., 1973.

[26] J.D. Anderson. *Modern Compressible Flow with Historical Perspective*. McGraw-Hill, Boston, 1990.

[27] S.M. Yahya. *Fundamentals of Compressible flow with Aircraft and Rocket Propulsion*. New Age International Ltd., New Delhi, 2003.

[28] W.J.M. Rankine. On the thermodynamic theory of waves of finite longitudinal disturbances. *Phil. Trans. Roy. Soc.*, 160:277, 1870.

[29] P.H. Hugoniot. Sur la propagation du mouvement dans les corps et specialement dans les gaz parfaits. *J. de l'Ecole Polytechnique*, 57, 1887.

[30] R.G. McQueen, S.P. Marsh, J.W. Taylor, J.N. Fritz, and W.J. Carter. The equation of state of solids from shock wave studies. In R. Kinslow, editor, *High Velocity Impact Phenomena*, New York, 1970. Academic.

[31] G.F. Kinney. *Explosive Shocks in Air*. The Macmillan Company, New York, 1962.

[32] P.D. Smith and J.G. Hetherington. *Blast and Ballistic Loading of Structures*. Butterworth–Heinemann, Oxford, 1994.

[33] G.R. Heppler and J.S. Hansen. The response of a circular cylinder to a nuclear explosion. *J. Sound Vib* ., 113:559–584, 1987.

[34] A. Gupta, F. Gregory, R. Bitting, and S. Bhattacharya. Dynamic analysis of an explosively loaded hinged rectangular plate. *Comput. Struct.*, 26(1-2):339–344, 1987.

[35] D. Redekop and P. Azar. Dynamic response of a cylindrical shell panel to explosive loading. *J. Vib. Acoust.*, 113:273–278, 1991.

[36] J. Tedesco, J. Hayes, and D. Landis. Dynamic response of layered structures subject to blast effects of non-nuclear weaponry. *Comput. Struct.*, 26(1-2):79–86, 1987.

[37] M. Stoffel and R. Schmidt. Shock wave-loaded plates. *Int. J. Solids Struct.*, 38:7659–7680, 2001.

[38] L. Zhu. Transient deformation modes of square plated subjected to explosive loadings. *Int. J. Solids Struct.*, 33(3):301–314, 1996.

[39] A.C. Jacinto, R.D. Ambrosini, and R.F. Danesi. Experiment and computational analysis of plates under air blast loading. *International Journal of Impact Engineering*, 25:927–947, 2001.

[40] A.C. Jacinto, R.D. Ambrosini, and R.F. Danesi. Dynamic response of plates subjected to blast loading. *Proceedings of the Institution of Civil Engineers Structures and Buildings*, August(3):269–276, 2002.

[41] M. Klaus. Response of a panel wall subjected to blast loading. *Comput. Struct.*, 21:129–135, 1985.

[42] J.M. Santiago and S. Bhattacharya. Sensitivity of plate response calculations to blast load definition. *Comput. Struct.*, 40:375–392, 1991.

[43] D. Kraus, J. Roetzer, and K. Thoma. Effect of high explosive detonations on concrete structures. *Nucl. Eng. Des.*, 150:309–314, 1994.

[44] J.L. O'Daniel and T. Krauthammer. Assessment of numerical simulation capabilities for medium-structure interactions systems under explosive loads. *Comput. Struct.*, 63(5):875–887, 1997.

[45] K. Williams, S. McClennan, R. Durocher, B. St.-Jean, and J. Tremblay. Validation of a loading model for simulating blast mine effects on armoured vehicles. In 7^{th} *Int. LS-DYNA Users Conference*, Dearborn, USA, May 2002.

[46] L. Olovsson. *On the Arbitrary Lagrangian-Eulerian Finite Element Method*. PhD thesis, Linköpings Universitet, 2000.

[47] J. Hallquist. *LS-DYNA Theoretical Manual*. LSTC, California, 1998.

[48] C. Salisbury, D. Cronin, and F.S. Lien. Investigation of the arbitrary lagrangian eulerian formulation to simulate shock tube problems. In *LS-Dyna Users Conference 2004*, Detroit, 2004.

[49] M. Souli, A. Ouashine, and L. Lewin. ALE formulation for fluid–structure interaction problems. *Comput. Methods Appl. Mech. Engrg.*, 190:659–675, 2000.

[50] M. Souli. *LS-DYNA Advanced Course in ALE and Fluid/Structure Coupling*. LSTC, 2004.

[51] V.S. Deshpande and N.A. Fleck. Multi-axial yield behaviour of polymer foams. *Acta Materialia*, 49(10):1859 – 1866, 2001.

[52] F. Rammerstorfer, D. Pahr, T. Daxner, and W. Vonach. Buckling in thin walled micro and meso structures of lightweight materials and material compounds. *Comput. Mech.*, 37:470–478, 2006.

[53] F. Cote, B.P. Russell, V.S. Deshpande, and N.A. Fleck. The through-thickness compressive strength of a composite sandwich panel with a hierarchical square honeycomb sandwich core. *Journal of Applied Mechanics*, 76(6):061004 (8 pp.) –, 2009.

[54] N.A. Fleck, V.S. Deshpande, and M.F. Ashby. Micro-architectured materials: Past, present and future. *Proceedings of the Royal Society A: Mathematical, Physical and Engineering Sciences*, 466(2121):2495 – 2516, 2010.

[55] O. B. Olurin, N. A. Fleck, and M. F. Ashby. Deformation and fracture of aluminium foams. *Materials Science and Engineering A*, 291(1-2):136 – 146, 2000.

[56] W.T. Kelvin. On the division of space with minimum partitional area. *Philosophical Magazine*, 24(151):503, 1887.

[57] D. Weaire and R. Phelan. A counterexample to Kelvin's conjecture on minimal surfaces. *Philosophical Magazine Letters*, 69:107–110, 1994.

[58] D. Weaire and R. Phelan. Physics of foams. *Journal of Physics Condensed Matter*, 8:9519–9524, 1996.

[59] Y.C. Fung. A model of the lung structure and its validation. *J. Appl. Physiol.*, 64(5):2132–2141, 1988.

[60] N.J. Mills and H.X. Zhu. The high strain compression of closed–cell polymer foams. *Journal of the Mechanics and Physics of Solids*, 47:669–695, 1999.

[61] N.J. Mills. The high strain mechanical response of the wet kelvin model for open-cell foams. *International Journal of Solids and Structures*, 44(1):51 – 65, 2007.

[62] R. Sullivan, L. Ghosn, and B. Lerch. A general tetrakaidecahedron model for open celled foams. *International Journal of Solids and Structures*, 45:1754–1765, 2008.

[63] M. Vesenjak and Z. Ren. Advanced simulations of cellular structures with Ls-dyna. In *6^{th} European Ls-dyna User's Conference*, 2007.

[64] M. Vesenjak, A. Ochsner, M. Hribersek, and Z. Ren. Behaviour of cellular structures with fluid fillers under impact loading. *The International Journal of Multiphysics*, 1(1):101–122, 2007.

[65] G.R. Cowper and P.S. Symonds. Strain hardening and strain rate effects in the impact loading of cantilever beams. Technical report, Brown University, Applied Mathematics Report, 1958.

[66] Wen-Yea Jang, A.M. Kraynik, and S. Kyriakides. On the microstructure of open-cell foams and its effect on elastic properties. *International Journal of Solids and Structures*, 45(7-8):1845 – 75, 2008.

[67] M. De Giorgi, A. Carofalo, V. Dattoma, R. Nobile, and F. Palano. Aluminium foams structural modelling. *Computers and Structures*, 88(1-2):25 – 35, 2010.

[68] C. Veyhl, I.V. Belova, G.E. Murch, and T. Fiedler. Finite element analysis of the mechanical properties of cellular aluminium based on micro-computed tomography. *Materials Science and Engineering A*, 528(13-14):4550 – 4555, 2011.

[69] N. Michailidis, F. Stergioudi, H. Omar, and D.N. Tsipas. An image-based reconstruction of the 3d geometry of an al open-cell foam and fem modeling of the material response. *Mechanics of Materials*, 42(2):142 – 7, 2010/02/.

[70] N. Michailidis. Strain rate dependent compression response of Ni-foam investigated by experimental and fem simulation methods. *Materials Science and Engineering A*, 528(12):4204 – 4208, 2011.

[71] A. Tasdemirci, C. Ergonenc, and M. Guden. Split Hopkinson pressure bar multiple reloading and modeling of a 316 l stainless steel metallic hollow sphere structure. *International Journal of Impact Engineering*, 37(3):250 – 9, 2010/03/.

[72] R. Lakes, P. Rosakis, and A. Ruina. Microbuckling instability in elastomeric cellular solids. *Journal of Materials Science*, 28:4667–4672, 1993.

[73] J.G.F. Wismans, L.E. Govaert, and J.A.W. Van Dommelen. X-ray computed tomography-based modeling of polymeric foams: The effect of finite element model size on the large strain response. *Journal of Polymer Science, Part B: Polymer Physics*, 48(13):1526 – 1534, 2010.

[74] X.H. Zhu, J.F. Knott, and N.J. Mills. Analysis of the elastic properties of open-cell foams with tetrakaidecahedral cells. *J. Mech. Phys. Solids*, 45(3):319–343, 1997.

[75] X.H. Zhu, N.J. Mills, and J.F. Knott. Analysis of the high strain compression of open-cell foams. *J. Mech. Phys. Solids*, 45(11–12):1875–1904, 1997.

[76] X.H. Zhu and N.J. Mills. Modelling the creep of open–cell polymer foams. *J. Mech. Phys. Solids*, 47:1437–1457, 1999.

[77] N.J. Mills. Finite element models for the viscoelasticity of open–cell polyurethane foam. *Cellular Polymers*, 25(5):293 – 316, 2006.

[78] C.P. Salisbury. Spectral analysis of wave propagation through a polymeric Hopkinson bar. Master's thesis, University of Waterloo, 2004.

[79] Bacon C. and Brun A. Methodology for a Hopkinson test with a non–uniform viscoelastic bar. *International Journal of Impact Engineering*, 24:219–230, 2000.

[80] Bacon C. An experimental method for considering dispersion and attenuation in a viscoelastic Hopkinson bar. *Experimental Mechanics*, 38:242–249, 1998.

[81] C.P. Salisbury and D.S. Cronin. Mechanical properties of ballistic gelatin at high deformation rates. *Experimental Mechanics*, 49(6):829–840, 2009.

[82] D.A. Doman, D.S. Cronin, and C.P. Salisbury. Characterization of polyurethane rubber at high deformation rates. *Experimental Mechanics*, pages 367–376, 2006.

[83] H. Kolsky H. A investigation of the mechanical properties of materials at high rates of loading. *Proceedings of the Physical Society-Section B*, 62:676–700, 1949.

[84] E.D.H. Davies and S.C. Hunter. The dynamic compression testing of solids by the method of the split Hopkinson pressure bar. *Journal of the Mechanics Physics Solids*, 11:155–179, 1963.

[85] N.N. Dioh, P.S. Leevers, and J.G. Williams. Thickness effects in split Hopkinson pressure bar tests. *Polymer*, 34:4230–4234, 1993.

[86] N.N. Dioh, A. Ivankovic, P.S. Leevers, and J.G. Williams. High strain rate behaviour of polymers. *Journal de Physique IV*, 4, C8:119–124, 1994.

[87] N.N. Dioh, A. Ivankovic, P.S. Leevers, and J.G. Williams. Stress wave propagation effects in split Hopkinson pressure bar tests. *Proc. Roy. Soc. of London-A-Mathematical and Physical Sciences*, 449:187–204, 1995.

[88] Y.C. Fung. *Fundamentals of Solid Mechanics*. Prentice–Hall, Englewood Cliffs, N.J., 1965.

[89] R.S. Rivlin. Large elastic deformations of isotropic materials. *Philosophical Transactions of the Royal Society of London. Series A*, 240(822):459–490, 1948.

[90] R.S. Rivlin and D.W. Saunders. Large elastic deformations of isotropic materials. vii. experiments on the deformation of rubber. *Philosophical Transactions of the Royal Society of London. Series A (Mathematical and Physical Sciences)*, 243(865):251 – 288, 1951.

[91] R.S. Rivlin. Some topics in finite elasticity. In *First Symposium on Naval Structural Mechanics*, pages 169–199, 1960.

[92] R.W. Ogden. Large deformation isotropic elasticity–on the correlation of theory and experiment for incompressible rubberlike solids. *Proceedings of the Royal Society of London Series A*, 326:565–584, 1972.

[93] A. Hoger and D. Carlson. On the derivative of the square root of a tensor and Gou's rate theorems. *Journal of Elasticity*, 14:329–336, 1984.

[94] A. Hoger and D. Carlson. Determination of the stretch and rotation in the polar decomposition of the deformation gradient. *Quarterly of Applied Mathematics*, 42(1):113–117, 1984.

[95] J. Stickforth. The square root of a three-dimensional positive tensor. *Acta Mechanica*, 67:233–235, 1986.

[96] M.A. Crisfield. *Non–linear Finite Element Analysis of Solids and Structures V1 and V2*. John–Wiley and Sons, New York, 1991.

[97] L.E. Malvern. *Introduction to the Mechanics of a Continuous Media*. Prentice–Hall, Englewood Cliffs, N.J., 1969.

[98] J.C.Simo and T.J.R. Hughes. *Computational Inelasticity*. Springer–Verlag, New York, 1998.

[99] D. Mohan and J. Melvin. The generalized strain measure with application to nonhomogeneous deformation in rubber–like solids. *Journal of Applied Mechanics*, 53:726–728, 1986.

[100] W.M. Scherzinger and C.R. Dohrmann. A robust algorithm for find the eigenvalues and eigenvectors of 3x3 symmetric matrices. *Computer Methods in Applied Mechanics and Engineering*, 197:4007–4015, 2008.

[101] K.J. Bathe. *Finite Element Procedures*. Prentice–Hall, New Jersey, 1996.

[102] D.A. Doman. Modeling of the high rate behaviour of polyurethane rubber. Master's thesis, University of Waterloo, 2004.

[103] M.A. Puso and J.A. Weiss. Finite element implementation of anisotropic quasi-linear viscoelasticity using a discrete spectrum approximation. *Transactions of the ASME*, 120:62–79, 1998.

[104] R.M. Christensen. A nonlinear theory of viscoelasticity of application to elastomers. *Journal of Applied Mechanics*, 47:762–768, 1980.

[105] Dassault Systemes. *ABAQUS Theory manual Version 6.8*. Dassault Systemes, Providence, RI, 2008.

[106] L.M. Yang, V.P.W. Shim, and C.T Lim. A visco-hyperelastic approach to modelling the constitutive behavior of rubber. *International Journal of Impact Engineering*, 24:545–560, 2000.

[107] L. Wilkinson. *SYSTAT: The System for Statistics*. SYSTAT, Inc., Illinois, 1990.

[108] T. Chen. Determining a prony series for a viscoelastic material from time varying strain data. Technical report, NASA, 2000.

[109] MathWorks. *Matlab R2009b*. MathWorks Inc., Massachusetts, 2009.

[110] J.C.F Millett and N.K. Bourne. Shock response of the elastomer, polycholorprene. *Journal of Applied Physics*, 85(1):2576–2579, 2001.

[111] N.K. Bourne and J.C.F. Millett. The high–rate response of and elastomer. *Proc. R. Soc. London A*, 459:567–576, 2003.

[112] T. Belytschko, W.K. Liu, and B. Moran. *Nonlinear Finite Elements for Continua and Structures*. John Wiley and Sons Ltd., West Sussex, England, 2000.

[113] Y.C. Fung. *A First Course in Continuum Mechanics*. Prentice–Hall, Englewood Cliffs, N.J., 1969.

[114] R. Brannon. *Introduction to Continuum Mechanics; Kinematics:The Mathematics of Deformation*. University of New Mexico, Albuquerque, New Mexico, 2003.

[115] T. J.R. Hughes. *The Finite Element Method; Linear Static and Dynamic Finite Element Analysis*. Prentice–Hall Inc., Englewood Cliffs, NJ, 1987.

[116] P. Moin. *Fundamentals of Engineering Numerical Analysis*. Cambridge University Press, Cambridge, 2001.

[117] D.J. Benson. Computational methods in lagrangian and eulerian hydrocodes. *Computer Methods in Applied Mechanics and Engineering*, 99:235–394, 1992.

Appendix A

Governing Equations

A.1 Preliminaries

As a starting point, the initial domain of the body is defined as Ω_0 with boundary Γ_0. The initial domain can also be thought of as a reference configuration to which various equations refer. The current (deformed) domain of the body is given as Ω with boundary Γ. In one–dimensional space, Ω refers to a line, in two–dimensional space it refers to a surface and in three dimensions a volume. Similarly, Γ refers to two end points in one dimension, a line in two dimensions and a surface in three–dimensional space. These definitions are outlined graphically in Figure A.1.

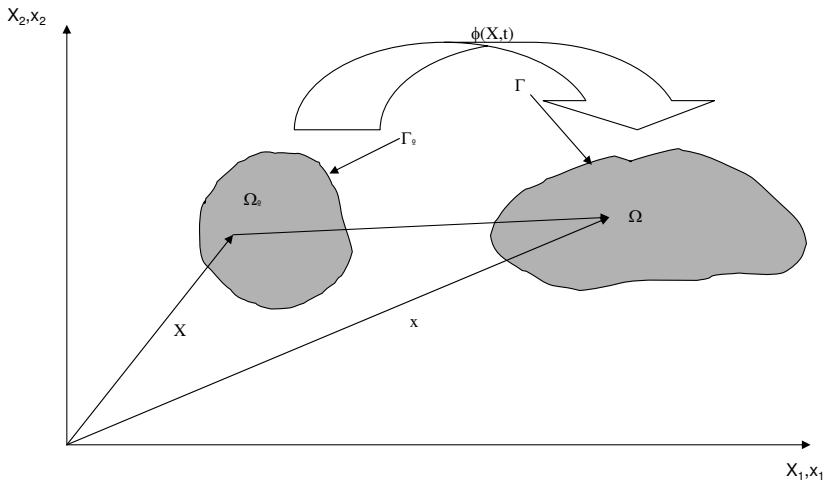

Figure A.1: Definition of domain in the deformed and reference configuration, modified from [112].

A.1.1 Notation

Following are notation of some terms that will be used throughout the text.

Summation Convention

- A dummy index occurs *exactly* twice in a term and implies summation from 1 to 3 for that term only.
- A free index occurs *exactly* once in every term.

Examples

- $\mathbf{C} = \mathbf{a} \cdot \mathbf{b} = a_i b_j = C_{ij}$; a second order tensor.
- $\mathbf{C} = \mathbf{A} \cdot \mathbf{B} = a_{ik} b_{kj} = C_{ij}$; a second order tensor.
- $c = \mathbf{a} : \mathbf{b} = a_i b_i = \sum_{i=1}^{3} a_i b_i$; a scalar.
- $c = \mathbf{A} : \mathbf{B} = A_{ij} B_{ij} = \sum_{j=1}^{3} \sum_{i=1}^{3} A_{ij} B_{ij}$; a scalar.

Define the Kronecker delta as

$$\delta_{ij} = \begin{cases} 1 & i = j \\ 0 & i \neq j \end{cases}$$

which equals

$$\delta_{ij} = \mathbf{I} = \begin{bmatrix} 1 & 0 & 0 \\ 0 & 1 & 0 \\ 0 & 0 & 1 \end{bmatrix}$$

where $\mathbf{I}$ is the identity matrix.

Following are two theorems that will be used to aid in the derivation of the conservation equations given in Section A.2. Proof of these theorems can be found in many continuum books such as Fung [113], Malvern [97] and in the review given by Belytschko [112].

A.1.2 Gauss' Theorem

Gauss' theorem intuitive can be though of as a way of relating the total volume of all sinks and sources in a body to the net flow across the volume's boundaries. Mathematically, Gauss' theorem can be expressed as,

$$\int_{\Omega} \frac{\partial f(\mathbf{x})}{\partial x_i} d\Omega = \int_{\Gamma} n_i f(\mathbf{x}) d\Gamma \tag{A.1.1}$$

where $f(\mathbf{x})$ is a piecewise continuously differentiable (C^0) function and n_i is the outer normal to the surface. This theorem applies for a tensor of any order. This is often called the divergence theorem (among many other names) as the first integrand on the LHS is the divergence of a vector function with respect to the spatial coordinates (i.e. $\frac{\partial f(\mathbf{x})}{\partial x_i} = \operatorname{div} f = \nabla \cdot f$). Mathematically this theorem is used to transform a surface integral to a volume integral and vise versa.

A.1.3 Spatial Description of the Motion of a Continuum A.K.A. The Material Derivative

The material derivative, denoted by the symbol D/Dt, is the rate of change of some property in a fixed reference frame. Mathematically, it is expressed as

$$\frac{DA}{Dt} = \frac{\partial A}{\partial t} + v_i \cdot \frac{\partial A}{\partial x_i} \tag{A.1.2}$$

where A is a tensor of any order and v_i is the material velocity. Intuitively, equation A.1.2 indicates that the time rate of change of property A as it flows through a continuum is equal to the change of A with time at a fixed point plus the net flux of A past the fixed point.

Consider the situations shown in Figure A.2. In the first situation, Figure A.2a), the flow is steady and uniform. Observing the velocity the fluid from the fixed viewpoints at A, B and C one would see that

$$\frac{\partial v_A}{\partial t} = \frac{\partial v_B}{\partial t} = \frac{\partial v_C}{\partial t} = 0$$

where the subscript on v refers to the velocity at the particular location. Since the flow is steady, its change with respect to time at a fixed point is zero everywhere. Furthermore, since the flow is uniform,

$$\frac{\partial v}{\partial x} = 0$$

since the flow velocity is not changing in space. Therefore, the material derivative is zero, i.e. $Dv/Dt = 0$.

In the second situation, Figure A.2b), the flow is unsteady but uniform. This indicates that the velocity of the fluid changes with time, i.e. $v = f(t)$. Therefore at points A, B and C,

$$\frac{\partial v}{\partial t} \neq 0$$

but flow is still uniform so $\partial v/\partial x = 0$. Therefore, the material derivative is $Dv/Dt = \partial v/\partial t$.

In the third situation, Figure A.2c), the flow is steady but not uniform. This indicates that the velocity of the fluid does not changes with time. Therefore at points A, B and

C,

$$\frac{\partial v}{\partial t} = 0$$

However, the fluid velocity does change with space. i.e. the fluid velocity at point A differs from B which differs from C. Therefore the material derivative is $Dv/Dt = v_i(\partial v/\partial x) \neq 0$. This gives the change in the velocity the fluid at a fixed point considering the convective change of the velocity of the fluid as it moves through space.

The fourth situation, Figure A.2d), is a combination of the previous two situations.

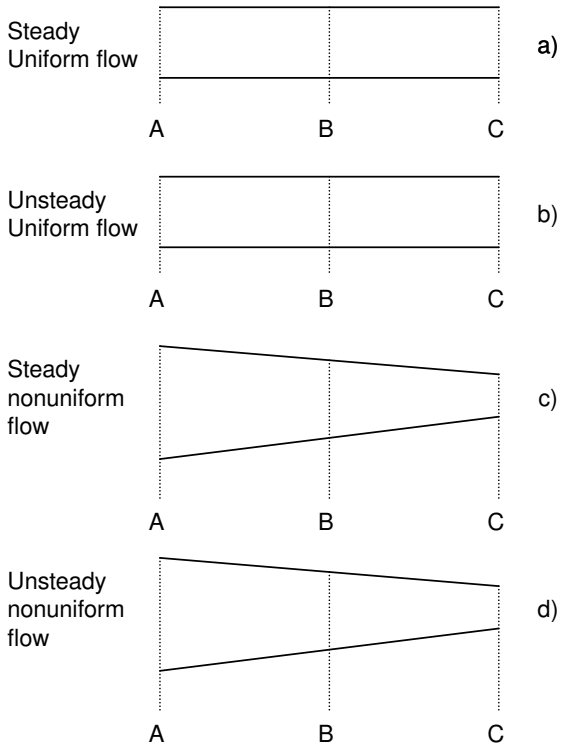

Figure A.2: Four situations that outline the need for the material derivative

A.1.4 Material Time Derivative of the Volume Integral

The time rate of change of a property over a volume is important for expressing the conservation equations. If a surface which defines the volume is fixed in space (an three dimensional Eulerian perspective) then the relatively simple relation

$$\frac{\partial}{\partial t}\int_{\Omega} A d\Omega = \int_{\Omega} \frac{\partial A}{\partial t} d\Omega \tag{A.1.3}$$

applies where A is a material property. If however, we wish to determine the time rate of change of A over a material domain which moves with the material (a Lagrangian perspective) then the rate of increase of A inside the control surface is equal to the time rate of change of A inside the control surface minus the net outward flux of A through the control surface. Mathematically, this is expressed as

$$\int_\Omega \frac{\partial A}{\partial t} d\Omega = \frac{D}{Dt}\int_\Omega A d\Omega - \int_\Gamma A\mathbf{v}\cdot\hat{\mathbf{n}} d\Gamma \tag{A.1.4}$$

where A is a continuous function which can be a tensor of any order. Solving Equation A.1.4 for D/Dt gives,

$$\frac{D}{Dt}\int_\Omega A d\Omega = \int_\Omega \frac{\partial A}{\partial t} d\Omega + \int_\Gamma A\mathbf{v}\cdot\hat{\mathbf{n}} d\Gamma \tag{A.1.5}$$

which is one (of many) forms of the Reynolds transport theorem. The second integral on the RHS can be converted to a volume integral using Gauss' theorem to give, in a rectangular Cartesian coordinate system ($\mathbf{v}\cdot\hat{\mathbf{n}} = v_j n_j$),

$$\frac{D}{Dt}\int_\Omega A d\Omega = \int_\Omega \left[\frac{\partial A}{\partial t} + \frac{\partial (Av_j)}{\partial x_j}\right] d\Omega \tag{A.1.6}$$

Expanding second integrand on the RHS using the product rule results in

$$\frac{D}{Dt}\int_\Omega A d\Omega = \int_\Omega \left[\frac{\partial A}{\partial t} + v_j\frac{\partial A}{\partial x_j} + A\frac{\partial v_j}{\partial x_j}\right] d\Omega \tag{A.1.7}$$

Recognizing that the first and second integrand on the RHS is just the material derivative of A, Equation A.1.7 can be written as

$$\begin{aligned}\frac{D}{Dt}\int_\Omega A d\Omega &= \int_\Omega \left[\frac{DA}{Dt} + A\frac{\partial v_j}{\partial x_j}\right] d\Omega \\ &= \int_\Omega \left[\frac{DA}{Dt} + A\,\mathrm{div}(v)\right] d\Omega\end{aligned} \tag{A.1.8}$$

If the function A is a product of density and another function f, then a special form of Reynold's transport theorem ensues (sometime referred to as Reynold's theorem for a density–weighted integrand).

So if $A = \rho f$ then Equation A.1.7 becomes

$$\frac{D}{Dt}\int_\Omega (\rho f) d\Omega = \int_\Omega \left[\frac{\partial (\rho f)}{\partial t} + v_j\frac{\partial (\rho f)}{\partial x_j} + (\rho f)\frac{\partial v_j}{\partial x_j}\right] d\Omega$$

expanding the derivative of ρf using the product rule gives

$$= \int_\Omega \left[\rho \frac{\partial f}{\partial t} + f \frac{\partial \rho}{\partial t} + v_j \rho \frac{\partial f}{\partial x_j} + v_j f \frac{\partial \rho}{\partial x_j} + \rho f \frac{\partial v_j}{\partial x_j} \right] d\Omega$$

and regrouping gives

$$= \int_\Omega \left[\rho \left(\frac{\partial f}{\partial t} + v_j \frac{\partial f}{\partial x_j} \right) + f \left(\frac{\partial \rho}{\partial t} + v_j \frac{\partial \rho}{\partial x_j} + \rho \frac{\partial v_j}{\partial x_j} \right) \right] d\Omega$$

recognizing that the last two terms is just the product rule of differentiation expanded gives

$$= \int_\Omega \left[\rho \left(\frac{\partial f}{\partial t} + v_j \frac{\partial f}{\partial x_j} \right) + f \left(\frac{\partial \rho}{\partial t} + \frac{\partial \rho v_j}{\partial x_j} \right) \right] d\Omega$$

the two terms inside the first parentheses is the product of the material derivative and density so

$$= \int_\Omega \left[\rho \frac{Df}{Dt} + f \left(\frac{\partial \rho}{\partial t} + \frac{\partial \rho v_j}{\partial x_j} \right) \right] d\Omega$$

It will be shown in Section A.2.1 that the terms in the last parentheses is zero through the conservation of mass, Equation A.2.10. Therefore, the above results in the relation

$$\frac{D}{Dt} \int_\Omega (\rho f) d\Omega = \int_\Omega \rho \frac{Df}{Dt} d\Omega \tag{A.1.9}$$

A.1.5 Deformation and the Deformation Gradient

A key measure of deformation in finite element analysis is given by the deformation gradient. To first understand the purpose and meaning of the deformation gradient you have to understand the reference frames under which deformation is being analysed. In finite elements, two reference frames, a Lagrangian frame (denoted by $\mathbf{X}$) which moves with the material, and an Eulerian frame (denote by $\mathbf{x}$) which remains static during deformation, are commonly used. The coordinates of a particle of the continuum in the initial, or Lagrangian, coordinate frame can be related to the current, or Eulerian, reference frame through a mapping function. In general terms, the mapping function is given by:

$$\mathbf{x} = \phi\{\mathbf{X}, t\} \tag{A.1.10}$$

where the mapping function ϕ is a function of X and t.

As outlined by Brannon [114], the deformation gradient is then defined such that an

infinitesimal line segment $d\mathbf{X}$ deforms into a new infinitesimal line segment $d\mathbf{x}$ so that

$$\begin{aligned} d\mathbf{x} &= \mathbf{F} \cdot d\mathbf{X} \\ &= d\mathbf{X} \cdot \mathbf{F}^T \end{aligned} \tag{A.1.11}$$

or,

$$\mathbf{F} = \frac{d\mathbf{x}}{d\mathbf{X}} \quad F_{ij} = \frac{\partial x_i}{\partial X_j} \tag{A.1.12}$$

The Jacobian of the deformation gradient is the ratio of the undeformed to deformed volume. This is expressed mathematically as,

$$J \equiv \frac{V}{V_0} = \det F_{ij} \tag{A.1.13}$$

For realistic volume changes, both the deformed and undeformed volumes must be positive indicating that

$$J > 0 \tag{A.1.14}$$

Integrals in the current and reference configurations can be related using the Jacobian determinant by

$$\int_{\Omega} f d\Omega = \int_{\Omega_0} f J d\Omega_0 \tag{A.1.15}$$

Polar Decomposition Theorem The deformation gradient can be further broken into a combination of pure rotation, $\mathbf{R}$, and pure stretch. Two stretch tensors exist in the literature as $\mathbf{U}$ for the right stretch tensor and $\mathbf{V}$ for the left stretch tensor corresponding to which is performed first, stretch and then rotation or rotation and then stretch respectively. Expressed mathematically, the polar decomposition theorem states

$$\mathbf{F} = \mathbf{R} \cdot \mathbf{U} = \mathbf{V} \cdot \mathbf{R} \tag{A.1.16}$$

Since the order of stretching and rotating matters, it can be stated that $\mathbf{U} \neq \mathbf{V}$. Some key polar decomposition formulas are as follows [114]:

$$\begin{array}{cc} \mathbf{U} = \left(\mathbf{F}^T \cdot \mathbf{F}\right)^{1/2} & \mathbf{V} = \left(\mathbf{F} \cdot \mathbf{F}^T\right)^{1/2} = \mathbf{R} \cdot \mathbf{U} \cdot \mathbf{R}^T \\ \mathbf{R} = \mathbf{F} \cdot \mathbf{U}^{-1} & \mathbf{R} = \mathbf{V}^{-1} \cdot \mathbf{F} \end{array} \tag{A.1.17}$$

Examples

Two examples will be used to illustrate the functionality of the deformation gradient.

Example 1–Uniaxial and Associated Deformation Consider uniaxial and associated deformation along a principle direction as shown in Figure A.3.

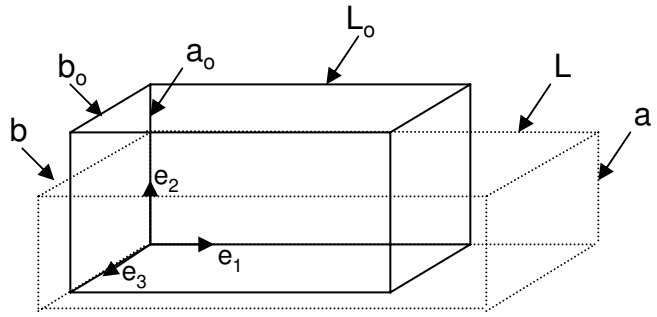

Figure A.3: Undeform (solid lines) and deformed (dotted lines) of a material under unaxial tension.

If we define $\mathbf{e_i}$ to be orthonormal unit vectors in space (in essence lab coordinates) then the initial location of each particle can be given by:

$$\mathbf{X} = X_1\mathbf{e_1} + X_2\mathbf{e_2} + X_3\mathbf{e_3} \tag{A.1.18}$$

and in the deformed configuration:

$$\mathbf{x} = x_1\mathbf{e_1} + x_2\mathbf{e_2} + x_3\mathbf{e_3} \tag{A.1.19}$$

For uniaxial strain, the mapping function is given as,

$$\begin{aligned} x_1 &= f(X_1) \\ x_2 &= f(X_2) \\ x_3 &= f(X_3) \end{aligned} \tag{A.1.20}$$

The deformation imposed in the $\mathbf{e_1}$ direction could be considered a consequence of an applied force. The deformation in the other two directions could then be considered a consequence of the material response. The deformation gradient as given by equation A.1.12 is given by,

$$F_{ij} = \frac{\partial x_i}{\partial X_j} = \begin{bmatrix} \lambda_1 & 0 & 0 \\ 0 & \lambda_2 & 0 \\ 0 & 0 & \lambda_3 \end{bmatrix} \tag{A.1.21}$$

where λ_i is the "stretch" along each principal direction. If the stretch is constant then

$$x_1 = \frac{L}{L_0}X_1,\ x_2 = \frac{a}{a_0}X_2,\ x_3 = \frac{b}{b_0}X_3 \tag{A.1.22}$$

The above equation is, in essence, the mapping function between the initial and current positions. Therefore, the stretches are given by

$$\lambda_1 = \frac{L}{L_0},\ \lambda_2 = \frac{a}{a_0},\ \lambda_3 = \frac{b}{b_0} \tag{A.1.23}$$

Intuitively, from Figure A.3 it is evident that the initial volume is $V_0 = a_0 b_0 L_0$ and the deformed volume is $V = abL$. Mathematically, this is determined through the Jacobian determinant, Equation A.1.13, as,

$$J = \det \mathbf{F} = \frac{abL}{a_0 b_0 L_0} \tag{A.1.24}$$

which corresponds to the ratio of initial to deformed volumes.

Interestingly, a physical interpretation of the deformation gradient can be found through examination of the k^{th} column. Each column is related to an edge vector, $\mathbf{g_k}$, of the deformed unit body. This outlined in Figure A.4 below.

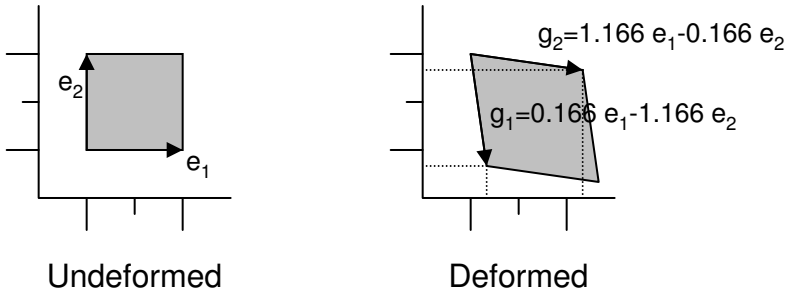

Figure A.4: Deformed and undeformed units with corresponding edge vectors[114].

The body, initially of unit length, has edge vectors that correspond to the lab space of e_i $i = 1, 2, 3$. After deformation, the edge vectors can be determined visually. This indicates that if

$$g_1 = \left\{ \begin{array}{c} 0.166 \\ -1.166 \\ 0 \end{array} \right\},\ g_2 = \left\{ \begin{array}{c} 1.166 \\ -0.166 \\ 0 \end{array} \right\} \tag{A.1.25}$$

then

$$F_{ij} = \begin{bmatrix} 0.166 & 1.166 & 0 \\ -1.166 & -0.166 & 0 \\ 0 & 0 & 1 \end{bmatrix} \tag{A.1.26}$$

Example Two–Large Rotation An example of the deformation gradient for large rotations is given by Brannon [114]. Figure A.5 shows a bar, initially of height H, bending into a curved shape wedge segment until the top surface is oriented at an angle θ_{max}. The geometry can be described by using the radius, R, of the centreline and the stretch of the centreline given by λ^c. From the definition of stretch the following relation holds,

$$R\theta_{max} = \lambda^c H \tag{A.1.27}$$

In this example, the mapping function, deformation gradient, and the polar rotation and right stretch tensor are desired. Note that in the figure, the ˜ symbol below any notation indicates a first order tensor (vector).

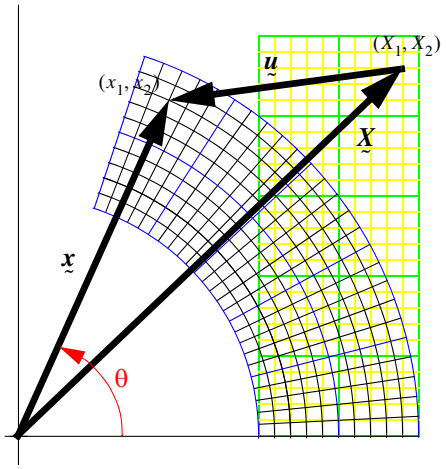

Figure A.5: Large rotation of a bar along a constant radius.[114]

As before, let $\mathbf{e_i}$ be orthonormal unit vectors in space. The initial location of each particle can be given by:

$$\mathbf{X} = X_1\mathbf{e_1} + X_2\mathbf{e_2} + X_3\mathbf{e_3} \tag{A.1.28}$$

and in the deformed configuration:

$$\mathbf{x} = x_1\mathbf{e_1} + x_2\mathbf{e_2} + x_3\mathbf{e_3} \tag{A.1.29}$$

Each initial vertical line bends into an arc of radius X_1 with an arc length of θX_1. As

the arc angle increases proportionally to X_2 the following relation must hold,

$$\theta = \alpha X_2 \tag{A.1.30}$$

The arc length of a point originally at (X_1, X_2) is given by,

$$s = \alpha X_1 X_2 \tag{A.1.31}$$

so along the centreline,

$$\begin{aligned} &R\theta_{max} = \alpha RH \\ &\text{so} \\ &\alpha = \frac{\theta_{max}}{H} = \frac{\lambda^c}{R} \end{aligned} \tag{A.1.32}$$

which in combination with A.1.30 results in

$$\theta = \frac{X_2}{H}\theta_{max} \tag{A.1.33}$$

Now consider a point (X_1, X_2) that is not necessarily on the centreline. After deformation, the point is located at a distance $r = X_1$ from the origin at a point (x_1, x_2). This indicates that

$$\begin{aligned} x_1 &= r\cos(\theta) = X_1 \cos\left(\frac{X_2}{H}\theta_{max}\right) \\ x_2 &= r\sin(\theta) = X_1 \sin\left(\frac{X_2}{H}\theta_{max}\right) \end{aligned} \tag{A.1.34}$$

This is the mapping function $x_i = \phi(X_i)$.

The deformation gradient components are then given as

$$F_{ij} = \begin{bmatrix} \cos\left(\frac{X_2}{H}\theta_{max}\right) & -\lambda^c \frac{X_1}{R}\sin\left(\frac{X_2}{H}\theta_{max}\right) \\ \sin\left(\frac{X_2}{H}\theta_{max}\right) & \lambda^c \frac{X_1}{R}\cos\left(\frac{X_2}{H}\theta_{max}\right) \end{bmatrix} \text{for} \quad i = 1, 2 \tag{A.1.35}$$

For convenience define,

$$\begin{aligned} A &\equiv \frac{X_1\theta_{max}}{H} \equiv \frac{\lambda^c X_1}{R} \\ c &\equiv \cos\left(\frac{X_2}{H}\theta_{max}\right) \equiv \cos\left(\frac{X_2\lambda^c}{R}\right) \\ s &\equiv \sin\left(\frac{X_2}{H}\theta_{max}\right) \equiv \sin\left(\frac{X_2\lambda^c}{R}\right) \end{aligned} \tag{A.1.36}$$

so the deformation gradient can be written as,

$$F_{ij} = \begin{bmatrix} c & -As \\ s & Ac \end{bmatrix} \text{ for } \quad i = 1, 2 \tag{A.1.37}$$

The Jacobian is then computed as,

$$J = \det\left(F_{ij}\right) = A \tag{A.1.38}$$

Polar decomposition of the deformation gradient $F_{ij} = R_{ik}U_{kj}$ give,

$$\begin{aligned} R_{ik} &= \begin{bmatrix} c & -s \\ s & c \end{bmatrix} \\ U_{kj} &= \begin{bmatrix} 1 & 0 \\ 0 & A \end{bmatrix} \end{aligned} \tag{A.1.39}$$

This indicates that first a stretch of A in the e_2 direction is applied and then a rotation.

A.1.6 Velocity Gradient

Similar to the way in which the deformation gradient was defined as $F_{ij} = \partial x_i / \partial X_j$ the velocity gradient is defined as

$$L_{ij} \equiv \frac{\partial v_i}{\partial x_j} \tag{A.1.40}$$

The velocity gradient can be decomposed into a symmetric and skew–symmetric parts through

$$\mathbf{L} = \underbrace{\frac{1}{2}\left(L_{ij} + L_{ji}\right)}_{\text{Symmetric}} + \underbrace{\frac{1}{2}\left(L_{ij} - L_{ji}\right)}_{\text{skew–symmetric}} \tag{A.1.41}$$

so

$$L_{ij} = v_{i,j} = D_{ij} + W_{ij} \tag{A.1.42}$$

where

$$\begin{aligned} D_{ij} &= \frac{1}{2}\left(L_{ij} + L_{ji}\right) = \frac{1}{2}\left(\mathbf{L} + \mathbf{L}^T\right) \\ W_{ij} &= \frac{1}{2}\left(L_{ij} - L_{ji}\right) = \frac{1}{2}\left(\mathbf{L} - \mathbf{L}^T\right) \end{aligned} \tag{A.1.43}$$

and

$$\begin{aligned} D_{ij} &= D_{ji} \\ W_{ij} &= -W_{ji} \end{aligned} \tag{A.1.44}$$

The symmetric part of $\mathbf{L}$, denoted $\mathbf{D}$, is the rate–of–deformation where as the skew–symmetric part, $\mathbf{W}$, is referred to as the spin tensor. Only in the absence of deformation does the spin equal angular velocity.

It is useful to find a relation between the velocity and deformation gradients. If

$$\mathbf{L} = \frac{\partial \mathbf{v}}{\partial \mathbf{x}}$$

expanding using the chain rule

$$= \frac{\partial \mathbf{v}}{\partial \mathbf{X}} \frac{\partial \mathbf{X}}{\partial \mathbf{x}} \tag{A.1.45}$$

If, by definition

$$\dot{\mathbf{F}} = \frac{\partial \mathbf{v}}{\partial \mathbf{X}} \tag{A.1.46}$$

and expanding $\partial x_i / \partial x_j = \delta_{ij}$

$$\begin{aligned} \frac{\partial x_i}{\partial X_k} \frac{\partial X_k}{\partial x_j} &= \delta_{ij} \\ F_{ik} \frac{\partial X_k}{\partial x_j} &= \delta_{ij} \\ \frac{\partial X_k}{\partial x_j} &= F^{-1}_{kj} \delta_{ij} \end{aligned} \tag{A.1.47}$$

Using the above two relations, Equation A.1.45 becomes

$$\mathbf{L} = \dot{\mathbf{F}} \cdot \mathbf{F}^{-1} \tag{A.1.48}$$

A.1.7 Strain and Strain Rate

Strain Although several measures of strain exist, only Green strain common will be presented here. Green strain $\mathbf{E}$, also known as Lagrange Strain, refers the deformation in regards to the reference coordinates. It is defined so that it results in the change of the square of the material vector $d\mathbf{X}$ length. For rectangular Cartesian coordinates, the Green strain tensor is

$$(ds)^2 - (dS)^2 = 2d\mathbf{X} \cdot \mathbf{E} \cdot d\mathbf{X} \tag{A.1.49}$$

where ds is the current length and dS is the reference length of an infinitesimal line segment. Then

$$(ds)^2 = d\mathbf{x} \cdot d\mathbf{x}$$

which from Equation A.1.11

$$\begin{aligned} &= \left(d\mathbf{X} \cdot \mathbf{F}^T\right) \cdot (\mathbf{F} \cdot d\mathbf{X}) \\ &= d\mathbf{X} \cdot \left(\mathbf{F}^T \cdot \mathbf{F}\right) \cdot d\mathbf{X} \end{aligned} \tag{A.1.50}$$

Similarly,

$$\begin{aligned} (dS)^2 &= d\mathbf{X} \cdot d\mathbf{X} \\ &= d\mathbf{X} \cdot \mathbf{I} \cdot d\mathbf{X} \end{aligned} \tag{A.1.51}$$

where $\mathbf{I}$ is the identity tensor. Using Equations A.1.50 and A.1.51 in Equation A.1.49 gives,

$$\begin{aligned} d\mathbf{X} \cdot \left(\mathbf{F}^T \cdot \mathbf{F}\right) \cdot d\mathbf{X} - d\mathbf{X} \cdot \mathbf{I} \cdot d\mathbf{X} - 2d\mathbf{X} \cdot \mathbf{E} \cdot d\mathbf{X} &= 0 \\ d\mathbf{X} \cdot \left(\mathbf{F}^T \cdot \mathbf{F} - \mathbf{I} - 2\mathbf{E}\right) \cdot d\mathbf{X} &= 0 \end{aligned} \tag{A.1.52}$$

which indicates that

$$\mathbf{E} = \frac{1}{2}\left(\mathbf{F}^T \cdot \mathbf{F} - \mathbf{I}\right) \tag{A.1.53}$$

Relating Equation A.1.53 in terms of displacement gradients gives

$$E_{ij} \equiv \frac{1}{2}\left[\frac{\partial u_i}{\partial X_j} + \frac{\partial u_j}{\partial X_i} + \frac{\partial u_k}{\partial X_i}\frac{\partial u_k}{\partial X_j}\right] \tag{A.1.54}$$

Referring back to Example 1, and using Equation A.1.53, the Green strain can be solved for as

$$\begin{aligned} E_{11} &= \frac{1}{2}\left(F_{11}^T F_{11} + F_{12}^T F_{21} + F_{13}^T F_{31} - 1\right) \\ &= \left(\frac{l^2}{l_o^2} - 1\right) \\ &= \left(\frac{l^2 - l_o^2}{2l_o^2}\right) \end{aligned}$$

Similarly,

$$E_{22} = \left(\frac{a^2 - a_o^2}{2a_o^2}\right), \quad E_{33} = \left(\frac{b^2 - b_o^2}{2b_o^2}\right)$$

Strain Rate The rate of Green strain can be obtained by taking the material derivative of Equation A.1.53 which gives,

$$\dot{\mathbf{E}} = \frac{1}{2}\frac{D}{Dt}\left(\mathbf{F}^T \cdot \mathbf{F} - \mathbf{I}\right) = \frac{1}{2}\left(\mathbf{F}^T \cdot \dot{\mathbf{F}} + \dot{\mathbf{F}^T} \cdot \mathbf{F}\right) \tag{A.1.55}$$

From equation Equation A.1.48 and A.1.43, $\mathbf{D}$ can be expressed as

$$\mathbf{D} = \frac{1}{2}\left(\dot{\mathbf{F}} \cdot \mathbf{F}^{-1} + \left(\mathbf{F}^{-1}\right)^T \cdot \dot{\mathbf{F}^T}\right) \tag{A.1.56}$$

Premultiplying and postmultiplying Equation A.1.56 by $\mathbf{F}^T$ and $\mathbf{F}$ respectively gives

$$\mathbf{F}^T \cdot \mathbf{D} \cdot \mathbf{F} = \frac{1}{2}\left(\mathbf{F}^T \cdot \dot{\mathbf{F}} + \dot{\mathbf{F}^T} \cdot \mathbf{F}^T\right) \tag{A.1.57}$$

Which, when compared to Equation A.1.55, indicates that

$$\dot{\mathbf{E}} = \mathbf{F}^T \cdot \mathbf{D} \cdot \mathbf{F} \tag{A.1.58}$$

A.1.8 Stress and Its Definition

Similar to strain, there are several definitions of stress. The stress measure that will be used most often in for this work is the Cauchy stress which uses the current, deformed, area instead of the reference area, which nominal and second Piola-Kirchhoff stress measures use. In essence, Cauchy stress is a measure of the true stress. The definition of Cauchy stress is illustrated in Figure A.6.

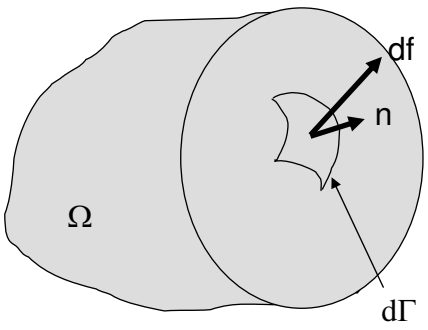

Figure A.6: Definition of stress in current configuration

A surface traction can be defined as the force, $d\mathbf{f}$ exerted upon an infinitesimal surface element $d\Gamma$. Expressed mathematically, this is,

$$\mathbf{T} = \frac{d\mathbf{f}}{d\Gamma} \tag{A.1.59}$$

and so the traction can be thought of as a stress vector with the same direction as $d\mathbf{f}$ and of magnitude of $d\mathbf{f}/d\Gamma$. Using the normal $\mathbf{n}$, the traction vector can be broken into

components through

$$\begin{aligned} \mathbf{T}d\Gamma &= \mathbf{n} \cdot \boldsymbol{\sigma} d\Gamma = \boldsymbol{\sigma}^T \cdot \mathbf{n} d\Gamma \\ T_i d\Gamma &= n_j \sigma_{ji} d\Gamma \end{aligned} \tag{A.1.60}$$

which is often called Cauchy's law or hypothesis. Conveniently, the trace of Cauchy stress gives pressure

$$\frac{1}{3}\operatorname{tr}(\boldsymbol{\sigma}) = \frac{1}{3}\sigma_{ii} = -p \tag{A.1.61}$$

The convention that normal components of Cauchy stress are positive in tension which results in a positive pressure in compression. The components of the Cauchy stress tensor are illustrated in Figure A.7. In σ_{ij} the stress component can be thought of as acting on

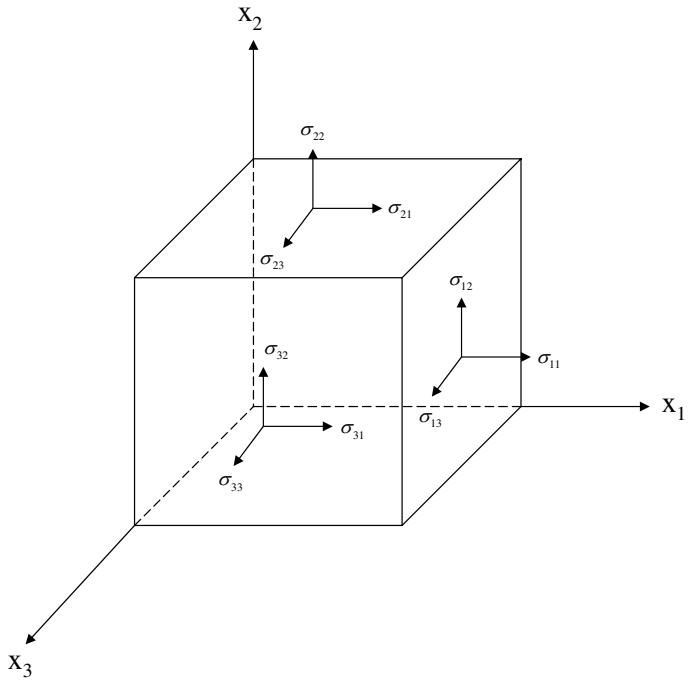

Figure A.7: Orientation of positive stress components

the surface normal to i in the j^{th} direction. The Cauchy stress tensor is symmetric. i.e. $\boldsymbol{\sigma} = \boldsymbol{\sigma}^T$.

A.2 Governing Equations

Three conservations equations plus two additional equations are used to solve for non-linear deformations in finite element codes. This set of governing equations is listed as:

1. Conservation of mass (continuity).
2. Conservation of energy.
3. Conservation of momentum.
4. A measure of deformation (often called the strain–displacement equation).
5. A constitutive equation based on the material behaviour which relates stress to deformation.

A.2.1 Conservation of Mass

If the mass of in a material domain is given by $m = \int_\Omega \rho(\mathbf{X}, t) d\Omega$ then using a Lagrangian description, mass conservation, in absence of mass to energy conversion, can be easily stated as,

$$\frac{Dm}{Dt} = \frac{D}{Dt} \int_\Omega \rho d\Omega = 0 \tag{A.2.1}$$

Integrating over time yields

$$\int_\Omega \rho d\Omega = \int_{\Omega_0} \rho d\Omega_0 \tag{A.2.2}$$

Through application of Equation A.1.15 the integral on the left hand can be converted to the reference domain resulting in

$$\int_{\Omega_0} \rho J - \rho_0 d\Omega_0 = 0 \tag{A.2.3}$$

This leads to

$$\rho J = \rho_0 \tag{A.2.4}$$

Intuitively, the above equations holds if

$$\rho_0 V_0 = \rho_c V_c \tag{A.2.5}$$

where the subscript 0 refers to the initial conditions and the subscript c refers to the current conditions. Then as the material undergoes deformation, the volume of the element and the density will change in proportion. The relative volume can then be defined as

the proportion between the initial and current volume expressed mathematically as:

$$V = \frac{V_c}{V_0} \tag{A.2.6}$$

which from Section A.1.5 is equivalent to the Jacobian determinant of the deformation tensor restated here as,

$$J \equiv \frac{V_c}{V_0} = \det F_{ij} \tag{A.2.7}$$

The conservation of mass can then be stated as,

$$\rho J = \rho_0 \tag{A.2.8}$$

which is equivalent to Equation A.2.4.

The continuity equation can be expressed in an Eulerian frame of reference by applying Reynolds transport theorem, Equation A.1.8, to Equation A.2.1 which gives

$$\int_\Omega \left[\frac{D\rho}{Dt} + \rho \operatorname{div}(\mathbf{v}) \right] d\Omega = 0$$

indicating

$$\frac{D\rho}{Dt} + \rho \operatorname{div}(\mathbf{v}) = 0 \tag{A.2.9}$$

If the material derivative is expanded out, an alternative form of Equation A.2.9 is achieved as

$$\frac{D\rho}{Dt} + \rho \operatorname{div}(\mathbf{v}) = \frac{d\rho}{dt} + v_i \frac{\partial \rho}{\partial x_i} + \rho \frac{\partial v_i}{\partial x_i}$$

recognizing that the last two terms a the consequence of the product rule for differentiation

$$= \frac{d\rho}{dt} + \frac{\partial(\rho v_i)}{\partial x_i}$$

and so

$$\frac{d\rho}{dt} + \frac{\partial(\rho v_i)}{\partial x_i} = 0 \tag{A.2.10}$$

A.2.2 Conservation of Momentum

Linear Momentum Consider a body of arbitrary domain Ω with boundary Γ subjected to a body force, $\mathbf{b}$ per unit mass, and surface tractions, $\mathbf{T}$ measured in force per unit area. Figure A.8 outlines these forces as applied to the domain. The net force

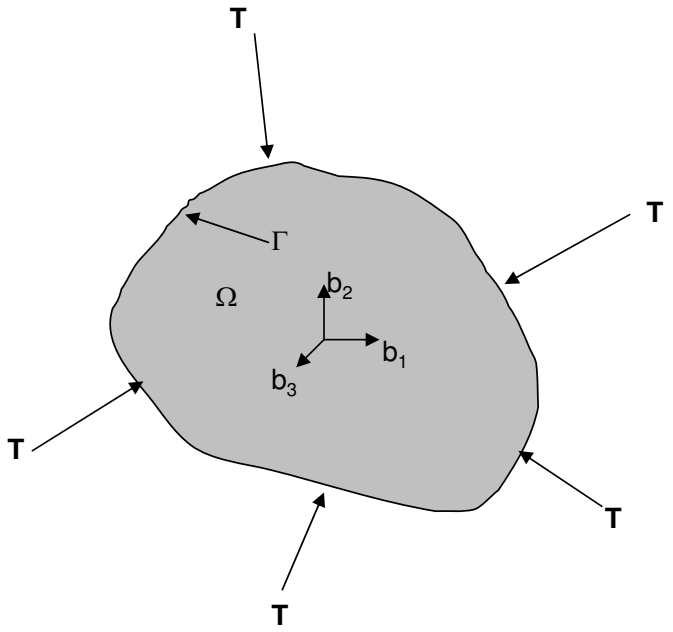

Figure A.8: An arbitrary body subjected to a body force and surface tractions

applied to the domain is then given by

$$\mathbf{f} = \underbrace{\int_{\Omega} \rho \mathbf{b}(\mathbf{x}, t) d\Omega}_{\text{Body Force}} + \underbrace{\int_{\Gamma} \mathbf{T}(\mathbf{x}, t) d\Gamma}_{\text{Traction}} \tag{A.2.11}$$

Linear momentum in the domain is given as the product of the mass of the domain and its velocity. i.e.

$$\mathbf{p}(t) = \int_{\Omega} \rho \mathbf{v}(\mathbf{x}, t) d\Omega \tag{A.2.12}$$

where $\mathbf{p}$ is the linear momentum and $\rho\mathbf{v}$ is the linear momentum per unit volume.

The conservation of linear momentum (Newton's second law) states that the sum of the forces on a particle, when not zero, is equal to the rate of change of linear momentum of the particle. If mass is constant, then the linear momentum is given by the product of the mass of the particle and its acceleration. Mathematically, this is stated as the

material time derivative of linear momentum equals the net force which is given by

$$\frac{D\mathbf{p}}{Dt} = \mathbf{f} \tag{A.2.13}$$

which, using Equations A.2.11 and A.2.12, becomes

$$\frac{D}{Dt}\int_\Omega \rho\mathbf{v}d\Omega = \int_\Omega \rho\mathbf{b}d\Omega + \int_\Gamma \mathbf{T}d\Gamma \tag{A.2.14}$$

Ideally, we would like to have a single domain integral to aid in the discretization of the equation. Applying Reynolds transport theorem, Equation A.1.8, to the LHS of Equation A.2.14 results in,

$$\frac{D}{Dt}\int_\Omega \rho\mathbf{v}d\Omega = \int_\Omega \left[\frac{D(\rho\mathbf{v})}{Dt} + \operatorname{div}\mathbf{v}(\rho\mathbf{v})\right] d\Omega \tag{A.2.15}$$

which through the derivative of a product becomes

$$= \int_\Omega \left[\rho\frac{D\mathbf{v}}{Dt} + \mathbf{v}\left(\frac{D\rho}{Dt} + \rho\operatorname{div}\mathbf{v}\right)\right] d\Omega$$

The last term inside the braces can be identified as the continuity equation, Equation A.2.9, which is zero. Equation A.2.15 then becomes

$$\frac{D}{Dt}\int_\Omega \rho\mathbf{v}d\Omega = \int_\Omega \left[\rho\frac{D\mathbf{v}}{Dt}\right] d\Omega \tag{A.2.16}$$

To convert the surface intergral in Equation A.2.14 to a volume integral first apply Cauchy's relation $\mathbf{T} = \mathbf{n}\cdot\boldsymbol{\sigma}$ and then Gauss' theorem giving

$$\int_\Gamma \mathbf{T}d\Gamma = \int_\Gamma \mathbf{n}\cdot\boldsymbol{\sigma}d\Gamma = \int_\Omega \nabla\cdot\boldsymbol{\sigma}d\Omega = \int_\Omega \frac{\partial\sigma_{ij}}{\partial x_i}d\Omega \tag{A.2.17}$$

Combining Equations A.2.17 and A.2.16 with A.2.14 results in

$$\int_\Omega \left[\rho\frac{D\mathbf{v}}{Dt}\right] d\Omega = \int_\Omega \rho\mathbf{b}d\Omega + \int_\Omega \nabla\cdot\boldsymbol{\sigma}d\Omega \tag{A.2.18}$$

which after collecting integrands becomes

$$\int_\Omega \left[\rho\frac{D\mathbf{v}}{Dt} - \rho\mathbf{b} - \nabla\cdot\boldsymbol{\sigma}\right] d\Omega = 0 \tag{A.2.19}$$

Since this holds for any arbitrary domain Ω, the following applies

$$\rho \frac{D\mathbf{v}}{Dt} = \nabla \cdot \boldsymbol{\sigma} + \rho \mathbf{b} \tag{A.2.20}$$

or in indicial notation

$$\underbrace{\rho \frac{Dv_i}{Dt}}_{\text{Inertial Term}} = \underbrace{\frac{\partial \sigma_{ij}}{\partial x_j}}_{\text{Internal Term}} + \underbrace{\rho b_i}_{\text{Body Term}} \tag{A.2.21}$$

Angular Momentum Angular momentum is simply stated as $\sigma_{ij} = \sigma_{ji}$ if the Cauchy stress tensor is used and it is symmetric. This indicates that no additional equations are generated from the conservation of angular momentum if Cauchy stress is used.

A.2.3 Conservation of Energy

Consider a continuum which contain kinetic energy K, gravitational energy G and internal energy E. The total energy of the continuum is then given by

$$energy = K + G + E \tag{A.2.22}$$

From the first law of thermodynamics, the change in energy is a consequence of the absorption of heat Q and the work done on the system W. Mathematically, this is expressed as

$$\Delta energy = Q + W \tag{A.2.23}$$

Combining Equations A.2.22 and A.2.23 and expressing in rate form results in

$$\frac{D}{Dt}(K + G + E) = \dot{Q} + \dot{W} \tag{A.2.24}$$

The kinetic energy in a domain is given by

$$K = \int_\Omega \frac{1}{2} \rho v_i v_i d\Omega \tag{A.2.25}$$

where v_i are the components of velocity of each particle.

The gravitational energy under uniform gravitation is given by

$$G = \int_\Omega \rho g z d\Omega \tag{A.2.26}$$

where g is the gravitational acceleration and z is the height from a reference plane to the body.

The internal energy is

$$E = \int_\Omega \rho e d\Omega \tag{A.2.27}$$

where E is the total internal energy and e is the internal energy per unit mass.

The heat flow $\dot{Q}$ is given by

$$\begin{aligned}\dot{Q} &= \int_\Omega \rho s d\Omega - \int_\Gamma \mathbf{n} \cdot \mathbf{q} d\Gamma \\ &= \int_\Omega \rho s d\Omega - \int_\Gamma n_i q_i d\Gamma\end{aligned}$$

where, applying Gauss' theorem to the boundary integral, results in

$$\dot{Q} = \int_\Omega \rho s - \frac{\partial q_i}{\partial x_i} d\Omega \tag{A.2.28}$$

where the heat flux, q, is defined as positive outwards and s is the heat source per unit mass.

The rate at which work is done on the body from body forces (b per unit mass) and applied surfaces tractions (T_i) is

$$\dot{W} = \int_\Omega \rho v_i b_i d\Omega + \int_\Gamma T_i v_i d\Gamma \tag{A.2.29}$$

where, using Cauchy's law on the last integrand on the RHS gives

$$\int_\Gamma T_i v_i d\Gamma = \int_\Gamma n_i \sigma_{ji} v_i d\Gamma$$

applying Gauss' theorem to the boundary integral, results in

$$= \int_\Omega \frac{\partial \sigma_{ji} v_i}{\partial x_j} d\Omega$$

applying product rule of differentiation gives

$$= \int_\Omega v_i \frac{\partial \sigma_{ji}}{\partial x_j} + \frac{\partial v_i}{\partial x_j} \sigma_{ji} d\Omega$$

using the decomposition of the velocity gradient, Equation A.1.41, results in

$$= \int_\Omega v_i \frac{\partial \sigma_{ji}}{\partial x_j} + D_{ji}\sigma_{ji} + W_{ji}\sigma_{ji} d\Omega$$

where

$$= \int_\Omega v_i \frac{\partial \sigma_{ji}}{\partial x_j} + D_{ji}\sigma_{ji} d\Omega$$

since the product of a symmetric and skew–symmetric tensor is zero. This results in:

$$\int_\Gamma T_i v_i d\Gamma = \int_\Omega (\nabla \cdot \boldsymbol{\sigma}) \cdot \mathbf{v} + \mathbf{D} : \boldsymbol{\sigma} d\Omega \tag{A.2.30}$$

Combining Equations A.2.29 and A.2.30, the rate at which work is done is expressed as

$$\dot{W} = \int_\Omega \rho v_i b_i + v_i \frac{\partial \sigma_{ji}}{\partial x_j} + D_{ji}\sigma_{ji} d\Omega \tag{A.2.31}$$

Substituting Equations A.2.25, A.2.26, A.2.27 into Equation A.2.24 gives

$$\frac{D}{Dt}(K + G + E) = \frac{D}{Dt} \int_\Omega \left(\frac{1}{2} \rho v_i v_i + \rho g z + \rho e \right) d\Omega$$

applying Reynolds transport theorem for a density weighted integrand, Equation A.1.9, to the RHS gives

$$\begin{aligned} &= \int_\Omega \rho \left(\frac{1}{2} \frac{D v_i v_i}{Dt} + \frac{Dgz}{Dt} + \frac{De}{Dt} \right) d\Omega \\ &= \int_\Omega \rho \left(v_i \frac{Dv_i}{Dt} + \frac{Dgz}{Dt} + \frac{De}{Dt} \right) d\Omega \end{aligned} \tag{A.2.32}$$

Substituting Equations A.2.32, A.2.31 and A.2.28 into Equation A.2.24 and bringing all terms to the LHS results in,

$$\int_\Omega \rho v_i \frac{Dv_i}{Dt} + \rho \frac{Dgz}{Dt} + \rho \frac{De}{Dt} - \rho v_i b_i - v_i \frac{\partial \sigma_{ji}}{\partial x_j} - D_{ji}\sigma_{ji} - \rho s + \frac{\partial q_i}{\partial x_i} d\Omega = 0 \tag{A.2.33}$$

Since this holds for any domain,

$$\rho v_i \frac{Dv_i}{Dt} + \rho \frac{Dgz}{Dt} + \rho \frac{De}{Dt} - \rho v_i b_i - v_i \frac{\partial \sigma_{ji}}{\partial x_j} - D_{ji}\sigma_{ji} - \rho s + \frac{\partial q_i}{\partial x_i} = 0 \tag{A.2.34}$$

rearranging gives

$$\rho \frac{De}{Dt} = -\rho \frac{Dgz}{Dt} + D_{ji}\sigma_{ji} + \rho s - \frac{\partial q_i}{\partial x_i} - v_i \left(\rho \frac{Dv_i}{Dt} - \rho b_i - \frac{\partial \sigma_{ji}}{\partial x_j} \right) \tag{A.2.35}$$

the terms in the parentheses is the conservation of momentum, Equation A.2.20, which equals zero, and so the above equation becomes

$$\begin{aligned}\rho\frac{De}{Dt} &= D_{ji}\sigma_{ji} + \rho s - \frac{\partial q_i}{\partial x_i} - \rho\frac{Dgz}{Dt} \\ &= \mathbf{D} : \boldsymbol{\sigma} + \rho s - \nabla \cdot \mathbf{q} - \rho\frac{Dgz}{Dt}\end{aligned} \tag{A.2.36}$$

Neglecting heat transfer and in the absence of heat sources and gravitational effects (a process which is then purely mechanical), Equation A.2.36 becomes

$$\rho\frac{De}{Dt} = \mathbf{D} : \boldsymbol{\sigma} = \boldsymbol{\sigma} : \mathbf{D} \tag{A.2.37}$$

since $\boldsymbol{\sigma}$ and $\mathbf{D}$ are symmetric.

Appendix B

Finite Element Approximation

B.1 Introduction

A recap of the equations govering equations is given here as the finite element method will seek to solve these equations. The conservation of mass, momentum and energy is simply stated as:

$$\rho J = \rho_0 \tag{B.1.1}$$

$$\int_\Omega \left[\rho \frac{D\mathbf{v}}{Dt} - \rho \mathbf{b} - \nabla \cdot \boldsymbol{\sigma} \right] d\Omega = 0 \tag{B.1.2}$$

$$\rho \frac{De}{Dt} = \mathbf{D} : \boldsymbol{\sigma} + \rho s - \nabla \cdot \mathbf{q} - \rho \frac{Dgz}{Dt}$$

which, in a purely mechanical process neglecting gravitational effects becomes,

$$\rho \frac{De}{Dt} = \mathbf{D} : \boldsymbol{\sigma} = \boldsymbol{\sigma} : \mathbf{D} = \sigma_{ij} D_{ij} \tag{B.1.3}$$

In the application of the finite element method (FEM) to a domain, a mesh (of elements) is embedded within the material and the above equations are discretized in space. The movement of the mesh, since it follows a point in the material, then corresponds the deformation of the material. Equation B.1.1 is inherently satisfied by the FEM since there is no mass flux out of the element. The conservation of energy equation, Equation B.1.3, will be used in the evaluation of the equation of state and as a means of calculating global energy balances. Therefore, the solution of the conservation of linear momentum equation, Equation B.1.2, which governs the movement of the material, is required. It will be seen that two additional governing equations, which relate strain to

displacement, and a constitutive equation, which relates stress to strain, will be required to solve the momentum equation.

The momentum equation, as given in Equation B.1.2, is a more complicated form of Newton's second law $F = ma$. In essence, with a mesh superimposed on a material, we seek to determine the discrete forces at each node subjected boundary conditions.

B.2 Development of the Weak form of the Momentum Equation

As outlined by Malvern [97] consider a body, initially in equilibrium, subjected to arbitrary infinitesimal displacements δu_i throughout. Assume that the displacements are such that the derivatives $\partial(\delta u_i)/\partial x_j$ are continuous (C^0) and are zero anywhere an actual displacement boundary condition, u_i, is applied. The displacements δu_i are termed "virtual displacements" since they aren't physical displacements as a consequence of applied loads but displacements as a result of fictitious forces. In terms of variational methods, the virtual displacement can be thought of a a test function. Mathematically, the space in which the test function exists can be expressed as

$$\partial u_i \left(X \right) \in \mathscr{U}_\circ \quad \mathscr{U}_\circ = \delta u_i | \in C^0 \left(X \right), \delta u_i = 0 \text{ on } \Gamma_{u_i} \tag{B.2.1}$$

Correspondingly, the product of a force applied over the virtual displacement results in virtual work δW.

Similarly, virtual velocities, δv_i, can be used such that

$$\partial v_i \left(X \right) \in \mathscr{V}_\circ \quad \mathscr{V}_\circ = \delta v_i | \in C^0 \left(X \right), \delta v_i = 0 \text{ on } \Gamma_{v_i} \tag{B.2.2}$$

In this sense, the virtual displacements can be thought of taking place in an infinitesimal time interval, δt, resulting in a virtual velocity, v_i. This subtle difference allows the notion of "infinitesimal" displacements to be bypassed for an arbitrary finite virtual velocity [97]. Similar to before, the product of a force (which is assumed to be constant for the time interval) and virtual velocity results in virtual power denoted $\delta \mathscr{P}$. This is the method which Belytschko [112] adopts and also shall be used here.

The weak form of the momentum equation is developed taking the product of the virtual velocities and the momentum equation as

$$\int_\Omega \left[\delta v_i \rho \dot{v}_i - \delta v_i \rho b_i - \delta v_i \frac{\partial \sigma_{ji}}{\partial x_j} \right] d\Omega = 0 \tag{B.2.3}$$

where $\dot{v} \equiv Dv/Dt$. The traction boundary and traction continuity conditions which

apply to the above equation are:

$$n_j\sigma_{ji} = \bar{T}_i \quad \text{on} \quad \Gamma_{T_i} \tag{B.2.4}$$

$$[\![n_j\sigma_{ji}]\!] = n_j^A\sigma_{ji}^A + n_j^B\sigma_{ji}^B = 0 \quad \text{on} \quad \Gamma_{int} \tag{B.2.5}$$

where $\bar{T}_i$ is the specified traction and jumps in tractions across domains A and B are denoted by the double brackets.

The last integrand in Equation B.2.3 can alternatively be expressed using the product rule

$$\int_\Omega \frac{\partial(\delta v_i\sigma_{ji})}{\partial x_j}d\Omega = \int_\Omega \delta v_i\frac{\partial\sigma_{ji}}{\partial x_j} + \sigma_{ji}\frac{\partial\delta v_i}{\partial x_j}d\Omega$$

which, rearranging becomes

$$\int_\Omega \delta v_i\frac{\partial\sigma_{ji}}{\partial x_j}d\Omega = \int_\Omega \frac{\partial(\delta v_i\sigma_{ji})}{\partial x_j} - \sigma_{ji}\frac{\partial\delta v_i}{\partial x_j}d\Omega \tag{B.2.6}$$

In determining the continuity of the above terms the following arguments are made. The rate of deformation tensor, D_{ij} is function of the spatial derivative of the velocities, δv_i which, by definition are C^0. Therefore, the rate of deformation tensor is C^{-1} indicating that it is discontinuous. Since the stress, σ_{ij}, is a function of the rate of deformation tensor, D_{ij}, via the constitutive equation, it too is C^{-1}. This assumes that the constitutive equation leads to stress being a "well–behaved" function of the rate of deformation tensor. The same argument can be made using the Green strain tensor under small displacement gradients.

Therefore inspection of the above equation leads to the term $\delta v_i\sigma_{ji}$ being discontinuous. It is assumed that these discontinuities are finite and occur on boundaries Γ_{int}. Applying a modified version Gauss' theorem from Chapter A to the first term on the RHS leads to

$$\int_\Omega \frac{\partial(\delta v_i\sigma_{ji})}{\partial x_j}d\Omega = \int_\Gamma \delta v_i n_j\sigma_{ji}d\Gamma + \int_{\Gamma_{int}} \delta v_i[\![n_j\sigma_{ji}]\!]d\Gamma \tag{B.2.7}$$

where the second integral accounts for the discontinuities in stress which vanish according to Equation B.2.5. At the boundaries where δv_i is zero or $\bar{T}_i$ is specified, so Equation B.2.7 becomes,

$$\int_\Omega \frac{\partial(\delta v_i\sigma_{ji})}{\partial x_j}d\Omega = \int_{\Gamma_{T_i}} \delta v_i\bar{T}_i d\Gamma \tag{B.2.8}$$

Although i appears to occur three times in the above equation (violating the summation convention) it is included to reinforce the idea that the traction boundary conditions are applied only over the boundaries where they occur.

Substitute Equation B.2.8 into Equation B.2.6 to get

$$\int_{\Omega} \delta v_i \frac{\partial \sigma_{ji}}{\partial x_j} d\Omega = \int_{\Gamma_{T_i}} \delta v_i \bar{T}_i d\Gamma - \int_{\Omega} \sigma_{ji} \frac{\partial \delta v_i}{\partial x_j} d\Omega \tag{B.2.9}$$

and so Equation B.2.3 becomes,

$$\delta \mathscr{P} = \int_{\Omega} \delta v_i \rho \dot{v}_i d\Omega - \int_{\Omega} \delta v_i \rho b_i d\Omega - \int_{\Gamma_{T_i}} \delta v_i \bar{T}_i d\Gamma + \int_{\Omega} \sigma_{ji} \frac{\partial \delta v_i}{\partial x_j} d\Omega = 0 \tag{B.2.10}$$

which is called the weak form of virtual power or the principal of virtual power. For a more intuitive feel for the above equation, the terms can be associated with physical meanings.

The first integral term represents the virtual inertial or kinetic power $\delta \mathscr{P}^{Kinetic}$, the second and third terms are a consequence of externally applied loads and is so deemed virtual external power $\delta \mathscr{P}^{Ext}$. The last term develops from internal forces and is therefore called virtual internal power denoted $\delta \mathscr{P}^{Internal}$. A mathematic statement for the virtual power terms as a consequence of virtual velocities is

$$\delta \mathscr{P} = \delta \mathscr{P}^{Kinetic} - \delta \mathscr{P}^{External} + \delta \mathscr{P}^{Internal} = 0 \quad \forall \delta v_i \in \mathscr{V}_{\circ} \tag{B.2.11}$$

An alternate version of the internal virtual power can be formulate by recognizing that

$$\frac{\partial \delta v_i}{\partial x_j} = \delta L_{ij}$$

and so the virtual power becomes

$$\begin{aligned} \delta \mathscr{P}^{Internal} &= \int_{\Omega} \sigma_{ji} \frac{\partial \delta v_i}{\partial x_j} d\Omega \\ &= \int_{\Omega} \sigma_{ji} \delta L_{ij} d\Omega \\ &= \int_{\Omega} \sigma_{ji} \left[\delta D_{ij} + \delta W_{ij} \right] d\Omega \\ &= \int_{\Omega} \sigma_{ji} \delta D_{ij} + \sigma_{ji} \delta W_{ij} d\Omega \end{aligned}$$

where the second integrand is zero due to the symmetry of σ_{ji} and antisymmetry of W_{ij}, leading to

$$\delta \mathscr{P}^{Internal} = \int_{\Omega} \sigma_{ji} \delta D_{ij} d\Omega = \int_{\Omega} \sigma_{ij} \delta D_{ij} d\Omega \tag{B.2.12}$$

which expresses the virtual power in terms of the rate of deformation tensor.

The external virtual power is comprised of body forces and prescribed tractions as

$$\delta\mathscr{P}^{External} = \int_{\Omega} \delta v_i \rho b_i d\Omega + \int_{\Gamma_{T_i}} \delta v_i \bar{T}_i d\Gamma \tag{B.2.13}$$

Similarly, the virtual kinetic power is given by

$$\delta\mathscr{P}^{Kinetic} = \int_{\Omega} \delta v_i \rho \dot{v}_i d\Omega \tag{B.2.14}$$

B.3 Semi–Discretization

In order to solve the virtual power approximation, the domain Ω is divided into sub–domains Ω_e where the subscript e represents the domain of the element. Mathematically, this can be stated as $\Omega = \underset{e}{\cup}\Omega_e$. This is termed semi–discretization as discretization occurs only in space and not in time. The nodes which make up each element have the current coordinates $x_{\alpha i}$ and reference coordinates $X_{\alpha i}$ where α refers to the node number and, as before, i refers to the directional component. It is assumed that any point in the domain can then be determined through interpolation between nodes. If an interpolation function between nodes is defined as N_α, then

$$x_i(x,t) = N_\alpha(x) x_{\alpha i}(t) \tag{B.3.1}$$
$$X_i(x,t) = N_\alpha(x) X_{\alpha i}(t) \tag{B.3.2}$$

where α is summed from 1 to the number of nodes either in the total or element domain.

Nodal displacements are then given by

$$\begin{aligned} u_{\alpha i} &= N_\alpha x_{\alpha i} - N_\alpha X_{\alpha i} \\ &= N_\alpha (x_{\alpha i} - X_{\alpha i}) \\ &= N_\alpha (x_{\alpha i} - X_{\alpha i}) \end{aligned}$$

leading to

$$u_{\alpha i}(x,t) = N_\alpha(x) u_{\alpha i}(t) \tag{B.3.3}$$

Similarly, the velocities and accelerations are given by

$$\begin{aligned} \dot{u}_{\alpha i}(x,t) &= N_\alpha(x) \dot{u}_{\alpha i}(t) \\ &= N_\alpha(x) v_{\alpha i}(t) \end{aligned} \tag{B.3.4}$$

and

$$\begin{aligned}\ddot{u}_{\alpha i}(x,t) &= N_\alpha(x)\ddot{u}_{\alpha i}(t)\\ &= N_\alpha(x)\dot{v}_{\alpha i}(t)\\ &= N_\alpha(x)a_{\alpha i}(t)\end{aligned} \tag{B.3.5}$$

The virtual velocities can also be interpolated between the nodes as

$$\delta v_i x = N_\alpha(x)\delta v_{\alpha i} \tag{B.3.6}$$

The velocity gradient can also be expressed in terms interpolation functions between the nodes as

$$\begin{aligned}L_{ij} &= \frac{\partial v_i}{\partial x_j}\\ &= \frac{\partial(N_\alpha v_{\alpha i})}{\partial x_j}\\ &= N_\alpha \frac{\partial v_{\alpha i}}{\partial x_j} + v_{\alpha i}\frac{\partial N_\alpha}{\partial x_j}\end{aligned}$$

but, by definition $v_{\alpha i}$ does not vary with x_i since it is a point, resulting in

$$L_{ij} = v_{\alpha i}\frac{\partial N_\alpha}{\partial x_j} = v_{\alpha i}N_{\alpha,j} \tag{B.3.7}$$

and so the rate of deformation is

$$\begin{aligned}D_{ij} &= \frac{1}{2}\left(L_{ij} + L_{ji}\right)\\ &= \frac{1}{2}\left(v_{\alpha i}N_{\alpha,j} + v_{\alpha j}N_{\alpha,i}\right)\end{aligned} \tag{B.3.8}$$

Equations B.3.1 to B.3.8 constitute the spatial discretization formulas. Substituting these equations into the weak form of the momentum equation, Equation B.2.10 results

in

$$\begin{aligned}
\delta\mathscr{P}^{Internal} &= \int_\Omega \sigma_{ji}\frac{\partial \delta v_i}{\partial x_j}d\Omega \\
&= \int_\Omega \sigma_{ji}\delta v_{\alpha i}\frac{\partial N_\alpha}{\partial x_j}d\Omega \qquad \text{(B.3.9)} \\
\delta\mathscr{P}^{External} &= \int_\Omega \delta v_{\alpha i}N_\alpha \rho b_i d\Omega + \int_{\Gamma_{T_i}} \delta v_{\alpha i}N_\alpha \bar{T}_i d\Gamma \qquad \text{(B.3.10)} \\
\delta\mathscr{P}^{Kinetic} &= \int_\Omega \delta v_{\alpha i}N_\alpha \rho N_\alpha \dot{v}_{\alpha i}d\Omega \qquad \text{(B.3.11)}
\end{aligned}$$

Using the above in combination with Equation B.2.11 and factoring out $\delta v_{\alpha i}$ from every term results in

$$\delta v_{\alpha i}\left[\int_\Omega \sigma_{ji}\frac{\partial N_\alpha}{\partial x_j}d\Omega - \int_\Omega \rho b_i d\Omega - \int_{\Gamma_{T_i}} N_\alpha \bar{T}_i d\Gamma + \int_\Omega N_\alpha \rho N_\alpha \dot{v}_{\alpha i}d\Omega\right] = 0 \quad \forall(\alpha, i) \notin \Gamma_{v_i} \qquad \text{(B.3.12)}$$

since δv_i is zero on Γ_{v_i} by definition.

B.4 Nodal Forces

The idea of virtual power is a constant force acting over a virtual displacement for a given time interval. As such, nodal forces for each virtual power term can be determined. The internal nodal forces are given by

$$\begin{aligned}
\delta\mathscr{P}^{Internal} &= \delta v_{\alpha i} f_{\alpha i}^{Internal} \\
&= \int_\Omega \frac{\partial(\delta v_i)}{\partial x_j}\sigma_{ji}d\Omega \\
&= \delta v_i \int_\Omega \frac{\partial N_\alpha}{\partial x_j}\sigma_{ji}d\Omega
\end{aligned}$$

which, since this holds for any arbitrary velocity, leads to

$$f_{\alpha i}^{Internal} = \int_\Omega \frac{\partial N_\alpha}{\partial x_j}\sigma_{ji}d\Omega \qquad \text{(B.4.1)}$$

It should be noted that the above equation requires the derivative of the interpolation function with respect to space as well as integration over the current (deformed) config-

uration. Similarly, the external nodal forces are given by

$$\begin{aligned}\delta\mathscr{P}^{External} &= \delta v_{\alpha i} f_{\alpha i}^{External} \\ &= \int_{\Omega} \delta v_{\alpha i} N_\alpha \rho b_i d\Omega + \int_{\Gamma_{T_i}} \delta v_{\alpha i} N_\alpha \bar{T}_i d\Gamma \\ &= \delta v_{\alpha i} \int_{\Omega} N_\alpha \rho b_i d\Omega + \delta v_{\alpha i} \int_{\Gamma_{T_i}} N_\alpha \bar{T}_i d\Gamma\end{aligned}$$

which, as before, leads to

$$f_{\alpha i}^{External} = \int_{\Omega} N_\alpha \rho b_i d\Omega + \int_{\Gamma_{T_i}} N_\alpha \bar{T}_i d\Gamma \tag{B.4.2}$$

The kinetic or inertial forces are given by

$$\begin{aligned}\delta\mathscr{P}^{Kinetic} &= \delta v_{\alpha i} f_{\alpha i}^{Kinetic} \\ &= \int_{\Omega} \delta v_{\alpha i} \rho \dot{v}_i d\Omega \\ &= \delta v_{\alpha i} \int_{\Omega} N_\alpha \rho \dot{v}_i d\Omega \\ f_{\alpha i}^{Kinetic} &= \int_{\Omega} N_\alpha \rho \dot{v}_i d\Omega\end{aligned} \tag{B.4.3}$$

However, recall that from Equation B.3.5, $\dot{v}_i(x,t) = \dot{v}_{\alpha i}(t) N_\alpha(x)$, and so Equation B.4.3 becomes,

$$\begin{aligned}f_{\alpha i}^{Kinetic} &= \int_{\Omega} \rho N_\alpha \dot{v}_{\beta j} N_\beta d\Omega \\ &= \int_{\Omega} \rho N_\alpha N_\beta d\Omega \dot{v}_{\beta j}\end{aligned} \tag{B.4.4}$$

The integrated term is called the consistent mass matrix denoted M^c. Often a lumped mass matrix, denoted M, is used where the mass of each element is distributed over its nodes resulting in a diagonal matrix reducing the computational cost. The lumped mass matrix is defined by

$$M_{\alpha i \beta j} = \delta_{ij} \int_{\Omega} \rho N_\alpha N_\beta d\Omega \tag{B.4.5}$$

From the conservation of mass, developed in Chapter A, it can be noted that the mass matrix is independent of time and therefore only needs to be computed once.

Using the lumped mass matrix, the kinetic force can be written as,

$$f_{\alpha i}^{Kinetic} = M_{\alpha i \beta j} \dot{v}_{\beta j} \tag{B.4.6}$$

Using Equations B.4.1, B.4.2 and B.4.6, Equation B.2.11 becomes

$$f_{\alpha i}^{Internal} - f_{\alpha i}^{External} + f_{\alpha i}^{Kinetic} = 0$$
$$f_{\alpha i}^{Internal} + M_{\alpha i \beta j}\dot{v}_{\beta j} = f_{\alpha i}^{External} \quad \forall(\alpha, i) \notin \Gamma_{v_i} \tag{B.4.7}$$

which is the discrete approximation of the weak form of the momentum equation also called the equations of motion.

B.5 Element Coordinates

It is convenient to write the interpolation functions in terms of coordinates local to the element. For the purpose of explanation, an isoparametric quadrilateral formulation will be used. Figure B.1 shows a quadrilateral in the reference and current states. Additional to these two configurations is the parent configuration which defines the element coordinates and shape. The domains associated with each configuration are denoted by Ω_0, Ω and $\square$ respectively. This particular element has four nodes number counterclockwise. The coordinates in the parent element are denoted by ξ_i and are in the range ± 1. The interpolation functions are subject to the following conditions:

1. They must be continuous within the element.
2. Their sum must equal one at any point within the element.
3. The value of N_α at node β is given by $\delta_{\alpha\beta}$.

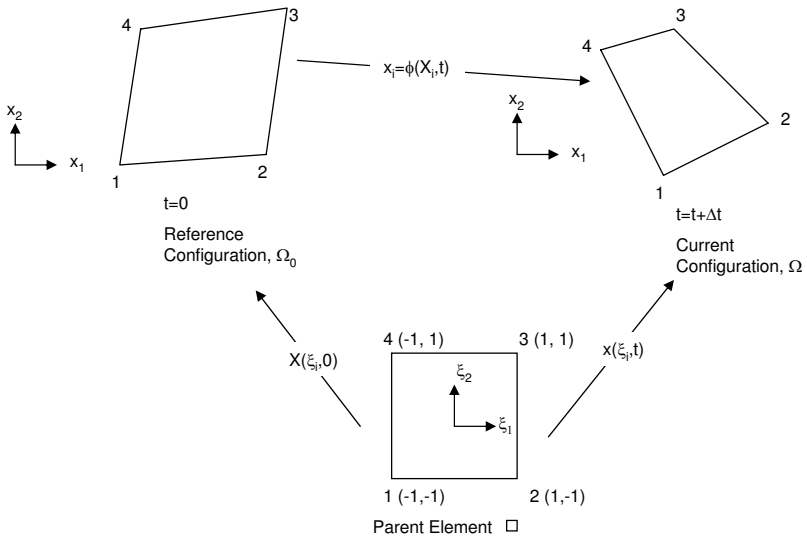

Figure B.1: Parent element and its relation to the current and reference configurations.

Maps, similar to those developed in Section A.1.5 can be formulate for the current and reference configurations to the parent element. The reference and current maps are then expressed as

$$x_i = x_i(\xi_i, t) \tag{B.5.1}$$
$$X_i = X_i(\xi_i, 0) \tag{B.5.2}$$
$$\tag{B.5.3}$$

These maps must be

1. One–to–one (i.e. two points in one domain don't get mapped to a single point in another domain).
2. At least C^0 in space.
3. The Jacobian determinant must be positive.

An example of a interpolation function for the quadrilateral element is given by

$$N_\alpha = \frac{1}{4}\left(1 + \xi_\alpha \xi\right)\left(1 + \eta_\alpha \eta\right) \tag{B.5.4}$$

where $\xi_1 = \xi$ and $\xi_2 = \eta$. The coordinates for ξ_α and η_α are given in Table B.1.

α	ξ_α	η_α
1	-1	-1
2	1	-1
3	1	1
4	-1	1

Table B.1: Coordinate for quadrilateral parent element with four nodes.

So the N_1 shape function at node 1 is then $N_1 = 1/4(1+1)(1+1) = 1$ but zero at nodes 2, 3 and 4 for example.

Similar to Equations B.3.3 to B.3.5 the displacement, velocities and accelerations can be expressed in terms of shape functions as

$$u_i(\xi_i, t) = u_{\alpha i}(t) N_i \xi_i \tag{B.5.5}$$
$$\dot{u}_i(\xi_i, t) = v_i(\xi_i, t) = v_{\alpha i}(t) N_i \xi_i \tag{B.5.6}$$
$$\ddot{u}_i(\xi_i, t) = \dot{v}_i(\xi_i, t) = \dot{v}_{\alpha i}(t) N_i \xi_i \tag{B.5.7}$$

The internal forces require the spatial gradient of the interpolation functions. By the chain rule the following holds

$$\frac{\partial v_i}{\partial \xi_j} = \frac{\partial v_i}{\partial x_k}\frac{\partial x_k}{\partial \xi_j} \tag{B.5.8}$$

The second term on the RHS can be viewed as the deformation gradient with respect to the parent element denoted $F^{\xi}_{ij} = \partial x_i / \partial \xi_j$. Rearranging the above equation for $\partial v_i / \partial x_k = L_{ik}$ gives

$$\begin{aligned} L_{ij} &= \frac{\partial v_i}{\partial \xi_k} \frac{\partial \xi_k}{\partial x_j} \\ &= \frac{\partial v_i}{\partial \xi_k} \left(F^{\xi}_{kj} \right)^{-1} \end{aligned} \tag{B.5.9}$$

Note that the above equation requires the inverse of the of the deformation gradient between the current and parent configurations.

Similarly in terms of shape functions

$$\begin{aligned} L_{ij} &= \frac{\partial v_i}{\partial x_j} \\ &= v_{\alpha i} \frac{\partial N_\alpha}{\partial x_j} \\ &= v_{\alpha i} \frac{\partial N_\alpha}{\partial \xi_k} \frac{\partial \xi_k}{\partial x_j} \end{aligned} \tag{B.5.10}$$

The rate of deformation tensor can be determined from $D_{ij} = 1/2(L_{ij} + L_{ji})$ as before. The Jacobian determinant is then given by

$$j = \det \frac{\partial x_i}{\partial \xi_j} \tag{B.5.11}$$

where a small j is used to distinguish it from the Jacobian determinant of the deformation gradient with respect the reference configuration.

If integration of an arbitrary function g is required on over the current domain, it can be related to the reference and parent domain through the following relations

$$\begin{aligned} \int_{\Omega^e} g(\mathbf{x}) d\Omega &= \int_{{\Omega_0}^e} g(\mathbf{x}(\mathbf{X})) J d\Omega_0 \\ &= \int_{\square} g(\xi) j d\square \end{aligned}$$

and

$$\int_{{\Omega_0}^e} g(\mathbf{X}) d\Omega_0 = \int_{\square} g(\mathbf{X}(\xi)) j^0 d\square \tag{B.5.12}$$

B.6 Numerical Integration

Inspection of the equations presented to this point indicate that integration over the domain must be performed (see Section B.4 for instance). In all but the rarest cases, analytical forms of integration do not exist. As such, numerical integration methods, such as Gauss quadrature, are employed. So, in essence we wish to determine

$$\int_{\Omega^e} f(x,y,z)d\Omega$$

where f is a smooth, integrable, function. Performing this integration using the parent domain (called pull back integration [115]), the above integral, in three dimensions, becomes

$$\int_{\Omega^e} f(x,y,z)d\Omega = \int_{-1}^{1}\int_{-1}^{1}\int_{-1}^{1} f\left[x\left(\xi,\eta,\zeta\right), y\left(\xi,\eta,\zeta\right), z\left(\xi,\eta,\zeta\right)\right] j\left(\xi,\eta,\zeta\right) d\xi d\eta d\zeta$$

or in general

$$\underbrace{\int_{-1}^{1}\cdots\int_{-1}^{1}}_{n_{sd}\text{integrals}} \underbrace{f(\xi,\ldots)}_{n_{sd}\text{arguments}} \quad \underbrace{d\xi\ldots}_{n_{sd}\text{differentials}}$$

where n_{sd} is the number of space dimensions. This can be approximated using

$$\begin{aligned}\int_{-1}^{1} g(\xi)d\xi &= \sum_{l=1}^{n_{int}} g\left(\tilde{\xi}_l\right) W_l + R \\ &\cong \sum_{l=1}^{n_{int}} g\left(\tilde{\xi}_l\right) W_l \end{aligned} \tag{B.6.1}$$

where n_{int} is the number of integration points, $\tilde{\xi}_l$ is the coordinate of the l^{th} integration point, W_l is the weight of the l^{th} integration point and R is the remainder. In Gauss quadrature, the locations and weights of the integration points are determined to achieve the most accurate solution. The constants outlined previous are specific to each element type. Integration over several dimensions is achieved through repeat application of the one dimensional equation. For example, Figure B.2 shows a quadrilateral element with a 2x2 Gaussian rule applied. Integration of a function $g(x,y)$ over the domain is then

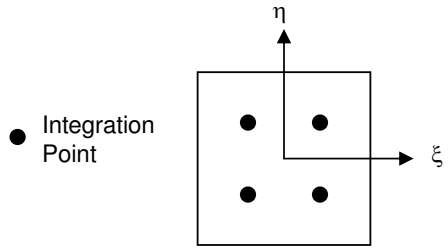

Figure B.2: Integration points for a quadrilateral element with 2x2 Gaussian rule applied.

given by

$$\begin{aligned}\int_{\Omega^e} g(\xi,\eta)d\Omega &= \int_{-1}^{1}\int_{-1}^{1} g\left(\xi,\eta\right)d\xi d\eta \\ &= \int_{-1}^{1}\left\{\sum_{Q_1=1}^{n_{Q_1}} g\left(\tilde{\xi}_{Q_1},\eta\right)W_{Q_1}\right\}d\eta \\ &= \sum_{Q_1=1}^{n_{Q_1}}\sum_{Q_2=1}^{n_{Q_2}} g\left(\tilde{\xi}_{Q_1},\tilde{\eta}_{Q_2}\right)W_{Q_1}W_{Q_2} \end{aligned} \tag{B.6.2}$$

where, $n_Q = 2\cdot 2 = 4$ is the number of integration points and from [115], the weights and integration points are given as

$$W_1 = W_2 = W_3 = W_4 = 1 \quad \text{and,}$$

Q	$\tilde{\xi}_Q$	$\tilde{\eta}_Q$
1	$\frac{-1}{\sqrt{3}}$	$\frac{-1}{\sqrt{3}}$
2	$\frac{1}{\sqrt{3}}$	$\frac{-1}{\sqrt{3}}$
3	$\frac{1}{\sqrt{3}}$	$\frac{1}{\sqrt{3}}$
4	$\frac{-1}{\sqrt{3}}$	$\frac{1}{\sqrt{3}}$

which leads to

$$\begin{aligned}\int_{\Omega^e} g(\xi,\eta)d\Omega &= \int_{-1}^{1}\int_{-1}^{1} g\left(\xi,\eta\right)d\xi d\eta \\ &= g\left(\frac{-1}{\sqrt{3}},\frac{-1}{\sqrt{3}}\right)+g\left(\frac{1}{\sqrt{3}},\frac{-1}{\sqrt{3}}\right)+g\left(\frac{1}{\sqrt{3}},\frac{1}{\sqrt{3}}\right)+g\left(\frac{-1}{\sqrt{3}},\frac{1}{\sqrt{3}}\right)\end{aligned} \tag{B.6.3}$$

Similar techniques can be used for three dimensional elements.

B.7 Selective Reduced Integration

In finite element methods, it is advantageous to decompose the stress tensor into the hydrostatic and deviatoric components. Similarly, the rate of deformation tensor can be split into dilational and deviatoric components. In this way, a different number of integration points can be used for different terms. This helps to prevent locking of elements (which is to say that displacements are small and converge slowly).

The stress can be decomposed as follows,

$$\sigma_{ij} = \sigma_{ij}^{dev} + \sigma^{hyd}\delta_{ij}$$

where

$$\sigma^{hyd} = 1/3\sigma_{kk} = -p \tag{B.7.1}$$
$$\sigma_{ij}^{dev} = \sigma_{ij} - \sigma^{hyd}\delta_{ij} \tag{B.7.2}$$

where the pressure is denoted as p. Similarly, the rate of deformation is decomposed as

$$D_{ij} = D_{ij}^{dev} + D^{vol}\delta_{ij}$$

where

$$D_{ij}^{dev} = D_{ij} - D^{vol}\delta_{ij} \tag{B.7.3}$$
$$D^{vol} = \frac{1}{3}D_{kk}\delta_{ij} \tag{B.7.4}$$

Equation B.2.12 can then be written as

$$\begin{aligned}\mathscr{P}^{Internal} &= \int_\Omega \delta D_{ij}\sigma_{ij}d\Omega \\ &= \int_\Omega \delta D_{ij}^{dev}\sigma_{ij}^{dev}d\Omega - \int_\Omega \delta D_{ii}pd\Omega\end{aligned} \tag{B.7.5}$$

Discretization of the rate of deformation tensor is given by

$$\delta D_{ii}p = \delta v_{\alpha i}\frac{\partial N_\alpha}{\partial x_i}$$
$$\delta D_{ij}^{dev}\sigma_{ji}^{dev} = \frac{1}{2}\left(N_{\alpha,j}\delta v_{\alpha i} + N_{\alpha,i}\delta v_{\alpha j}\right)\sigma_{ji}^{dev}$$

which, since $\sigma_{ji}^{dev} = \sigma_{ij}^{dev}$, gives

$$\delta D_{ij}^{dev}\sigma_{ji}^{dev} = \delta v_{\alpha i}N_{\alpha,j}\sigma_{ji}^{dev} \tag{B.7.6}$$

If single point quadrature is used for the hydrostatic part and full quadrature is used for the deviatoric components, the for a quadrilateral Equation B.7.5 becomes,

$$\mathscr{P}^{Internal} = \delta v_{\alpha i} \left\{ \sum_{Q_2=1}^{4} \sum_{Q_1=1}^{4} W_{Q_1} W_{Q_2} j N_{\alpha,j} \sigma_{ji}^{dev} - j N_{\alpha,i} p \right\} \tag{B.7.7}$$

where the deviatoric component is evaluated at the quadrature points and the hydrostatic portion is evaluated at the centre of the element. The internal nodal forces are equal to the terms inside the braces as before.

B.8 Temporal Discretization

B.8.1 Central Difference Scheme

A central difference method is adopted to advance the solution through time. The method is developed from difference formulas for the displacement, velocity and acceleration. Explicit time integration is used for the current study. As outlined in [116], the central difference scheme is approximated by the subtraction of two Taylor series expansions as follows.

The general Taylor series expansion is given by

$$f\left(t_{n+1}\right) = f\left(t_n\right) + \left(t_{n+1} - t_n\right) \frac{df\left(t_n\right)}{dt} + \frac{\left(x_{j+1} - x_j\right)^2}{2} \frac{d^2 f\left(t_n\right)}{dt^2} + \ldots \tag{B.8.1}$$

which, rearranging and using $\Delta t = t_{n+1} - t_n$, gives

$$\frac{df\left(t_n\right)}{dt} = \frac{f\left(t_{n+1}\right) - f\left(t_n\right)}{\Delta t_n} - \frac{\Delta t_n}{2} \frac{d^2 f\left(t_n\right)}{dt^2} + \ldots \tag{B.8.2}$$

If two series are constructed as

$$f_{n+1} = f_n + \Delta t f_n' + \frac{\left(\Delta t\right)^2}{2} f_n'' + \frac{\left(\Delta t\right)^3}{6} f_n''' + \ldots \tag{B.8.3}$$

$$f_{n-1} = f_n - \Delta t f_n' + \frac{\left(\Delta t\right)^2}{2} f_n'' - \frac{\left(\Delta t\right)^3}{6} f_n''' + \ldots \tag{B.8.4}$$

$$\tag{B.8.5}$$

where the $'$ indicates differentiation with respect to time and n is the time step. Subtract

Equation B.8.4 from B.8.3 leads to

$$f_{n+1} - f_{n-1} = f_n - f_n + \Delta t f'_n + \Delta t f'_n + \frac{(\Delta t)^2}{2} f''_n - \frac{(\Delta t)^2}{2} f''_n + \frac{(\Delta t)^3}{6} f'''_n + \frac{(\Delta t)^3}{6} f'''_n + \dots \tag{B.8.6}$$

$$= 2\Delta t f'_n + 2\frac{(\Delta t)^3}{6} f'''_n + \dots \tag{B.8.7}$$

which, solving for f'_n gives

$$\begin{aligned} f'_n &= \frac{f_{n+1} - f_{n-1}}{2\Delta t} - \frac{(\Delta t)^2}{6} f'''_n + \dots \\ &= \frac{f_{n+1} - f_{n-1}}{2\Delta t} + O\left(\Delta t\right)^2 \end{aligned} \tag{B.8.8}$$

where ignoring the higher order terms indicates that it is second order accurate in time. A slightly different approach can be taken for solving for the displacements, velocities and accelerations to account for variable time step size.

B.8.2 Modified Temporal Discretization

Define the displacement, velocity, acceleration and force vectors as

$$\mathbf{d} = \begin{Bmatrix} u_1 \\ u_2 \\ \vdots \\ u_m \end{Bmatrix}, \quad \dot{\mathbf{d}} = \begin{Bmatrix} v_1 \\ v_2 \\ \vdots \\ v_m \end{Bmatrix}, \quad \ddot{\mathbf{d}} = \begin{Bmatrix} a_1 \\ a_2 \\ \vdots \\ a_m \end{Bmatrix}, \quad \mathbf{f} = \begin{Bmatrix} f_1 \\ f_2 \\ \vdots \\ f_m \end{Bmatrix}$$

where m is the number of nodes. If the mass matrix is denoted $\mathbf{M}$, the discrete weak form of the momentum equation, Equation B.4.7, can be written as

$$\ddot{\mathbf{d}}^n = \mathbf{M}^{-1}\left[(\mathbf{f}^{External})^n - (\mathbf{f}^{Internal})^n\right] \tag{B.8.9}$$

Define the increments in time as

$$\Delta t^{n+1/2} = t^{n+1} - t^n \tag{B.8.10}$$

$$t^{n+1/2} = 1/2\left(t^{n+1} + t^n\right) \tag{B.8.11}$$

$$\Delta t^n = t^{n+1/2} - t^{n-1/2} \tag{B.8.12}$$

The velocity is then given as

$$\dot{\mathbf{d}}^{n+1/2} = \frac{\mathbf{d}^{n+1} - \mathbf{d}^n}{t^{n+1} - t^n} = \frac{1}{t^{n+1} - t^n}\left(\mathbf{d}^{n+1} - \mathbf{d}^n\right) \tag{B.8.13}$$

$$= \frac{\mathbf{d}^{n+1} - \mathbf{d}^n}{t^{n+1} - t^n} = \frac{1}{\Delta t^{n+1/2}}\left(\mathbf{d}^{n+1} - \mathbf{d}^n\right) \tag{B.8.14}$$

The above formula can rearranged to get an integration formula as

$$\mathbf{d}^{n+1} = \mathbf{d}^n + \Delta t^{n+1/2}\dot{\mathbf{d}}^{n+1/2} \tag{B.8.15}$$

Correspondingly, the acceleration is given by

$$\ddot{\mathbf{d}}^n = \frac{\dot{\mathbf{d}}^{n+1/2} - \dot{\mathbf{d}}^{n-1/2}}{t^{n+1/2} - t^{n-1/2}}$$

$$= \frac{\dot{\mathbf{d}}^{n+1/2} - \dot{\mathbf{d}}^{n-1/2}}{\Delta t^n} \tag{B.8.16}$$

$$\tag{B.8.17}$$

The above equation can be rewritten as

$$\dot{\mathbf{d}}^{n+1/2} = \Delta t^n \ddot{\mathbf{d}}^n + \dot{\mathbf{d}}^{n-1/2} \tag{B.8.18}$$

B.8.3 Stability

The Courant number, C, is required to be less than one so that the mesh motion during a timestep is less than the dimension of the smallest element.

$$C \equiv \frac{a\Delta t}{\Delta x} \leq 1$$

where x is the smallest dimension of an element and a is the speed of sound or dilational wave speed ($a = \sqrt{E/\rho}$).

B.9 Implementation

It is convenient to use Voigt notation which expresses the rate of deformation tensor and stress tensor in a column matrix. For two dimensions, this can be expressed as

$$\{\mathbf{D}\} = \begin{bmatrix} D_x \\ D_y \\ D_{xy} \end{bmatrix} \quad \text{and} \quad \{\boldsymbol{\sigma}\} = \begin{bmatrix} \sigma_x \\ \sigma_y \\ \sigma_{xy} \end{bmatrix}$$

Using the above relations, a matrix $\mathbf{B}$ can be defined as the relation between the rate of deformation and velocities as,

$$\{\mathbf{D}\} = \mathbf{B}\dot{\mathbf{d}} \tag{B.9.1}$$

Using the above definition and Equation B.2.12, the internal nodal forces are then given by

$$\{\mathbf{f}\} = \int_{\Omega} \mathbf{B}^T \{\boldsymbol{\sigma}\}\, d\Omega \tag{B.9.2}$$

The algorithm for explicit time integration is then given by

1. Set initial conditions ,
   (a) $\dot{\mathbf{d}}^0$
   (b) $\boldsymbol{\sigma}^0$
   (c) $\mathbf{d} = 0$
   (d) n=0, t=0
   (e) compute $\mathbf{M}$
2. Initialization of force vectors and accelerations
   (a) Set global force vector to zero $\mathbf{f}^n = 0$
   (b) Set global external nodal forces $\mathbf{f}^{External,n} = 0$
   (c) Set local internal forces to zero $\mathbf{f}_e^{Internal,n} = 0$
   (d) Loop over each element
      i. Loop over quadrature points ξ_Q
         A. Calculate internal nodal forces $\mathbf{f}_e^{Internal,n} = j\mathbf{B}\sigma W_l$
   (e) Compute external nodal forces on element $\mathbf{f}_e^{External,n}$
   (f) Compute the difference between external and internal nodal forces on element $\mathbf{f}_e^n = \mathbf{f}_e^{External,n} - \mathbf{f}_e^{Internal,n}$
   (g) Reassemble global force vector $\mathbf{f}^n$ from $\mathbf{f}_e^n$
   (h) Compute accelerations $\ddot{\mathbf{d}}^n = \mathbf{M}^{-1}\mathbf{f}^n$
   (i) Determine Δt
3. Increment time $t^{n+1} = t^n + \Delta t^{n+1/2}$ and $t^{n+1/2} = \frac{1}{2}\left(t^n + t^{n+1}\right)$
4. Update nodal velocities $\dot{\mathbf{d}}^{n+1/2} = \dot{\mathbf{d}}^n + \left(t^{n+1/2} - t^n\right)\ddot{\mathbf{d}}^n$
5. Apply boundary conditions on Γ

6. Calculate displacements $\mathbf{d}^{n+1} = \mathbf{d}^n + \Delta t^{n+1/2}\dot{\mathbf{d}}^{n+1/2}$
7. Apply constitutive model knowing displacements for each element
   (a) Loop over quadrature points ξ_Q
      i. Based on constitutive model, calculate measure of deformation, ex $D_{ij}^{n-1/2}$, F_{ij}^n or E_{ij}^n
      ii. Determine stresses, σ_{ij}, at quadrature points via constitutive equation
      iii. Calculate internal nodal forces $\mathbf{f}_e^{Internal,n} = j\mathbf{B}\sigma W_l$
   (b) Compute external nodal forces on element $\mathbf{f}_e^{External,n}$
   (c) Compute the difference between external and internal nodal forces on element $\mathbf{f}_e^{n+1} = \mathbf{f}_e^{External,n+1} - \mathbf{f}_e^{Internal,n+1}$
   (d) Reassemble global force vector $\mathbf{f}^{n+1}$ from $\mathbf{f}_e^{n+1}$
   (e) Calculate internal energy
8. Determine accelerations $\ddot{\mathbf{d}}^{n+1}$
9. Calculate external and kinetic energies. Ensure energy conservation $W_{kinetic} + W_{internal} - W_{External} \leq$ Tolerance O(10^{-2})
10. Using internal energy, density and the equation of state, update pressures inside elements.
11. Calculate new time step Δt.
12. Return to step 3. unless simulation time reached.

Appendix C

Arbitrary Lagrangian Eulerian Formulation

C.1 Introduction

In finite element methods materials that undergo large deformations are difficult to simulate due to severe mesh distortions. A method to combat this problem is the arbitrary Lagrangian Eulerian (ALE) formulation which uses a remapping step to correct for large element deformations. In this formulation, simulation of the material movement is carried out as outlined in the previous section. However, before continuing on, the mesh is mapped from its current state back to either its original state, which in essence is performing a purely Eulerian calculation, or to some arbitrary intermediate state. How the mesh is remapped is the topic of several types of algorithms as outlined by Benson [117]. In the present work, a complete remapping to the original state is used and so the topic of remapping algorithms is omitted here.

In addition to the presentation of the governing equations and numerical implementation of the ALE formulation, a section regarding fluid structure interaction (FSI) is included. A discussion of the penalty coupling method which is utilized in the present proposal is given.

C.2 An Introduction to ALE

In the ALE formulation the main concern, as was with the finite element formulation, is the advection (movement from one element to another) of momentum as well as other conserved variables (mass and energy). Instead of calculating the momentum at the element level and then advecting the momentum through the faces of the element, a staggered mesh is developed so that the momentum at the nodes is advected directly. In essence, the ALE computation is given by:

1. Perform a Lagrangian time step.

2. Perform an advection step.

   (a) Calculate the transport of the element centered variables such as density, energy, stress tensor, and plastic strain.

   (b) Calculate the momentum transport (nodal centered) and update the velocity.

The element centered variables are advected first since the mass is required to update the velocities in the new orientation.

C.3 Fluid Structure Interaction

A penalty coupling methodology is used to model the fluid structure interaction within LS-Dyna [49]. This method tracks the relative displacement between the node of the solid material (sometimes referred to as the Lagrangian material) and the fluid material (sometimes referred to as the Eulerian material). As the fluid material penetrates the surface of the solid material a proportional force, based on the constitutive properties of the interacting materials, was distributed to the Eulerian and Lagrangian nodes. Figure C.1 is a schematic of the penalty coupling algorithm.

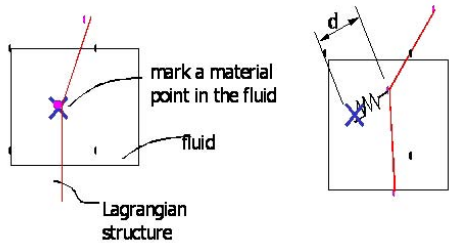

Figure C.1: Schematic of the penalty couple implementation [50].